Interface behavior of fiber reinforced polymer composites externally glued to quasi-brittle substrates

Dissertation
submitted to and approved by the

Department of Architecture, Civil Engineering and Environmental Sciences
University of Braunschweig – Institute of Technology

and the

Department of Civil and Environmental Engineering
University of Florence

in candidacy for the degree of a
Doktor-Ingenieur (Dr.-Ing.) /
Dottore di Ricerca in "Processes, Materials and Constructions in Civil and Environmental Engineering and for the Protection of the Historic-Monumental Heritage"

by
Pietro Carrara
born 24/08/1984
from Parma, Italy

Submitted on   20/March/2014

Oral examination on   05/May/2014

Professorial advisors   Prof. A. Vignoli
                          Prof. H. Budelmann

2014

To the people who teach me life, my father, my mother, my brothers, my uncle Giuseppe, my aunt Angela and to Daniela.

..and finally, to me, I deserve it!

Alle persone che mi hanno insegnato la vita, mio padre, mia madre, i miei fratelli, i miei zii Giuseppe e Angela e a Daniela.

...e, in ultimo, a me, credo di meritarlo!

Acknowledgements

Summary

Large part of world monumental heritage and many existing structures (e.g. public and private buildings and bridges) need structural intervention to be preserved and protected from ageing, fixing all the vulnerabilities that, especially in case of seismic events, may lead to serious consequences. The use of externally glued fiber-reinforced polymers (FRP) as reinforcement to overcome the tensile deficiency of quasi-brittle structural members (e.g. concrete beams and shear walls or masonry arches and vaults) has gained great popularity during the last years. Experimental and theoretical studies demonstrated that, among the different failure mechanisms observable in this kind of glued joints, one of the most important is the debonding. It occurs when the shear capacity of the system is reached and a crack develops underneath the bond plane a few millimeters inside the substrate, causing the detachment of the composite element.

The debonding failure is extremely brittle and can be considered as the results of the accumulation of damage in a limited number of critical zones, corresponding to the joint interface where the bonding stresses between reinforcement and substrate are exchanged. Consequently, a deep understanding of the stress transfer mechanisms taking place at the interface level and the related problems is mandatory for a safe and correct employment of this technique.

In the present work the interface behavior of FRP joints is studied by means of experimental and numerical studies. In particular, a new single-lap test setup is proposed in order to stably follow, for the first time, the entire failure process, usually not completely available due to its unstable and brittle nature. By means of this setup, two experimental campaigns, the first on concrete and the second on ancient masonry, are performed. The test results highlighted a dependence of the global behavior from the initial bonded length and suggested the presence of non-negligible stresses orthogonal to the bonding plane as possible responsible for such peculiarity. Moreover, comparing the results on concrete and on masonry, it has been shown how, for this latter kind of substrates, the behavior is strongly influenced by the material texture and composition.

To simulate the effects of the interaction between normal and tangential stresses, a novel cohesive zone model based on a coupled normal-tangential interface law is presented. Then, the model is validated by means of comparisons with well established models and experimental data from literature. Finally, the results has been debated, highlighting in particular the effects on the failure mechanism and on the bonding strength along the bonded length.

Furthermore, the problem of the fatigue failure behavior is addressed. A new thermodynamically consistent numerical model is formulated coupling damage and plasticity and assuming

pure shear loading conditions. Two damage parameters were introduced, while a linear softening function is defined into an ad-hoc admissible states domain ruling the plastic behavior. Comparisons with experimental data from the literature confirm the validity of the model and its accuracy in predicting the global behavior of an FRP reinforcement subject to cyclic loading.

Finally, taking advantage of new experimental studies and starting from theoretical considerations, a modified practical design formula for the debonding capacity for FRP reinforcements applied on masonry substrates is proposed. A database of bond test results between fiber reinforced polymer and masonry is collected and, after an overview of the design rules at disposal, an alternative formula is calibrated using statistical methods. The main parameters influencing the ultimate load are defined through a correlation analysis and different assessment approaches are accounted for. The proposed approaches are then discussed highlighting the improvements with respect to design formulas available to date.

"Tell me and I forget, teach me and I may remember, involve me and I learn."

BENJAMIN FRANKLIN
Politician, 1706-1790

"I don't want to be that guy mumbling into his drink at a bar."

BILL MURRAY
Actor, 1950

Contents

CONTENTS

List of Figures

List of Tables

Glossary

Roman Symbols

$\boldsymbol{A}_j$	Matrix of the coefficient of the discretized differential equations problem.
$\boldsymbol{K}$	Linear elastic interface stiffness matrix.
$\boldsymbol{R}_j$	Matrix of the non-linear coefficient relative to the point $j+1$ in the final difference solution method.
$\boldsymbol{S}_j$	Matrix of the non-linear coefficient relative to the point j in the final difference solution method.
$\boldsymbol{y}(x)$	Vector collecting the unknown functions solving a differential equations system.
$\boldsymbol{y}^{(i)}$	Vector collecting the values of the unknown quantities solving a differential equations system at the point i.
$\hat{F}$	Peak load of a pull-out test.
$\hat{s}$	Slip corresponding to the maximum bond stress attainable in power-fractional interface law.
$\mathcal{G}_a$	Tangent modulus of the adhesive.
$\mathcal{G}_c$	Tangent modulus of the concrete.
$\mathcal{G}_f$	Tangent modulus of the composite.
$\mathcal{G}_m$	Tangent modulus of the masonry.
$\mathcal{L}_{cr}$	Energy released by the crack propagation.
$\mathcal{L}_{ext}$	External work.

$\mathcal{W}_d$	Dissipated work.
$\overline{s}$	Slip computed at the top surface of the composite element.
A	Generic cross-sectional area.
a	Length of the crack.
A_f	Cross-sectional area of the composite element.
b	Generic width.
b^*	Effective detached width.
b_f	Width of the applied FRP reinforcement.
b_p	Width of the regularizing epoxy putty.
b_{fl}	Width of a three-point-bending specimen.
c	Generic parameter. Only in Sect. 4: cohesion parameter.
C_p	Coefficient of porosity.
D	Scalar damage parameter.
D_K	Damage parameter related to the fatigue stiffness degradation.
D_τ	Damage parameter related to the loss of bond strength due to cyclic actions.
E_c	Young's modulus of the concrete.
E_f	Young's modulus of the fibers or of the composite element.
E_m	Young's modulus of the masonry.
$E_{f,eff}$	Effective or measured Young's modulus of the composite.
F	Applied force.
f	Deflection in a three-point-bending test. Frequency distribution (only in Sect. 5).
$F(\cdots)$	Admissible states domain function or yielding criterion.

GLOSSARY

f_c — Generic compressive strength.

f_t — Generic tensile strength.

f_{ck} — Characteristic compressive strength.

f_{cm} — Mean compressive strength.

$f_{ct,fl}$ — Flexural strength of the concrete.

f_{ctm} — Mean value of the concrete tensile strength.

F_{Max} — Maximum or asymptotic debonding force. Pulling force corresponding to the effective bonded length.

$f_{t,flex}$ — Tensile strength form flexural test.

$f_{t,split}$ — Tensile strength from splitting test.

$f_{tm,fl}$ — Flexural strength of the masonry.

G — Generic energy release rate.

G_F — Measured mode-I (or opening) fracture energy.

G_I — Fracture energy at disposal (or energy release rate) in mode-I (i.e. opening) in a mixed mode process.

G_{II} — Fracture energy at disposal (or energy release rate) in mode-II in a mixed mode process.

G_{TOT} — Total fracture energy at disposal for the equivalent interface law in a mixed mode process. $G_{TOT} = G_I + G_{II}$.

h — Generic height.

$h(\xi)$ — Heaviside step function.

h_n — Spatial decomposition step in the finite difference procedure.

h_{fl} — Height of a three-point-bending specimen.

I_f — Cross sectional moment of inertia of the composite element.

k_b — Generic width coefficient.

k_f — Stiffness per unit width of the composite element. $k_f = E_f t_f$.

K_0^{1D} — Initial stiffness in power-fractional interface law.

$k_{5\%}$ — Coefficient defining the characteristic values of a parameter.

K_σ — Linear elastic interface stiffness in normal direction.

K_τ — Linear elastic interface stiffness in tangential direction.

$K_{el,0}$ — Undamaged (or initial) linear elastic stiffness for the fatigue interface model.

K_{el} — Linear elastic initial stiffness in a pure shear cohesive model.

K_{eq} — Equivalent linear elastic stiffness in the equivalent interface law.

k_N — 5% characteristic fractile factor for N measurements.

K_{pl} — Plastic hardening (if $K_{pl} > 0$) or softening (if $K_{pl} < 0$) modulus.

L — Complessive length of the FRP reinforcement applied.

l — Generic length.

l_b — Bonded length of the FRP reinforcement applied.

l_{eff} — Effective bonded length.

l_{fl} — Length of a three-point-bending specimen.

M — Generalized sectional bending moment.

N — Generalized sectional axial force.

N_f — Number of fatigue cycles prior to failure.

q — Kinematic hardening back stress.

R — Thermodynamical force associated with the plastic behavior.

R^2 — Coefficient of determination of a linear regression.

R_i i^{th} extreme studentized deviation value for the G-ESD outliers research test.

s Relative displacement in tangential direction between the composite element and the substrate, namely *slip*.

s_1 Slip corresponding to the maximum bond stress attainable τ_{max}.

s_2 Ultimate slip or slip corresponding to the complete de-cohesion of the interface.

s_{el} Elastic part of the slip.

$s_{f,u}$ Fatigue endurance parameter.

$s_{i+1/2}$ Slip between two subsequent strain gauges.

s_{pl} Plastic part of the slip.

$sign(\xi)$ Sign function.

t Time variable.

t_m^* Effective depth of the substrate.

t_c Thickness of the compliance volume.

t_f Nominal thickness of the FRP reinforcement applied.

$t_{f,eff}$ Effective of measured thickness of the FRP reinforcement applied.

$t_{f,eq}$ Equivalent thickness of the FRP reinforcement applied. Thickness of solely fibers which provide machanical characteristics equal to the laminated element.

$t_{p,d}$ p^{th} percentile of a t distribution with d degrees of freedom (i.e. d is the sample size).

u Generic longitudinal (or tangential) displacement.

U_e Internal energy of the material.

V Generalized sectional shear force.

v Relative displacement in normal direction between the composite element and the substrate.

v_1 Opening displacement corresponding to the maximum normal stress attainable σ_{max}.

v_2 Ultimate opening displacement in normal direction.

w Generic displacement jump.

w_i Weigth of the ith value in a wighted statistical regression (Sect. 5).

$X(\alpha, R)$ Thermodynamical force associated with the internal hardening or softening variable.

Y_K Damage source related to the fatigue loss of bond strength.

Y_τ Damage source related to the fatigue stiffness degradation.

$\boldsymbol{A}(x, \boldsymbol{y}(x))$ Matrix associated with the differential equations problem.

$\boldsymbol{B}_0$ Matrix associated with the boundary conditions at the free end.

$\boldsymbol{B}_{l_b}$ Matrix associated with the boundary conditions at the loaded end.

Greek Symbols

α Internal plastic hardening or softening variable.

α_{outl} Significance level of the G-ESD outliers research test.

β_i Generic exponent to be applied to the compressive strength of the substrate in the formula defining the maximum debonding force attainable as calculated at the ith statistical regression (Sect. 5).

β_{outl} Confidence interval of the G-ESD outliers research test.

$\overline{\boldsymbol{\alpha}}$ Non-zero part of the imposed right-hand-side vector term.

$\boldsymbol{\rho}$ Vector collecting the displacement jumps in normal and tangential direction.

$\boldsymbol{\rho}_1(v_1, s_1)$ Vector collecting the displacements in normal and tangential direction at the onset of the softening branch. $\boldsymbol{\rho}_1 = \{v_1, s_1\}^T$.

$\boldsymbol{\rho}_2(v_2, s_2)$ Vector collecting the displacements in normal and tangential direction at complete debonding. $\boldsymbol{\rho}_2 = \{v_2, s_2\}^T$.

$\boldsymbol{\sigma}(v, s)$ Vector collecting the normal and tangential stresses at the interface level.

χ Curvature of the composite element.

δ Generic displacement measured during a pull-out test. Only in Sect. 5: safety ratio between the experimental and theoretical value of the maximum debonding force attainable.

$\delta(v, s)$ Total displacement jump in the equivalent cohesive law (Sect. 4).

δ_1 Loaded end displacement (or slip) during a pull-ou test.

$\delta_1(v_1, s_1)$ Total displacement at the onset of the softening branch in the equivalent interface law.

δ_2 Free end displacement (or slip) during a pull-ou test.

$\delta_2(v_2, s_2)$ Total displacement at the complete debonding in the equivalent interface law.

δ_p Displacement of the application point of the pulling force during a pull-out test.

η Kinematic hardening relative stress.

γ Generic shear deformation or generic plastic multiplier or plastic flow rate (par. 4.5).

Γ_f Generic fracture energy (or toughness).

Γ_{II} Fracture energy (or toughness) in pure mode-II.

Γ_I Fracture energy (or toughness) in pure mode-I (or opening).

$\hat{\sigma}_0$ Adimensionalization stress parameter in the finite difference method strategy for the mixed mode model.

$\hat{\tau}$ Maximum bond stress attainable in power-fractional interface law.

$\hat{\tau}_0$ Adimensionalization stress parameter in the finite difference method strategy for the pure shear model.

$\hat{\varepsilon}(c_j, \beta_j)$ Object function to be minimized in a generic statistical regression (Sect. 5).

λ_w Width ratio. $\lambda_w = b_f / b_m$.

λ_i i^{th} extreme studentized deviation threshold value for the G-ESD outliers research test.

ν Generic Poisson's ratio.

ν_c Poisson's ratio of the concrete.

$\overline{\varepsilon}$ Axial strain computed at the top surface of the composite element.

$\overline{\sigma}_{eq}$ Equivalent maximum stress attainable in the equivalent interface law.

ϕ Internal friction angle.

$\psi(\cdots)$ Potential of dissipation.

ρ Ratio between the stiffness per unit width of the composite and of the substrate.

$\rho_{i,j}$ Pearson's coefficient of correlation between the aleatory variables X_i and X_j.

σ Generic stress or normal stress.

$\sigma_{cohes.}$ Generic cohesive stresses.

$\sigma_{i,j}$ Covariance between the aleatory variables X_i and X_j.

σ_i Standard deviation of the aleatory variable X_i.

σ_{max} — Maximum stress attainable in normal-tensile direction.

σ_{yy} — Normal stresses in y direction in the finite element analyses.

τ — Generic tangential or bonding stress.

$\tau(s)$ — Bond-slip law expression.

τ_0 — Maximum bond stress attainable in pure mode-II or pure shear strength.

τ_y — Actual yielding stress for the fatigue interface model.

τ_{frict} — Tangential friction at the interface level.

$\tau_{i+1/2}$ — Bonding stress halfway between two subsequent strain gauges.

τ_{max} — Maximum bond stress attainable or bond strength.

τ_{xy} — Tangential stress in the finite element analyses.

$\tau_{y,0}$ — Initial (or monotonic) yielding stress of the interface for the fatigue interface model.

θ — Generic sectional rotation.

$\Theta(\cdots)$ — Helmholtz free energy.

ε — Generic cross sectional axial strain.

ε_i — FRP strain at the position x_i.

$\varepsilon_i(c_j, \beta_j)$ — Error between the ith experimental value and the corresponding theoretical value as defined by the jth statistical regression (Sect. 5).

ε_m — Mean strain.

φ — Cross sectional plane rotation of the composite element.

Subscripts

a — Quantity relative to the adhesive.

b — Quantity relative to the bonded area.

c — Quantity relative to concrete.

f — Quantity relative to fibers or composite element.

k — Characteristic quantity.

m — Quantity relative to masonry.

p — Quantity relative to the regularizing epoxy putty.

s — Quantity relative to the substrate.

x — Quantity in the x direction.

y — Quantity in the y direction.

z — Quantity in the z direction.

ACI — Quantity from the ACI 440.2R-08 guideline [10].

CNR — Quantity from the CNR-DT 200 Italian guideline [7, 8].

DMG — Quantity related to damage processes.

el — Elastic quantity.

exp — Experimental value.

FIB — Quantity from the *fib* bulletin 14 guideline [9].

fl — Quantity relative to a flexural test.

$JSCE$ — Quantity from the Japanese Society of Civil Engineers 2001 guideline [11].

num — Numerical quantity.

pl — Plastic quantity.

th — Theoretical value.

$TRIAL$ — Trial value.

Other Symbols

$\Delta\bullet$ — Finite time variation of a variable.

$\dot{\xi}$ — Time derivative or rate of variation of the variable ξ.

$\bar{\bullet}$ — Imposed quantity.

$\tilde{\bullet}$ — Adimensional quantity.

Acronyms

GLOSSARY

B_new   Recent Clay Brick.

B_old   Ancient Clay Brick.

BC   Boundary Conditions.

BFRP   Basalt Fiber Reinforced Polymer.

CFRP   Carbon Fiber Reinforced Polymer.

COD   Crack Opening Displacement.

CPD   Cumulative Probability Function.

CZ   Cohesive Zone.

FDM   Finite Difference Method.

FEM   Finite Element Method.

FRP(s)   Fiber Reinforced Polymer(s).

G-ESD   Generalized Extreme Studentized Deviate test (outliers research test).

GFRP   Glass Fiber Reinforced Polymer.

LE   Linear Elastic.

LEFM   Linear Elastic Fracture Mechanics.

LVDT   Linear Variable Displacement Transducer.

NS_limes.   Natural Stone - Limestone or calcareous stone.

NS_tuff   Natural Stone - Tuff.

OLS   Ordinary Least Square.

PDF   Probability Density Function.

SRP   Steel Reinforced Polymer.

W/C   Water-to-cement ratio.

WLLS   Weighted Linear Least Square.

1

Synopsis

1.1 Introduction and general framework

Large part of world monumental heritage and many existing structures (e.g. public and private buildings and bridges) need structural interventions to be preserved and protected from aging, fixing all the vulnerabilities that, especially in case of seismic events, may lead to serious consequences. In the last years, a few standard codes [14, 15] dealing with strengthening, rehabilitation and seismic assessment of monumental structures have been developed. One of the widely accepted key aspects of these guidelines is the adoption of low invasive and high efficient strengthening techniques, in order to keep intact the historical and artistic goods stored and conserved in such monumental buildings. The low-invasiveness concept finds its relevance also in existing buildings (private or public), since it permits to retrofit and restore structures generating minimum drawbacks to the users, thus limiting the economic impact of the interventions.

Some recent structural restorations [16, 17] demonstrated that the adoption of Fiber Reinforced Polymer (FRP) as external strengthening ensures the respect of the afore-mentioned properties. In fact, the high resistance of the fibers employed and their low weight-to-strength ratio made of this technique one of the most attractive to overcome the tensile deficiency of quasi-brittle structural members (e.g. concrete beams and shear walls or masonry arches and vaults). These circumstances stimulated in the last years the study of new numerical and analytical models to understand the ultimate behavior of this kind of reinforcement. Simultaneously, experimental and theoretical studies clarified different aspects of the behavior of the externally glued FRPs. In particular, it has been

demonstrated that, among the different failure mechanisms observable in this kind of glued joints [18], one of the most important is the debonding. It occurs when the shear capacity of the system is reached and a cohesive crack nucleates and develops underneath the bond plane a few millimeters inside the substrate, causing the detachment (or de-cohesion) of the composite element.

The debonding failure is extremely brittle and can be considered as the results of the accumulation of damage in a limited number of critical zones, while, usually, the remaining parts of the structure remain in elastic regime. These zones, where the damaging and failure processes are depleted (i.e. the process zones) and the bonding stresses between reinforcement and substrate are exchanged, correspond to the joint interface. Consequently, a deep understanding of the bonding behavior is essential to provide design rules which ensure the prescribed safety requirements from both serviceability and ultimate standpoint, as also mentioned in some design guidelines [8–11, 19].

1.2   Aims and objectives

The present work is focused on the interface behavior of the fiber-reinforced polymers (FRP) composites externally bonded on quasi-brittle materials, i.e. concrete and masonry. The problem of debonding failure is investigated by means of experimental and numerical studies. Particular attention is paid to the full-range development of the debonding crack and to the effects of cyclic loadings and peeling stresses (i.e. orthogonal to the bonding plane). In particular, both the fracture mechanics processes as well as the failure mechanisms are deeply investigated.

Concerning the concrete substrate, the effects of the bonded length on the global behavior are experimentally investigated and a new test setup is designed and validated in order to overcome some drawbacks of the setups available to date. The same apparatus is used to study various peculiarities of the bonding behavior of FRP-masonry joints, trying to overcome a knowledge gap regarding the FRP effectiveness that separate masonry from concrete substrates. As a matter of fact, for this latter, many studies are available, while the interest for the FRP reinforced masonry has grown up only recently. The effects of mortar joints and the role of the micro-structure and texture of the masonry substrate on the maximum debonding load is herewith faced, especially in the case of ancient masonry.

The main goals of the present work are essentially three. Firstly, the development of a new numerical tool able to correctly reproduce the interactions between: (i) the damage at the interface level, (ii) the mode-mixity of the fracture propagation process and (iii) the failure mechanisms exhibited by this kind of joints. The second aim is to propose a new simple model able to predict the fatigue behavior of an FRP glued joint. Finally, the third goal is to calibrate new design formulas to correctly predict the debonding load of FRP reinforcement externally applied on masonry substrates.

1.3 Outline of the thesis

To illustrate the work performed, here a brief explanation on how this thesis is organized is given.

In **Section 2**, the main topics related to the externally glued FRPs mechanics and employment are introduced. Moreover, a brief state of the art concerning the experimental and numerical studies available to date is given. The major open issues that lead to the present studies will be highlighted as well as some problems not yet solved that can constitute a natural development of the present work.

In **Section 3**, a new single-lap test setup is proposed in order to permit to stably follow the entire failure process, usually not completely available because of its unstable and brittle nature. Main peculiarity of the proposed setup is the driving technique, which permits to obtain the entire equilibrium path highlighting how it is dependent from the bonded length. Two experimental campaigns, the first on concrete and the second on ancient masonry, are performed, showing that, decreasing the bonded length, there is a transition in the post-peak phase of the tests form an unstable behavior (i.e. snap-back) to a softening branch. Furthermore, in both concrete and masonry a "*two-way debonding*" is observed in specimen with a bonded length greater than the effective bonded length (i.e. the minimum bonded length that allows to reach the maximum debonding force). This mechanism involves a debonding crack that firstly nucleates at the loaded-end and propagates toward the opposite side, thus reducing the bonded length. When the snap-back regime is reached, the propagation of the first crack stops and a second crack starts at the free-end of the plate while the central part of the joint interface is still sound. Then, the second crack propagates toward the loaded-end until the complete detachment of the reinforcement from the substrate. Differently, for short bonded length a unique

crack nucleating at the free-end and propagating toward the opposite side is noticed. The changes in the failure scheme between *"short"* and *"long"* specimens are related to out-of-plane displacements causing non-negligible peeling stresses (i.e. orthogonal to the bonding plane) arising at the free-end of the reinforcement during the post-peak phases of the tests. Thus, as the bonded length decrease the debonding cannot be considered uniquely a mode-II (i.e. pure shear) fracture process, but mode-I (i.e. opening) influence becomes more prominent leading to a mixed-mode mechanism. Such evidence is also confirmed by the fracture energy, which diminishes changing from long to short bonded lengths, and by the maximum shear stress attainable that decreases in those areas where out-of-plane displacement are observed. In addition, for masonry substrates, the tests point out some differences in behavior in comparison with concrete, although the main mechanical processes are similar. Indeed, for masonry some peculiarities related to the texture (e.g. presence of heterogeneities) and the permeability to the glue of the substrate are noticed. These parameters have a role in governing both the debonding behavior and the volume of substrate involved in the stress transfer process, leading thus to a variation in the fracture energy at disposal that is not accounted for in the models available to date in literature. Finally, it is pointed out how the mortar joints, even not responsible for a change in the maximum pulling force attainable, trigger some peculiarity in the local behavior in comparison with composites applied on bricks only.

In **Section 4**, is firstly summarized a model to simulate the joint behavior between FRP and quasi-brittle materials under the hypothesis of pure shear loading (i.e. mode-II process). Then, a novel cohesive zone model based on interface laws coupling tangential and normal (i.e. peeling) behavior is formulated to reproduce the effects of the mode-mixity on the global behavior as well as on the failure mechanisms. To the purpose, a cracking criterion governing the interface strength in normal-tensile and tangential direction is introduced, while the complete debonding is ruled by an energy-based criterion providing mode-I and -II fracture energies at disposal. The softening branch of the interface law is controlled by a scalar damage parameter, defined on a global cohesive law relating a total displacement with an equivalent stress. The model is then validated through comparisons with performed and published experimental tests. Improvements with respect to available models are then illustrated and discussed. In particular, differently from classic models available in the literature, the proposed approach can reproduce the failure mechanisms observed during the experimental tests as well as the change in

the interface strength along the joint (i.e. the interface law is not unique along the glued length). Finally, after a brief introduction to the models devoted to the simulation of the cyclic behavior of the interfaces, a new numerical interface model is proposed. The interface behavior is described by means of a coupled plastic-damage model based on a bi-linear cohesive law. Moreover, to account for the loss of strength at the interface level due to both monotonic and cyclic loadings, an asymmetric elastic states domain is defined, whose lower limit (or lower yielding conditions) is always set at $\tau=0$ while the upper one (upper yielding condition) changes coherently with the experimental evidence. To the purpose a linear isotropic softening law as well as an evolution law for the damage parameter is adopted, further, a softening-dependent kinematic hardening is defined as a natural outcome from the hypothesis of non-negative bond stress. Once more, the model is validated using experimental results available in the literature and its capabilities to predict the fatigue interface behavior are debated.

In **Section 5**, an overview of the design rules available to date is given and their capability to correctly predict the maximum load attainable in an FRP-masonry bond test is statistically assessed. Then, following what suggested by the Eurocode 0 [20] and taking advantage of new experimental studies and theoretical considerations, a modified semi-empirical design formula for the debonding capacity is proposed. In particular, the main parameters influencing the ultimate load are defined through a correlation analysis, while a novel empirical power relationship is introduced relating compressive and tensile strength to avoid direct dependence of the maximum debonding force from the latter. Differently form the Italian guideline CNR-DT 200 [8], which is taken as the only guideline providing a specific section for the design of FRP-masonry reinforcements, here the empirical coefficient calibrated on the collected database of experimental results are directly stated into the relationship providing the maximum debonding force. The proposed approaches are finally discussed highlighting the improvements with respect to the available design formulas.

In **Section 6**, the major evidence arisen during the development of the present work are summarized and the principal results debated. To conclude, future possible developments are illustrated in detail.

1. SYNOPSIS

2

State of the art

Abstract

In this section a brief introduction to the major issues related to the FRP external reinforcements behavior is given, trying to highlight the most important knowledge gaps to date. Starting from experimental evidence, the major parameters involved in the failure of the glued joints are defined. The principal mechanical models (numerical and analytical) are described with particular attention to fracture mechanics approach and cohesive crack theory. Finally, some relevant issues and special problems needing more investigations are addressed.

2.1   Physics of the failure process

As introduced in Sect. 1, FRP reinforcements are commonly used to strengthen and retrofit existent buildings (see for instance Refs. [16, 17, 21–23]). In externally glued reinforcements a thin layer (in the range of about 1–2 mm for single layer applications to 3–4 mm for multiple layers applications) of composite is glued by means of epoxy resins in zones of structural members liable to tensile failure or cracking (see [24, 25] among others).

Since the very high tensile strength of the fibers employed, the most important failure mode is related to the loss of adhesion of the reinforcement [21, 26]. Usually, de-cohesion takes place inside the substrate suggesting the *debonding* as one of the major failure mode [3, 18, 27–30] (case A Fig. 2.1). It occurs when the stresses at the interface level reach the shear capacity of the reinforced system and the FRP fabric is detached from its support. Other detachment schemes are represented in Fig. 2.1 and are: the shear failure of the adhesive (case C Fig. 2.1), the delamination that takes place along the surface separating
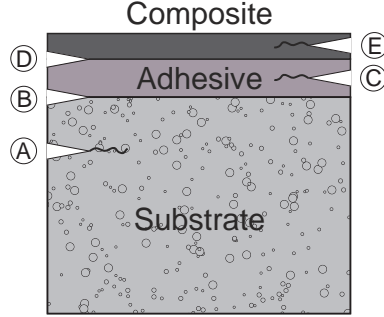
Figure 2.1: Different kind of failures in a glued joint (A - Debonding; B - Adhesive-substrate delamination; C - Shear failure of the adhesive; D - Adhesive-composite delamination; E - Fiber-matrix interlaminar failure).
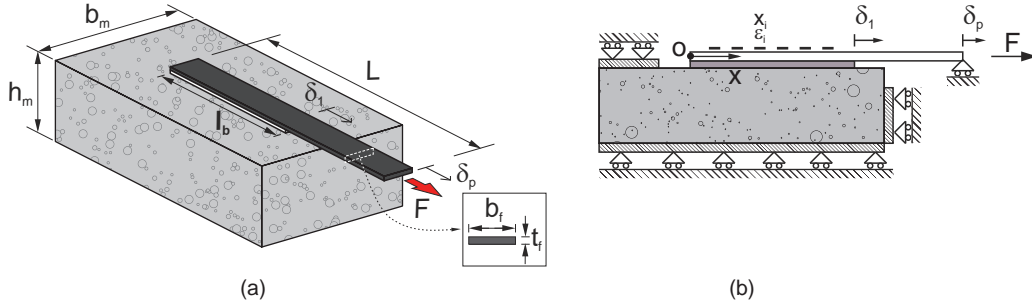
Figure 2.2: General scheme of a pull-out test: (a) geometry; (b) static scheme.

two distinct domains (e.g. FRP-adhesive or adhesive-substrate, respectively cases B and D Fig. 2.1) or phases (e.g. fiber-matrix interlaminar failure, case E Fig. 2.1).

For the practical employment of such technique it is unavoidable to pass through the experimental characterization of the strengthening effectiveness [8–10, 29, 31]. Pull-out tests are commonly used to the purpose [2, 25, 28–33]. In the literature different test setup have been proposed during the years, both dealing with the in-situ characterization and the laboratory tests. A brief review of the principal tests and the related problems is given in par. 2.4 (see Refs. [12, 30, 34, 35] for a comprehensive review). Generally, each test setup allows to apply a tensile force to a composite plate or sheet glued on a face of a properly restrained supporting prism, until the complete detachment of the composite from its substrate. A common type of test is schematically represented in Fig. 2.2.

During tests, the force F and the displacement of its point of application δ_p (i.e. the displacement of the actuator of the testing machine) together with the displacement of the first loaded section of the FRP glued area, namely the loaded end, δ_1 (Fig. 2.2)

are usually recorded, as the strain measured over the glued length of the reinforcement [2, 3, 25, 30, 32, 33, 36–38], i.e. ε_i measured at x_i from the free end (Fig. 2.2b). This permits to obtain the main peculiarities related to the failure process [8–10, 29, 31], as the global equilibrium path $F - \delta_1$ (Fig. 2.3), the peak load $\hat{F}$ and the strains profiles (Fig. 2.4).
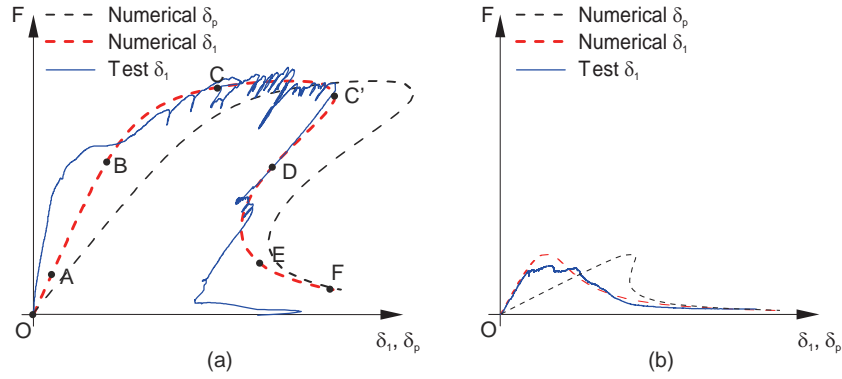
Figure 2.3: Global equilibrium paths of a pull-out tests: (a) long bonded length; (b) short bonded length.
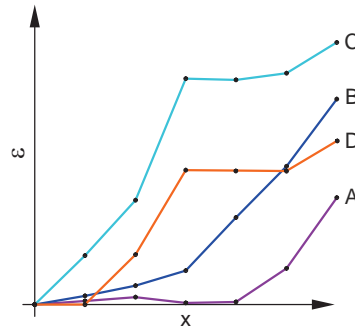
Figure 2.4: Typical strain profiles at given instant of the pull-out test for a long bonded length specimen (points are indicated in Fig. 2.3a).

The equilibrium paths are different for specimens with different bonded length [3, 39–41], namely *"long"* bonded length displays a snap-back behavior (Fig. 2.3a) while *"short"* bonded length are characterized by a softening post-peak branch (Fig. 2.3b). More in detail, for long bonded length there is an initial linear ascending branch (segment O-B in Fig. 2.3a) followed by a short non-linear path (segment B-C in Fig. 2.3a) where the load still increase until reaching the peak load (segment C-C' in Fig. 2.3a). Meanwhile, along this latter branch, the debonding crack nucleates at the loaded end and it starts to propagate

toward the opposite side. After the peak, a sub-horizontal plateau is usually present associated with a precarious phase where equilibrium is affected by frequent load drops (Fig. 2.3a). This peculiar response is due to propagation of the debonding crack which takes place in spots, where instantaneously the crack experience a widening of some tenths of millimeter [32], as pointed out by the subsequents crack fronts in Fig. 2.5 (highlighted with white dashed curves). The post peak stage is characterized by an unstable snap-back behavior where both the load and the displacement decrease (segment C'-E in Fig. 2.3a). It ends with an almost horizontal branch (segment E-F in Fig. 2.3a) where the residual load carrying capacity is principally due to the friction within the asperities of the debonding crack. In this phase the definitive failure of the reinforcement occurs. For short bonded lengths the initial ascending branch is similar to the one observed for long bonded lengths, but after the peak load a softening behavior is present instead of the unstable branch [39] (Fig. 2.3).

The different behaviors of long and short specimens has been clarified by means of numerical simulations [39–41]. This studies confirmed that the nature of the equilibrium path depends on both the bonded l_b and the unbonded $l_{ub} = L - l_b$ lengths of the plate. Indeed, if the bond length l_b is short (compared to the effective anchorage length l_{eff}), debonding occurs gradually and the pull-out curve $F - \delta_1$ displays a softening branch (Fig. 2.3b). However, also in this case, if the plate is clamped far from the edge, the unbonded part of the plate stores a big amount of strain energy. When debonding occurs, the load is reduced and the strain energy, which is suddenly released, causes a snap-back in the $F - \delta_p$ diagram (Fig. 2.3b). In other words, when debonding occurs, the elastic shortening of the free plate caused by unloading prevails against the elongation δ_1 produced by slippage of the bonded plate, and their sum δ_p diminishes.

If the bond length l_b is long enough, the snap-back in the curve $F - \delta_1$ (Fig. 2.3a) can be explained considering that, when debonding propagates from the loaded end to the free one, the unbonded part of the plate releases the stored strain energy like in the previous case.

The strain measurements are used to observe the local behavior, in particular the progress of the debonding process and the stress transfer at the joint interface [2, 3, 6] (Fig. 2.6c). It must be clarified here that, in this case, interface just means the surface separating two distinct domains, such as the reinforcement (i.e. composite plus adhesive) and the substrate.
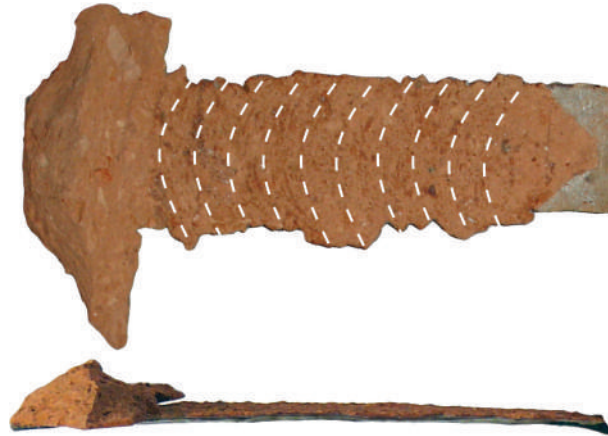
Figure 2.5: Propagation of the debonding crack in spots. Crack fronts are highlighted with white dashed lines.
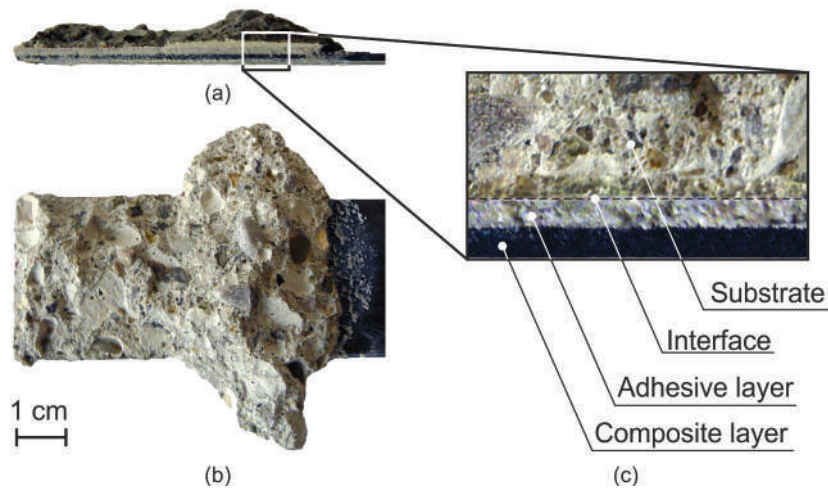
Figure 2.6: FRP reinforcement after a pull-out test. (a) side view of the debonded plate; (b) front view of the debonded plate; (c) different layers of the glued joint.

Considering Fig. 2.4 it is observable how during the linear ascending branch of the equilibrium path the strains monotonically increase from the free end toward the loaded one following an exponential-like trend [36, 39] (curves A, B in Fig. 2.4). Such variation, stating the linear elastic behavior until rupture of the composite material (see par. 3.2.1.3), accounts for the stress-transfer across the interface [25, 42, 43], as schematically reported in Fig. 2.7. Reaching about the 60-70% of the peak load $\hat{F}$, in correspondance of the segment B-C in Fig. 2.3, at the loaded end the rate of increase of the strains starts to reduce pointing out a minor effectiveness of the transfer mechanism due to the nucleation

of the debonding crack [3, 6]. At the peak load and for the entire sub-horizontal plateau the debonding and its propagation are denoted by the nearly absence of variation in the value of two subsequent strain gauges, making thus the strain profile flat [25, 36, 37, 39] (curves C, D in Fig. 2.4).
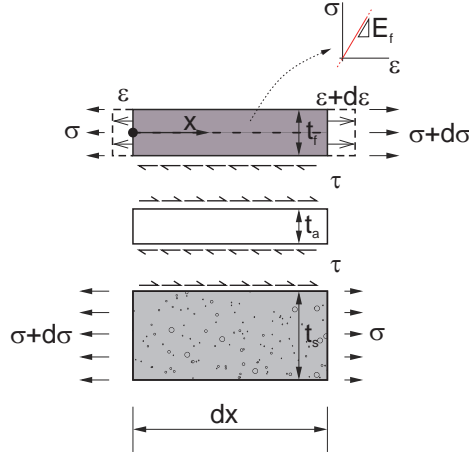
Figure 2.7: Stress transfer mechanism in a glued joint.

Whether the debonding crack develops and propagates only inside the substrate material (as reported also in [3, 25, 28, 30, 37]) is evident from Figs. 2.6a,b and 2.8. In this latter, two specimens are shown, namely a long (Fig. 2.8a) and a short (Fig. 2.8b) bonded length specimen, which display, in addition to different equilibrium paths as previously explained (Fig 2.3), different profiles of the detached substrate (as also reported in [33]). In long bonded lengths, besides a central portion displaying a uniform and thin layer of material detached, at the ends of the glued portion of the plate bulbs of material are removed. This kinking of the debonding crack suggests that in these regions takes place a change in the direction of the principal stresses, therefore the stress-transfer can be related not only to shear stresses but also to normal stresses. Differently, short bonded lengths are mostly characterized by a unique bulb with increasing thickness from the free end toward the loaded one (Fig. 2.8b). This evidence imply that out-of-plane stresses can participate to the failure mechanism.

Another peculiarity related to the bonded length of the externally glued FRP reinforcements, is the presence of a value of the bonded length over which if it is further increased the peak load does not. Indeed, it has been extensively demonstrated by many studies ([3, 25, 39–41, 44–46] among others) that, assuming constant value for all other

Figure 2.8: FRP reinforcements detached from the support prism: (a) long bonded length; (b) short bonded length.
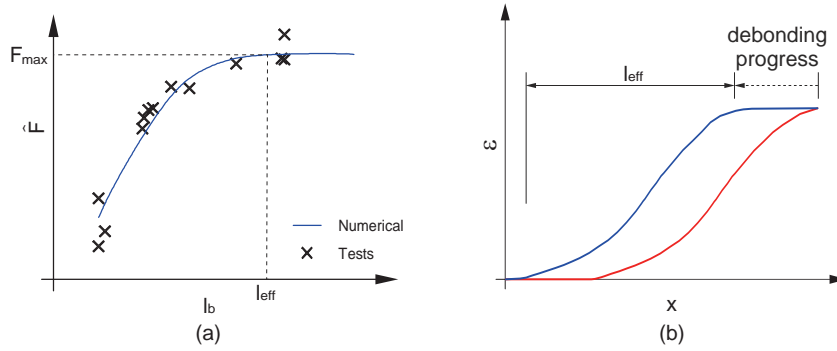
Figure 2.9: (a) Relation between bonded length and peak load $\hat{F}$. (b) Evolution of the strains profile during debonding and identification of the effective bonding length l_{eff}.

parameters, the peak load $\hat{F}$ experiences a sub-linear increase with the bonded length until a certain value, namely the *effective* or *asymptotic* bonded length l_{eff} for which the maximum debonding force F_{max} is asymptotically attained (Fig. 2.9a). In other words, for a given plate width b_f and mechanical characteristics of the reinforced system, the peak load is upper limited by a well defined value F_{max} that is reached for $l_b = l_{eff}$ and it remains constant for each $l_b > l_{eff}$.

The name *effective* bonded length is more related to the local behavior than to the maximum force attainable, since it corresponds to the maximum attained length over which the stress transfer is active [36], i.e. where the strain profile exhibit a gradient (Fig. 2.9). Fig. 2.4 clearly shows how the classical *S-shaped* trend is assumed by the strain profile along the effective bonded length [25, 36, 37, 39]. It has been shown (see [36, 39] among others) that during the debonding, along the sub-horizontal plateau of the equilibrium path (section C-C' in Fig. 2.3a), the S-shaped part of the strain profile
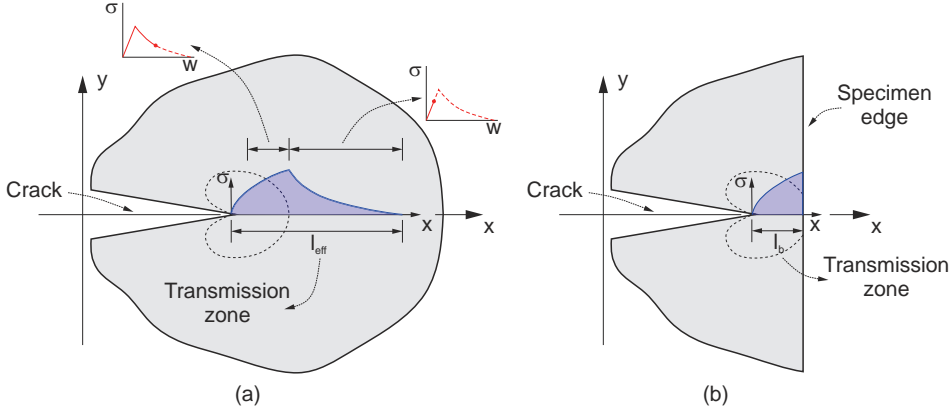
Figure 2.10: Transmission zone in different conditions: (a) l_{eff} fully established (i.e. long bonded lengths); (b) l_{eff} full development prevented by the specimen edge (i.e. short bonded length).

translate in a self-similar manner along the bonded length following the debonding crack progression (Fig. 2.9b).

For growing values of the stiffness per unit width of the reinforcement (i.e. $k_f = E_f t_f$) the effective bonded length value increases (see for instance Refs. [12, 45, 47, 48]), until approaching infinity for an ideally rigid reinforcement. This means that the stress transfer occurs in a narrower zone for soft plate compared to a stiff one.

The aforementioned evidence demonstrate the existence of a length over which the perfect bonding between the FRP and the substrate is established (Fig. 2.10a) and that this well defined length l_{eff} mostly depends upon the mechanical parameters of the composite [44, 46, 47, 49, 50]. Indeed, if the bonding is short (i.e. $l_b < l_{eff}$) the stress transfer process cannot attain its maximum efficiency and only a fraction of maximum force transmissible from the plate to the substrate can be developed [39] (Fig. 2.10b). Differently, in long bonded lengths, the transmission zone is fully established along l_{eff}, and after this, no stress transfer takes place, i.e. no strain gradient is present (Fig. 2.10a). The peak load $\hat{F}$ results thus limited by the amount of bond stresses transmissible along a portion of interface with a length $l_b = l_{eff}$ (Fig. 2.10a).

2.1.1 Fracture mechanics approach and relevant formulations

From what stated above, it follows that the study of the debonding fracture propagation is mandatory to correctly understand the mechanics of the FRP external joints. To

the purpose, it is possible to adopt the linear elastic fracture mechanics approach (*LEFM*) [26, 45, 49, 51].

In materials like masonry or concrete the stable propagation of a crack is strongly related to the tensile behavior and strength [52]. Indeed, differently from brittle materials, the stable propagation of a crack is ensured by a, even small, certain amount of tensile toughness [52], this is the reason why these materials are commonly referred as quasi-brittle. As reported in [52], it is possible to measure the resistance against the unstable propagation of a crack with the fracture energy Γ_f, which is defined as the energy required to create a unit area of a crack. It can be conceived as the part of energy provided to the system that is dissipated by the separation process in a narrow zone ahead of an imperfection or a crack tip, commonly called *"fracture process zone"* or *"damage zone"* (Fig. 2.11). This is a transition zone where voids and imperfections of the material trigger the nucleation of micro-cracks which, as the loading process advance, coalesce in a macro-crack leading to the material separation. In that zone the non-linear dissipative processes as plasticity, damage, strain softening and micro-cracking take place [41, 44, 49, 52] (Fig. 2.11), while the other parts of the domain usually remain in the linear elastic regime. Because of the displacement discontinuity introduced by the cracking process, in such area is not possible to locally define a constitutive $\sigma - \varepsilon$ law with or without work dissipation $\mathcal{W}_d$ as in the remaining part of the domain [52] (Fig. 2.12). Instead a $\sigma - w$ relationship is used, where w is an *additional deformation* [52] conceived as a the displacement jump across the crack smeared over the fracture process zone. The fracture energy Γ_f can be defined as the integral of the $\sigma - w$ relationship, i.e. its area (Fig. 2.12). Thus, the specific energy dissipated during a generic loading process is composed of two terms, the internal energy absorbed by the uncracked material U_e and the fracture energy Γ_f dissipated to create a separation surface into the domain (Fig. 2.12).

The displacement jump w represents thus the relative displacement between two faces of a crack. In case of FRP external joints it is the relative displacement between the plate and the substrate, which in tangential direction (i.e. parallel to the bonding plane) is called *slip* or s. Moreover, the $\sigma - w$ relationship turns into a $\tau - s$ law defining the bonding and the stress-transfer behavior of the joint. It is commonly called interface or bond law and it must encompass all the major peculiarities of the bonding behavior [6, 53]. In case of a perfect shear behavior, it has to define correctly the maximum stress attainable (or bond strength) τ_{max} and the corresponding slip s_1 together with the ultimate slip
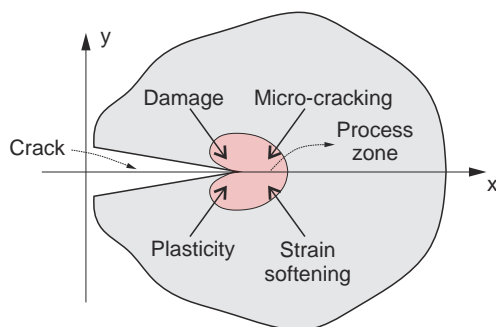
Figure 2.11: Process zone ahead of a crack with the major dissipative processes.
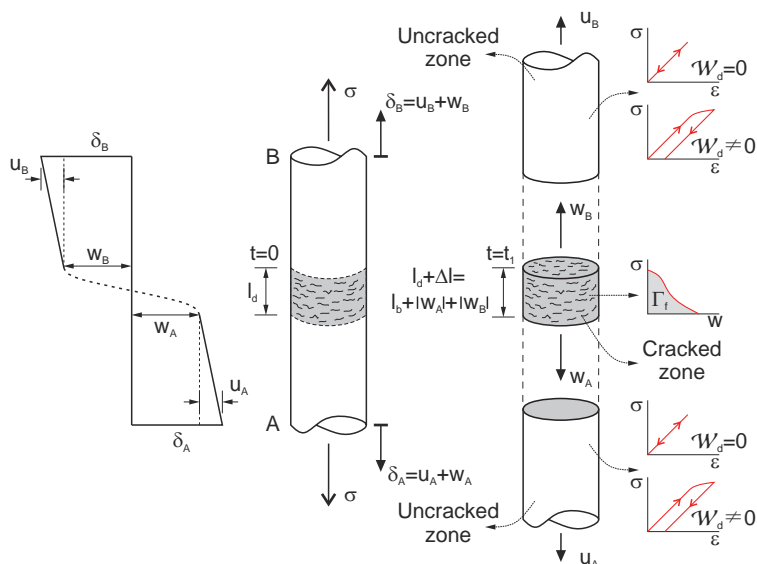
Figure 2.12: Cracked zone in a body with and behavior of the different domains.

s_2 and, obviously, the fracture energy Γ_f (i.e. the area encompassed by the curve). In particular, this latter is of primary concern in LEFM analysis of glued joints, being the major parameter influencing the monotonic maximum load attainble F_{max} [6, 37, 41].

It is worth to highlight that, the area where the displacement jumps w are present corresponds to the process zone of Fig. 2.11. This identifies the bond law as a "constitutive relationship" governing the behavior of a zone in which a $\sigma - \varepsilon$ law cannot be defined because of the presence of cracks and microcracks.

LEFM analysis is based on an energy balance between the external work furnished to the system, and the energy released by the dissipative (or non-conservative) processes [26, 45, 49, 51, 54]. Exploiting the pioneering work of Täljsten [49] and assuming that

the joint is exposed only to shear forces (i.e. mode-II fracture process), all the materials are isotropic, homogeneous and linear elastic and following the schematic representation of a glued joint in Fig. 2.13 (i.e. the transversal effects are considered negligible over the width b_f), it is possible to write a balance of work between the elastic internal energy U_e, the external work $\mathcal{L}_{ext}$ and the energy released by the crack propagation $\mathcal{L}_{cr}$.

$$U_e - \mathcal{L}_{ext} + \mathcal{L}_{cr} = 0 \,. \tag{2.1}$$
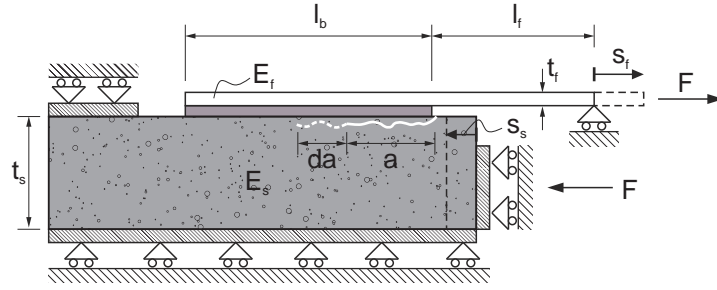
Figure 2.13: Scheme of an externally glued joint subject to shear forces and debonding crack propagation.

By differentiating Eq. 2.1 with respect to the crack length a, it is possible to define the fracture energy release rate G as

$$G = \frac{\partial \mathcal{L}_{cr}}{da} = \frac{\partial}{da} \left(\mathcal{L}_{ext} - U_e \right) \,. \tag{2.2}$$

The condition of incipient crack propagation, i.e. when the crack experience a widening from a to $a+da$, can be stated introducing the fracture energy Γ_f that here clearly assumes the role of a fracture toughness parameter, i.e. $G = \Gamma_f \Rightarrow a \to a+da$. Γ_f is also considered as an energy associated crack resistance force because comes form differentiation of the work to create a unit area crack.

During the crack propagation, the displacement jump of the system $s = s_f + s_s$ (Fig. 2.13) undergoes an increment of ds, thus

$$\frac{\partial \mathcal{L}_{ext}}{da} = Fds \,. \tag{2.3}$$

Furthermore, because of the hypothesis of linear elastic materials, the displacement s can be expresses as a linear function of the applied load F as $s = FD = Fk^{-1}$, where D is

the compliance of the system, i.e. the inverse of the stiffness k. Thus, the elastic energy stored in the elastic materials can be assumed equal to

$$U_e = \frac{1}{2}Fs = \frac{1}{2}F^2D\,. \tag{2.4}$$

It is now possible to express the incipient crack propagation condition, i.e. when a widening of the crack length da occurs, as

$$\Gamma_f = \frac{1}{b_f}\left(F\frac{\partial s}{da} - \frac{\partial}{da}\frac{1}{2}F^2D\right) = \frac{F^2}{2b_f}\frac{\partial D}{da}\,, \tag{2.5}$$

The compliance of the system can be simply expressed as

$$D = \frac{l_f + a}{E_f A_f} + \frac{a}{E_s A_s}\,, \tag{2.6}$$

where $A_f = b_f t_f$ and $A_s = b_s t_s$ are the cross-sectional areas of the reinforcement and of the support respectively. Indeed, the force at which starts and propagates the debonding until failure can be written as

$$F_{max} = b_f\sqrt{\frac{2E_f t_f \Gamma_f}{1 + \rho}}\,, \tag{2.7}$$

where

$$\rho = \frac{E_f t_f}{E_s t_s}\,. \tag{2.8}$$

In common applications, it is usual to consider $\rho \to 0$ because the thickness of the member to be strengthen t_s is much greater than the composite thickness t_f that usually is about of 1–2 mm [48].

The relationship of Eq. 2.7 has been validated in a number of studies (among others [44, 45, 48, 49, 55]) and highlights the key role of the fracture energy Γ_f in the maximum debonding load as well as the influence of the plate stiffness, confirming what previously stated in par. 2.1. Indeed, for a fixed set of parameters, increasing the plate stiffness leads to a longer stress transfer length and thus to a higher maximum debonding force F_{max}.

Even if this is a very simple way to describe the debonding behavior it allows to understand its main physical basis. Furthermore, it is worthy to note that most of the more complicate and complete approaches degenerate, for the maximum load attainable, in Eq. 2.7.

2.2 Evaluation of the fracture energy

The evaluation of fracture energy in FRP external joints to predict the maximum debonding load attainable is of primary concern [6, 25, 41, 44, 46], but, to date, not trivial. Indeed, there is not a standard protocol to measure it from pull-out tests [30], and usually it is back-calculated from Eq. 2.7 once the maximum debonding force is known [3, 56]. Nevertheless, it is well known that even apparently insignificant changes in the setups or in the specimens preparation can lead to very different values of maximum debonding force thus resulting in different values of Γ_f as well (see Refs. [30, 34, 35, 57–60]), even if the fracture energy should be a property of the system independent from the test setup or specimen features.

The situation is worsened by the impossibility, until now, to perform tests following the entire debonding process because of the unstable and brittle snap-back behavior in long bonded lengths (see par. 2.4 for a more detailed descriptions of this issues). In [30] it is proposed to fix the free end of the reinforcement in a pull-out test to avoid dynamic failures, but, even if this solution is effective for the snap-back related problems it does not allow to observe entirely the failure process.

Furthermore, it is not possible to determine the effects on the global behavior of the bulbs of material visible in Fig. 2.8 together with their formation. In particular, the role of the out-of-plane displacement related to such bulbs need more investigations. They can be representative for a mixed-mode fracture process, i.e. characterized by a non-negligible influence of mode-I (opening) process, which can reduce the fracture energy at disposal [61–63]. Indeed, it has been extensively demonstrated that the fracture energy in mode-I is much lower than in mode-II [53, 64, 65] (see also par. 3.2). Concerning the interaction between mode-I and -II in FRP glued joints there is a lack of studies in the literature, especially from the experimental standpoint [66]. In fact, although for the pure shear behavior a number of tests are available, only few studies are focused on mixed tests [28, 57] (i.e. peeling tests).

To evaluate the fracture energy, different relationships calibrated on different databases have been proposed in the literature [7–11, 67, 68]. In Sect. 5 an overview of the principal formulas is given. One of the most common assumption is that, since the debonding crack propagates inside the substrate only, Γ_f can be considered as a parameter of the substrate material only, i.e. of the tensile f_t and compressive f_c strengths [7–11]. Anyway, such

formulations are not given as a natural outcome of a test but are rather empirical or semi-empirical, thus the scattering of the results can be very high. Once more, a standard protocol to characterize externally glued joints and that permits to stably follow the entire debonding process will be useful in solving this issue.

2.3 Cohesive crack modelling and interface laws

The LEFM approach based on the energy balance is quite intuitive as far asF it is not taken into account the local softening response of the interface behavior. The analysis of the full range behavior of the interface using LEFM is possible assuming a given crack length a, and evaluating the stresses corresponding to such situation and the energy release rate and, finally, following a Griffith type criterion [69] is possible to establish whether the crack will develop stably or not [51, 70]. This imply that the LEFM approach is subdivided in two phases: the stress analysis and the fracture propagation analysis [70].

Different models were proposed to overcome the aforesaid difficulties. One of the most used is the *cohesive zone* model (see Refs. [71, 72] for a comprehensive overview of the method), which permits to describe the full range behavior, from the nucleation to the complete de-cohesion of the joint at once [61, 66, 70], i.e. in a unique phase by means of a non-linear interface law, namely the bond law. Finally, it covers the gap between stress and energy approaches that remain separate in LEFM method [46, 48, 66].

The cohesive zone or cohesive crack approach is very effective in those cases where the crack path in known a priori. To the purpose, it is necessary to introduce a new concept of interface, which is in contrast with the definition of area separating two distinct phases of a system. Here the interface is conceived from the mechanical standpoint as the surface over which the crack will develop separating thus two distinct domains of a body. The debonding process between the FRP reinforcements and its quasi-brittle support takes place with a crack usually located a few millimeters inside the substrate underneath the composite and propagates parallel to the latter (see [3, 28] among others).

The cohesive zone approach is based on the fictitious crack theory (Fig. 2.14) [73–76], which consider the interface subdivided in three different zones (as also reported in [36, 37]): (i) a fully damaged zone; (ii) a stress-transfer zone and (iii) an undamaged zone. These areas are coherently outlined with the mechanics of the problem illustrated in par. 2.1.1, therefore the fully damaged and the undamaged zones are straightforwardly

defined as the zones where the two adherents are respectively completely separated or undamaged, while the stress-transfer zone is the portion of the interface over which the stress transfer takes place (Fig. 2.10).
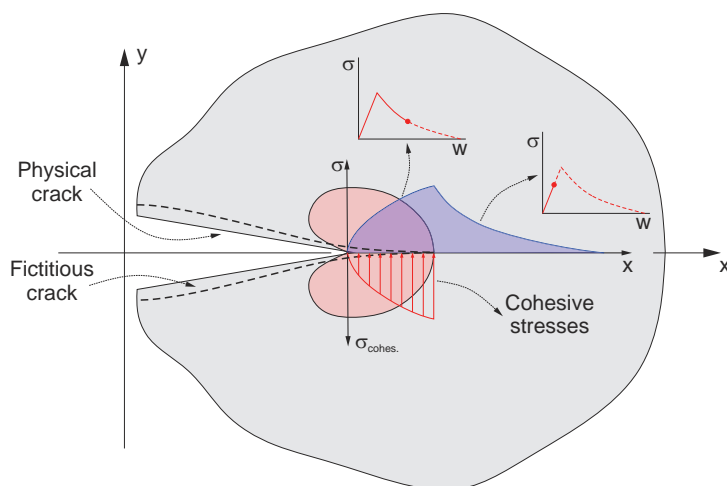
Figure 2.14: Fictitious crack approach to the crack analysis.

Basically, the fictitious crack approach accounts a virtual crack extension ahead of the tip of the physical crack (i.e. the portion of the domain effectively separated, namely where no stress can be exchanged between two adjoining surfaces of the body, Fig. 2.14). To permit the analysis of the stress and strain fields in the neighborhood of the crack apex, it is assumed that a certain amount of cohesive stresses act on the fictitious extension of the crack (Fig. 2.14), accounting for the softening behavior of the damaged material and avoiding thus the singularity at the crack tip provided by the classic LEFM theory [73–76]. In other words, the cohesive zone can be conceived as a fictitious crack which extends beyond the crack tip able to transfer stresses between its faces.

In cohesive interface models the process zone is lumped into the interface, thus a constitutive law, i.e. the interface law, is defined governing the gradual de-cohesion of the domains and the amount of cohesive stresses developed. Indeed, as two initially superimposed points along the interface start to separate, namely when the displacement jump (or gap) between the two increases, the cohesion (i.e. the capacity of the interface to transmit stresses) gradually vanishes until complete separation (i.e. the crack is fully developed and the two domains are detached). Differently, the bonding stresses (i.e. the cohesive tractions) at first increase until a maximum value (i.e. a cracking limit) then

start to decrease reaching zero at complete debonding [76]. The complete evolution of the process is thus described at once, from perfect bonding to complete separation, with a unique non linear interface relationship [61, 66].

During the years a number of models have been proposed by different authors ([6, 40, 45, 46, 48–50, 53, 61, 66, 77] among others). What makes the difference among different studies is mainly the definition of the bond law (or *cohesive law*). As a matter of fact, most of the models available to date are based on two simplifying assumptions about the bond behavior. Firstly, the whole layer in which the effect of adhesion are depleted (*compliance volume* or *bulk layer*) is lumped into the zero-thickness interface layer. Secondly, the interface is considered subject to shear stresses only, neglecting thus the stresses normal to the bonding plane (either in compression or in tension). If this hypothesis is not assumed to hold (e.g. as in [53, 78]), the compressive behavior is commonly modeled by means of an indefinite linear elastic law characterized by a very high penalty stiffness coefficient to avoid interpenetration of the domains (FRP and substrate). Concerning the tensile behavior, usually the coupling between normal and tangential stresses is neglected (i.e. the magnitude and the behavior of the interface in normal direction is not affected by the stress or displacement state in tangential direction and vice-versa). This lack of studies is mainly related to the fact that, while for the tangential cohesive law significant amount of experimental data are available, in normal direction very limited information are at disposal [53]. Among others, it can be of interest to brief introduce some studies. Alfano and Chrisfield [71] deeply investigated the mathematical and numerical implementation in a finite element environment of cohesive zone models for FRP glued joints, debating also some issues on convergence and numerical strategies to solve the non-linear debonding problem. Alfano and Sacco [72] combined the damage process at the interface level with the friction behavior among the faces of the debonding crack. Rabinovitch [61] proposed a high order solution for coupled cohesive zone models based on the Xu and Needleman interfacial potential. De Lorenzis and Zavarise [53] proposed a model with coupled mode-I and -II energies for reinforcements subject to inclined loads; here the pure shear condition could be seen as a particular case. Martinelli et al. [78] proposed a model in which the interface laws in normal and tangential direction are coupled at the instant of cracking, while the softening stage is ruled by the shear behavior only. Turon et al. [64] implemented a coupled cohesive law into a finite element code to simulate the delamination of composite

materials. Finally, a comprehensive review on numerical models for FRP debonding is presented and debated in [66].

2.4 Experimental test setup

In order to mechanically characterize the bonding between FRPs and quasi-brittle substrates, different bond-test setups were proposed in the literature. All of them are useful to define the ultimate force that causes debonding failure, to experimentally calibrate the bond-slip relationships and to measure the effective anchorage length l_{eff}. However, at the moment a widely accepted bond test does not exist even if it is known that different test setups give different results [30].

Setups can differ by many features. Firstly, boundary conditions play an important role in the global behavior. Indeed, different restraints can induce either compression or tension in the supporting prism, thus changing the failure mechanism and the maximum debonding force [34, 40, 41, 79]. Further, according to [12, 31, 34, 35] bond tests can be classified substantially depending on the test setup: double-shear tests, bending tests, and single-shear tests.

In double-shear tests, two plates are glued symmetrically on the surface of a concrete prism. An axial force is applied either to the plate or to concrete. In both cases the debonding occurs differently in the two plates because of force eccentricities or imperfections at the interface level [30, 80]. For this reason, the symmetry of the system is inevitably missed and the specimen displays a bending that may vary during the test [30, 80]. This causes tensile stresses normal to the plate (called peeling stresses) that reduce the bond strength [56].

In bending tests, the plate is glued at the bottom of a concrete beam and the tensile force in the reinforcement is induced by specimen bending [59]. The bending of the plate produces compressive stresses orthogonal to the plate, which increase the bond strength [34, 59].

In single-shear tests a pulling force is applied to a plate that is glued to a concrete block restrained by a suitable supporting system. Single shear tests seem to be less prone to the aforementioned problems, thus they have been preferred by some guidelines [8, 9].

2.4.1 Open issues on bond test setups

Some important issues are still open also for single lap shear tests. Recently, a Round Robin shown that single-shear tests carried out with different supporting systems may lead to an important scatter of the results [58, 81, 82]. Indeed, since the specimen is not symmetric, the applied load produces a couple and the concrete block can rotate, i.e. the load is applied with an initial angle. Some authors [34, 57], observed that even a small loading angle (about $1° - 2°$) is able to reduce the bond strength. For this reason, the specimens should be properly fixed and the rotations should be prevented or, at least limited.

A second issue to deal with is the extreme brittleness of debonding failure, as also briefly introduced in pars. 2.1 and 2.2. Usually single-shear tests are driven controlling the force F or the displacement δ_p of the loaded end of the plate (Fig. 2.15). Both the approaches permit to measure the peak load $\hat{F}$. However, since debonding failure is extremely brittle, the control of the test either driving the applied force or the loaded end displacement driving technique is prematurely lost and the complete equilibrium path is not available. Indeed, Fig. 2.15a shows where the control is theoretically lost controlling the force or the displacement. Anyway, the unstable behavior of the sub-horizontal plateau illustrated in par. 2.1 can trigger a premature failure also before, as stated in Fig. 2.15b. In other words, it is not possible to observe the propagation of debonding up to a complete separation of the plate from its substrate. To partially overcome this problem, in [30] it was proposed to modify the single-shear setup by fixing the loaded end of the plate. In this way it was possible to observe more complete tau-slip relationships, even if it did not allow to observe the unloading branch of the $F - \delta$ curve as well as the local behavior at the free end.

As illustrated in par. 2.1, the processes leading to the brittle behavior of the externally glued FRPs were numerically analyzed, but the experimental evidence are lacking. Other numerical investigations (among others [40, 83]) show that the displacement of the free end of the plate δ_2 increases monotonically in both long and short specimens (Fig. 2.16), and, in principle, could be used to drive the test up to the complete debonding. However, in the case of long bond length (Fig. 2.16b), the ascending branch of the curve reaches the peak with displacements δ_2 that are very small compared with δ_1 (indeed the curve
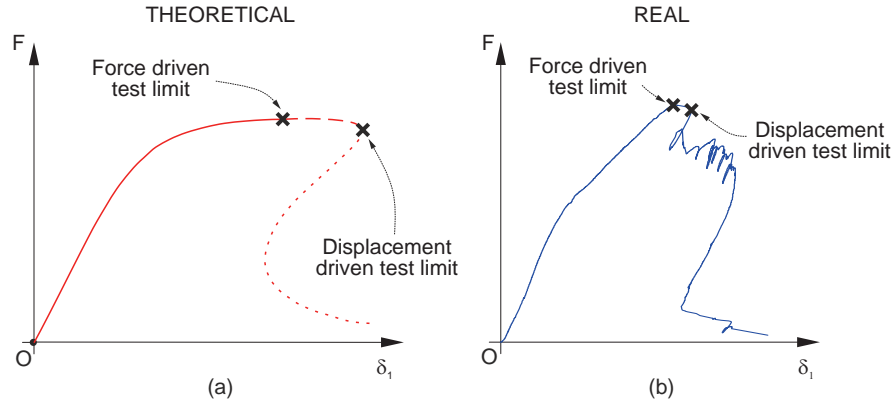
Figure 2.15: Force and displacement driven test limits: (a) theoretical behavior; (b) real behavior.

virtually disappears behind the vertical axis). This would imply some problems driving the test in specimens with very long bond lengths.
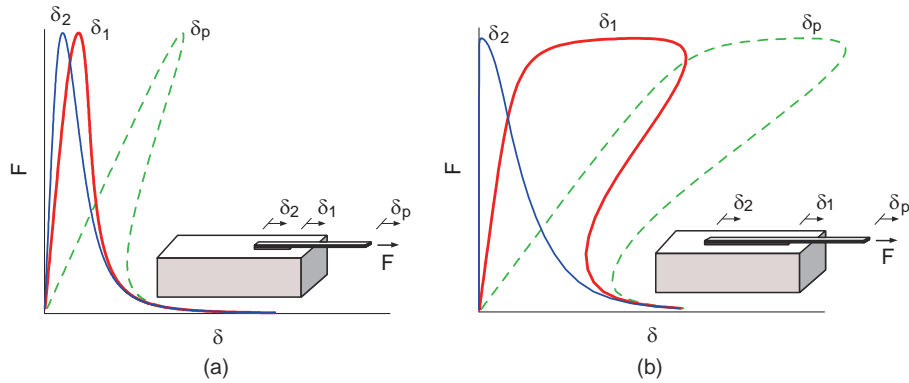
Figure 2.16: Snap-back in single shear test: (a) short bonded length l_b; (b) long bonded length.

2.5 Relevant issues and particular problems

2.5.1 Masonry substrates

It must be emphasized that there is a lack of studies concerning masonry. Indeed, the mechanical processes related to the bond of the FRPs have been widely studied for applications to concrete elements both from the experimental [25, 30, 36, 59, 84] and the numerical point of view [85–87], but for what it concerns masonry, only a limited

number of studies can be found in literature, either dealing with natural stone or clay bricks substrates. As a matter of fact, some standard codes [7–9] adjusted the design principles developed for concrete structures to masonry, even if these materials may present different mechanical behavior (e.g. orthotropy of masonry and presence of mortar joints representing discontinuities in the bonding plane, [37]). In addition, for masonry elements, it is well accepted the hypothesis of limited influence of the mortar joints [8, 9, 37], thus resulting that the bonding behavior mainly depends on the compressive and tensile strengths of the units (natural stone or clay bricks). Nevertheless, some studies highlighted an influence of the mortar joint in the local behavior, suggesting the possibilities that in certain circumstances they could govern the debonding behavior, but this issue needs a deeper investigation.

Furthermore, some recent studies points out that the the permeability to the glue of the substrate can have a key role in the global behavior [38]. In particular, Aiello et al. [88–90] focused their investigations on the bonding between FRP and two kinds of natural stone largely used to build masonry structures: Naples tuff and Leccese limestone. These experimental studies revealed differences in the failure mode related to the adopted material. More specifically, Leccese limestone displayed a very thin layer of detached substrate compared with Naples tuff specimens. Therefore, the ultimate load values changed using different kinds of stone. The differences between the two materials (Leccese limestone presents high specific weight, limited dimensions and percentage of voids and higher strength compared with Naples tuff) could justify changes in the bonding behavior, but the role played by each single parameter is not completely defined. Some similar differences were found in clay bricks masonry by Grande et al. in [38].

This aspect is more relevant for masonry than for concrete, since the first is highly influenced by the texture, composition and porosity of the substrate. Indeed, in concrete the cementitious matrix rules the crack propagation (i.e. usually the fracture does not pass through aggregates but it involves the aggregate/matrix interface, Fig. 2.17). Further, concrete texture and micro-structure, which is more or less the same even for different types of cement, barely influence the bonding behavior once the compressive strength is duly accounted. In masonry the heterogeneities (e.g. impurities and firing waste) lead to a complex behavior since they have mechanical characteristics comparable with the support material. Moreover, particularly for ancient masonry and natural stone, there

are a wide variety of textures that may trigger peculiar behaviors because of either the antique non-standardized production or the orogeny of the stones [38].

Despite the aforesaid evidence , usually experimental studies investigated the bonding behavior of new bricks, which are produced with standard processes so to guarantee an homogeneous production [28, 33, 37, 37, 88–92]. Conversely, less attention has been paid to ancient clay brick or natural stones masonry (i.e. only a few studies are present in literature, for example [33, 55, 91, 93]).

Figure 2.17: Propagation of the debonding crack at the aggregate/cementitious matrix interface: (a) support block after debonding; (b) front view of the debonded plate; (c) side view of the debonded plate.

2.5.2   FRP behavior under cyclic actions

Despite the debonding behavior has been widely studied from both numerical and experimental standpoint in case of monotonic loading ([25, 37, 48, 83, 94] among others), to date, only little attention has been paid to cyclic loading, even if some relevant cases, such as the strengthening of bridges or structures liable to seismic events, are of primary concern [5, 95, 96]. Moreover, the experimental studies available on the cyclic response of the FRP reinforcements usually deal with the behavior of reinforced structural members [5, 95]. As reported by Carloni et al. in [5], one of the principal drawbacks of this kind of tests is that they do not permit to characterize the fatigue interface behavior because of many factors "filter" (i.e. influence) the final mechanical response (i.e. presence of tensile or shear steel reinforcements or scaling effects). However, recently, some studies dealing with single or double lap cyclic shear tests appeared in the literature, overcoming partially this lack of knowledge and giving more details on the interface behavior (among others [4, 5, 95–99]). It has been demonstrated that fatigue can trigger a debonding failure even if the maximum load in a cycle is smaller than the maximum monotonic force attainable. This is the result of a gradual deterioration of the bonding effectiveness because of the fatigue micro-cracking and of the accumulation of irreversible damage at the interface level [65, 100]. A degradation of the global stiffness increasing the loading cycles has been also observed as well as the key role of the applied load amplitude, i.e. $\Delta F = F_{up} - F_{low}$ where the subscripts *up* and *low* stand respectively for the upper and lower force reached in a cycle [5]. Hence, low values of amplitude imply a high number of cycles prior to failure (high cycle fatigue), while high amplitudes are related to a high values of plastic deformations and to the nucleation of a wide number of micro-cracks leading to a shorter cyclic life (low cycle fatigue). Moreover, some studies suggest the presence of a load threshold under which the fatigue debonding failure is circumvented [101, 102]. A quite common value for such infinite cyclic life limit is about 25-30% of the maximum monotonic debonding force F_{max}. Also, a displacement threshold under which no damage due to failure occurs is reported in literature, but it should be experimentally evaluated (i.e. no general rules ara available) [103, 104]. Anyway, many aspects remain almost unknown as the role of the friction and interlocking between the faces of the debonding crack.

Nowadays, the cyclic life assessment is usually performed by means of evolution laws such the Whöler curve or the Paris law [101, 102]. However, in these terms the fatigue

life prediction remains an empirical abstraction, since the parameter of the evolution laws must be calibrated following a case-by-case approach, i.e. it is not possible to formulate a general rule [101, 102]. Moreover, any deviation from the ideal condition underlying each theory, can lead to a significant mismatch in the previsions, hence many laws have been proposed for different specific situations [101, 102].

The empirical laws have been used also in some numerical models [4, 65, 100]. Even if such models can give a deep insight into the interface fatigue mechanics, their use is conditioned by the specific set of tests used to calibrate the laws. Thus, the results obtained cannot be generally extended, limiting their employment to the interpretation of the experimental data. Differently, damage mechanics, plasticity or a mix of the two (either coupled or not) have been used by other authors to define the interface law (e.g. [101, 102]). Anyway, these models are usually computationally demanding and sometime the definition of the parameters is not straightforward. Differently, for simple first order model [105, 106] (similar to what used for the monotonic behavior of FRP reinforcements) the thermodynamical definition of the parameters involved can be questionable.

3

Experimental studies

Abstract

In the present section the problem of debonding between FRP fabrics and quasi-brittle substrates (concrete and masonry) is investigated by means of experimental tests. In particular, one of the most used setup, the single lap shear test, has been modified thus permitting a complete and deep investigation of the debonding process.

A first series of experimental tests on concrete substrate is performed showing that the failure mode and its brittleness strongly depend upon the bond length. Furthermore, results suggest that debonding occurs with a gradual transition from a predominantly mode-II to a mixed mode I+II fracture as the bond length decreases pointing out the influence of the peeling stresses. These latter are also responsible for a change in the tangential bond strength along the bonded length and to a variation of the failure mechanism. The capabilities of classic non-linear interface models to reproduce experimental findings are also checked by finite element simulations.

An experimental campaign focused on the bond behavior of different ancient clay bricks and masonry blocks reinforced with composite sheets is also presented. Obtained results are analyzed showing different peculiarities of the detachment process especially in relation to the substrate properties. Moreover, particular consideration is paid to similarities and differences with the behavior of the FRP reinforcements applied to concrete. Finally, the fracture energies at disposal are evaluated starting from the experimental data and compared with the previsions of the Italian guideline CNR-DT 200.

3.1 Proposed experimental setup

Trying to solve the aforesaid issues (par. 2.4.1), a new setup is herewith proposed. To avoid applying inclined pulling forces, a steel support was specifically designed (Fig. 3.1a) to reduce the elastic rotations, i.e. to limit the deformations of the support plus specimen. In particular, linear elastic 3D finite element simulations were performed to check weather the steel support was enough stiff to maintain the elastic displacements under acceptable values (Fig. 3.1b). The supporting steel plates were controlled by bolts that permitted to reduce small geometrical eccentricities by adjusting the position of the specimen.
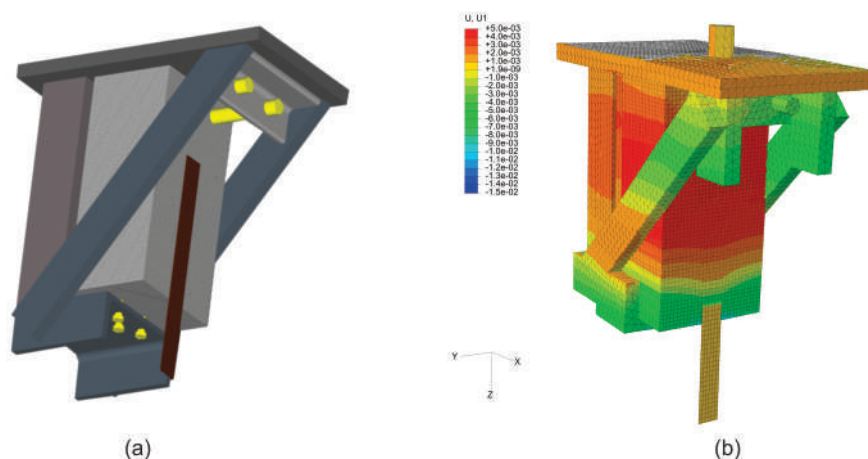
Figure 3.1: (a) Render of the supporting steel cage and (b) 3D finite element simulation of the setup to check elastic rotations.

A Crack Opening Displacement gauge (also named clip-gauge or COD-gauge) was used to control the relative displacement between the plate and the concrete substrate at the free end of the plate δ_2 (Fig. 3.2), avoiding thus the dynamic failure of the specimen before the complete detachment of the reinforcement. This instrument, usually employed in experimental fracture mechanics, permitted to measure very small displacements on the order of 1-2 μm.

The steel cage (Fig. 3.3a) was then mounted on a standard testing machine (Fig. 3.2a). The pulling force was applied by clamping the end of the FRP fabric within two steel plates (Fig. 3.3b) compressed by six bolts twisted with a dynamo-metric wrench at 80 Nm. The clamping system was finally hinged at the actuator of the testing machine (Fig. 3.3b).

Figure 3.2: (a) Picture of the entire setup with a mounted specimen and (b) particular of the COD-gauge used to control the test.
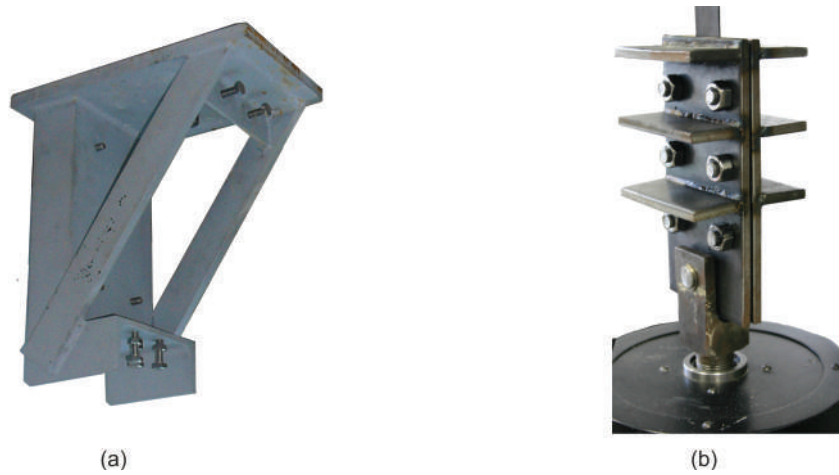
Figure 3.3: (a) Steel support cage and (b) particular of the clamping system.

The proposed setup was then useful to observe stably the complete debonding process in specimens with different bonded lengths, and to capture their failure modes.

3.1.1 Control of the test

To permit proper comparisons between different results and to ensure their reproducibility a unified protocol to perform tests has been studied.

Initially, a first pre-load cycle (about 1 kN in 60 s) is applied to remove backlashes

between mechanical parts. Moreover, this permitted to check the behavior of the specimen revealing possible unwanted bending of the plate that were removed by centering the specimen. Then the specimen is unloaded and data acquisition is started.

Initially, tests are load-controlled with a rate of 1 kN/min until the displacement measured by the clip-gauge reaches its measuring range ($\approx 2\mu$m). Then, the control is switched to the clip-gauge, with an initial speed of 0.5 μm/min. This very low speed is maintained until the end of the snap-back branch, then the speed is gradually increased up to 20 μm/min.

The precision of the clip-gauge dictates the maximum bond length of the plate. As a matter of fact, increasing the bond length decreases the slip of the free end of the plate attained at peak load. Since displacements smaller than 1μm are not measured by the clip-gauge, the testing machine would not be able to stably control the free end slip, causing a catastrophic failure.

3.2 Experimental campaign on concrete

The proposed setup is tested and validated by means of an experimental campaign on concrete substrate.

In addition, the performed tests aim to investigate the full range behavior of the FRP glued joints and the role of the bonded length on the failure process. In fact, the transition from the post-peak softening to the unstable snap-back behavior has been observed only with numerical studies [30, 39–41], but no experimental validations are at disposal.

Another issue to deal with is the calibration of the interface bond-slip laws. Becuase of the problems in controlling the tests which affect the shear tests of this joints, it was not clear if the local interface law could change along the bonded length. Indeed, the experimental bond-slip relationships are usually estimated either for a limited number of points at the laoded-end [3, 107, 108] or correlating the bond stresses and the slips along the whole bonded length for a given load value (usually at the load peak) [5, 25, 36] or by means of a back calculation as [109], but no direct observations of the full range local behavior along the bonded length are available.

3.2.1 Materials and methods

3.2.1.1 Geometry

The geometry of the specimens is represented in Fig. 3.4. The nominal dimensions of the concrete prisms were $150 \times 90 \times 300$ mm. Thirteen specimens were prepared and five bond lengths $l_b = 30; 60; 90; 120; 150$ mm have been considered.
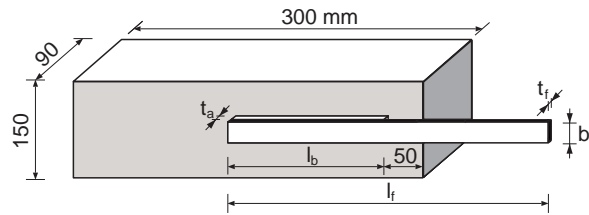
Figure 3.4: Geometry and dimensions of the specimens.

It is known that the plate width b_f influences the bond properties [25, 94]. The width of the plate b_f was chosen equal to the characteristic length of concrete, which is generally assumed 2-3 times the maximum aggregate size. This should limit the influence of the

heterogeneities produced by the aggregates, allowing to treat the concrete substrate as a continuum.

The minimum bond length $l_b = 30$ mm was limited as well by the requirement to consider the concrete substrate as a continuum, like in the case of plate width. A maximum length $l_b = 150$ mm, which is close to the theoretical anchoring length l_{eff} [9] predicted during the preliminary test design, was chosen to permit the stable control of the test. Indeed, at the peak load, longer bond lengths would display very small slips at the free end of the plate, which are not measurable with standard transducers.

The effective dimensions of all the specimens are summarized in Tab. 3.1.

Table 3.1: Geometrical properties of the specimens.

Specimen	l_f [mm]	b_f [mm]	t_f [mm]	l_b [mm]	$\hat{F}$ [kN]	Γ_f [N/mm]
30A	280	30.5	1.29	34	3.2	0.31
30B	280	30.5	1.32	31	5.4	0.34*
30C	280	29.3	1.32	30	2.2	0.25
60A	310	29.6	1.31	61	11.2	0.65
60B	310	30.3	1.31	59	10.7	0.44
60C	310	30.3	1.33	61	10.0	0.55
90A	365	30.0	1.25	66[†]	11.3	0.30
90B	370	29.3	1.31	91	12.6	0.44
120A	425	30.4	1.35	122	14.3	0.35*
120B	425	29.8	1.22	78[†]	12.8	0.43
150A	400	29.0	1.31	153	14.6	0.53
150B	400	30.7	1.32	151	14.6	0.57
150C	400	27.6	1.31	153	16.2	0.62

[†] reduced length due to bonding defects

* pull-out curve not complete

3.2.1.2   Specimen preparation

The prisms were casted into steel molds with a normal strength concrete, then vibrated by means of a vibrating table. Prisms were demolded after 24h and wrapped into saturated

clothes for 28 days. Then, they were stored in laboratory room conditions for three months before applying the plates.

It is worth to note that the treatments of the bonding surface of the support blocks influence the bonding effectiveness [30, 59, 60]. Here, the top surface of the concrete blocks was sandblasted with quartz sand to remove the thin layer of mortar that covered the aggregates, improving the grip between adhesive and plate.

Then, the plates have been glued to the top surface of the blocks by using a 1.2 mm thick layer of a two-components epoxy adhesive. The plates have been positioned by means of steel guides (2.5 mm thick) fixed with clamps to control the glue thickness and the lineup of the plate.

The bonded area started 50 mm far from the front side of the specimen (Fig. 3.4). In this way the interface behavior was not influenced by the edge effects that may cause the expulsion of a concrete wedge, modifying debonding mechanisms [3, 41]. The thickness of the pultruded FRP plates was $t_f = 1.3$ mm.

Tests were performed after one month to permit the complete hardening of the glue.

3.2.1.3 Material characterization

Concrete To cast the specimens, a low strength concrete was used, with a mix-design similar to the one used in old buildings. Concrete was prepared with a content of 300 kg/m^3 of Type II Portland cement, water-to-cement ratio $W/C = 0.50$, no admixtures. River sand was used as fine aggregate and crushed gravel as coarse, with a maximum aggregate size of 16 mm.

Three prisms of nominal dimensions $90 \times 90 \times 180$ mm obtained by sawing the blocks of concrete used for single-shear tests, were tested in compression. The average compression strength was $f_{cm} = 37.2$ MPa, Young's modulus $E_c = 28\,700$ MPa, and Poisson's ratio $\nu_c = 0.2$.

Three beams of nominal dimensions $60 \times 90 \times 300$ mm were tested in three-point-bending (Fig. 3.5a), and an average flexural tensile strength $f_{ct,fl} = 4.8$ MPa was obtained. Moreover, an LVDT was applied in order to measure the deflection f during the test (Fig. 3.5b). This permitted to evaluate the experimental mode-I fracture energy G_F by writing a balance between two terms: (i) the external work done by the force F and (ii) the internal work dissipated by the fracture process. Dividing the former term, which is know by integrating numerically the $F - f$ curves (Fig. 3.5c), by the cross sectional area

37
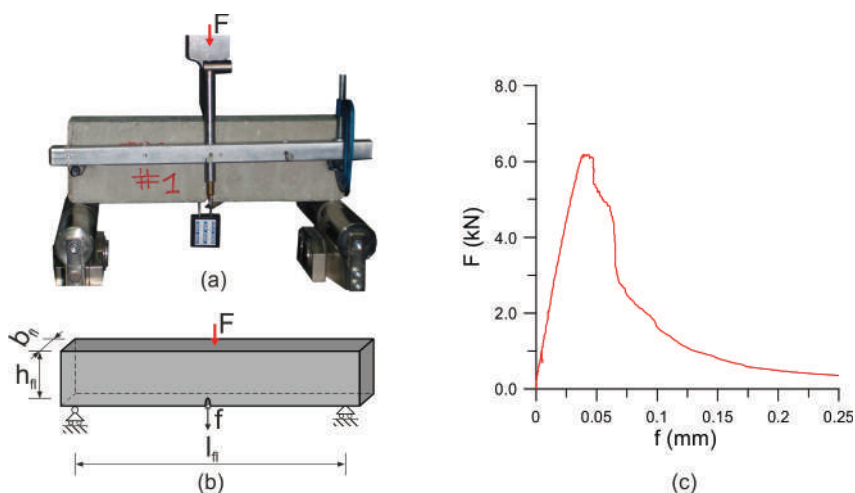
Figure 3.5: Three-point bending test on concrete: (a) specimen during the test; (b) scheme of the specimen and nomenclature; (c) applied force-deflection curve $F - f$.

$b_{fl} \times h_{fl}$ of the specimen, allowed to evaluate an average value of the energy dissipated. The computed average value of the mode-I fracture energy was $G_F = 104$ N/m.

By means of the expressions proposed in [110] the measured data permitted to compute the characteristic compression strength $f_{ck} = f_{cm} - 8 = 29.2$ MPa and the tensile strength $f_{ct} = f_{ctm,fl}/\max(1.6 - h_{fl}/1000, 1) = 3.2$ MPa (with height of the cross section $h_{fl} = 90$ mm).

Adhesive A two-components epoxy-adhesive has been used to glue the FRP plates to the concrete blocks. The mechanical properties of the adhesive have been measured by means of tensile and torsional tests.

A tensile test has been carried out according to [111]. A specimen was obtained pouring the adhesive in a mold realized by means of a wooden pattern. The specimen was stored at room temperature and 65% R.H. for 14 days. After curing, four strain gauges have been placed to measure longitudinal and transversal deformations. Geometry and dimensions of the specimen are depicted in Fig. 3.6a, together with the experimental stress-strain $\sigma_a - \varepsilon_a$ relationship.

For the torsional test, a specimen has been realized by pouring the epoxy adhesive into a mold realized with two coaxial plastic pipes. This permitted to obtain a pipe in epoxy-adhesive (Fig. 3.6b).
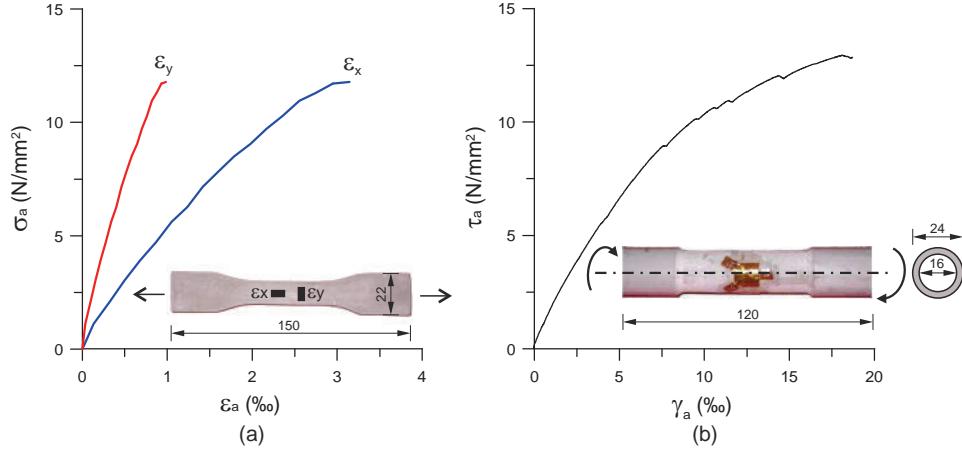
Figure 3.6: Mechanical tests for the adhesive material and corresponding specimens: (a) tensile stress-strain relationships in longitudinal ($\sigma_a - \varepsilon_x$) and transversal ($\sigma_a - \varepsilon_y$) direction; (b) torsional shear stress-strain relationship $\tau_a - \gamma_a$.

A strain gauge rosette was applied on the surface of the specimen to measure the principal strains. The specimen was tested by means of a torsional testing machine controlling the torsional angle. Measured deformations confirmed that the specimen was subjected to pure torsion and permitted to plot the shear stress-strain relationship $\tau_a - \gamma_a$ represented in Fig. 3.6b together with the geometry of the specimen.

The mechanical properties obtained by means of tensile and torsional tests are Young's modulus $E_a = 3\,517.3$ MPa, shear modulus $\mathcal{G}_a = 1\,350.0$ MPa, Poisson's ratio $\nu_a = 0.315$, tensile strength $f_{ta} = 12.01$ MPa, tensile strain $\varepsilon_{au} = 0.326$ %, and shear strength $\tau_{au} = 12.94$ MPa.

FRP reinforcement For the FRP plate the mechanical properties have been measured by means of a uniaxial tensile test according to [112] (Fig. 3.7). The specimen was made of a FRP rectangular plate with aluminum tabs glued at the ends to permit to grip the specimen up to failure. Strain gauges were used to measure longitudinal and transversal strains (Fig. 3.7b).

The mechanical properties of the FRP plate are Young's modulus $E_f = 168\,500$ MPa, Poisson's ratio $\nu_f = 0.248$, tensile strength $f_f = 2\,434$ MPa, ultimate strain $\varepsilon_{fu} = 1.37$ %.
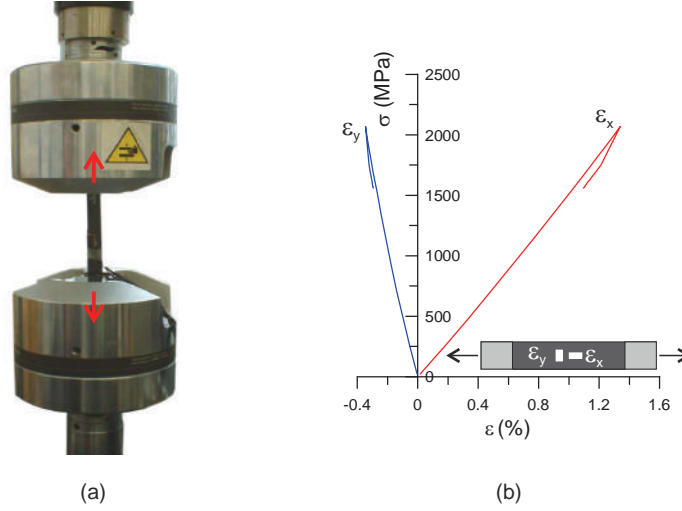
Figure 3.7: Mechanical characterization of the FRP plate: (a) specimen during the test; (b) tensile stress-strain relationship in longitudinal ($\sigma_f - \varepsilon_x$) and transversal ($\sigma_f - \varepsilon_y$) direction.

3.2.1.4 Setup validation and instrumentation

A scheme of the experimental setup is represented in Fig. 3.8a while a picture of a specimen before the test is given in Fig. 3.8b.

The applied measuring devices are depicted in Fig. 3.8a as well. In particular, two LVDTs δ_1' and δ_1'' (base 10 mm) have been placed at the end of the plate to measure the average slip $\delta_1 = (\delta_1' + \delta_1'')/2$ between concrete and FRP and to detect in-plane rotations of the bonded plate (Fig. 3.8a). At the end of the plate the clip-gauge of the testing machine was installed to measure the slip δ_2 and to drive the tests as reported in par. 3.1.1. Moreover, an LVDT was applied orthogonally to the plate to measure normal displacements δ_3 between FRP and concrete.

Along the bonded plate, a series of equally spaced strain gauges was glued to measure longitudinal strains (Fig. 3.8a). To detect out-of-plane and in-plane bending of the plate, three strain gauges measured the strains ε_A', ε_A'', and ε_B on the unbonded part of the plate.

Fig. 3.9a,c shows the pull-out curves obtained respectively for the specimens 90B and 150B considering the displacements δ_1' and δ_1'' measured by the LVDTs on the left and on the right of the bonded plate together with the average displacement δ_1. The curves reveal an unavoidable, albeit small, difference that is related to an in-plane rotation of the plate with respect to the concrete block. The rotation, which is probably due to heterogeneities
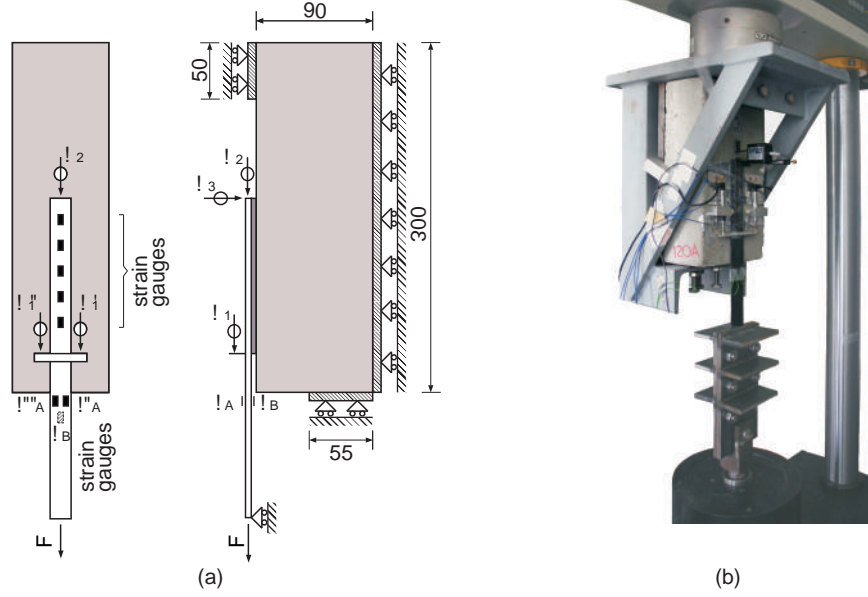
Figure 3.8: Test setup: (a) Scheme of the specimen with LVDT's and strain gauges applied on the plate; (b) picture of the specimen on the supporting system.

of adhesive layer and concrete surface, varies during the test, but always remaining smaller than 0.1°, which can be considered acceptable [34, 57].

Also the two strains ε'_A and ε''_A of the loaded end of the plate confirm a small in-plane rotation (Fig. 3.9b,d) whose magnitude agrees with the one measured by the LVDTs. The average strain $\varepsilon_m = (\varepsilon'_A + \varepsilon''_A)/2$ is compared to the one measured at the back of the plate ε_B (Fig. 3.9b,d) showing that its out-of-plane bending is small.

Finally, in order to validate the test setup proposed (par. 3.1), the rotation of the setup (prism and support) was recorded by four LVDTs $\delta_4 - \delta_7$ applied orthogonally to the concrete block (Fig. 3.10a). Another transducer δ_8 was placed on the top of the steel support to detect the in plane displacement in the direction of the applied load (Fig. 3.11).

The LVDTs (Fig. 3.10) permitted to measure the displacements of the specimen (caused by elastic deformations and backlashes) with respect to the frame of the testing machine and to determine its in-plane and out-of-plane rotations θ_y and θ_z with respect to y and z axis. Fig. 3.10 shows the rotations of the specimens 30C and 60B. Their different behavior is due to the inevitable backlashes between the concrete block, which is irregular, and the steel support. In any case, both the angles θ_y and θ_z remain smaller than 0.1° up to failure. According to [34, 57], these small rotations do not affect the experimental re-
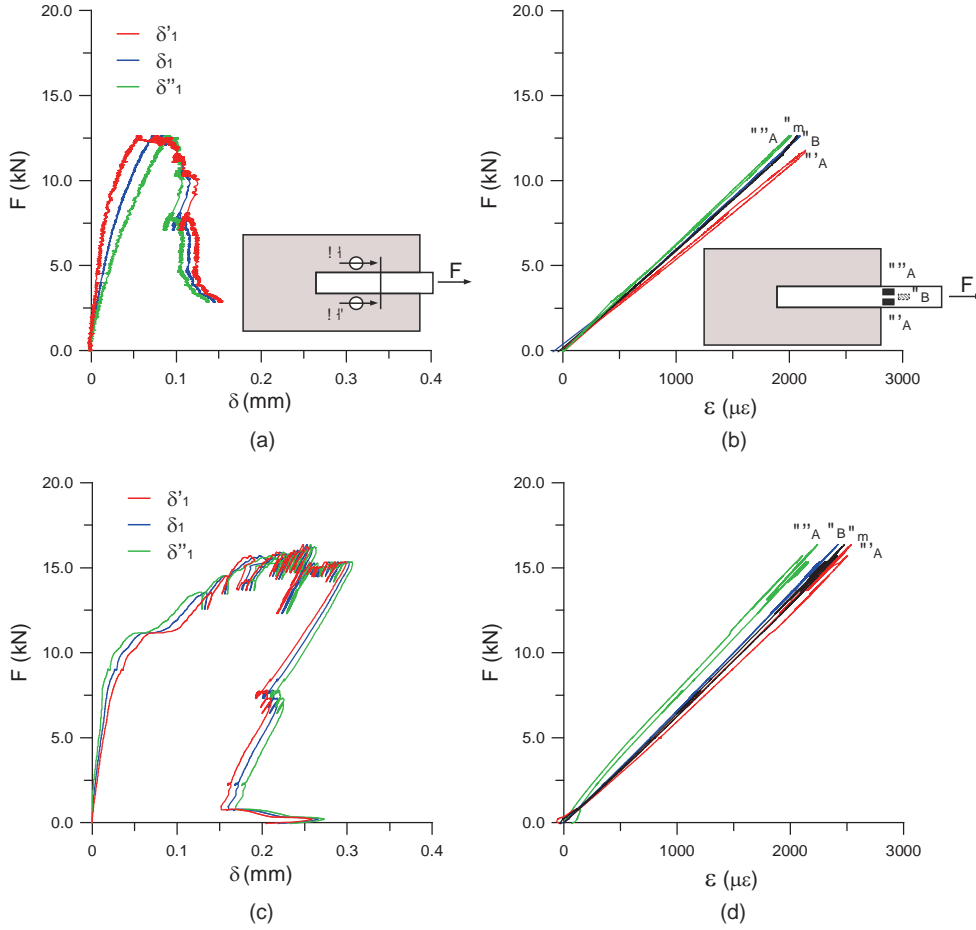
Figure 3.9: (a) Pull-out curves $F - \delta_1'$ and $F - \delta_1''$ for the specimen 90B; (b) Force-strain curves $F - \varepsilon$ for the specimen 90B; (c) Pull-out curves $F - \delta_1'$ and $F - \delta_1''$ for the specimen 150B; (d) Force-strain curves $F - \varepsilon$ for the specimen 150B.

sults, confirming the effectiveness of the test setup. The in plane displacement δ_8 remains as well under acceptable values (Fig. 3.11).

3.2.2 Experimental results

In the following the obtained results are illustrated using the curves of the specimen 150B, which has been chosen as paradigmatic example. Particular attention is paid to illustrate the peculiarities appeared in the tests.

Fig. 3.12a represents the pull-out curve $F - \delta_1$ together with the force-displacement curve $F - \delta_2$ measured by the clip-gauge at the free end of the plate.
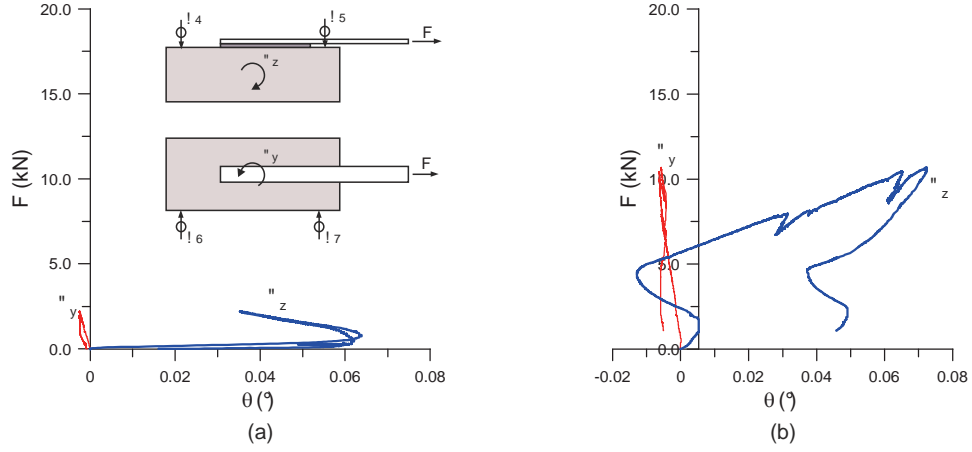
Figure 3.10: In plane rotations θ_y and out-of-plane rotations θ_z: (a) specimen 30C; (b) specimen 60B.
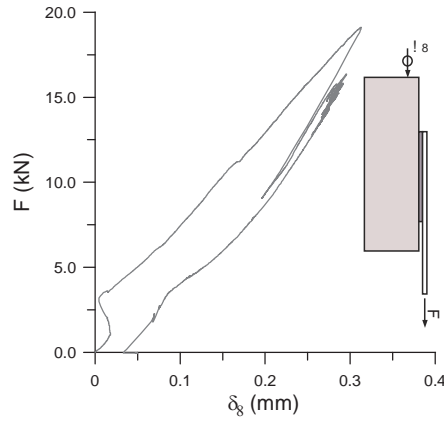
Figure 3.11: In plane displacement δ_8 of the specimen 150A.

The peak load $\hat{F}$ is reached for a displacement δ_2 that is very small ($\approx 20\mu$m). After the peak, the curve $F - \delta_2$ shows a softening branch followed by a sub-horizontal plateau when debonding is almost completed. At the same time, the curve $F - \delta_1$ displays an important snap-back, which explains the catastrophic failure usually observed in load or displacement driven tests.

The strain-gauges applied along the plate (whose position is shown in Fig. 3.12d) permitted to plot the distribution of strains $\varepsilon(x)$ for different load levels (Fig. 3.12c). During the ascending branch (points A-C in Fig. 3.12a) the strain decays from the maximum value which is reached at the loaded end of the plate, up to zero at the opposite end. Approaching the peak (point D in Fig. 3.12a) the strain distribution close to the loaded

end becomes flat. This is due to debonding which starts at the loaded side of the plate propagating toward the opposite side where strains continue to increase with load.

During the softening equilibrium path, when the residual bonded length is about 60 mm (point E in Fig. 3.12a), the strain gauge closer to the free end starts to display a reduction of strains up to a sign inversion (curve E in Fig. 3.12c). The same effect is noticed, as the debonding progresses, in correspondence of other strain gauges (curves F and G in Fig. 3.12c). At the same time a peeling crack appears at the free end and propagates toward the central part of the plate, which is still sound.

To detect this phenomenon, the LVDT measuring the orthogonal displacements δ_3 between concrete and free end of the plate is employed. The curve $F - \delta_3$ (Fig. 3.12b) reveals that the peeling crack appears between the sub-horizontal plateau and the steepest branch of the softening curve $F - \delta_2$ (points D and E in Fig. 3.12a).
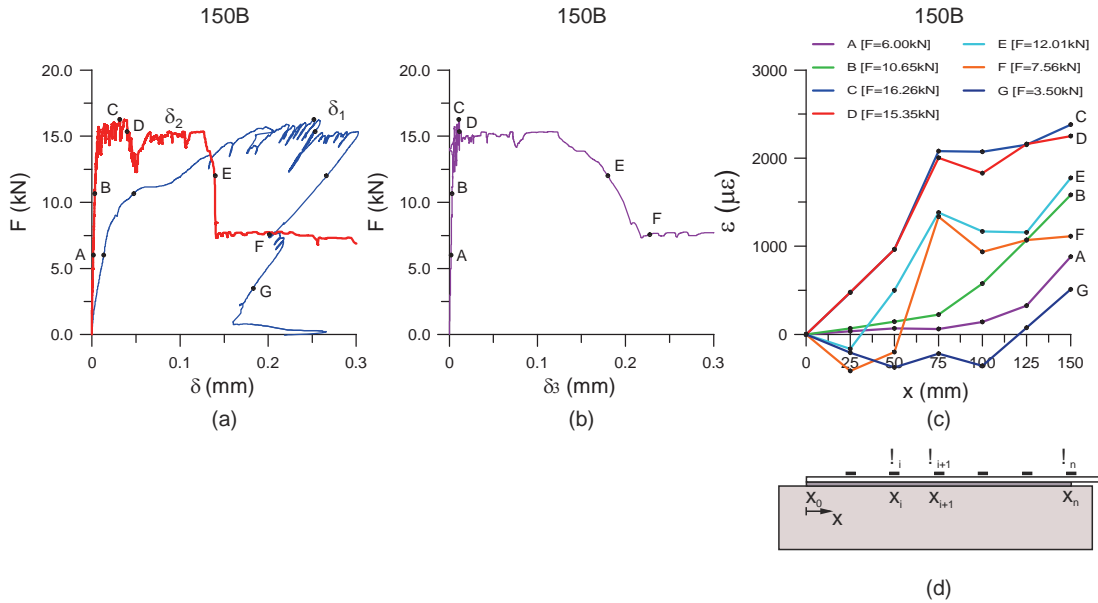
Figure 3.12: Results for specimen 150B; (a) Pull-out curves; (b) Force-orthogonal displacement curve; (c) Evolution of the strains along the plate for different load levels; (d) Position of the strain-gauges.

The peeling crack depicted in Fig 3.13a allows bending of the plate which explains the compression strains detected by the strain gauges. Moreover, during this stage, the displacement δ_2 recorded by the clip-gauge, which rotates following the free end of the plate, is greater than true slip s (Fig. 3.13b). For this reason, the curves $F - \delta_1$ and $F - \delta_2$
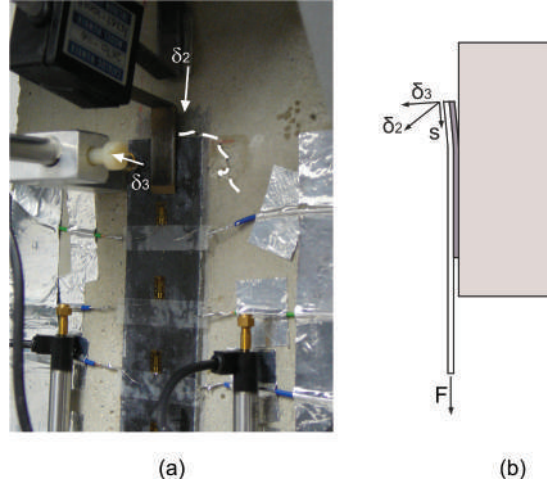
Figure 3.13: Peeling crack at the free end of the plate: (a) details; (b) displacements δ_2 and δ_3 measured by clip-gauge and LVDT respectively.

twist each other, i.e. $\delta_2 > \delta_1$ (Fig. 3.12a). Anyway, this effect influences the results only during the final phase of the test, differently during the first phase until the late snap-back branch the uplifting influence on the measured δ_2 is negligible (i.e. $\delta_2 \simeq s_2$). The results are confirmed for all the specimens of length $l_b = 150$ mm (Figs. 3.23e, f).

3.2.2.1 Effect of the bond length of the plate

A variation of the bond length of the specimens produces important consequences on their behavior. For the shortest specimens, with $l_b = 30$ mm, the pull-out curves $F - \delta_1$ display a softening branch, and snap-back disappears (Fig. 3.14). Moreover, the slips δ_1 and δ_2 are nearly the same, i.e. the bonded area is characterized by almost uniform slips.

The peak loads $\hat{F}$ of the three specimens 30A, 30B, and 30C are scattered, because the bonded area is very small and the local effects are important. The failure mechanism is characterized by a peeling crack that starts at the free end, propagating toward the loaded end.

Specimens with bond length $l_b = 60$ mm still display a softening behavior (Fig. 3.15a) and failure occurs by peeling at the free end (Fig. 3.15b). In this case the plateau in the strain diagram disappears (Fig. 3.15c).

The transition from softening to snap-back behavior is shown by the specimens with bond length $l_b = 90$ mm (Fig. 3.15d). The phenomenon is complete for specimens with
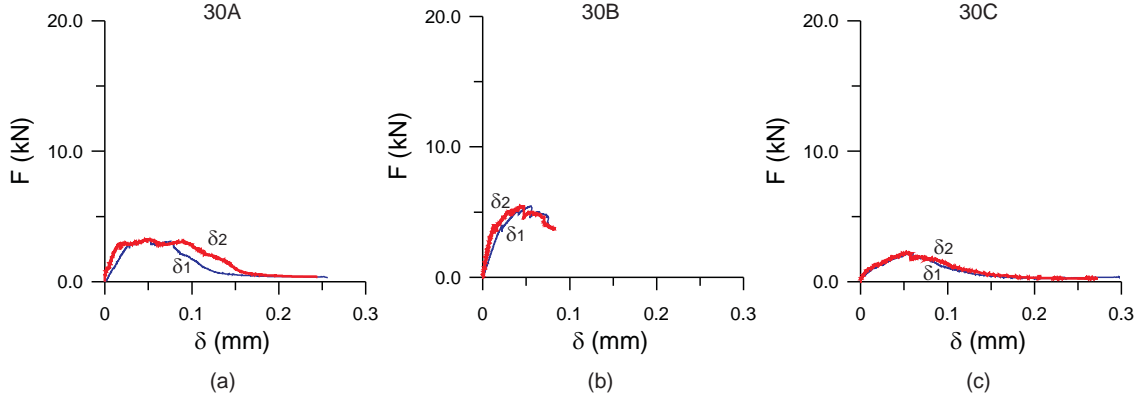
Figure 3.14: Pull-out curves for specimens of bond length $l_b = 30$ mm: (a) specimen 30A; (b) specimen 30B; (c) specimen 30C.

$l_b = 120$ mm, which display a clear snap-back regime (Fig. 3.15g). Fig. 3.15i shows that, in this case, strains display an horizontal plateau, i.e. debonding at the loaded end.

The curves $F - \delta_3$ (Figs. 3.15b,e,h) show that the peeling cracks at the free end always take place. Moreover, all the specimens present compression strains (Fig. 3.15c, f, i).

The peak loads $\hat{F}$ for all the specimens are summarized in Fig. 3.16a as a function of the bond length l_b while numerical values are reported in Tab. 3.1. Specimens 90A, 90B, and 120B showed bond defects (i.e. absence of glue at the loaded end) that were revealed after complete debonding. Thus, to obtain realistic results, the measured value of the intact bond was used as l_b in Fig. 3.16a. Differently, specimens 30B and 120A the peak load was achieved but because of controlling problems they failed before the end of the final unloading branch.

The debonded plates are depicted in Fig. 3.17. In short specimens it is possible to observe the formation of a concrete bulb of thickness 4-8 mm (Fig. 3.17a,b). In long specimens the concrete bulbs appear at both the edges of the bonded plate (Fig. 3.17c).

3.2.2.2 Experimental fracture energy

The experimental value of fracture energy is obtained writing a balance between the work done by the applied force and the energy dissipated by debonding, which is the only source of dissipation since the plate always remains in the linear elastic regime. The approach is similar to three-point bending tests carried out to measure fracture energy in concrete. At the loaded end of the plate the applied force F and the corresponding
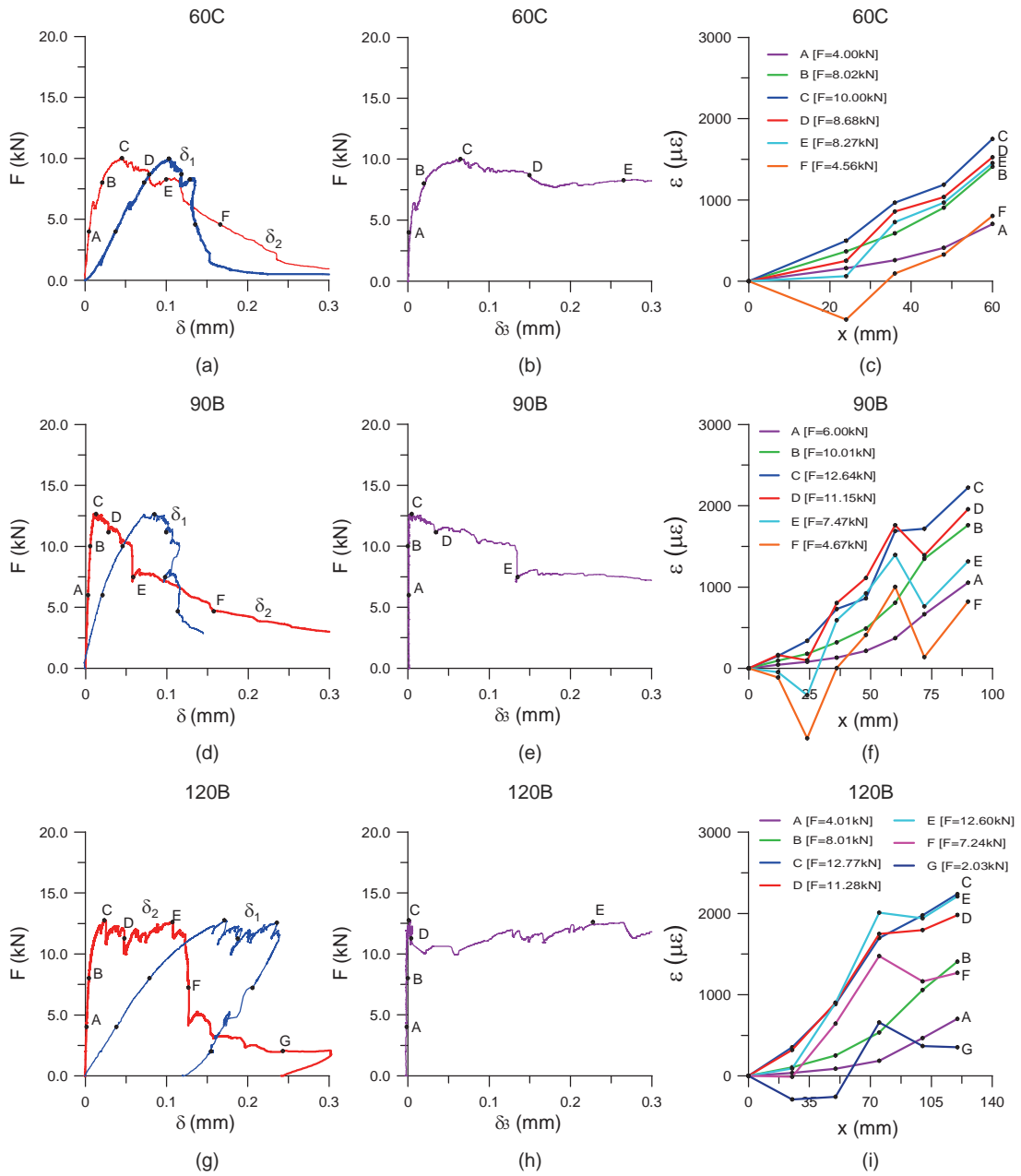
Figure 3.15: Results for specimens with different bonded lengths; (a),(d),(g) pull-out curves; (b),(e),(h) force-orthogonal displacement curves; (c),(f),(i) evolution of the strains along the plate for different load levels.
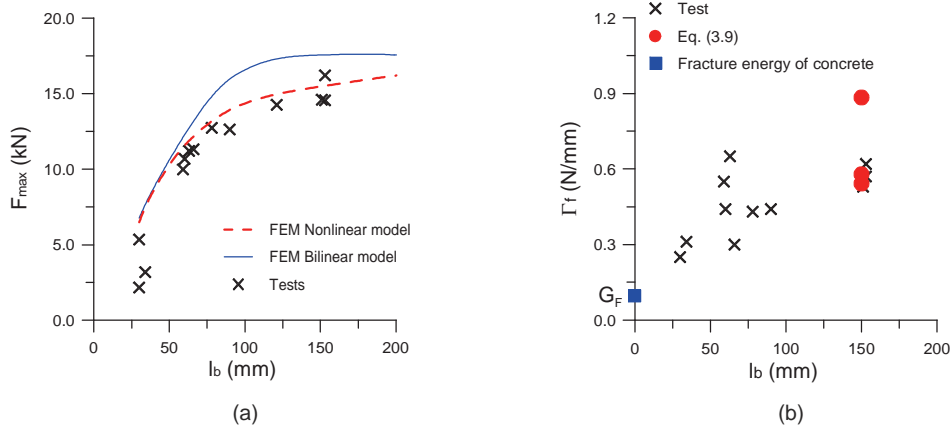
Figure 3.16: Effect of bond length l_b: (a) maximum force-bonded length $F_{max} - l_b$ and comparison with the nonlinear model [6] and the bilinear model [7]; (b) fracture energy-bond length $\Gamma_f - l_b$.
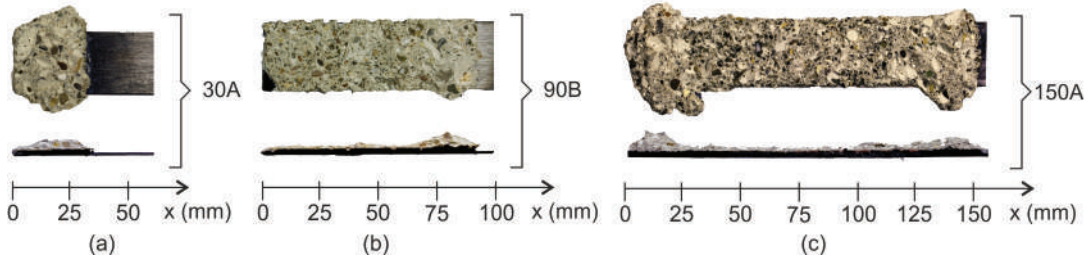
Figure 3.17: Debonded plates of different lengths: (a) specimen 30A; (b) specimen 90B; (c) specimen 150A.

displacement δ_1 are both known. Therefore, the work done by the applied force is obtained integrating numerically the curve $F - \delta_1$. Dividing the result of integration by the effective bonding area $l_b \times b_f$, provides an average value of fracture energy Γ_f.

For the complexity of the processes involved in the debonding, the measured energy spatially mediates different contributions [66]. In particular, this approach "lump" into the interface all the contributions depleted in different media (e.g. damage in the concrete bulk material and in the adhesive layer) and different processes at different length scale (e.g. microcracking, plastic sliding at the fiber level, friction between the asperities of the debonding crack, scaling effects related to the plate width) [66]. Thus, the value of Γ_f experimentally esteemed with the proposed approach must be conceived as an energy in general sense useful to characterize the macroscopic structural performance of the externally bonded joints [66].
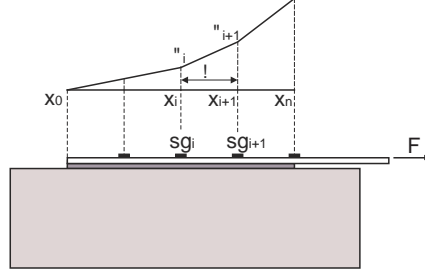
Figure 3.18: Linear scheme for the calculation of the experimental bond-slip relationships.

In Tab. 3.1 the numerical values of the computed values of Γ_f are reported while Fig. 3.16b shows the variation of Γ_f with respect of the measured value of bond length l_b. It must be highlighted that in Fig. 3.16b the points corresponding to specimens that showed anomalous pull-out behavior (i.e. incomplete curves as marked in Tab. 3.1) are omitted. In short specimens, where peeling cracks prevail, Γ_f tends to the mode-I fracture energy G_F measured in concrete (square marker in Fig. 3.16b). Increasing l_b, the value of fracture energy increases, approaching the mode-II theoretical values (dots in Fig. 3.16b) computed using the expressions proposed in [3] , which are based on perfect shear behavior (see par. 3.2.3.2).

3.2.2.3   Experimental bond-slip relationship

The experimental strains ε_i measured by the m strain gauges located at position x_i (with $i = 1 \ldots m$ starting from the free end, Fig. 3.12d) were used to compute the local bond-slip relationships following a procedure already proposed in [3].

In particular, assuming a linear variation of strains between two subsequent transducers (Fig. 3.18), the average value of bond stresses $\tau_{i+1/2}$ is obtained writing the equilibrium of this portion of plate

$$\tau_{i+\frac{1}{2}} = \frac{(\varepsilon_{i+1} - \varepsilon_i)E_f t_f}{\Delta} \tag{3.1}$$

where $\Delta = x_{i+1} - x_i$ is the distance between the strain gauges.

Neglecting the deformability of concrete, the corresponding slips $s_{i+1/2}$ are approximated with the displacement of the plate, which are obtained by integrating strains
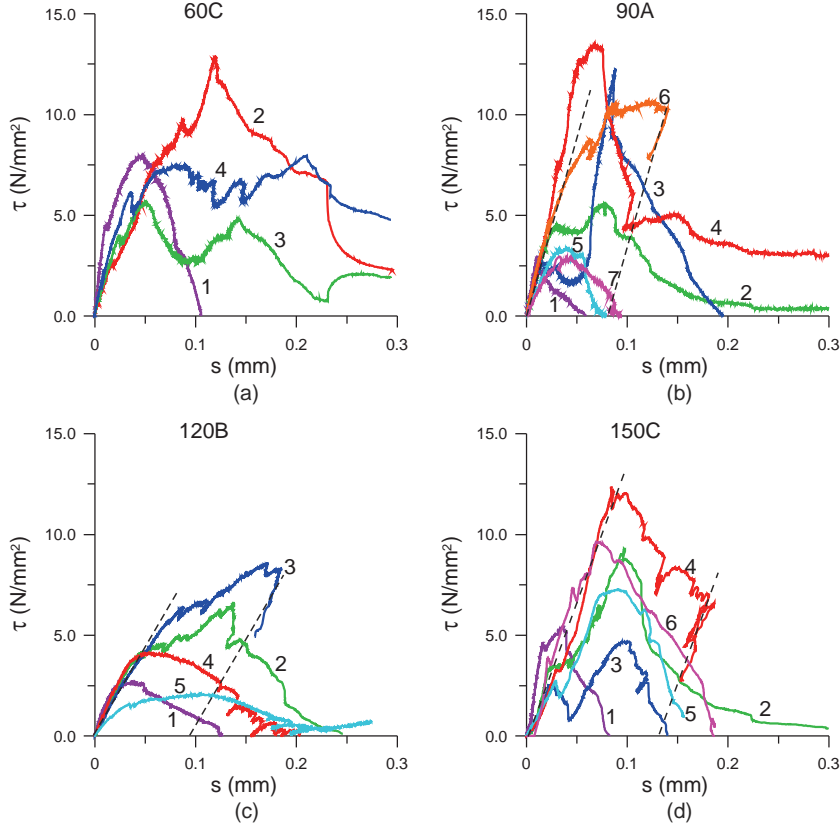
Figure 3.19: Local bond-slip curves $\tau-s$ measured for different bonded lengths: (a) Specimen 60C; (b) Specimen 150C.

$$s_{i+1} = s_i + \int_{x_i}^{x_{i+1}} \varepsilon(x)x = s_i + \frac{\varepsilon_{i+1} + \varepsilon_i}{2}\Delta \quad (i = 0, 1, \ldots, m-1) \tag{3.2}$$

$$s_{i+\frac{1}{2}} = s_i + \frac{3\epsilon_i + \varepsilon_{i+1}}{8}\Delta \quad (i = 0, 1, \ldots, m-1) \tag{3.3}$$

Differently to [3], the slip at the end of the plate was assumed being equal to the value measured by the clip-gauge, i.e. $s_0 = \delta_2$.

Increasing the load, the points $(\tau_{i+1/2}, s_{i+1/2})$ permit to plot the local bond slip curves represented in Fig. 3.19 for four specimens (60C, 90A, 120B and 150C). The index i is represented close to the curves.

Even for the same specimen the curves are quite irregular (Fig. 3.19). Apart the initial slope, which is nearly the same, the peak and the softening branches are rather

different. In particular, the peak stresses $\hat{\tau}$ are always smaller at the free end of the plate (curve 1), maximum bond stresses are attained in the central part of the plate, whereas a reduction appears at the loaded end (last curve in the figures). In specimens 120B (curve 3 Fig. 3.19c) and 150C (curve 4 Fig. 3.19c), some curves describe the behavior of zones in the middle of the bonded length, which are not reached by debonding cracks. For this reason, an unloading path occurs, with a slope approximately equal to the initial one. The same behavior is visible in specimen 90A but near the loaded end (curve 6 Fig. 3.19b). Probably, in this case, interlocking phenomena occurred because of the concrete bulbs detached at the loaded end.

One of the causes of scattering is due to the small number of strain gauges applied along the FRP plate. Since the strain varies in a rather complicated way, the results obtained from Eqs. 3.1-3.3 are approximated. Moreover, presence of big aggregates and the bulbs highlighted in Fig. 3.17 leads to uncertainties in the strain measurements and thus in the $\tau - s$ curves.

In any case all the specimens evidenced a clear variation of the bond-slip curves along the length of the plate. To study this variation, in Fig. 3.20 the bond-slip relationships for specimens 150B and 150C are plotted separating the different positions i.

In this case, the curves corresponding to the same zone are more similar and the dispersion of the results is remarkably reduced (Fig. 3.20). The differences in the curves 3 and 4 (Fig. 3.20) can be explained considering the local effects caused by aggregates and other defects. Indeed, observing the debonded surfaces of the plates, it is worth noting that specimen 150C presents, in the neighborhood of third strain gauge, the mark of a big aggregate (Fig. 3.20h) which could have increased the strength in that position (Fig. 3.20c). For specimen 150B an area close to the fourth strain gauge where glue did not grip to concrete is well observable (Fig. 3.20g). This could explain the reduction of strength in Fig. 3.20d. Of course, two specimens are not sufficient to confirm experimentally a general behavior, and in the future a wider experimental program on the topic would be advisable.

3.2.3   Numerical simulations

3.2.3.1   FEM model

The experimental tests have been numerically investigated via finite element method using classical nonlinear interface laws proposed in literature (see [41] for an exhaustive
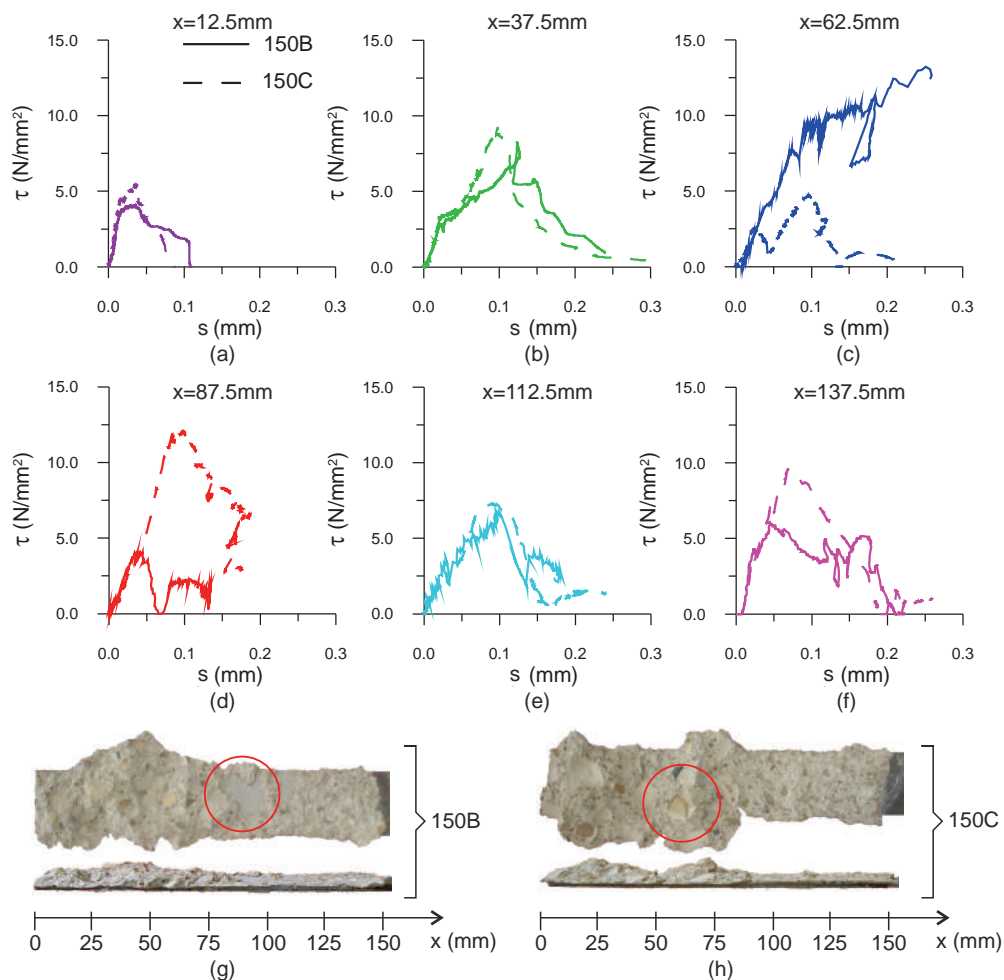
Figure 3.20: Comparison between local bond-slip relationships measured at the same positions and debonded plates (specimens 150B and 150C).

review) to: (a) explain the different behavior of the specimens; (b) check the capability of the bond-slip relationships proposed by some code standards [7–9] to describe the snap-back regime of the test usually performed to calibrate them.

To the purpose, a specific finite element code based upon the Open Source library deal.II [113] was developed.

The problem was modeled in two dimensions. A picture of the model, with mesh details and boundary conditions is showed in Fig. 3.21a.

Right side, top and bottom portions of the specimen are constrained in order to have no displacements in the direction normal to the surface and free displacements tangent to

it (Fig. 3.21a).

In the spirit of the code standards [7–9], debonding is described by bond-slip relationships, whereas concrete and FRP plate display a linear elastic behavior.

The non-linear bond-slip relationships analytically presented in the following Sect. 3.2.3.2 have been implemented into a four-node interface element as described in [71]. For the bulk materials, linear elastic two-dimensional plane-strain model and bilinear quadrilateral elements were adopted. Orthotropy along the thickness of the plate was neglected because of its very limited influence on the results.

The problem has been solved using a quasi-static incremental/iterative solution procedure. In order to follow the (possibly) unstable structural response, an arc-length method has been used and a local control function analogous to that proposed in [41, 114] was introduced. Accordingly, only the unknowns related to the non-linear behavior were introduced in the control equation. No line-search procedures have been necessary to successfully terminate the analyses. A suitable increment size has been assigned at the beginning for each analysis and then a procedure with automatic increments has been used in order to adaptively adjust the increment size during the analysis.

Probably, the use of more complete and complex models like the ones proposed in [86, 115, 116] would permit to reproduce the physical phenomenon, but this is out of the scope of the present work. We prefer to analyze the new experimental results in the light of classical models that are used in common practice to design FRP reinforcements.

3.2.3.2 Mode II non-linear interface law

As for the bond-slip law, the power fractional equation proposed in [6] for shear stresses transmitted mainly by aggregate interlock was used. The law, which has been obtained by post-processing data of single lap shear tests dominated by mode-II cracks, writes the local bond stress τ as a function of slip s:

$$\frac{\tau}{\hat{\tau}} = \frac{s}{\hat{s}} \frac{n}{(n-1) + (|s|/\hat{s})^n} \, , \tag{3.4}$$

where $(\hat{\tau}, \hat{s})$ denote peak shear stress and corresponding slip, and $n > 2$ is a free parameter mainly governing the softening branch, and $|s|$ represents the absolute value of s.

In [6] it has been shown that, if boundary effects are avoided in tests, the parameters of the interface law are independent of the geometry of the specimens and test setup,

but they are a function of concrete strength, surface preparation, and reinforcement type (FRP plates or sheets).

The mechanical coefficients for the bond law were esteemed adopting the standard prescription [7] using the measured material properties. In particular, the value of the maximum shear stress $\hat{\tau}$ can be directly obtained from the expression [7]

$$\hat{\tau} = 0.64 \, k_b \sqrt{f_{ck} \cdot f_{ctm}} \, , \tag{3.5}$$

where, f_{ck} and f_{ctm} are the characteristic compression strength and mean tensile strength of concrete respectively; k_b is a geometric function depending on the plate and concrete width b_f and b, which reads [7]

$$k_b = \sqrt{\frac{2 - \frac{b_f}{b}}{1 + \frac{b_f}{400}}} \geq 1 \, , \tag{3.6}$$

with $b_f/b \geq 0.33$. In case $b_f/b < 0.33$, the correct value of k_b is determined assuming $b_f/b = 0.33$.

The fracture energy value of the interface law [6]

$$\Gamma_f = \hat{\tau}\hat{s}\pi \left(\frac{1}{n-1}\right)^{\left(1-\frac{2}{n}\right)} \csc\left(\frac{2\pi}{n}\right) \, . \tag{3.7}$$

is determined still following the code standard [7]:

$$\Gamma_f = k_G \, k_b \sqrt{f_{ck} \cdot f_{ctm}} \, , \tag{3.8}$$

with $k_G = 0.064$ for mean values of the fracture energy.

The value agrees with the one determined making use of the relation proposed in [7] for the maximum transmissible force $F_{\max}$ with $l_b \to \infty$ and pure shear failure (as reported also in par. 2.1.1)

$$F_{\max} = b_f \sqrt{2 \, E_f \, t_f \, \Gamma_f} \, , \tag{3.9}$$

where E_f, t_f, b_f are Young's modulus, thickness and width of the reinforcement, respectively [7]. In this case the fracture energy must be evaluated considering the values of $F_{\max}$ measured for long specimens only ($l_b = 150$ mm), for which the hypothesis of pure shear behavior is more probable. The results are showed with red dots in Fig. 3.16b.

According to [41], the initial slope of the interface law

$$K_0^{1D} = \left(\frac{\partial \tau}{\partial s}\right)_{s=0} = \frac{\hat{\tau}}{\hat{s}} \frac{n}{n-1} \, , \tag{3.10}$$

is obtained starting from the experimental values [7]

$$K_0^{1D} = K = \frac{c}{\frac{t_a}{\mathcal{G}_a} + \frac{t_c}{\mathcal{G}_c}} \, ,$$

(3.11)

with $\mathcal{G}_c$ and $\mathcal{G}_a$ being shear modulus of concrete and adhesive layer, t_a thickness of the adhesive and t_c thickness of concrete layer contributing to interface compliance. The coefficient c is usually taken equal to $0.5 \div 0.7$ (in the numerical simulation we considered $c = 0.5$ and $t_c = 15$ mm). The adopted bond-slip law [7] was proposed for one-dimensional models that assume rigid behavior of the concrete substrate. In the case of two-dimensional finite element analyses, as explained in [41], the compliance of concrete layer, which is already modeled by finite elements, must be subtracted from the overall compliance Eq. 3.11. Hence, for a given value of initial slope and Γ_f, the parameters $\hat{s}$ and n of the interface law for 2D model can be easily obtained from Eqs. 3.7 and 3.11 following [41].

It is worth noting that, the present tests do not permit to calibrate a mode-I non-linear interface law between normal stresses σ and crack opening w. Therefore, in the numerical analyses a linearly elastic law like the one used in [117] is adopted $\sigma = k_a \, w$, where k_a is the adhesive stiffness, i.e., $k_a = E_a/t_a$, E_a and t_a are Young's modulus and thickness of the adhesive layer, respectively. The parameters of the adopted power fractional law are reported in Tab. 3.2.

Table 3.2: Parameters adopted for the power fractional law.

$\hat{\tau}$	$\hat{s}$	n	Γ_f
[MPa]	[mm]	[-]	[N/mm]
7.70	0.03	2.83	0.77

In the numerical simulations the bilinear law proposed in [7, 9] has been also adopted for comparisons. The law has been defined by prescribing the same peak values $(\hat{\tau}, \hat{s})$ and fracture energy Γ_f of the power fractional law of Eq. 3.4.

3.2.3.3   Comparison between numerical and experimental results

Numerical and experimental pull-out curves are compared in Figs. 3.23 and 3.24. Numerical results are generally in good agreement with experimental data (considering the unavoidable scattering of the experimental results, and the adoption of standard parameters for the bond-slip laws). The behavior for low load levels is well predicted, so assuring
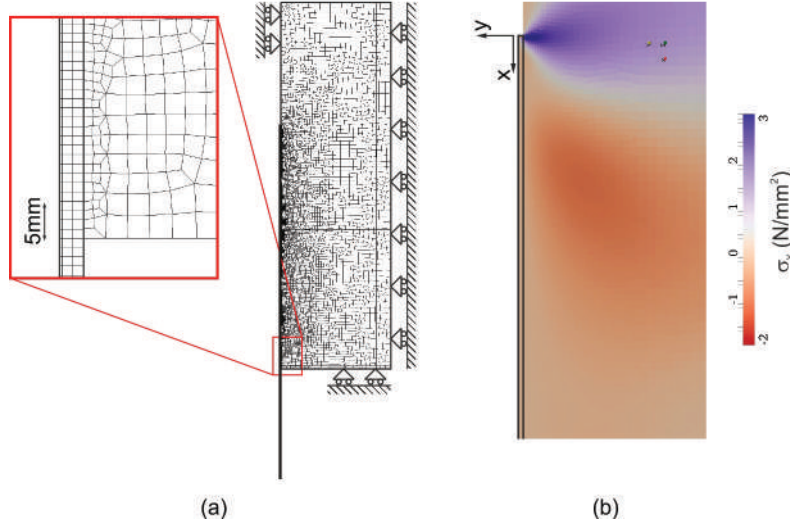
Figure 3.21: Nonlinear finite element analyses: (a) mesh; (b) normal stresses in the y direction at the beginning of the snap-back branch.

that initial (elastic) stiffness of the interface law is correctly estimated. Moreover, the bond-slip model with standard parameters permits to follow the debonding propagation at nearly constant load, with a good estimation of the length of the horizontal branch.

To take into account bond defects of some specimens, the simulations have been repeated with their effective bond length (Figs. 3.23c,d). The post failure branch, characterized by a sharp snap-back phenomenon, is weakly predicted by the numerical model due to the elastic nature of the interface law in normal direction, neglecting the possible formation of peeling cracks. The model is thus able to explain the onset of the peeling crack observed, although its propagation is missed. Moreover, for this reason, the numerical model overestimates the failure load $\hat{F}$ of the shortest specimens (Fig. 3.23a,b).

After the load peak, especially at the end of the plate, numerical simulations highlighted a mixed stress state into the substrate block characterized by high shear stresses τ_{xy} (Fig. 3.22a) and peeling stresses σ_{yy} of the same magnitude of tensile strength of concrete (Fig. 3.22b). In particular, peeling stresses appearing at the interface level (Fig.3.21b) are very important in the debonding process as the debonding progresses (Fig. 3.22b). This evidence can be seen in experiments because the layer of concrete attached to the plate often presents a higher thickness at the end of the plate where rupture is due to a mixed state of stress (Fig. 3.17c). In fact, the simultaneous presence of tangential and peeling

stresses induced in concrete a different failure mechanism.

Strain distribution in the FRP plate along the bond length are given in Fig. 3.25 for $l_b = 150$ mm at different load levels. The higher load level is close to the failure load obtained experimentally. Before failure, the numerical curves agree with the experimental points (Fig. 3.25b). However, in the snap-back regime the sign inversion of strains is completely missed by the numerical model, which does not consider peeling failure (Fig. 3.25c) and the formation of bulbs of detached material.

Computed values of failure load $\hat{F}$ as a function of bonding length l_b are reported in Fig. 3.16a, where are compared with the experimental results. Continuous and hidden lines indicate failure loads obtained by adopting power and bilinear interface laws respectively.

Fig. 3.16a clearly shows that failure loads are numerically overestimated for small bonded lengths. Obviously, the asymptotic values F_{max} (for infinite bonding length) are virtually the same because the two different interface laws have the same fracture energy. It should be mentioned that the results obtained with the bilinear law always present higher values than those predicted with the power fractional law. This fact has been clearly explained in [41].

3.2.4 Summary and final comments

The main important evidence arisen from the tests is that, as the bond length reduces, failure cannot be considered uniquely as a mode II fracture process.

Indeed, the debonding propagates as a shear type fracture up to the beginning of the descending branch of the pull-out curve. After that, the fracture propagates from the opposite side in a mixed mode, thus revealing a "two-way" debonding phenomenon similar to the one illustrated in [118] in short fibre composites. This is due to the presence of non-negligible out of plane displacements of the free end of the FRP plate that induce considerable peeling stress at concrete level. Certainly, the observed failure mode due to peeling stresses strongly depends on the mechanical properties of concrete (in particular compressive and tensile strengths). Moreover, it has been observed the detachment of bulbs of material together with a layer of substrate. In long bonded lengths two bulbs of concrete are detached at both the ends of the plate, while for short bonded lengths only one. These bulbs probably are partially responsible for the dispersion of the strain measurements and for the changing of the failure process especially at the free end of the plate. In that position, the overturning of the plate due to bending effects plus the slippage
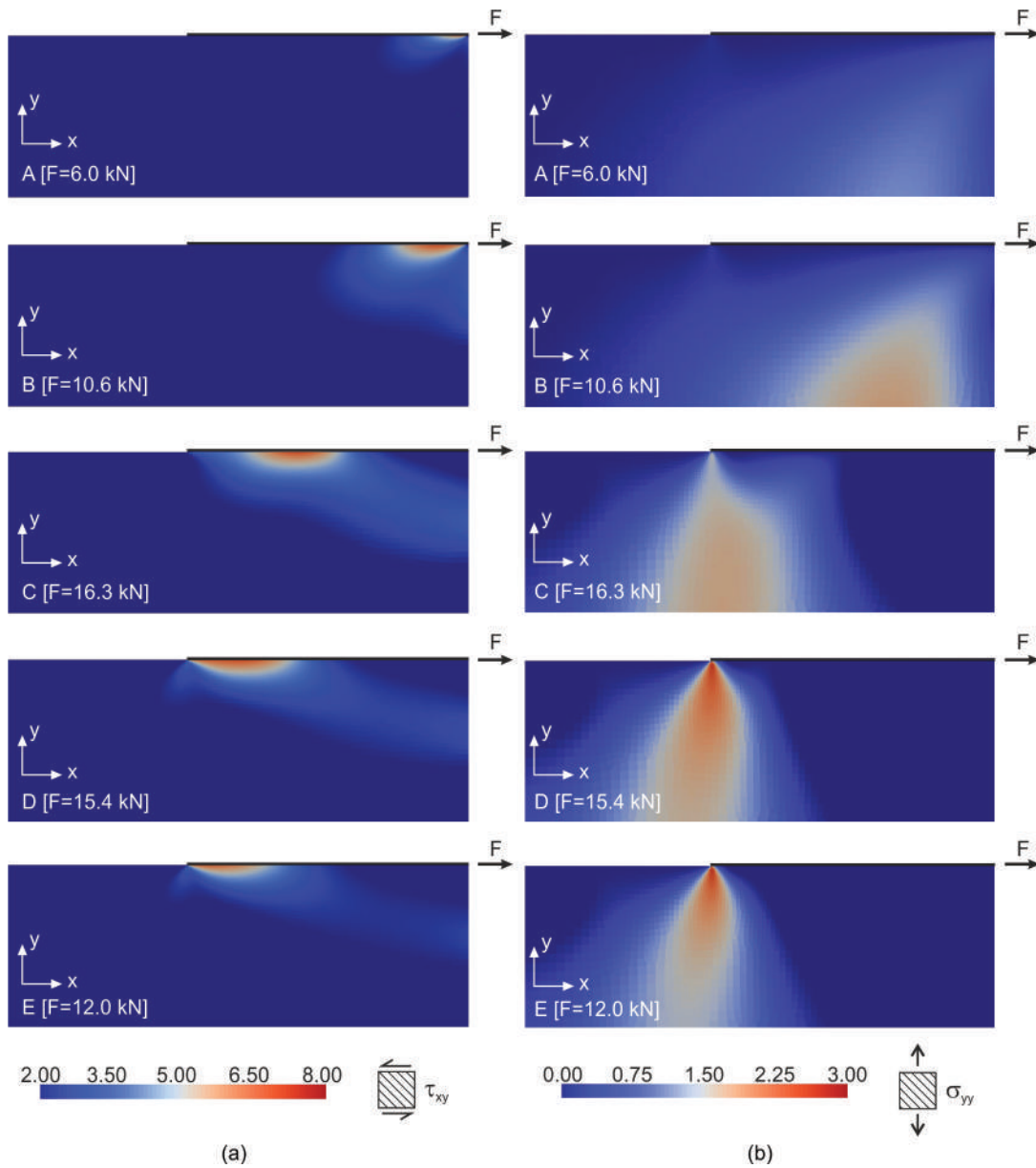
Figure 3.22: Stress maps from the finite element analysis of the specimen with $l_b = 150$ mm at the points equivalent to A-E of Fig. 3.12: (a) tangential bonding stress τ_{xy} and (b) normal (peeling) stresses σ_{yy}.
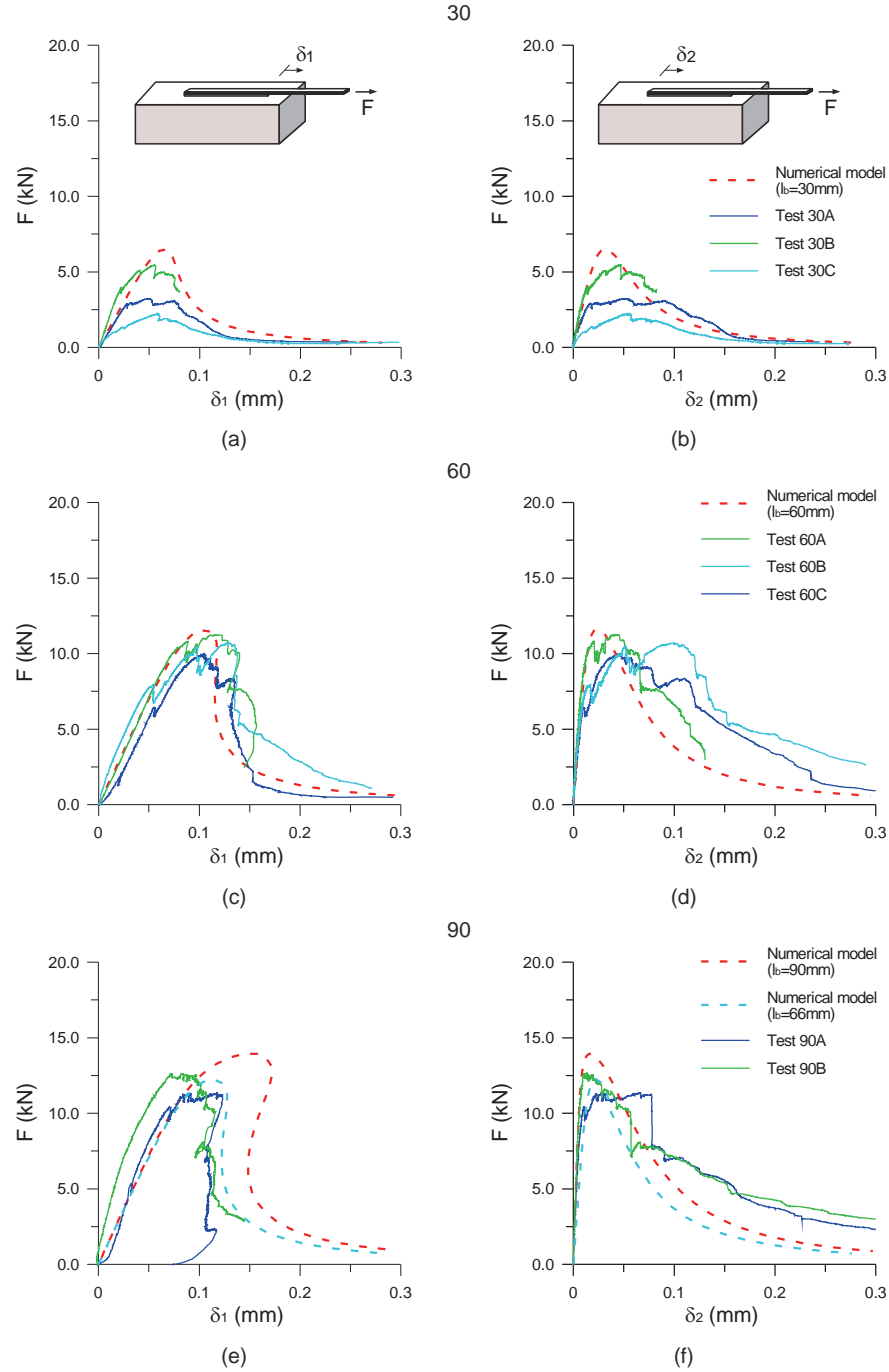
Figure 3.23: Comparison between numerical and experimental pull-out curves: (a) $F - \delta_1$ curve for the specimen with $l_b = 30$ mm; (b) $F - \delta_2$ curve for the specimen with $l_b = 30$ mm; (c) $F - \delta_1$ curve for the specimen with $l_b = 60$ mm; (d) $F - \delta_2$ curve for the specimen with $l_b = 60$ mm; (e) $F - \delta_1$ curve for the specimen with $l_b = 90$ mm; (f) $F - \delta_2$ curve for the specimen with $l_b = 90$ mm.
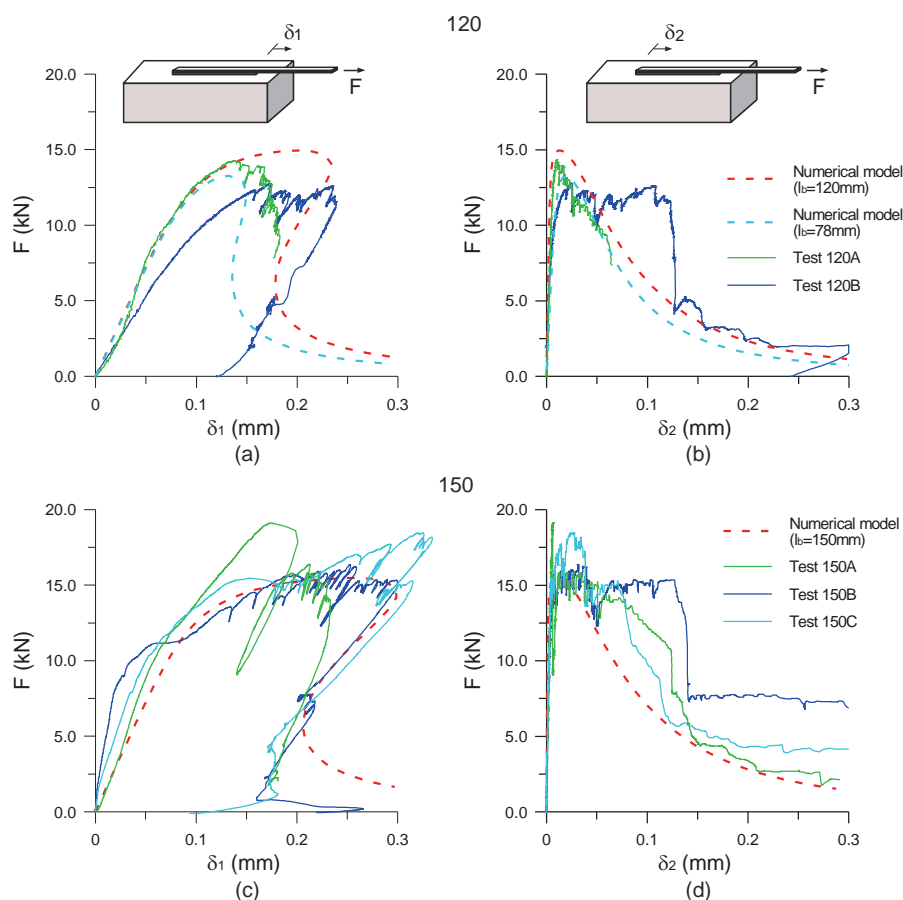
Figure 3.24: Comparison between numerical and experimental pull-out curves: (a) $F - \delta_1$ curve for the specimen with $l_b = 120$ mm; (b) $F - \delta_2$ curve for the specimen with $l_b = 120$ mm; (c) $F - \delta_1$ curve for the specimen with $l_b = 150$ mm; (d) $F - \delta_2$ curve for the specimen with $l_b = 150$ mm.

of the bulbs following its inclined fracture plane lead to an out-of-plane displacement which confirms the highlighted mode mixity.

Comparing experimental and numerical results from FEM analyses was possible to observe a good agreement until the laod peak. Anyway, classic models are unable to catch two important phenomena: the unloading path due to decreasing value of the slip in the snap-back process and secondly the mixed mode rupture due to combined shear and peel stresses at the interface level that appear when the anchorage length is short. Therefore, for a complete and general description of the debonding process of FRP plates, especially with short bonded lengths, it seems necessary to adopt a mixed and coupled dissipative
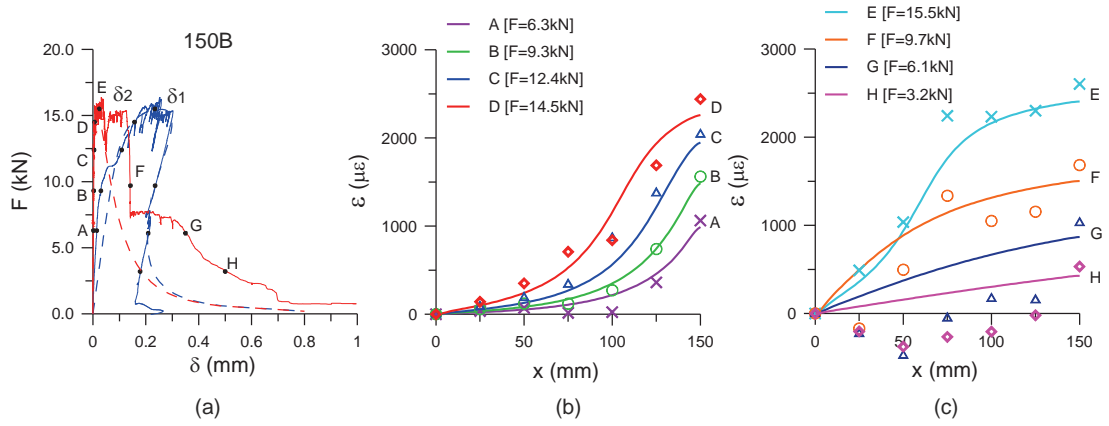
Figure 3.25: Comparison between numerical and experimental results (Specimen 150B): (a) pull-out curves; (b) strain profiles until the peak load; (c) strain profiles after the load peak.

interface law.

Finally, it has been experimentally observed for the first time the full range behavior of the externally glued FRP joints. In particular, the particular driving technique adopted allowed to directly observe the post-peak branch of the pull-out curves, the complete $\tau - s$ relationships for the entire bonded length and different failure modes.

3.3   Experimental campaign on masonry

In the present section an experimental campaign on ancient masonry is illustrated. One of the aim of the tests is to investigate the peculiar debonding behavior of ancient clay bricks, which has been demonstrated different from the one exhibited by modern bricks [38]. In particular, different failure modes have been observed which may be related to non-mechanical parameters, as permeability, surface texture and presence of heterogeneities [38]. Another issue to be studied is the influence in the local e global behavior of the mortar joints in case of masonry blocks. In fact, they constitute discontinuities in the bonding plane that can reduce the effectiveness of the reinforcement. Differently from concrete where heterogeneities are mainly represented by aggregates that have a strength much higher than the cementitious matrix, in masonry, mortar joints usually have mechanical properties comparable to the main support materials (i.e. clay bricks or natural stone ashlars).

To study the aforementioned issues, the setup presented in par. 3.1 is used. Moreover, a specifically designed lime mortar and three different types of ancient clay bricks were used to perform tests on bricks and on masonry specimens. In particular, each type of brick has been characterized measuring, besides the tensile and compressive strengths, also non-mechanical properties as porosity and microscopic structure.

The results have been discussed considering the observed differences in the failure mode, trying to identify the parameters related to such variations and their influence on the effectiveness of reinforcement. This approach is oriented to improve the mechanical model of debonding, introducing substrate parameters different from what usually adopted (i.e. compressive and tensile strengths).

3.3.1   Materials and methods

Three handmade 19th century brick types (A-B-C types in Fig. 3.26a-c) coming from different areas of the northern Italy (respectively provinces of Mantova - A, Parma - B and Piacenza - C) were considered. For each type, three bricks and three masonry blocks (Fig. 3.26d) were tested for a total of 18 specimens.
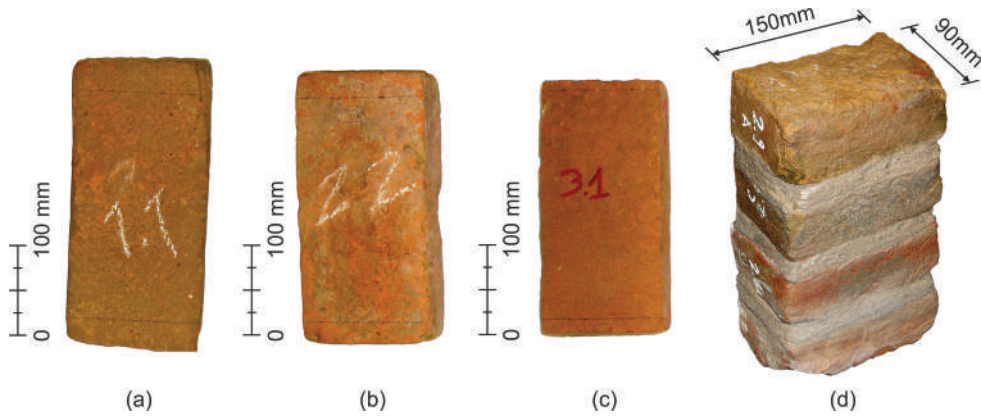
Figure 3.26: Types of brick employed: (a) A type; (b) B type; (c) C type and (d) masonry block before the reinforcement application.
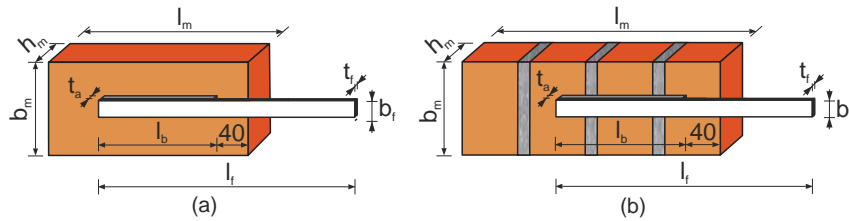
Figure 3.27: Geometry of the specimens: (a) brick; (b) masonry block.

3.3.2 Geometry

The specimen geometries are illustrated in Fig. 3.27 together with the used nomenclature whereas the average dimensions are given in Tab. 3.3-3.4. Ancient handmade preparation of the bricks leads to unavoidable scattering of specimen dimensions, as outlined in Fig. 3.26a-c and Fig. 3.28. The masonry blocks were realized with lime mortar and four superimposed units obtained sawing two bricks. Joints thickness was about 10 mm (an unavoidable, albeit small, scattering in the joint thickness is present due to the irregularities of the handmade bricks).

Each sample was reinforced using a single-layer unidirectional CFRP strip glued following the method proposed by the producer ([119]). A nominal length of the bonded zone l_b of 150 mm was chosen. This assumption assures that the effective anchoring length l_{eff} was shorter than the bonded length l_b, as confirmed by the experimental evidence commented later on (see par. 3.3.3). The same bond length has already been adopted in [1] permitting to accurately investigate the debonding process and fracture mechanism. A 40

mm long portion of sheet was left un-bonded (Fig. 3.27) at the loaded end so to prevent the expulsion of a prism as a result of edge effects and stress concentrations ([3]). A nominal width b_f of 35 mm was chosen to guarantee the development of an undisturbed central region within the CFRP sheet ([25]). The effective mean thickness of the laminated sheets $t_{f,eff}$ was 1.4 mm.

Table 3.3: Mean dimensions of the brick specimens with the relative standard deviations (in brackets).

Brick specimens	b_m [mm]	h_m [mm]	l_m [mm]	l_b [mm]	b_f [mm]
A	147±3	61±1	244±3	143±9	36.5±2 (σ=6.2%)
B	131±4	59±1	243±2	152±1	37.5±2 (σ=6.0%)
C	140±6	59±1	240±2	145±2	35.0±4 (σ=14.2%)

Table 3.4: Mean dimensions of the masonry block specimens specimens with the relative standard deviations (in brackets).

Brick specimens	b_m [mm]	h_m [mm]	l_m [mm]	l_b [mm]	b_f [mm]
MA	138±2	88±2	258±2	144±2	38.5±2 (σ=7.2%)
MB	130±1	88±4	260±10	143±7	38.0±2 (σ=5.5%)
MC	143±3	89±1	257±9	145±2	36.5±4 (σ=2.1%)

3.3.2.1 Specimen preparation

A specific mix-design of mortar has been chosen to reproduce the material used in ancient constructions. In particular, a natural hydraulic lime usually used in the restoration interventions on ancient masonry buildings and fine river aggregates with diameter spacing from 0.063 to 4 mm were used. In the case of brick specimens, reinforcement has been applied on brick top surfaces, whereas for masonry specimens the reinforcement has been applied on the non-sawed head of the bricks.

Before reinforcement application, the bonding surfaces of specimens were regularized by a grinding machine and then with a layer of epoxy putty as suggest by the producer

[119]. Regularizing layer width b_p was greater than the sheet width b_f to allow bonding of the reinforcement directly over the epoxy putty.

Ancient handmade masonry bricks present irregular surfaces (Fig. 3.28) thus, to permit a precise positioning inside the testing machine supporting frame, clay brick specimen bases were sawed. Finally, all the specimens were stored in laboratory conditions for one month to permit the complete hardening of the adhesive.

3.3.2.2   Material characterization

Bricks   At a first glance, it is possible to notice highly variable brick surface conditions for both the presence of heterogeneities and voids as well as for the color (Fig. 3.28). These aspects, depending on variable firing conditions or clay mixture, may lead to very different mechanical properties: for this reason the bricks were separately characterized. In particular, after debonding tests, each brick specimen was sawed to obtain two prisms for compression tests (Fig. 3.29a-b), a beam for three-point bending test (Fig. 3.31a-b), a sample to measure porosity and some thin sections for microscope analyses (according to standard codes [120, 121], Fig. 3.28). For the masonry specimens, the mean properties measured for each group of bricks are considered.

The compression prisms were equipped with strain gauges to measure Young's Modulus E_m and Poisson's ratio ν (Fig. 3.29c). Three-point bending specimens (Fig. 3.31) were tested controlling the crack mouth opening displacement to measure flexural strength $f_{tm,fl}$ and the mode-I fracture energy G_F, similarly to what explained for concrete in par. 3.2.1.3. Mean values of the compressive and flexural strengths of the bricks are reported in Fig. 3.30. Porosity C_p was measured by means of the water evaporation method (difference of weight of saturated and dried sample divided by density of water) [120]. Average values of compressive strength f_{cm}, Young's modulus E_m, Poisson's ratio ν, shear modulus $\mathcal{G}_m$ (determined as $\mathcal{G}_m = E_m/2(1+\nu)$), flexural strength $f_{tm,fl}$, fracture energy G_F and porosity C_p, together with their standard deviation coefficients σ, are summarized in Tab. 3.5. Despite the outlined differences in brick appearance, their mechanical parameters are comparable. The values of σ are rather high, but typical for the ancient masonry [38]. Differently, the porosity for A-series and B-series is higher than for C-series. Microscope analyses revealed that this difference might be related to the clay mixture. In particular, C-series showed silica impurities, like fine sand, while the clay mixture of A and B-series was characterized by large impurities and firing wastes, as showed in Fig. 3.28.
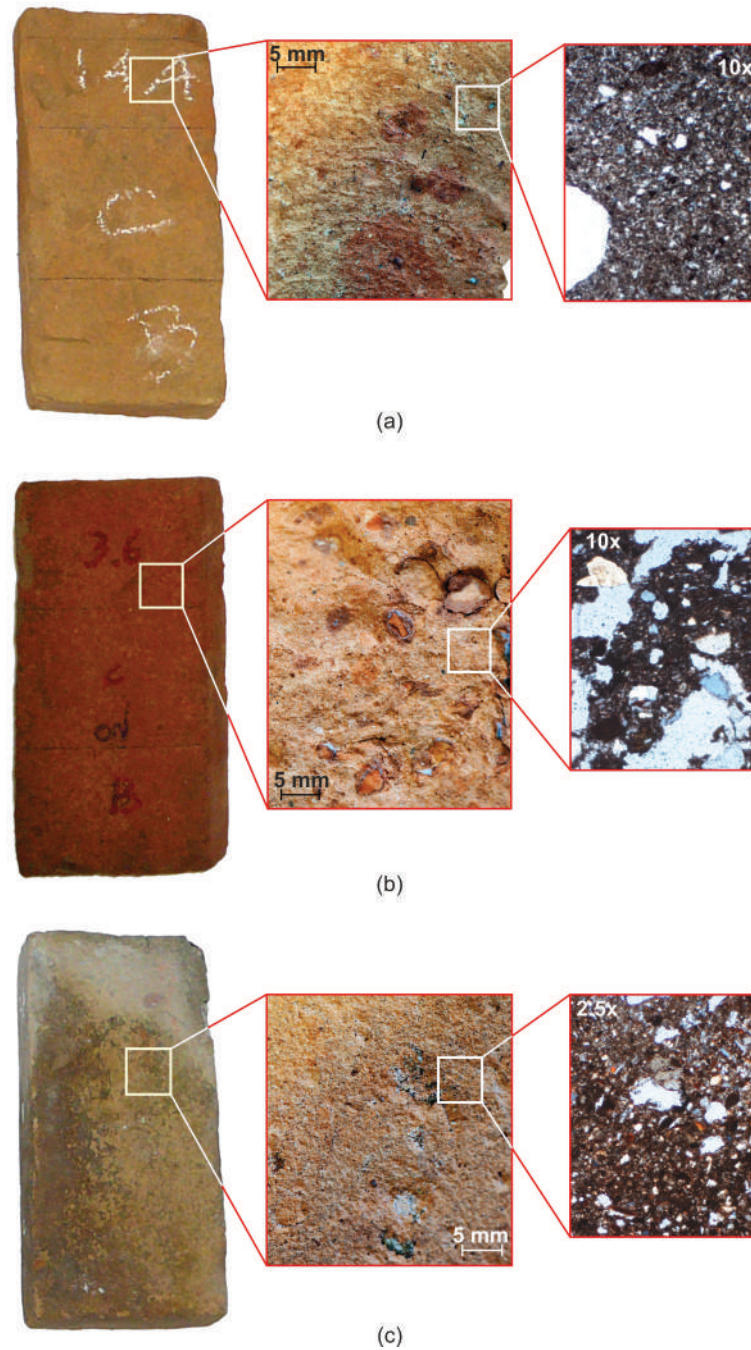
Figure 3.28: Different kinds of clay bricks employed with macro-photo and images from microscope: (a) A-series; (b) B-series; (c) C-series.
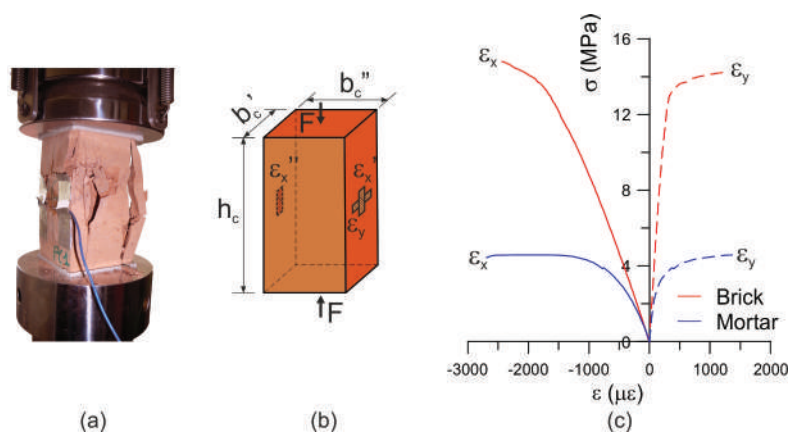
Figure 3.29: Compression test for bricks and mortar: (a) brick specimen during the test; (b) geometry of the specimens; (c) stress-strain relationship in longitudinal ($\sigma_x - \varepsilon_x$) and transversal ($\sigma_x - \varepsilon_y$) direction.

Moreover, in B-series samples pieces of crushed bricks from previous firings and large voids were observed (Fig. 3.28).
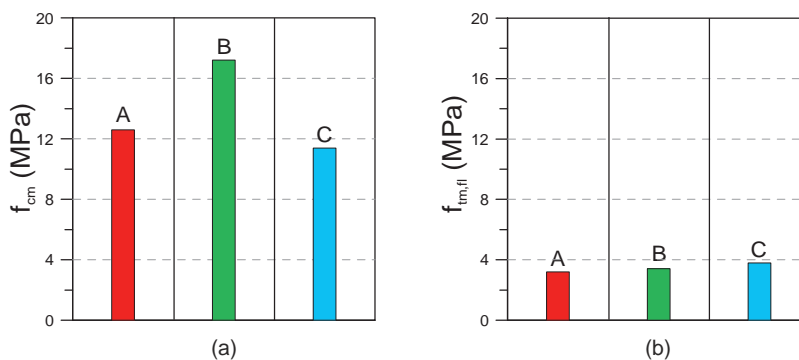
Figure 3.30: Mean values of the strengths of the various bricks: (a) compressive strength; (b) flexural strength.

Mortar To characterize the mortar, four beams (with dimensions 40x40x160mm) were cast into steel molds and demolded after four days. After 28 days of hardening in saturated environment, the prisms were first tested in three-point bending (Fig. 3.31c) to determine flexural tensile strength $f_{tm,fl}$ and fracture energy G_F, then, the two separated pieces were tested in compression, according to the standard code [122] (Fig. 3.29c). The mechanical properties of the mortar are summarized in Tab. 3.5.
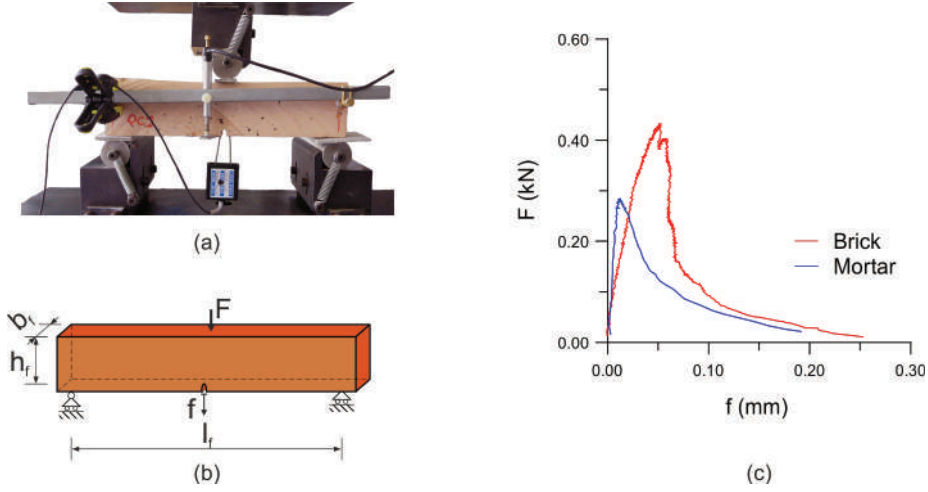
Figure 3.31: Three-point-bending test for bricks and mortar: (a) brick specimen during the test; (b) geometry of the specimens; (c) force vs. deflection curves $F - f$.

Adhesive and epoxy putty A two-component epoxy resin [119] was used to glue CFRP strips following the wet layup method prescribed by the material supplier [119]. The principal mechanical parameters of the glue declared by the producer are Young's modulus $E_a = 3000$ MPa, tensile strength $f_{ta} = 70.0$ MPa, ultimate tensile strain $\varepsilon_{au} = 6.0\%$, shear modulus $\mathcal{G}_a = 1250$ MPa [119]. The declared mechanical properties of the epoxy putty [119] are Young's modulus $E_p = 12800$ MPa and shear strength $\tau_{au} \geq 15.0$ MPa [119].

FRP reinforcement The declared nominal design thickness of the reinforcement (i.e. the thickness of carbon fibers that provide mechanical properties equal to the laminated strip) is $t_f = 0.23$ mm. The mean mechanical properties declared by the producer and related to the nominal thickness are Young's modulus $E_f = 390000$ MPa, tensile strength $f_f = 3000$ MPa and ultimate tensile strain $\varepsilon_{fu} = 0.8\%$ [119]. The average Young's modulus measured during present tests and referred to the effective mean thickness $t_{f,eff} = 1.4$ mm is $E_{f,eff} = 63500$ MPa.

3.3.2.3 Setup and instrumentation

The test setup was the same proposed and validated in [1] and described in par. 3.1. The specimens were mounted into the same steel cage used for the concrete substrate but, to avoid early failure of the bricks, the whole base of the specimen was set on steel plates:

Table 3.5: Mean values of the measured characteristics of the bricks and the mortar with the relative standard deviations σ (in brackets).

Material	f_{cm} [MPa]	E_m [MPa]	ν [-]	$\mathcal{G}_m$ [MPa]	$f_{tm,fl}$ [MPa]	G_F [N/m]	C_p [%]
Series A	12.6 (19.7%)	8300 (16.8%)	0.13	3670	3.2 (2.2%)	11 (3.2%)	23.7 (3.1%)
Series B	11.4 (24.2%)	8700 (12.4%)	0.2	3620	3.8 (43.8%)	15.8 (49.5%)	21.2 (11.9%)
Series C	17.2 (3.3%)	7350 (28.1%)	0.17	3140	3.4 (26.1%)	12.6 (22.0%)	16.7 (38.3%)
Mortar	4.8 (4.5%)	7500 (20.8%)	0.26	2970	1.1 (8.2%)	5.3 (14.7%)	-

the brick specimens were supported by an L-shape steel frame (Fig. 3.32a), whereas the masonry blocks were leaned on a steel plate (Fig. 3.32b). To provide a uniform support, the surface in contact with the plate was flattened with polyester putty. Fig. 3.32c depicts a specimen mounted into the setup before the test.

Each specimen was equipped with two LVDTs measuring the displacement δ'_1 and δ''_1 at the loaded end of the sheet: this permitted to obtain the global slip $\delta_1 = (\delta'_1 + \delta''_1)/2$ and to detect the presence of harmful in-plane rotations of the sheet (Fig. 3.32a-b), similarly to what illustrated in par. 3.2.1.4. The free end slip between the reinforcement and the substrate δ_2 (Fig. 3.32a-b) was measured by means of the clip-gauge used to control the test. In the same position, a third LVDT measured the out-of-plane relative displacement δ_3 (Fig. 3.32a-b) between brick and the composite. Strain values along the bonded length were recorded with a strain gauge chain glued over the sheet (Fig. 3.32a-b). The distance of the transducers was kept constant and equal to 25 mm for bricks, whereas for masonry no transducers were located over the mortar joints thus resulting in a variable step. The loaded end of the sheet was equipped with strain gauges that measured the free elongation (ε'_A, ε''_A and ε_B, Fig. 3.32a-b) and the Young's modulus $E_{f,eff}$.

The test protocol was the same described in par. 3.1.1.
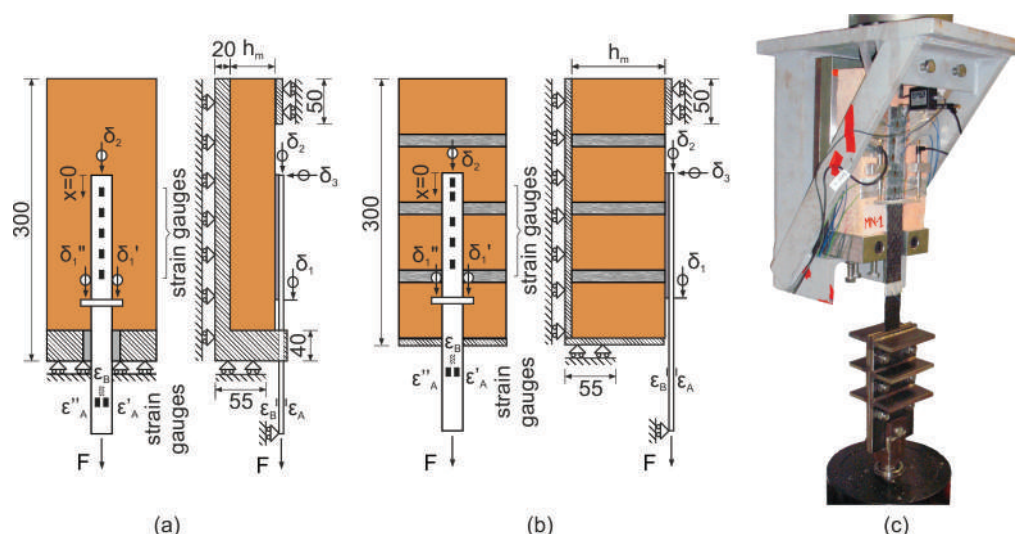
Figure 3.32: Static schemes and test setup with the applied instrumentation: (a) brick specimen; (b) masonry block specimen; (c) picture of a specimen mounted into the steel cage.

3.3.3 Experimental results

The in-situ wet-layup method led to unavoidable, albeit small, differences in the width b_f of the reinforcements, thus, to permit proper comparisons, the force F was normalized by the width b_f as explained in the following graphs.

3.3.3.1 Bond strength

The maximum load values $\hat{F}$ are reported in Tab. 3.6 while the values of the normalized maximum force $\hat{F}/b$ for all the widths accounted for and the rupture type for each specimen are reported in Tab. 3.7 and compared in Fig. 3.33. Specimen A-2 is missing in both the tables because the control of the test was prematurely lost before the peak load. Dissimilarities between the results arise from three main causes. Variations within specimens belonging to the same class of bricks are due to hand-made production and firing in non-standardized kilns. Moreover, different mixtures of clay coming from various areas are responsible for the changes in the average values among classes. Finally, the dispersion is also related to the damaging of bricks due to their ageing and previous employment.

No remarkable differences have been observed in the maximum load value $\hat{F}/b_f$ between brick and masonry specimens built up with the same class of bricks, confirming the largely accepted hypothesis of rather limited influence of the mortar joints on load

70
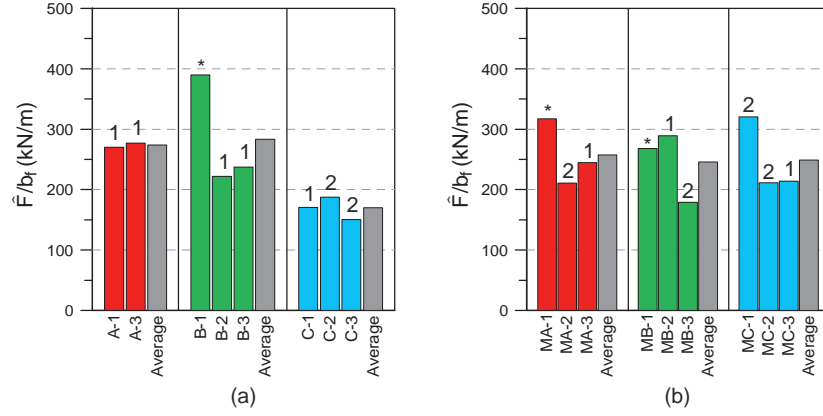
Figure 3.33: Normalized maximum load values F_{max}/b_f from the tests: (a) clay brick specimens; (b) masonry blocks. NOTE: 1 = type-1 failure; 2 = type-2 failure; * = Anomalous rupture

carrying capacity of the reinforcement [7–9, 37].

3.3.3.2 Failure modes

Considering the failure modes, except for a few specimens, which revealed anomalous ruptures due to defects (e.g. incorrect specimen preparation or unexpected weakness caused by significant heterogeneities or damaging of the brick), the visual inspection after failure revealed two types of debonding (summarized for each specimen in Tab. 3.6):

- Type 1: occurred with removal of a considerable and irregular brick portion of thickness 1-3 mm; the most common irregularity was the detachment of a wedge at the free end of the reinforcement (Figs. 3.34 and 3.36).

- Type 2: appeared with removal of a very thin and uniform brick layer with thickness about 0.8-1 mm (Fig. 3.35).

No failure occurred at the adhesive level and all FRP sheets supported the applied loads. The same rupture types were seen in brick and masonry specimens. For masonry, mortar joints introduced a kind of discontinuity in the specimens, which lead sometimes to irregularities in the removed substrate (Fig. 3.36b). Some other minor rupture phenomena were found such as the creation of a small wedge at the joint level or at the sheet beginning.

The two rupture types here evidenced have also been observed in [38]. In particular, the first detachment mechanism characterized both new and ancient masonry, while the

Table 3.6: Measured sheet width (b_f), regularization layer width (b_p), effective detached width (b^*), computed t_m^* values and $\hat{F}$ values, together with their mean values and standard deviation σ (in brackets) and the failure types observed for each specimen.

Specimen	$\mathbf{b_f}$ [mm]	$\mathbf{b_p}$ [mm]	$\mathbf{b^*}$ [mm]	$\mathbf{t_m^*}$ [mm]	**Failure**[†]	$\mathbf{\hat{F}}$ [kN]
A-1	33.8	42.3	46.1	11.6	1	9.1
A-3	30.5	44.4	48.4	9.1	1	8.5
Mean value A series						**8.8** (5.5%)
B-1	36.3	44.7	48.1	-	AR	14.1
B-2	37.0	44.7	52.0	9.5	1	8.2
B-3	37.9	42.3	43.1	11.3	1	9.0
Mean value B series						**10.5** (30.8%)
C-1	29.7	41.6	40.1	6.4	1	5.1
C-2	37.9	44.7	48.9	6.6	2	7.1
C-3	30.2	41.0	33.7	9.9	2	4.6
Mean value C series						**5.6** (24.3%)
MA-1	31.2	41.5	45.1	-	AR	9.9
MA-2	34.8	40.6	44.9	6.8	2	7.3
MA-3	37.9	41.3	50.9	10.2	1	9.3
Mean value MA series						**8.8** (15.1%)
MB-1	31.7	40.5	44.1	-	AR	8.5
MB-2	34.2	41.2	51.0	10.3	1	9.9
MB-3	35.3	39.0	42.1	6.9	2	6.3
Mean value MB series						**8.2** (21.8%)
MC-1	30.7	42.0	44	8.0	2	9.8
MC-2	34.1	41.4	43.9	8.0	2	7.2
MC-3	35.3	40.7	46.9	11.9	1	7.6
Mean value MC series						**8.2** (17.4%)

[†]1 = type-1 failure; 2 = type-2 failure; AR = anomalous rupture.

Table 3.7: Normalized maximum force applied and fracture energies computed with the sheet width ($\hat{F}/b_f$ and $\Gamma_f(b_f)$), the regularization layer width ($\hat{F}/b_p$ and $\Gamma_f(b_p)$), the effective detached width ($\hat{F}/b^*$ and $\Gamma_f(b^*)$) together with the standard deviations σ.

Specimen	$\hat{\mathbf{F}}/\mathbf{b_f}$ [kN/m]	$\hat{\mathbf{F}}/\mathbf{b_p}$ [kN/m]	$\hat{\mathbf{F}}/\mathbf{b^*}$ [kN/m]	$\mathbf{\Gamma_f(b_f)}$ [N/mm]	$\mathbf{\Gamma_f(b_p)}$ [N/mm]	$\mathbf{\Gamma_f(b^*)}$ [N/mm]
A-1	270.4	216.1	198.3	0.408	0.260	0.219
A-3	277.1	190.4	174.6	0.428	0.202	0.170
Mean	**273.7**	**203.2**	**186.4**	**0.418**	**0.231**	**0.195**
σ	1.7%	8.9%	9.0%	3.5%	17.8%	17.9%
B-1	389.8	316.5	294.2	-*	-*	-*
B-2	222.2	183.9	158.1	0.275	0.189	0.139
B-3	237.7	213.0	209.0	0.315	0.253	0.244
Mean	**283.2**	**237.8**	**220.4**	**0.295**	**0.221**	**0.191**
σ	32.7%	29.3%	31.2%	9.5%	20.6%	38.5%
C-1	171.0	122.1	126.7	0.163	0.083	0.089
C-2	187.9	159.3	145.6	0.197	0.141	0.118
C-3	150.7	111.0	135.0	0.127	0.069	0.102
Mean	**169.9**	**130.8**	**135.8**	**0.162**	**0.098**	**0.103**
σ	11.0%	19.3%	7.0%	21.7%	39.4%	14.0%
MA-1	317.3	238.5	219.5	-*	-*	-*
MA-2	210.9	180.8	163.5	0.248	0.182	0.149
MA-3	244.9	224.7	182.4	0.334	0.282	0.185
Mean	**257.7**	**214.7**	**188.4**	**0.291**	**0.232**	**0.167**
σ	21.1%	14.1%	15.1%	21.0%	30.3%	15.4%
MB-1	268.1	209.8	192.7	-*	-*	-*
MB-2	289.1	240.0	193.9	0.466	0.321	0.210
MB-3	179.1	162.1	150.2	0.179	0.146	0.126
Mean	**245.5**	**204.0**	**178.9**	**0.322**	**0.234**	**0.168**
σ	23.8%	19.3%	13.9%	63.0%	52.8%	35.4%
MC-1	320.5	234.3	223.6	0.573	0.306	0.279
MC-2	211.4	174.1	164.2	0.249	0.169	0.150
MC-3	214.2	185.8	161.2	0.256	0.192	0.145
Mean	**248.7**	**198.1**	**183.0**	**0.359**	**0.222**	**0.191**
σ	25.0%	16.1%	19.2%	51.5%	32.9%	39.6%

*Anomalous rupture of the specimen. See Tab. 3.6.
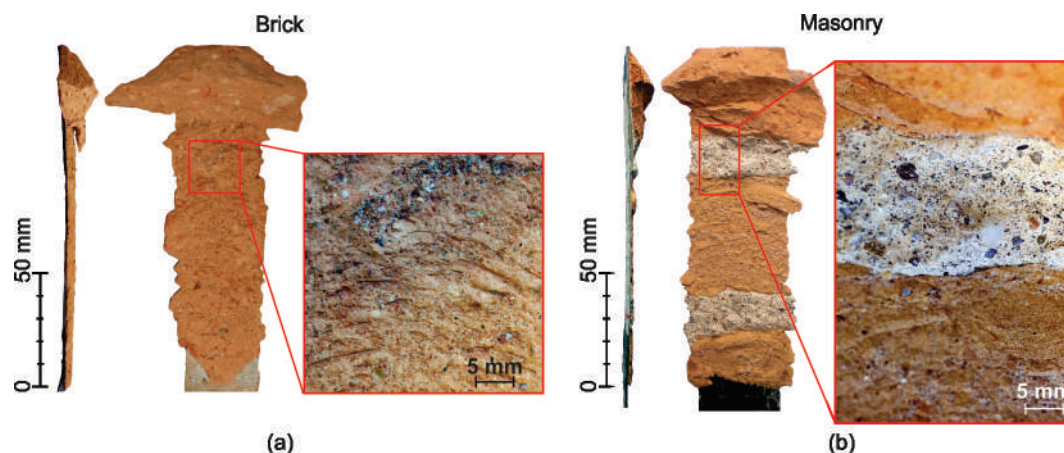
Figure 3.34: Type-1 failure observed for specimens built up with A-series bricks: (a) brick specimen A-1; (b) masonry specimen MA-3.

second appeared in ancient masonry only.

These rupture types are not merely related to compressive and flexural strengths, since comparable values have been measured for all the classes of bricks (Tab. 3.5). As already pointed out in [38, 123], in ancient brick masonry other properties like surface roughness and material heterogeneities (e.g. large voids and asperities) may play an important role. In particular, in the present tests, observed changes in failure type seem to depend on the different capacity of the glue to penetrate into the substrate. Indeed, A and B-series, which usually displayed type-1 failure, were characterized by highly heterogeneous structure with big voids and impurities that permitted a deeper penetration of the glue into the substrate. This is well observable in Fig. 3.36, where some gray spots of regularizing epoxy putty on the sheet-side of the debonded surface are clearly visible. Differently, C-series, which showed type-2 failure, was characterized by smaller values of load carrying capacity F_{max}/b_f, probably related to a fine texture with micro-voids and absence of impurities or large heterogeneities (Fig. 3.35).

Moreover, Figs. 3.34 and 3.36 show that the width of substrate detached by the sheet b^* (i.e. the width of the zone in which the cohesive crack propagates) was greater than the width of the sheet b_f and more similar to the width of the regularizing layer b_p (Tab. 3.7). This suggests that the regularizing putty, where is present, is able to ensure stress transfer between reinforcement and support.
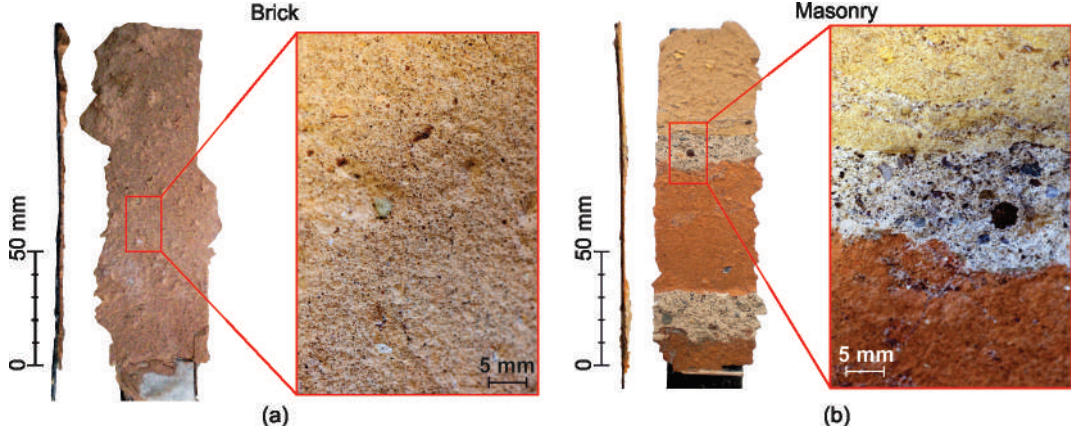
Figure 3.35: Type-2 failure observed for specimens built up with C-series bricks: (a) brick specimen C-2; (b) masonry specimen MC-2.

3.3.3.3 Pull-out curves and strain profiles

Apart some differences that will be discussed at the end of this section, bricks and masonry specimens shown similar pull-out curves and strain profiles. For this reasons test results will be illustrated choosing as paradigmatic examples the specimens A-1 and MA-3 for type-1 rupture and C-2 and MC-2 for type-2 rupture.

It should be highlighted here that the results are very similar for all the tests so attention is focused on the differences.

The ascending branch of the curves $F/b_f - \delta_2$ (Fig. 3.37a-d and Fig. 3.38a-d) is close to the vertical axis since, at the maximum load, the slip at the free end δ_2 is very small (2-3μm) compared with the global slip at the loaded end δ_1. After the peak, the displacement δ_2 displays a softening equilibrium path that ends in a horizontal plateau (Fig. 3.37). At this stage, the sheet was almost completely detached and the residual load carrying capacity of the specimen was due to friction within the asperities of the crack faces. The absence of unstable behavior in the $F/b_f - \delta_2$ curve permitted to control the test avoiding premature failure of the reinforcement, making thus available the entire equilibrium path $F/b_f - \delta_1$ (i.e. pull-out curve), including its snap-back branch. The observed pull-out curves $F/b_f - \delta_1$ (Fig. 3.37a-d and Fig. 3.38a-d) display a linear initial branch (points A-B) followed by a short nonlinear ascending path before approaching the peak load $\hat{F}$ (point D). After the peak, a sub-horizontal plateau occurs, followed by the snap-back branch (points F-G and H). The presence of a plateau confirms that the bonded length
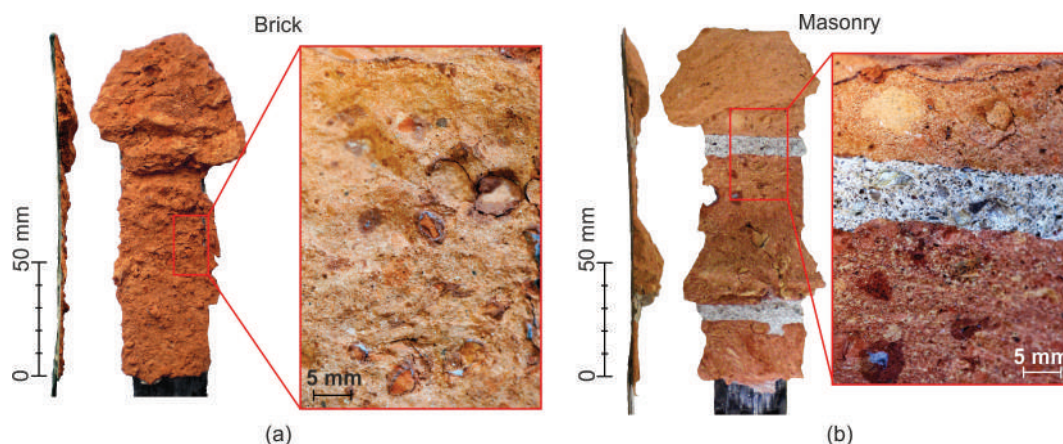
Figure 3.36: Type-1 failure observed for specimens built up with B-series bricks: (a) brick specimen B-2; (b) masonry specimen MB-3.

is longer than the effective bond length l_{eff}, therefore the maximum force capacity F_{max} was reached. Anyway, masonry specimens present a shorter plateau, as if mortar joints caused a reduction of the bonded length with respect to brick specimens.

In Fig. 3.37c-f and Fig. 3.38c-f the distribution of the strains along the sheet is depicted for different load values, which are identified with black dots in Fig. 3.37a-d and Fig. 3.38a-d as well. In the loading phase (points A-C in Fig. 3.37c-f and Fig. 3.38c-f) the strains monotonically decrease from the loaded end to the free one. Approaching F_{max} the strain profile assumes the classic *"S-shape"* (point D in Fig. 3.37c-f and Fig. 3.38c-f) along the stress transfer length. At this stage, a crack appeared at the loaded end, revealing debonding starting point. In the post-peak stage, the crack propagated from the loaded end toward the opposite side during all the sub-horizontal plateau of the pull-out curve (point E in Fig. 3.37c-f and Fig. 3.38c-f). This fact is highlighted by the strain profile at the loaded end that becomes flat. As mentioned in par. 2.1, for a given load, the absence of variations in the strain values along the glued length implies that no stress transfer is present (i.e. the sheet was detached from the substrate).

Some differences were observed in the local behavior of masonry specimens in the post peak stage. In particular, when mortar joints are involved in the stress transfer zone (curves E-H in Fig. 3.37f and Fig. 3.38f), the pull-out curves appear more scattered, with several load drops and the strain profiles at constant load exhibit oscillations (Fig. 3.37d and Fig. 3.38d). This behavior is probably due to the presence of mortar joints, which constitute heterogeneities of the bonding substrate. Similar behavior was also observed in
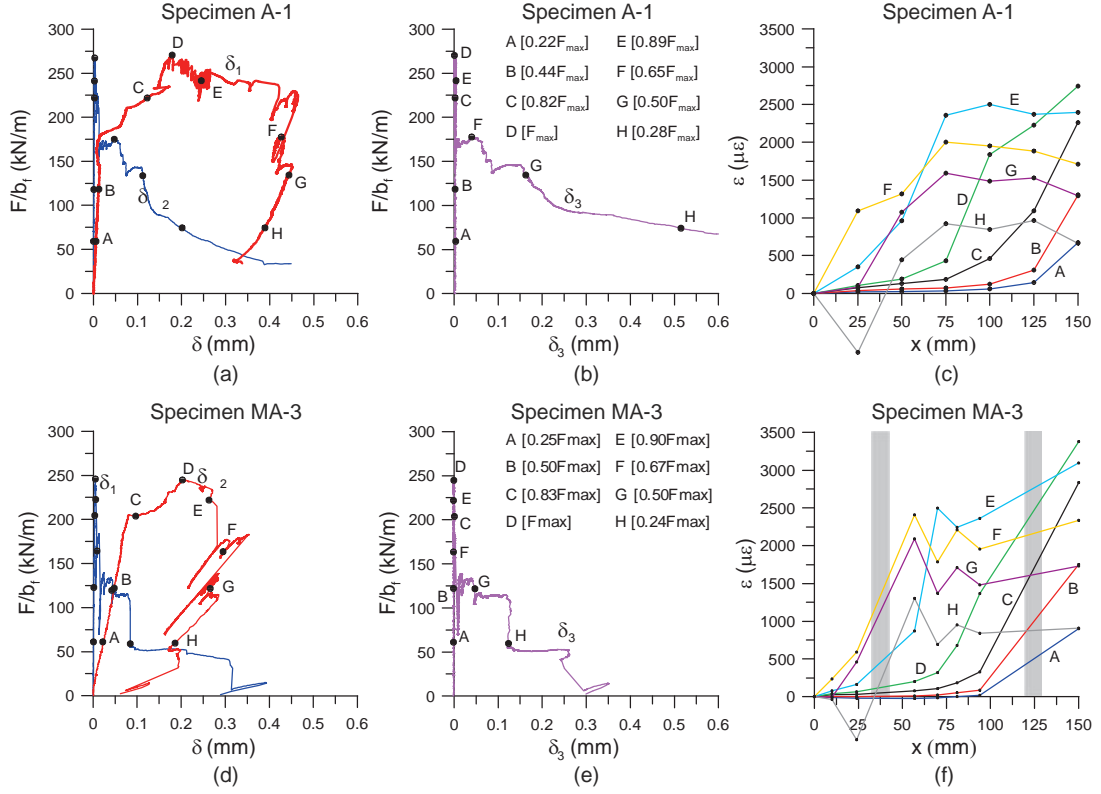
Figure 3.37: Experimental results: (a) pull out curves for the specimen A-1; (b) $F/b_f - \delta_3$ curve for the specimen A-1; (c) strain profiles for different load values for specimen A-1; (d) pull out curves for the specimen MA-3; (e) $F/b_f - \delta_3$ curve for the specimen MA-3; (f) strain profiles for different load values for specimen MA-3.

concrete specimens in correspondence of big aggregates (see Ref. [36]), which represent discontinuities with higher stiffness and strength than mortar joints. Differently, Fig. 3.38f shows a very regular strain profile. Here, limited interlocking phenomena were created by the joints. Finally it should be mentioned the fact that no macroscopic differences emerge comparing Fig. 3.37 and Fig. 3.38, even if rupture modes were different.

During the softening branch, when the load was about 60% of $\hat{F}$ (point F in Fig. 3.37a-d and Fig. 3.38a-d), the strain value at the free end started to decay, sometimes inverting its sign (point F in Fig. 3.37c-f). Here, the debonding crack stopped propagating and a peeling fracture appeared at the free end, while the central portion of the glued area was still sound. As evidenced by the relative out-of-plane displacement between sheet and substrate δ_3 (Fig. 3.37b-e and Fig. 3.38b-e), the peeling crack appeared during the snap-back regime (point F in Fig. 3.37a-d and Fig. 3.38a-d). Bending of the detached free
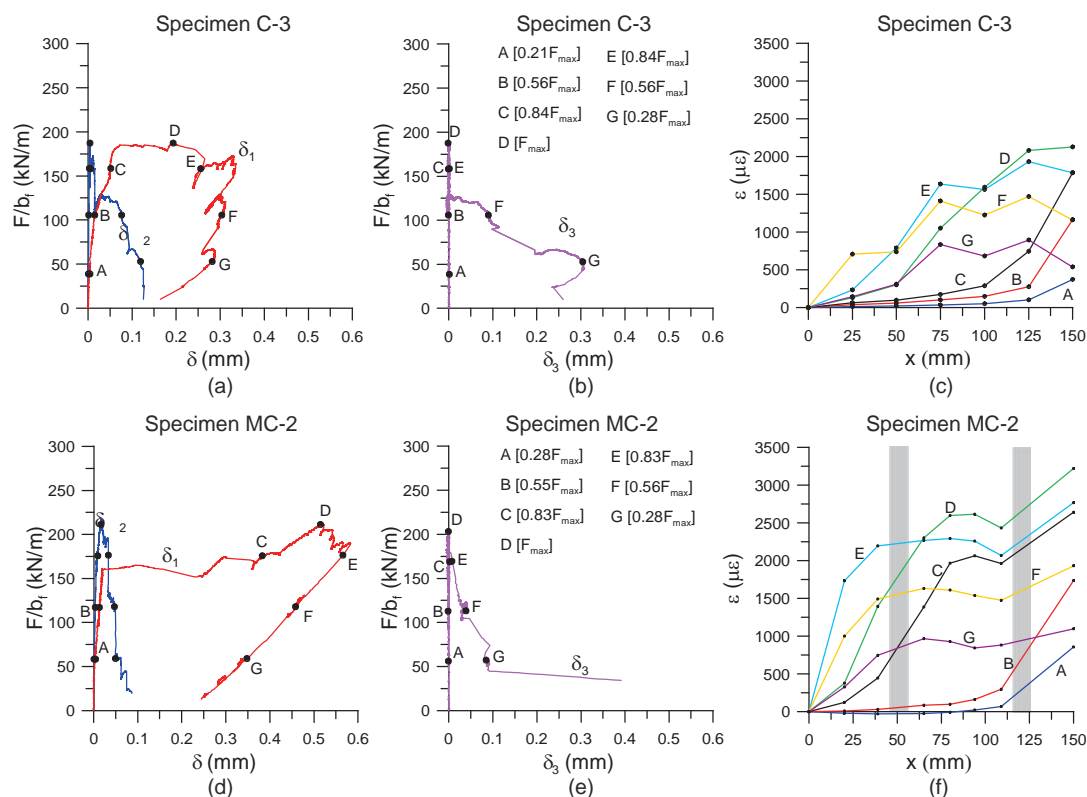
Figure 3.38: Experimental results: (a) pull out curves for the specimen C-2; (b) $F/b_f - \delta_3$ curve for the specimen C-2; (c) strain profiles for different load values for specimen C-2; (d) pull out curves for the specimen MC-2; (e) $F/b_f - \delta_3$ curve for the specimen MC-2; (f) strain profiles for different load values for specimen MC-2.

end of the sheet explains the reduction of strains. The same phenomenon was observed in experimental debonding test on concrete substrate illustrated in par. 3.2.

Concerning the B-series specimens (Fig. 3.39), the behavior confirms the findings for the type-1 rupture both for the bricks (Fig. 3.39a-c) and the masonry blocks (Fig. 3.39d-f). Nevertheless, it is possible to highlight more scattered curves, especially in the strain profiles (Fig. 3.39c,f). This is explicable considering that microscope analyses on B-series revealed an impure clay mixture characterized by big heterogeneities like crushed bricks and firing waste (Figs. 3.28 and 3.36).
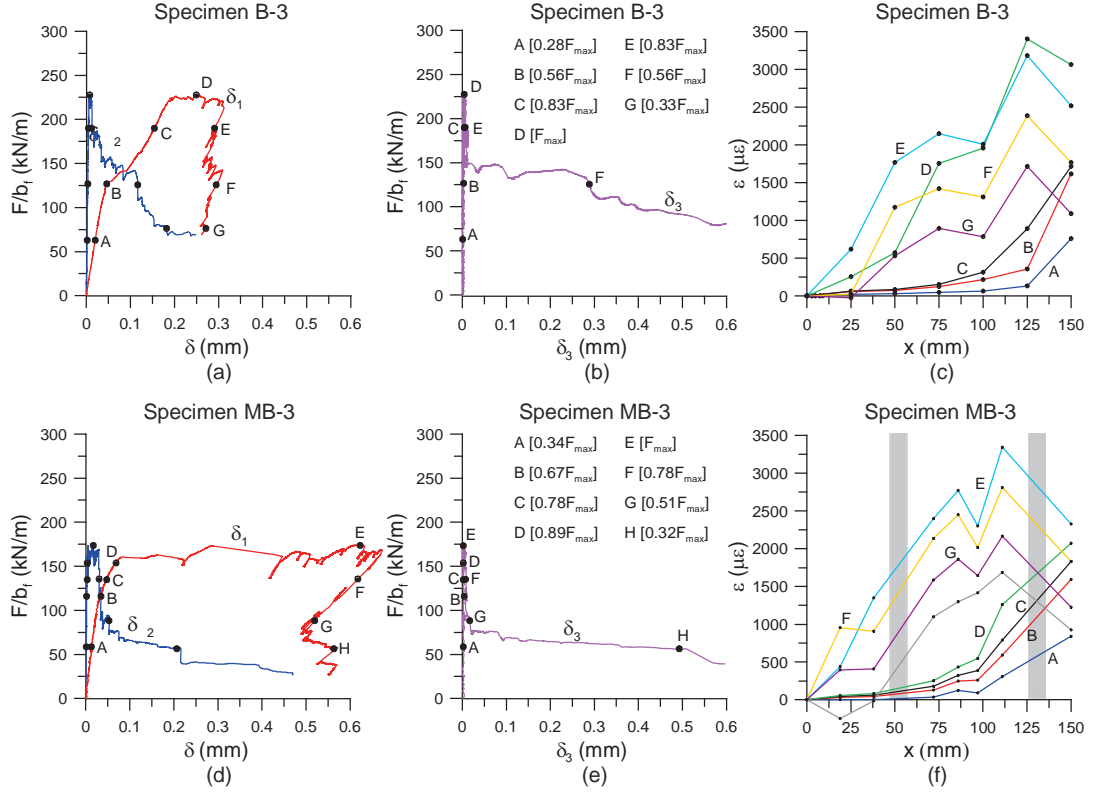
Figure 3.39: Experimental results: (a) pull out curves for the specimen B-3; (b) $F/b_f - \delta_3$ curve for the specimen B-3; (c) strain profiles for different load values for specimen B-3; (d) pull out curves for the specimen MB-3; (e) $F/b_f - \delta_3$ curve for the specimen MB-3; (f) strain profiles for different load values for specimen MB-3.

3.3.3.4 Experimental bond-slip relationships

Following the approach presented in [3] and already described in par. 3.2.2.3, based on the hypothesis of pure shear behavior of the sheet, the local bond-slip relationships have been computed from the experimental strain profile assuming a rigid substrate. The values of the bonding stress $\tau_{i+1/2}$ halfway between two subsequent strain gauges placed at the position x_i and x_{i+1} (with $i = 1 \ldots m$ starting from the free end) and the corresponding slip $s_{i+1/2}$ can be esteemed using Eqs. 3.1 and 3.3.

As pointed out in par. 3.2.2.3, the hypothesis of pure shear stress state is valid until the onset of the peeling crack, revealing the presence of non negligible peeling stresses. In Fig. 3.40 some relevant experimental bond-slip relationships $\tau - s$ for the specimens A-1 and MA-3 are reported, while in Fig. 3.41 the results obtained for the B-series specimen B-
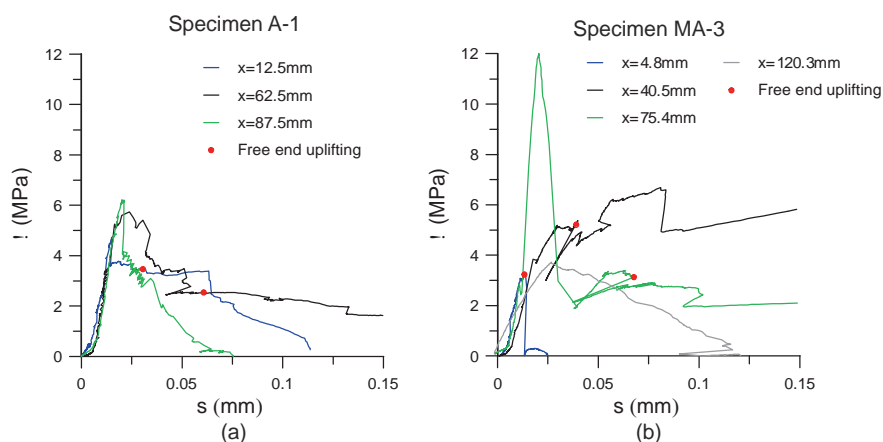
Figure 3.40: Experimental bond-slip curves at different positions along the bonded length for: (a) specimen A-1; (b) specimen MA-3 (red dots indicate the beginning of the uplifting of the free end).
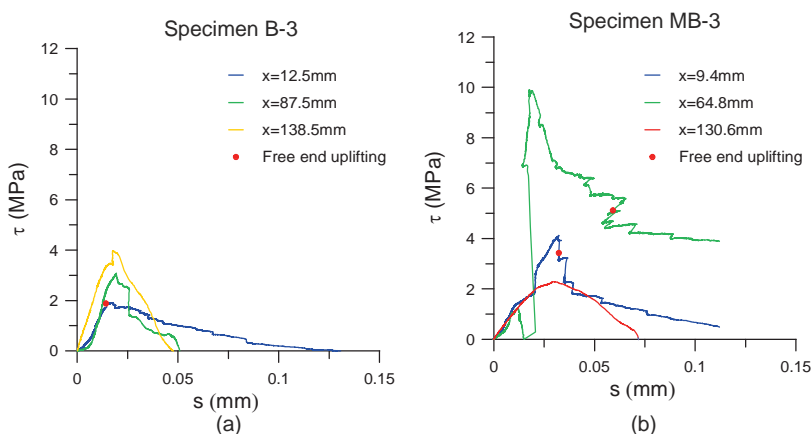
Figure 3.41: Experimental bond-slip curves at different positions along the bonded length for: (a) specimen B-3; (b) specimen MB-3 (red dots indicate the beginning of the uplifting of the free end).

3 and MB-3 are presented (red dots point out the beginning of the free end uplifting). The curves reveal that the bond-slip relationship is not unique: higher values of the maximum bond stress τ_{max} are attained in the central portion of the sheet, whereas smaller strengths are available at the free end. This issue is well highlighted in Fig. 3.42, where the maximum bond strengths attained along the plate are shown. In Fig. 3.42b, since the position of the strain gauges were slightly different in each masonry block specimen, the values of the average maximum bond strength were oppurtunely interpolated subdivinding the bonded

length in 25 mm portions, thus to allow a proper comparison also with brick results.

The bond strength reduction is due to tensile peeling stresses (i.e. normal to the bonding plane) at the free end of the plate. Indeed, here failure is no more associated with a mode II crack, like in the central part of the sheet, but to mixed mode fracture propagation. For the masonry specimens very high values of τ_{max} are observable in correspondence of mortar joints, where a wedge of material was usually detached, which causes interlocking phenomena between bulbs and bricks inducing thus high values of confinement stresses. This behavior is similar to what highlighted for concrete in par. 3.2.2.1.
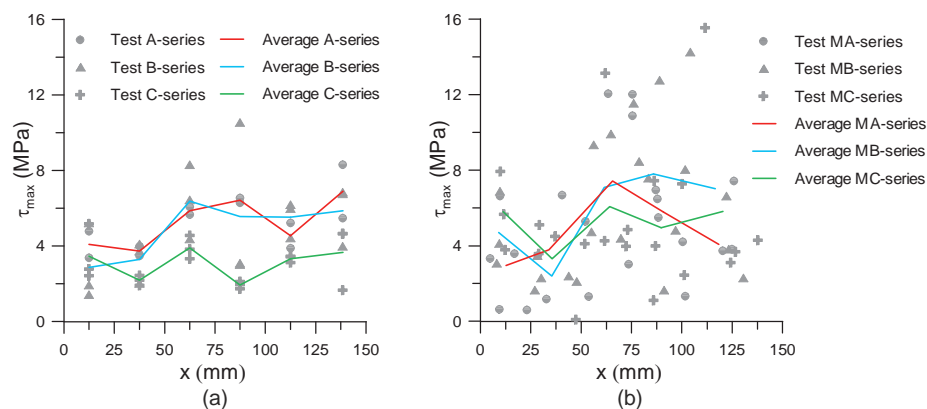
Figure 3.42: Maximum bond strength τ_{max} attained along the bonded length: (a) brick specimens; (b) masonry blocks.

To analyze type-2 rupture the experimental bond-slip relationships for specimens C-2 and MC-2 are reported in Fig. 3.43. Compared with type-1 failure, the curves are characterized by smaller values of τ_{max} and nearly no residual stresses due to friction. Furthermore, the trend of the curves is more regular and smooth with values of the bond strength τ_{max} more uniform along the bonded length (Fig. 3.42).

Irregular jagged bond-slip curves occur for two main reasons. First, in specimens related to type-1 failure, they are probably caused by heterogeneities (i.e. the presence of big voids and firing waste) with dimensions comparable with those of the bonded area; a similar behavior was observed for concrete substrate, where heterogeneities are mainly constituted by aggregates [3, 36, 123]. Second, the approach adopted to plot the curves is based on strain values measured in an exiguous number of points. Therefore, even in the case of finite element tests, the approach leads to irregular curves. For this reason,

alternative approaches, e.g. based on inverse analyses, have been proposed in literature [109].

It should be noted that the maximum value of tangential stress occurs at a value of slip about 0.02 mm for all cases. This value does not seem to be affected by the rupture type. Moreover, negligible stresses are usually present for slip values greater than 0.15 mm.
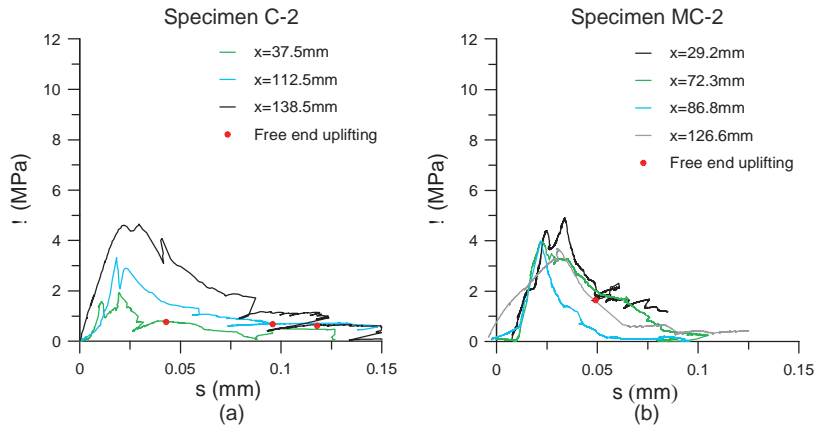
Figure 3.43: Experimental bond-slip curves at different positions along the bonded length for: (a) specimen C-2; (b) specimen MC-2 (red dots indicate the beginning of the uplifting of the free end).

3.3.3.5 Fracture energy

In [7] the maximum load carrying capacity of FRP reinforcement

$$F_{max} = b_f \sqrt{2 E_f t_f \Gamma_f} \tag{3.12}$$

is directly related to fracture energy Γ_f (Eq. 3.12), which is computed as a function of the characteristic compressive strength f_{mk} and mean tensile strength f_{mtm} of the substrate (Eq. 3.13):

$$\Gamma_f = c_1 \sqrt{f_{mk} f_{mtm}} \tag{3.13}$$

where c_1 is an experimental coefficient that, if no specific experimental tests are available, can be assumed equal to 0.015 mm [7]. Fracture energy can be normalized introducing a dimensional parameter d (i.e. an internal length), thus resulting in (Eq. 3.14):

$$\frac{\Gamma_f}{d f_{mk}} = \left(\frac{c_1}{d}\right) \left(\frac{f_{mtm}}{f_{mk}}\right)^{0.5} = \alpha \left(\frac{f_{mtm}}{f_{mk}}\right)^{0.5} \quad (\text{with} \quad \beta = 0.5) \tag{3.14}$$

which represents a line in a bi-logarithmic plot, (Eq. 3.15, Fig. 3.45).

$$\log\left(\frac{\Gamma_f}{d f_{mk}}\right) = \log\left(\alpha\right) + \beta \log\left(\frac{f_{mtm}}{f_{mk}}\right) \tag{3.15}$$

In particular, according to [7], the slope β of the line is constant and equal to 0.5, while the Y-axis intercept $\log\alpha$, which depends upon c_1, may be calibrated experimentally. Starting from Eq. 3.12 and following what suggested in [6, 56], experimental values of fracture energy Γ_f were calculated as:

$$\Gamma_f = \left(\frac{F_{\max}}{b}\right)^2 \frac{1}{2 E_f t_f} \tag{3.16}$$

using different values of the width b (i.e. the sheet width b_f, the regularizing layer width b_p, and the effective detached mean width b^*). The values of Γ_f computed considering the widths b_f, b_p and b^* are summarized in Tab. 3.7, while in Fig. 3.44 the values of $\Gamma_f(b_f)$ are compared. Then, they were sorted by the failure mode and normalized as in Eq. 3.14, choosing as internal length d the thickness of the material involved in the bonding mechanism t_m^* in the form defined in [55], also named the *"effective depth"* of the support (Eq. 3.17):

$$t_m^* = t_c \left(\frac{\mathcal{G}_a}{\mathcal{G}_m}\right) \tag{3.17}$$

where $\mathcal{G}_a$ and $\mathcal{G}_m$ are respectively the shear moduli of adhesive and of brick, while t_c (spacing from 20 mm to 30 mm) is the effective depth suggested in [7] for concrete substrate. Here, the value of 30 mm was chosen for the type-1 failure and 20 mm for type-2; this difference is due to the fact that diverse thicknesses of substrate were detached by the sheets during the tests. Moreover, in Eq. 3.14, the mean compressive strength f_{cm} and the flexural tensile strength $f_{tm,fl}$ were used instead of f_{ck} and f_{mtm}, since they are directly correlated and easily measurable.

The values of normalized energies $\Gamma_f/t_m^* f_{cm}$ are represented in Fig. 3.45a-c as a function of the ratio $f_{tm,fl}/f_{cm}$ for three different widths b and grouped by the failure mode. The same figures report Eq. 3.14 plotted using f_{cm} and $f_{tm,fl}$. This leads to overestimate the theoretical fracture energy since the adopted strength values are higher than the ones proposed by Eq. 3.14, but even in this case the predictions are very conservative with respect to the experimental evidence (i.e. experimental points are not accurately represented), as outlined in Fig. 3.45. To realize the reasons of these differences Eq. 3.15 have been recalibrated by means of minimum least square best fittings of the normalized
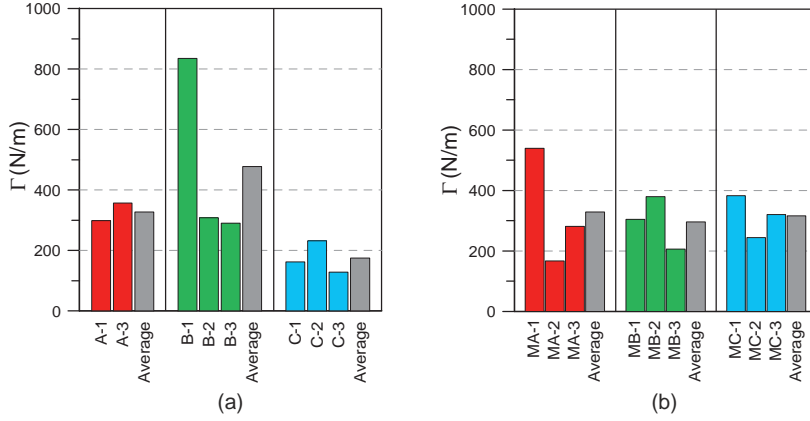
Figure 3.44: Experimental values of the fracture energy $\Gamma_f(b_f)$ computed using the sheet width b_f: (a) brick specimens; (b) masonry blocks.

energies for three different widths, both for the failure types 1 and 2 (Fig. 3.45a-c). In Tab. 3.8 the results of the fittings are reported. It should be noted that the slopes of the fitted lines are 2-3 times greater than the one suggested in [7] (Tab. 3.8). Even if the limited amount of available data and their dispersion, some interesting remarks can be made on.

Table 3.8: Parameters of the performed best fittings.

Width	Type-1 failure			Type-2 failure		
	α	β	$\mathbf{R^2}$	α	β	$\mathbf{R^2}$
	[mm]	[-]	[%]	[mm]	[-]	[%]
$\mathbf{b_f}$	$9.85 \cdot 10^{-3}$	1.00	34.1%	$7.31 \cdot 10^{-3}$	0.84	18%
$\mathbf{b_p}$	$1.18 \cdot 10^{-2}$	1.43	44.9%	$8.38 \cdot 10^{-3}$	1.20	30.6%
$\mathbf{b^*}$	$8.87 \cdot 10^{-3}$	1.38	52.2%	$4.92 \cdot 10^{-3}$	0.89	33.8%

The coefficient of determination R^2 is higher for the type-1 failure fittings than for the type-2 for every used width, revealing a more regular trend (Fig. 3.45a-c). This different behavior may be explained considering that the model proposed in [7] was calibrated for the concrete substrate, in which there are heterogeneities (i.e. aggregates) more similar to the ones present in the substrate characterized by type-1 rupture (i.e. big voids and firing waste) than in substrate displaying type-2 failure.

Furthermore, the coefficient of determination R^2 increases changing the width from b_f
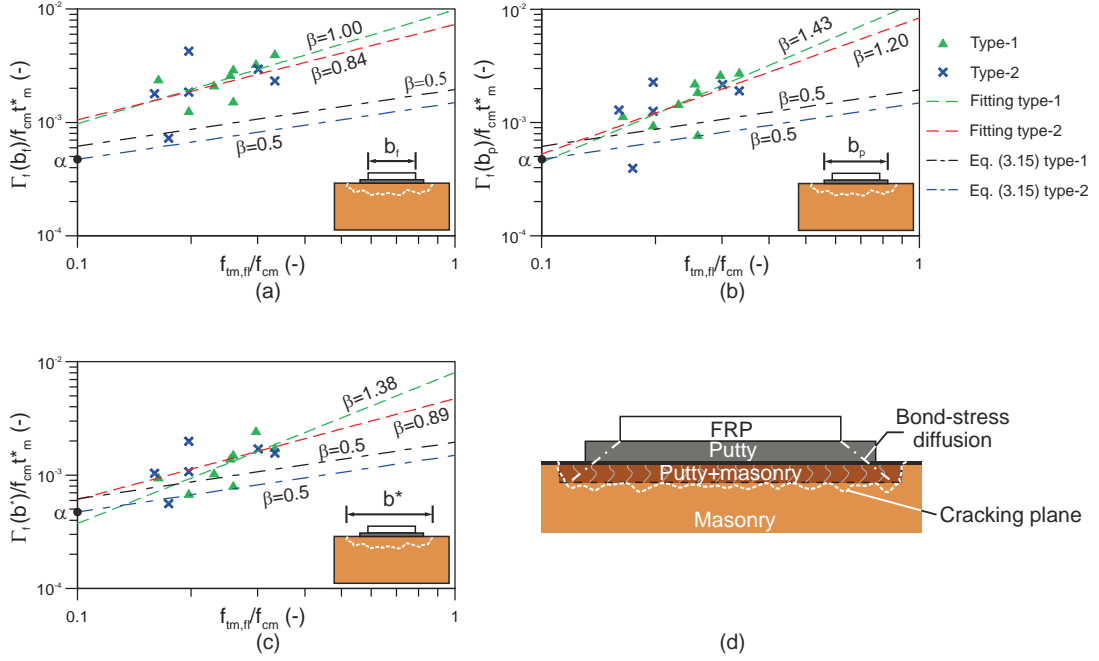
Figure 3.45: Performed fittings of the normalized fracture energy as a function of: (a) the sheet width b_f; (b) the width of the regularizing layer b_p; (c) the effective mean detached width b^* and (d) diffusion of the bond stresses through different layers.

to b^* (Tab. 3.8). This suggests that the energy dissipation during the debonding process occurs along a width larger than that of the sheet, involving a certain portion of the substrate. This fact is due to the diffusion of the bond stresses from the reinforcement to the cracking plane, as shown in Fig. 3.45d. Since the crack propagates in the weakest material, two different layers has been identified in the present tests: (i) the regularizing epoxy putty and (ii) the first layer of substrate where the glue penetrates, improving thus the strength of the masonry. While the first depends on the application method, the second is related to macro-porosity and permeability of the substrate to the glue, confirming what highlighted for the maximum loads and failure modes. Furthermore, it can be observed that for type-2 rupture the value of R^2 does not increase significantly changing from b_p to b^* (Tab. 3.8). This is due to the limited penetration of the glue into the substrate, which induces the formation of the debonding crack right beneath the surface of the support blocks, where regularizing putty was spread.

The evidence suggest that the width of the regularizing layer should be taken into account at least if its dimension is comparable with the influence bulb of the reinforcement

(i.e. the portion of substrate material affected by debonding process, [25]). Further improvements could be obtained if the presence of voids in the substrate is somehow considered.

3.3.4 Summary and final comments

Different bond behavior and failure mechanisms brought out by tests have been examined on the basis of different characteristics of the bricks, particularly in terms of mechanical strengths and substrate properties.

Tests shown peculiar features of ancient masonry specimens:

- the pull-out equilibrium path was similar to the one observed for the concrete substrate and mainly composed of three branches: an ascending part until the load peak, a nearly horizontal plateau and a snap-back branch. The adopted test setup permitted to observe the whole equilibrium path, including snap-back, up to complete debonding.

- the detachment of the reinforcement was related to a "two-way debonding" mechanism [118], in which the crack propagated toward the free end during the sub-horizontal plateau and stopped as the load started to decrease. In the snap-back branch, a peeling crack appeared at the free end of the sheet. Here, peeling stresses induced a reduction of bond strength τ_{max}, as evidenced by the experimental bond-slip relationships. This behavior is similar to what highlighted for the concrete substrate in long bonded lengths and described in par. 3.2.2.

- tests showed two main debonding mechanisms: type-1 failure characterized by a thick and irregular layer of substrate detached with a wedge of masonry at the free end; type-2 failure with lower load carrying capacity, no wedge at the free end and a thinner layer of detached material. This is not the case of new masonry that usually presents type-1 rupture, as evidenced by other experimental campaigns ([28, 33, 37]).

- the failure mode was strongly associated with the penetration depth of the glue into the substrate. Indeed, specimens where the glue has penetrated deeply displayed type-1 debonding, whereas a limited penetration induced type-2 failure.

- the performed fittings revealed that the model described in [7] is more accurate for type-1 than for type-2 rupture. In fact, type-2 failure occurs in material with a homogeneous and fine texture, whereas type-1 rupture is related to a substrate with significant heterogeneities like voids and firing waste, with dimensions similar to that of concrete, for which the design formula described in [7] was proposed and where heterogeneities are mainly constituted by aggregates.

- in the debonding process, the energy seems to be dissipated along a surface larger than the transverse dimension of the sheet, thus increasing the volume of involved material. The influence is directly related to the glue penetration inside the substrate.

For the design of composite reinforcement of ancient masonry, the type of substrate has a great influence both at ultimate and service conditions; in particular, the bond performance depends not only on the mechanical properties of the units but also on other physical properties. Therefore, considering the great variety of units generally utilized for masonry constructions, the need of a wider investigation to carry out design relationships to properly take into account all the involved phenomena is evident. In fact, the prescriptions in use [7–9] do not consider the outlined aspects. Finally, the obtained results open some questions concerning the numerical modeling of the different detachment mechanisms.

3.4 Concluding remarks

The two experimental campaign presented demonstrate that the setup proposed is suitable to be used to characterize the bond behavior of fiber reinforced polymer (FRP) fabrics externally glued on quasi-brittle materials. The particular driving technique adopted allowed to entirely follow its separation process form the substrate, exploiting the monotonic increment of the free end displacement of the reinforcement.

Besides the snap-back behavior in long bonded lengths, the tests permitted to observe the failure mechanisms, highlighting for both concrete and masonry a "*two-way debonding*" in long bonded lengths similar to what observed in [118] for embedded fibers. This peculiar phenomenon seems to be related to the effects of peeling stresses (i.e. orthogonal to the bonding plane) that, interacting with the tangential stresses, lead to a decrease of both the shear bond strength and the fracture energy. As a results debonding cannot be considered uniquely a mode-II process, but, as the bonded length decreases, either because the joint is "short" or due to the propagation of the debonding crack, the influence of mode-I fracture processes become more significant, changing thus the crack propagation processes. Macroscopic evidence of that behavior are the material bulbs usually observed at the ends of the debonded plates and sheets.

The results illustrated open some question on the analytical and numerical interpretation of the debonding process. Indeed, the major part of the models to simulate the interface behavior of externally glued FRPs (e.g. [40, 53, 61, 78, 87] among others) are based on the hypothesis of pure mode-II fracture process and thus they are not able to reproduce the changes in the debonding mechanism.

Finally, a comment is needed concerning the masonry tests. The results obtained highlighted some differences in behavior in comparison with the concrete substrate, although the main mechanical processes are similar. This can be explained considering that concrete is less prone to variations in the material texture compared to masonry (see par. 2.5.1). Indeed, bricks coming from different kilns can perform, concerning the bond processes, as two different materials, differently two types of concrete usually have similar behavior. It has been demonstrated that these peculiarities are related to other parameters than the ones usually accounted (e.g. the compressive and tensile strength of the substrate). In particular, it has been shown that the permeability to the glue of the substrate and its texture have an important role in the debonding load, changing the fracture energy

at disposal and the volume involved in the stress transfer process. Probably for these reasons, the models to evaluate the capacity of a strengthened system available in the literature seems to do not provide good previsions for the masonry substrate, especially for the ancient one. This subject will be better explained in Sect. 5.

4

Modelling of the debonding behavior

Abstract

To numerically investigate both the monotonic and cyclic debonding phenomena, various models were proposed in the literature. One of the most popular, the monotonic pure shear cohesive zone model, is briefly summarized here, pointing out its limits especially regarding the results illustrated in the previous Sect. 3. Then, a novel monotonic cohesive zone model based on a mixed interface law which accounts for the interaction between normal and tangential stresses is presented. To the purpose, a cracking criterion is introduced to rule the maximum stresses attainable in normal-tensile and tangential direction, while complete debonding is defined through an energy-based criterion providing the mode-I and -II fracture energies at disposal. The softening behavior is governed by a scalar damage parameter relating the total displacement jump with an equivalent stress. To validate the model, comparisons with already validated models and experimental data from the literature are presented and debated, highlighting in particular the effects of mode mixity on the failure mechanism as well as on the bond strength.

In the last parts of this section the problem of the modeling of the FRP external reinforcements failure due to cyclic actions is debated. In particular, a coupled damage-plasticity first-order model is presented stating the assumption of pure shear loading of the interface. The local interface law is ruled by an admissible domain function involving linear softening and two damage parameters: one related to the stiffness degradation and the other governing the loss of bond strength due to fatigue. The model is finally validated by comparing its predictions with experimental results from the available literature.

4.1 Introduction to monotonic models

To give a theoretical interpretation at the open questions arisen in the previous Sect. 3, here the effects at the interface level of the normal stresses are studied. In particular, because of the eccentricity between the pulling force applied and the interface, a bending moment is present, introducing tensile peeling stresses at the free end and compressive stresses at the loaded end of the plate. As demonstrated in Sect. 3 and also supposed in different studies ([24, 53, 86, 115, 124] among others), these stresses influence the bonding behavior primarily affecting the shear strength. This effect is present also in plated beams [24, 61, 63] in case of plate-end or intermediate crack-induced debonding and, even more, in curved elements (e.g., vaults and arches [66, 77]) or in FRP reinforcements subjected to inclined loads [53, 125]. Moreover, as outlined in Sect. 3, experimental results suggest that peeling stresses are responsible for the changes in the failure mechanism in single-lap shear tests.

To describe the behavior of the glued joints and to give interpretation to the bond tests, monodimensional models are very often employed because of their simplicity and good accuracy. In such models [8, 40], the FRP plate is modeled as a linear elastic axial element pulled at one side, whilst its interaction with the support is considered through a cohesive zone interface law (e.g. [6, 53, 66, 77] among others). Usually, these models assume a perfect mode-II cracking process occurring at the interface, neglecting the effects of peeling stresses (see [66] for a comprehensive review). Indeed, despite the great relevance of this issue only a few models account for the coupling of the normal and tangential stresses (e.g. [53, 61, 78]) but none of them is able to reproduce the changes in the failure mechanism observed for quasi-brittle materials as concrete (par. 3.2) or masonry (par. 3.3).

In the following, after a brief overview of the classic mode-II (i.e. shear) model, a novel cohesive zone approach to the debonding problem is presented. Similarly to [64], it includes the effects of the peeling stresses by means of a mixed-mode interface law. The resulting tangential and normal behaviors are coupled both for the fracture energies at disposal and for the maximum stresses attainable by means of a cracking and a failure criterion. The model has been implemented into an ad-hoc numerical code and solved via finite difference method. To validate the approach, some results from experimental campaigns available in the literature are simulated and compared.

4.2   A simple pure shear model

One of the most adopted method available to simulate debonding in FRP joints is based on cohesive interface models. Usually, some simplifying assumptions are introduced. Firstly, the materials, apart the interface which collect all the non-linearities of the process, are assumed homogeneous, isotropic and linear elastic. Secondly, bending moment and shear deformations are neglected, thus the composite reinforcement is idealized as an Euler-Bernuolli beam subject only to traction (i.e. a truss) bonded to supporting prism – the substrate – that can be considered rigid if compared to the FRP stiffness. This assumption leads to a plane model, even if edge effects induced at the border of the glued area [94] together with the diffusion phenomenon of the bonding stresses and the crack propagation into the substrate [62], are responsible for the formation of disturbed regions. This implies that, generally, the debonding process is three-dimensional [25, 126]. Nevertheless, if the reinforcement is sufficiently wide to permit neglecting such effects, a plane model is commonly intended as an acceptable engineering representation of the problem. This condition implies that uniformity of strains and stresses over the plate width b_f is assumed and three-dimensional effects are considered implicitly and on average while defining the parameters of the cohesive laws [66].

It is also assumed that the adherents (the FRP and the substrate) have a constant thickness along the bond line, while the interface separating the two adherents, which has to represent all the bonding layers, is considered a zero-thickness element. Finally, the interface is considered mostly stressed in shear, thus the effects of normal (peeling) stresses are neglected.
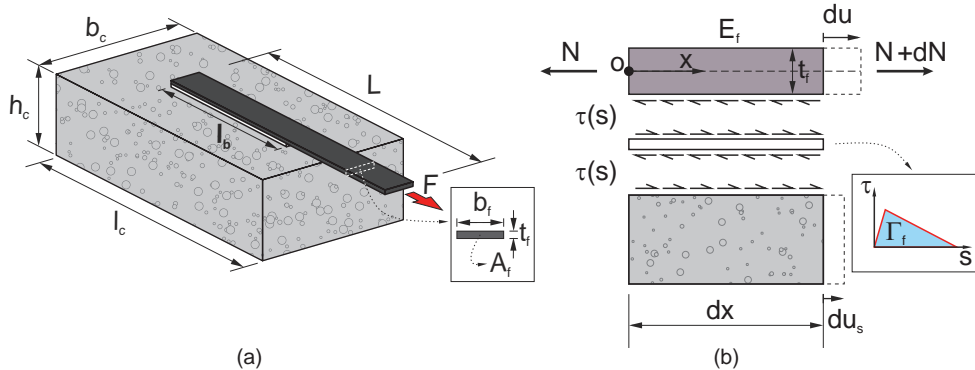
Figure 4.1: (a) Scheme of a pull-out test. (b) Free-body diagram of a differential element of the system.

4. MODELLING OF THE DEBONDING BEHAVIOR

4.2.1   Equilibrium and kinematic statements

In a typical pull-out test, as the one represented in Fig. 4.1a, the specimens presents an FRP plate with a cross-section of base b_f and thickness t_f, and a bonded length l_b shorter than the total plate length L (Fig. 4.1a) pulled by a force F. The plate is glued to a concrete block of sides $b_c \times l_c \times h_c$ by means of an adhesive layer of thickness t_a. Adopting the notations and sign conventions depicted in Fig. 4.1 and omitting for simplicity the dependence from the coordinate x, is possible to write the equilibrium equation for a differential element of the system (Fig. 4.1b) as

$$\frac{dN}{dx} = \tau(s)b_f \,, \tag{4.1}$$

being N the FRP axial force and $\tau(s)$ the tangential interface bonding stress dependent from the displacement gap in tangential direction, namely slip, s. Since the slip is defined as the relative displacement of the plate with respect to the substrate, which is taken here as rigid, the following relationships holds

$$s = u_f - u_s = u_f \,, \tag{4.2}$$

where u_s and u_f are the displacements respectively of the substrate and of the composite (Fig. 4.1b). By differentiation of Eq. 4.2 and introducing the Euler-Bernoulli relationship between the generalized axial force and the axial strain lead to the following kinematic statement

$$\frac{ds}{dx} = \frac{du_f}{dx} = \varepsilon_x = \frac{N}{E_f A_f} \,. \tag{4.3}$$

Eqs. 4.1 and 4.3 are the differential equations governing the debonding problem, for whose solution a set of boundary conditions (BC's) should be given. In the present context, three different sets of BC's are of interest and can be applied in relation of the parameter chosen to drive the test that can be: (i) the applied force (Fig. 4.2a); (ii) the loaded end displacement (Fig. 4.2b); (iii) the free end displacement (Fig. 4.2c).

The solution of the system arising from Eqs. 4.1 and 4.3 together with the conditions of Fig. 4.2 is allowed once the behavior of the interface is defined through a bond-slip law $\tau(s)$.
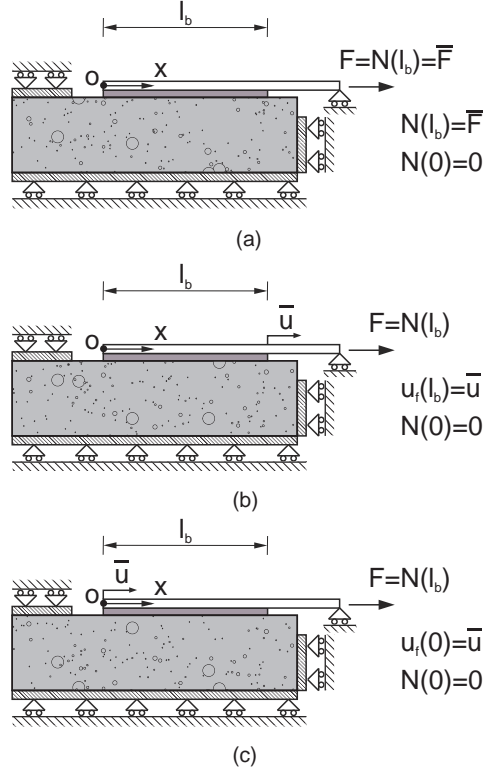
Figure 4.2: Suitable boundary conditions sets: (a) force driven test; (b) loaded end displacement driven test; (c) free end displacement driven test.

4.2.2 Interface behavior under pure shear loading

In the literature many different shapes of interface law were proposed (see [6, 12, 45, 46, 49, 50] among others). For FRP joints, pure-shear cohesive law composed by an ascending branch followed by a softening part (Fig. 4.3), is generally used [8, 9, 18, 53, 127].

The bilinear law (Fig. 4.3c), is frequently preferred because of its simplicity and sufficiently accurate description of the experimental global behavior, although experimental evidence shown that the relationship between shear stress τ and slip s is non-linear even for low stress values [6]. Indeed, many authors (e.g. [53, 61, 87] among others) demonstrated that the bilinear law correctly reproduces the main features of a pull-out test, like the peak load and the corresponding loaded end displacement.

Hence, the bilinear cohesive law (Fig. 4.4) can be described by the relationship

$$\tau(s) = (1 - D(s))K_{el}s \,. \tag{4.4}$$
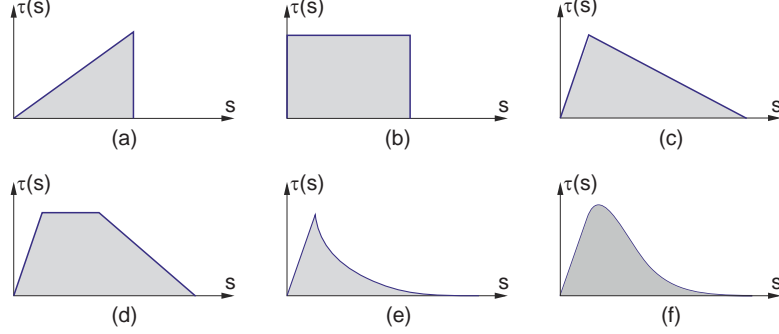
Figure 4.3: Different shapes of the interface law $\tau - s$: (a) elasto-brittle; (b) perfectly plastic; (c) bilinear; (d) trilinear; (e) linear loading and non-linear softening; (f) power-fractional type.

where K_{el} is the initial linear elastic stiffness of the interface and $D(s)$ is a damage parameter that rules the softening behavior (Fig. 4.4). To follow the linear softening branch of the law the damage parameter can be written as

$$D(s) = \begin{cases} 0 & s \le s_1 \\ \frac{s_2(s-s_1)}{s(s_2-s_1)} & s_1 < s \le s_2 \\ 1 & s > s_2 \end{cases} \tag{4.5}$$

where s_1 and s_2 are the displacements at the onset of debonding and at complete separation respectively. The maximum value of bonding stress τ attainable is called bond strength τ_{max} and it results equal to $\tau_{max} = K_{el}s_1$. The point (s_1, τ_{max}) marks the end of the linear elastic stage (i.e. the onset of the debonding), while the point $(s_2, 0)$ corresponds to the complete separation of the two adherents. The fracture energy $\Gamma_f = \Gamma_{II}$ at disposal is equal to the area under the interface law (Fig. 4.4) and can be calculated as $\Gamma_f = (\tau_{max}s_2)/2$.

4.2.3 Numerical solution using a finite difference strategy

Using the strategy suggested in [128], and already used in [40, 117], the system arising from Eqs. 4.1 and 4.3 can be formulated in vectorial form as

$$\boldsymbol{y}'(x) = \boldsymbol{f}(x, \boldsymbol{y}(x)), \tag{4.6}$$

where in $\boldsymbol{y}(x) = [N(x), s(x)]^T$ are grouped the functions of the unknown variables and $\boldsymbol{f}(x, \boldsymbol{y}(x))$ is the vectorial right-hand-side term. Eq. 4.6 can be written in matrix form as

$$\boldsymbol{y}'(x) - \boldsymbol{A}(x, \boldsymbol{y}(x))\boldsymbol{y}(x) = \boldsymbol{0} \quad 0 \le x \le l_b, \tag{4.7}$$
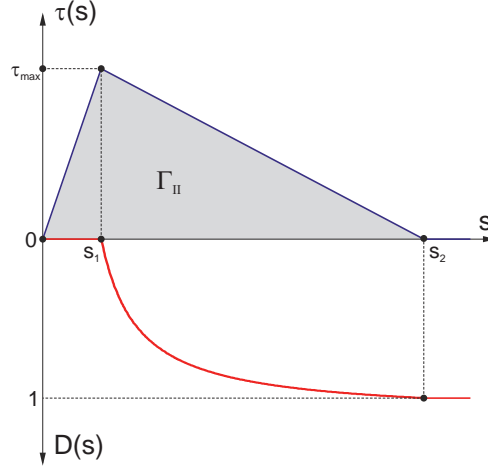
Figure 4.4: Bilinear cohesive law and the corresponding damage parameter D.

together with the boundary conditions of Fig. 4.2 which become

$$\boldsymbol{B}_0 \boldsymbol{y}(0) + \boldsymbol{B}_{l_b} \boldsymbol{y}(L) - \overline{\boldsymbol{\alpha}} = \boldsymbol{0} \,, \tag{4.8}$$

where $\overline{\boldsymbol{\alpha}}$ is the vectorial form of the right-hand-side term that is imposed for the BC's of Fig. 4.2.

To numerically solve the system it is necessary to introduce a decomposition of the interface domain (i.e. $0 < x < l_b$). To the purpose, a mesh of points $0 = x_1 < x_2 < \cdots < x_N = l_b$ with a constant step size $h_n = x_{i+1} - x_i$ is introduced along the bonded length. Then, the vectorial system of Eqs. 4.7 and 4.8 is solved via the trapezoidal finite difference scheme, which approximate Eq. 4.6

$$\frac{\boldsymbol{y}^{(i+1)} - \boldsymbol{y}^{(i)}}{h_n} - \frac{1}{2} \left(\boldsymbol{A}(x_i, \boldsymbol{y}^{(i)}) \boldsymbol{y}^{(i)} + \boldsymbol{A}(x_{i+1}, \boldsymbol{y}^{(i+1)}) \boldsymbol{y}^{(i+1)} \right) = 0$$
$$\text{with} \quad i = 1, 2, \ldots, N-1 \,, \tag{4.9}$$

where $\boldsymbol{y}^{(i)} = \boldsymbol{y}(x_i)$. Following the same procedure the boundary conditions become

$$\boldsymbol{B}_0 \boldsymbol{y}^0 + \boldsymbol{B}_{l_b} \boldsymbol{y}^N - \overline{\boldsymbol{\alpha}} = \boldsymbol{0} \,. \tag{4.10}$$

Writing the entire system in a matrix form for the N point leads, after an adimension-

Table 4.1: Parameters adopted for pure shear analyses.

$\tau_{\mathbf{max}}$	$\mathbf{K_{el}}$	$\mathbf{\Gamma_f}$	$\mathbf{s_1}$	$\mathbf{s_2}$
[MPa]	[MPa/mm]	[N/mm]	[mm]	[mm]
7.70	170	0.60	$3.8 \cdot 10^{-2}$	$1.8 \cdot 10^{-1}$

alization of the variables (see App. A for more details), to

$$
\begin{bmatrix}
\boldsymbol{S}_1 & \boldsymbol{R}_1 & & & & \\
& \ddots & \ddots & & & \\
& & \boldsymbol{S}_j & \boldsymbol{R}_j & & \\
& & & \ddots & \ddots & \\
& & & & \boldsymbol{S}_{N-1} & \boldsymbol{R}_{N-1} \\
\boldsymbol{B}_0 & & & & & \boldsymbol{B}_{l_b}
\end{bmatrix}
\left\{
\begin{array}{c}
\tilde{\boldsymbol{y}}_1 \\
\vdots \\
\tilde{\boldsymbol{y}}_j \\
\vdots \\
\tilde{\boldsymbol{y}}_{N-1} \\
\tilde{\boldsymbol{y}}_N
\end{array}
\right\}
-
\left\{
\begin{array}{c}
\mathbf{0} \\
\vdots \\
\mathbf{0} \\
\vdots \\
\mathbf{0} \\
\tilde{\boldsymbol{\alpha}}
\end{array}
\right\}
= \mathbf{0}
\tag{4.11}
$$

where $\boldsymbol{S}_j = -\boldsymbol{I}/h_n - \boldsymbol{A}_j/2$, $\boldsymbol{R}_j = \boldsymbol{I}/h_n - \boldsymbol{A}_{j+1}/2$, $\boldsymbol{I}$ is the identity matrix, $\tilde{\boldsymbol{\alpha}}$ and $\tilde{\boldsymbol{y}}_j$ are respectively the adimensional imposed right-hand-side and the vector of the unknown values corresponding to the jth node. The solution of the non-linear system of Eq. 4.11 is iteratively obtained using the Newton method and applying the prescribed right-hand-side term $\tilde{\boldsymbol{\alpha}}$ in steps. Moreover, the converged solution of the previous step is used as initial guess. The complete expressions of $\boldsymbol{B}_0$, $\boldsymbol{B}_{l_b}$, $\tilde{\boldsymbol{\alpha}}$, and $\boldsymbol{A}_j$ are reported, together with the complete description of the numerical scheme adopted in App. A.

4.2.4 Pure shear analyses

In Fig. 4.5 are simulated the pull-out tests on concrete specimens described in par. 3.2 for the two bonded length l_b=30 mm and 150 mm. The interface parameters that have to be defined are: the maximum bonding stress attainable τ_{max}, the initial linear elastic stiffness of the interface K_{el} and the fracture energy at disposal $\Gamma_f = \Gamma_{II}$. The slips at the onset and complete debonding are calculated respectively as $s_1 = \tau_{max}/K_{el}$ and $s_2 = (2\Gamma_f)/\tau_{max}$. For the analyses presented here the parameters are summarized in Tab. 4.1. A detailed explanation on how the interface parameters are calibrated is given in par. 4.3.6.1.

Even if the data are quite scattered especially for short bonded lengths (but this is usual for pull-out tests on FRP joints), some remarks can be drawn.

Figure 4.5: Pull-out curves from pure mode-II cohesive model for the tests described in par. 3.2: (a) specimen with l_b=30 mm; (b) specimen with l_b=150 mm.

The global behavior from numerical analyses agrees with the experimental evidence. In particular, the transition form a post peak softening branch for short bonded lengths (Fig. 4.5a) to an unstable snap-back behavior for long bonded lengths (Fig. 4.5b) is correctly reproduced. A certain mismatch in the pull-out curve at the free end $F - s(0)$ is observable in the final part of the test, especially for long bonded lengths. As reported in par. 3.2.2, this fact is probably due to rotation of the free end of the plate that leads to displacements at the free end bigger than the slip at the loaded end in the final part of the tests.

In Fig. 4.6 the local behavior of the specimen with l_b=30 mm for some load levels highlighted in Fig. 4.5a is given. It it observable how the bonding stresses and the slips are almost equally distributed along the entire bonded length (Fig. 4.6a,c), highlighting a uniform loading of the joint. For the same reason, axial force and strains experience a barely linear decrease from the loaded end toward the opposite side (Fig. 4.6a,c). This behavior is observable also in Fig. 4.6f, where the stress-state at the loaded and free end of the interface are almost equal. Concerning the failure mode, Fig. 4.6d reveals how the free end debonding experimentally observed in par. 3.2 is completely missed. Indeed, the damage of the interface starts at the loaded end and monotonically decrease toward the free one.

Concerning the long bonded lengths, Fig. 4.7 points out some peculiar features of the bonding behavior between FRPs and quasi-brittle substrates. For the points A-B-C of
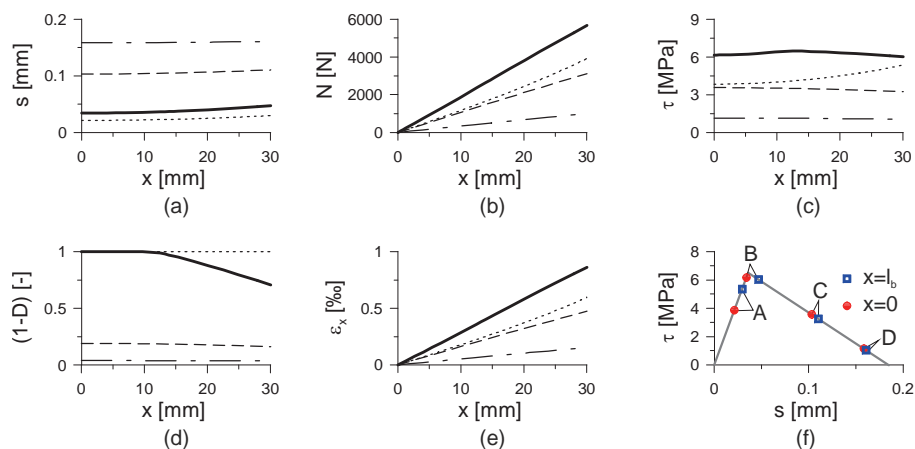
Figure 4.6: Results of the numerical analyses for the specimen with l_b=30 mm at the load levels A=$\cdots$, B=——, C=−− and D=− · − represented in Fig. 4.5a: (a) slips; (b) axial force; (c) bond stresses; (d) damage parameter; (e) axial strain; (f) $(\tau - s)$ values on the interface law for the free and loaded end.
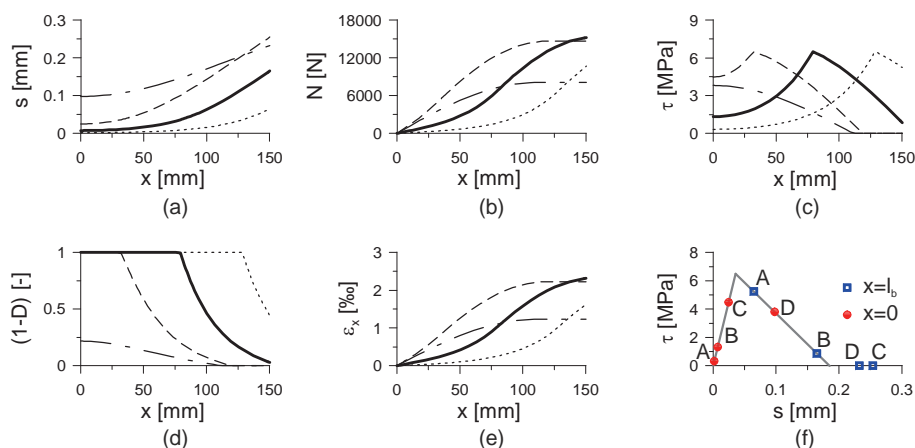
Figure 4.7: Results of the numerical analyses for the specimen with l_b=150 mm at the load levels A=$\cdots$, B=——, C=−− and D=− · − represented in Fig. 4.5b: (a) slips; (b) axial force; (c) bond stresses; (d) damage parameter; (e) axial strain; (f) $(\tau - s)$ values on the interface law for the free and loaded end.

Fig. 4.5b, the interface is divided in two segments, the first one, near the free end, which is undamaged (or linear elastic) followed by a zone that has experienced a certain level of damage (Fig. 4.7c,d). Along the elastic part of the interface, starting form the free end, the bonding stresses increase until reaching the interface bond strength τ_{max}, then they monotonically decrease within the damaged part of the joint, reaching τ=0 when $(1-D)$=0

(Fig. 4.7c,d). Differently, the axial force and strains exhibit a non-linear growth as long as $(1-D) \neq 0$, then they level off at a constant value pointing out a complete debonding of a portion of the interface. When all the interface undergoes to softening (Figs. 4.5b and 4.7d, point D), the stresses monotonically decrease from the free end toward the loaded one. Once more, the failure mechanism is not reproduced. In fact the damage $(1-D)$ gradually increase from the loaded moving to the free end for the entire test until the complete debonding of the interface, missing thus the two-way debonding experimentally observed in par. 3.2.

4.3 A novel mixed-mode model for the debonding of FRP reinforcement

The geometry and the general scheme used for this model is the same of Fig. 4.1a. The adopted notations, nomenclature and sign conventions are depicted in Figs. 4.1a, 4.8, 4.9.
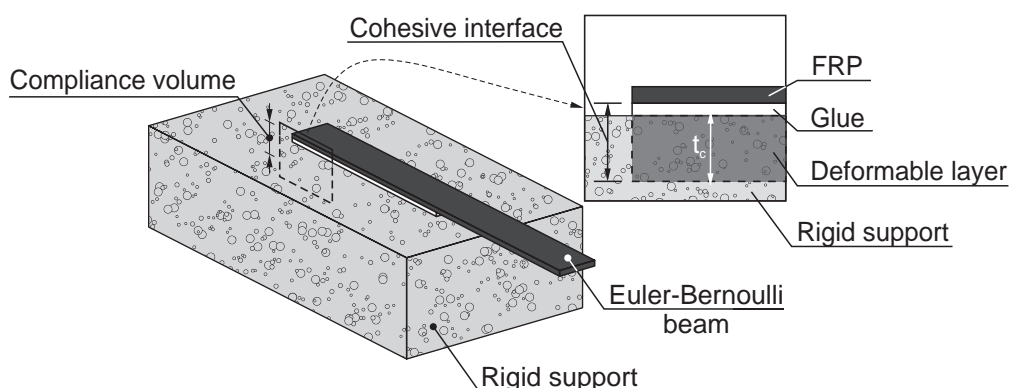
Figure 4.8: Scheme of the test specimen and definition of the compliance volume and modeled layers.
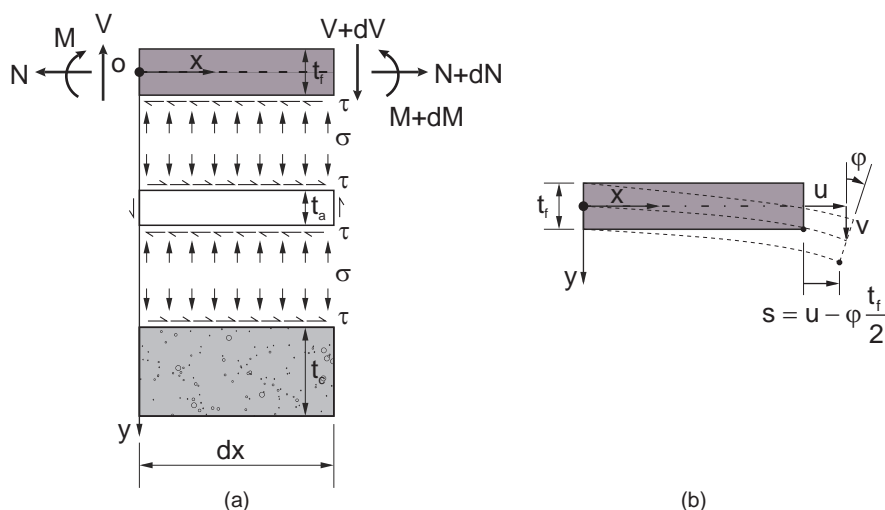
Figure 4.9: (a) Free-body diagram of an infinitesimal portion of FRP plate. (b) Kinematics of the FRP plate.

The proposed model may be considered as an extension of the classic cohesive zone model, as the one proposed in the previous par. 4.2 (or [40, 53, 61, 78, 87] among others), therefore its main hypotheses still apply. In particular, the hypotheses of small

displacements and constant direction of the force F are assumed. Even if debonding is a sudden unstable mechanism (as described in pars. 2.1 and 2.4.1), dynamic effects are neglected, thus limiting the application of the model to those cases where the process can be considered as static [61].

4.3.1 Main hypothesis

To properly define the interface behavior, a "*compliance volume*" (Fig. 4.8), defined as a portion of the block directly involved in the debonding process [41, 55], has to be accounted for. It is composed of the adhesive film and a bulb of concrete substrate where damage occurs and debonding crack propagates (bulk material). Because of the three-dimensional effects illustrated in par. 4.2, the compliance volume has a complex shape in the 3-D space, that, however, can be neglected under the hypothesis of sufficiently wide reinforcement. Indeed, the bulk volume can be characterized only by its thickness t_c, estimated by many authors [6, 40, 117] ranging between 20 and 50 mm. This portion of material can be seen as the outer layer of substrate where the effects of adhesion are depleted, permitting thus to consider the remaining parts of the support block as rigid (Fig. 4.8).

As stated before (par. 2.3), the cohesive interface laws collect all the non-linearities of the debonding process depleted inside the compliance volume, including nucleation, coalescence, and propagation of cracks [66, 87]. Differently from the pure shear models, here also the displacements in normal direction (and thus shear and bending forces acting on the composite) are taken into account. Indeed, once the plate is pulled, the displacements in tangential and normal direction between the plate and the rigid support (respectively called s or slip, and v or opening) induce, by means of the interface laws, a distribution of shear $\tau(v, s)$ and normal (peeling) stresses $\sigma(v, s)$ along the bonded length (Fig. 4.9a). In the framework of lower-order solutions, the assumption of constant interface stresses across the adhesive thickness – which is usually very thin (0.2-2.0mm) and soft – is allowed even if it leads to the violation of the zero-shear condition at the plate edges [63].

As a consequence of the aforementioned hypotheses, from a mechanical viewpoint the proposed model can be regarded as a linear-elastic Euler-Bernoulli beam leaning on a bed of tangential and normal non-linear springs [36].

4.3.2 Kinematic statements and compatibility equations

From a kinematic viewpoint the displacement gaps s and v, in the following collected into the vector $\boldsymbol{\rho} = \{v, s\}^T$, are defined as the difference of the displacements between FRP plate and substrate

$$\boldsymbol{\rho} = \begin{Bmatrix} v \\ s \end{Bmatrix} = \begin{Bmatrix} v_{FRP} - v_s \\ u_{FRP} - u_s \end{Bmatrix} \tag{4.12}$$

where the subscript 's' states for the support block that in the present model is considered as rigid, thus the related terms are nil. Furthermore, the displacements s_{FRP} and v_{FRP} of the plate are referred to its bottom face. Therefore, considering a generic deformed cross section of the beam, where φ describes its plane rotation and u, v represent longitudinal and transverse displacements of the centroid, Euler-Bernoulli hypotheses lead to $s = u - \varphi t_f/2$, whereas the transverse displacement v virtually coincides with the one of the section centroid (Fig. 4.9b).

Stating the hypothesis of linear-elastic behavior of the plate and according to the Euler-Bernoulli beam theory, axial strain of the middle plane ε and curvature of the cross-section χ con be expressed as:

$$\varepsilon = \frac{N}{E_f A_f}, \quad \chi = \frac{M}{E_f I_f} \tag{4.13}$$

where E_f is Young's modulus of the material and $A_f = t_f b_f$, $I_f = b_f t_f^3/12$ represent area and moment of inertia of the cross section.

Introducing the kinematic relationships between generalized displacements and strains of the Euler-Bernoulli beam and using Eq. 4.13, the following compatibility equations, which apply for the whole plate, can be written:

$$\frac{\mathrm{d}u}{\mathrm{d}x} = \varepsilon = \frac{N}{E_f A_f} \tag{4.14a}$$

$$\frac{\mathrm{d}v}{\mathrm{d}x} = \varphi \tag{4.14b}$$

$$\frac{\mathrm{d}\varphi}{\mathrm{d}x} = -\chi = -\frac{M}{E_f I_f} \tag{4.14c}$$

4.3.3 Equilibrium, governing equations and boundary conditions

Considering the free-body diagram of a portion of beam of infinitesimal length (Fig. 4.9a), its equilibrium equations, neglecting second order terms, are:

$$\frac{\mathrm{d}N}{\mathrm{d}x} = \tau(v,s)b_f \tag{4.15a}$$

$$\frac{\mathrm{d}V}{\mathrm{d}x} = \sigma(v,s)b_f \tag{4.15b}$$

$$\frac{\mathrm{d}M}{\mathrm{d}x} = V + \tau(v,s)b_f \left(\frac{t_f}{2} + t_a\right) \tag{4.15c}$$

where N, V, M represent axial force, shear force, and bending moment respectively. In the unbonded part of the plate the same equations apply provided that no cohesive stresses σ and τ are present.

To solve the system of first order differential equations arising from Eqs. 4.14 and 4.15, a set of boundary conditions is provided in Fig. 4.10. The model allows controlling the force applied at the loaded end or the axial displacement $\bar{u}$ either at the loaded end ($x = L$) or at the free end ($x = 0$). The restraint of the displacement at the loaded end of the plate reproduces the grip of the testing machine (Fig. 4.10).

4.3.4 Mixed bond-slip laws

Mixed cohesive interface laws $\sigma(v,s)$ and $\tau(v,s)$ are defined starting from simple bilinear models proposed for pure shear and traction behavior and adopting the fictitious crack model approach [73–76] (see par. 2.3).

As discussed in par. 4.2.2, the behavior of the interface in pure mode-II (shear) can be described by a bilinear law (Fig. 4.11a, $\sigma = 0$). In fact, it describes well the main characteristics of a pull-out test in spite of its simplicity [53, 61, 87].

To define the normal behavior, a bilinear cohesive law can be adopted in case of pure traction ($v \leq 0$ and $\tau = 0$, Fig. 4.11b). In compression, a linear elastic response is used ($v > 0$, Fig. 4.11b). The hypothesis is reasonable [53, 127] considering the low expected stresses in comparison with the compressive strength of the material [24, 129].

The coupled tangential and normal laws display a linear elastic behavior up to cracking, which occurs simultaneously [53, 78]. The maximum shear and normal stresses (τ_{max} and σ_{max}) attained in the linear-elastic regime are coupled by a cracking criterion (Fig. 4.12a)
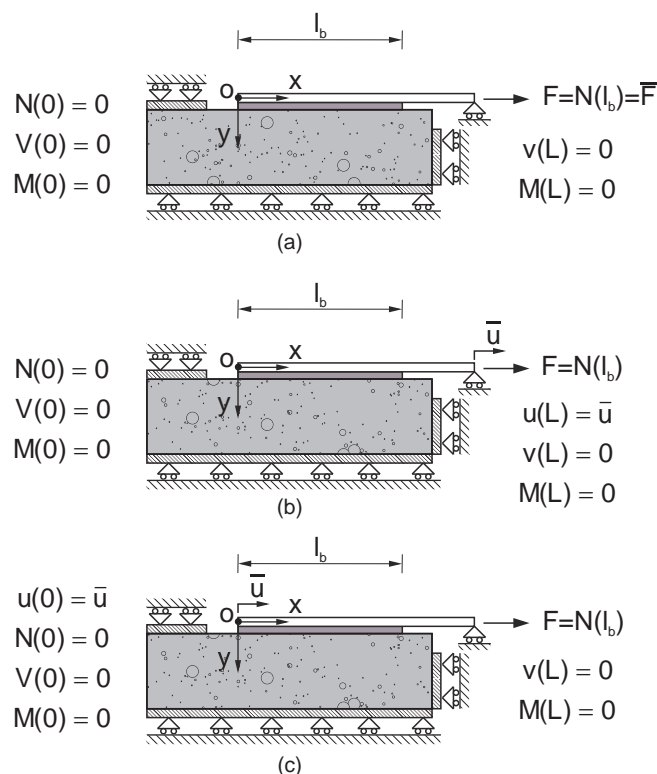
Figure 4.10: Mechanical model with boundary conditions: (a) applied force control; (b) displacement control at the loaded end; (c) displacement control at the free end.

while the failure is governed by an energy-based criterion (Fig. 4.12b). Moreover, because peeling and shear effects are both depleted in a unique compliance volume, the softening behavior of the laws in normal and tangential direction is governed by a scalar damage parameter.
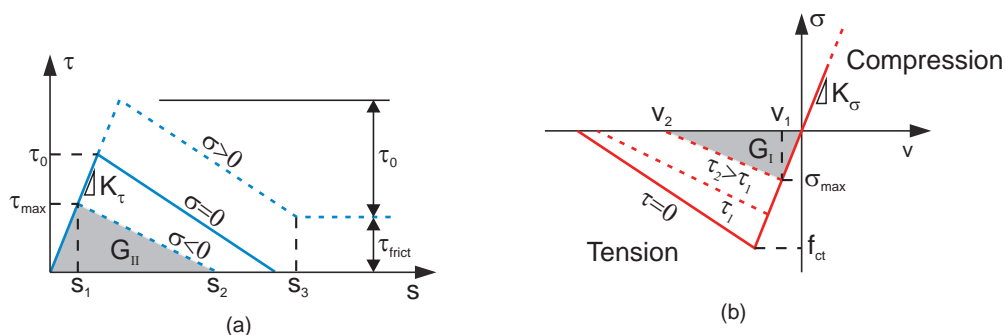
Figure 4.11: Implemented cohesive laws: (a) tangential direction; (b) normal direction.

4.3.4.1   Linear elastic behavior and cracking criterion

The cohesive laws implemented herein (Fig. 4.11) present an initial linear-elastic (LE) branch characterized by the stiffnesses K_σ and K_τ in normal and tangential direction respectively. In the LE branch the stresses σ and τ are dependent on the interfacial displacements gaps only. Thus, a point along the interface shows a linear-elastic behavior as long as it remains inside an "elastic domain" (Fig. 4.12a), which is here described through the relation proposed in [130]:

$$\tau \le \sqrt{(c - \sigma \tan \phi)^2 - (c - f_{ct} \tan \phi)^2} \tag{4.16}$$

where c, ϕ and f_{ct} are respectively the cohesion parameter, the friction angle, and the tensile strength of the substrate. The equal sign in Eq. 4.16 applies for the frontier of the elastic domain, also called "cracking limit surface" (Fig. 4.12a), which gives the values $(\sigma_{max}(s_1, v_1), \tau_{max}(s_1, v_1))$ at the onset of cracking (beginning of the softening stage).

Whilst ϕ is assumed as a material property, the value of the cohesion parameter c

$$c = \frac{(f_{ct} \tan \phi)^2 + \tau_0^2}{2 f_{ct} \tan \phi} \tag{4.17}$$

is obtained by imposing the passage of the criterion (Eq. 4.16) through the point $(0, \tau_0)$, i.e. point B in Fig. 4.12a, where τ_0 is the pure shear strength. From Eq. 4.16 it can be observed that the pure tensile strength of the interface is limited by the tensile strength of the substrate f_{ct} (point D in Fig. 4.12a), accordingly to the widely accepted hypothesis that the substrate is the weakest material composing the interface [18, 85]. The displacements v_1 and s_1 at the onset of cracking are calculated using the LE stiffnesses:

$$\boldsymbol{\rho}_1 = \left\{ \begin{matrix} v_1 \\ s_1 \end{matrix} \right\} = \underbrace{\begin{bmatrix} K_\sigma^{-1} & 0 \\ 0 & K_\tau^{-1} \end{bmatrix}}_{\boldsymbol{K}^{-1}} \left\{ \begin{matrix} \sigma_{max} \\ \tau_{max} \end{matrix} \right\} \tag{4.18}$$

where $\boldsymbol{K} = diag[K_\sigma, K_\tau]$ is the stiffness matrix of the interface, in which no dilatancy phenomena are accounted for.

The criterion in Fig. 4.12a shows the coupling of the maximum stresses at cracking: the maximum tangential stress τ_{max} decreases in presence of tensile stresses (point C in Fig. 4.12a), whilst increases in case of compression (point A in Fig. 4.12a). The adopted curve is asymptotic to the Coulomb criterion for $\sigma \to \infty$ (Fig. 4.12a), pointing out the predominant role of friction for high compressive stresses.
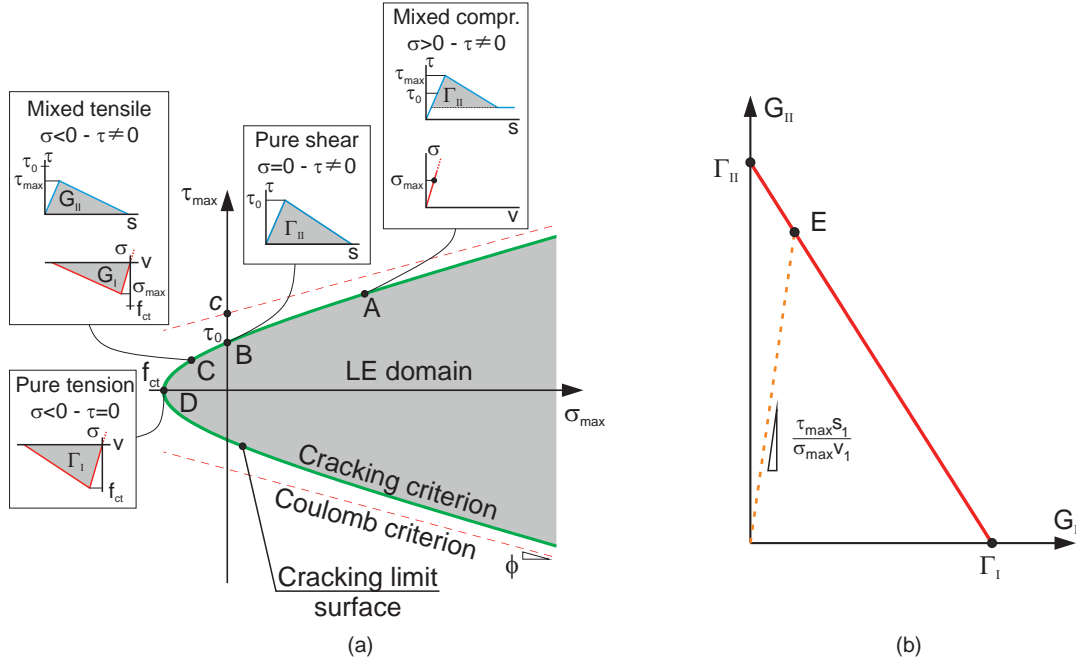
Figure 4.12: (a) Adopted cracking criterion. (b) Implemented energy-based failure criterion.

4.3.4.2 Softening branch and failure criterion

The post-peak behavior of the laws is defined assuming that, whatever displacement path is followed during the debonding process, the softening stages in normal and tangential direction ends together. This assumption seems reasonable because the compliance volume subject to damage is unique, thus the complete decohesion or failure occurs simultaneously in both directions. From this hypothesis follows the adoption of a unique damage parameter. To the purpose an equivalent cohesive law taking into account both opening and tangential displacements is defined following an approach similar to the one proposed in [64] for finite element analysis of analogous problems.

The bilinear equivalent law (Fig. 4.13a) relates an equivalent total stress σ_{eq} to the total displacement jump:

$$\delta(v, s) = \|\boldsymbol{\rho}\|_2 = \sqrt{\langle v \rangle_-^2 + s^2} \tag{4.19}$$

where $\langle \cdot \rangle_-$, namely the Macaulay brackets, selects the negative part of a number. The total energy at disposal G_{TOT} (i.e. the area encompassed by the equivalent curve) descends from the hypothesis of bilinearity of the equivalent law and must be equal to the sum of
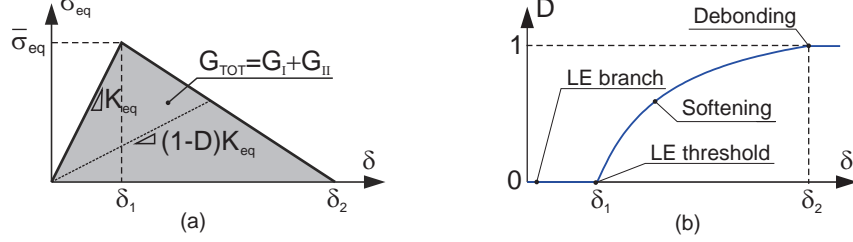
Figure 4.13: (a) Equivalent cohesive law. (b) Damage parameter D as a function of the total displacement jump δ.

the energies at disposal for the mode-I and -II processes $G_I(v, s)$ and $G_{II}(v, s)$

$$G_{TOT}(v, s) = \frac{1}{2}\delta_1 K_{eq}\delta_2 = \frac{1}{2}\overline{\sigma}_{eq}\delta_2 = G_I(v, s) + G_{II}(v, s) \qquad (4.20)$$

where K_{eq} is the equivalent initial LE stiffness, $\overline{\sigma}_{eq}$ is the maximum equivalent stress, and δ_1 and δ_2 are the total displacement jumps respectively at the onset of softening branch and at complete decohesion. Following Eq. 4.19 it is possible to define:

$$\delta_1(v_1, s_1) = \|\boldsymbol{\rho}_1\|_2 = \sqrt{v_1{}^2 + s_1{}^2} \qquad (4.21)$$

$$\delta_2(v_2, s_2) = \|\boldsymbol{\rho}_2\|_2 = \sqrt{v_2{}^2 + s_2{}^2} \qquad (4.22)$$

where $\boldsymbol{\rho}_2 = \{v_2, s_2\}^T$ is the vector collecting the ultimate displacements in normal-tensile and tangential direction. Moreover, using a vector notation, similarly to Eq. 4.20, it is possible to write:

$$G_{TOT}(v, s) = \frac{1}{2}\boldsymbol{\rho}_1^T \boldsymbol{K} \boldsymbol{\rho}_2 \qquad (4.23)$$

which implies that the areas encompassed by the cohesive laws $G_I(v, s)$ and $G_{II}(v, s)$, whatever softening path is followed, are equal to the ones of bilinear laws with the same strength and ultimate displacement. In Eq. 4.23 two unknowns are present, v_2 and s_2, thus a failure criterion must be adopted as additional equation.

Failure occurs when the complete decohesion of the interface (i.e., full debonding) is attained. In the present study an energy-based "failure criterion" similar to the one proposed in [53, 127] is adopted (Fig. 4.12b):

$$\frac{G_I(v, s)}{\Gamma_I} + \frac{G_{II}(v, s)}{\Gamma_{II}} = 1 \qquad (4.24)$$

where Γ_I, Γ_{II} are the pure mode-I and -II fracture toughnesses of the interface. In general, the values of $G_I(v,s)$ and $G_{II}(v,s)$ depend on the softening branch, thus on the displacement path followed. Assuming that:

$$s_2/v_2 = s_1/v_1 \qquad (4.25)$$

as suggested in [71, 72], permits to obtain the equation:

$$G_{II}(v,s) = \frac{\tau_{\max}s_1}{\sigma_{\max}v_1}G_I(v,s) \qquad (4.26)$$

which is represented in Fig. 4.12b with a dashed line in the $(G_I - G_{II})$ plane. The hypothesis in Eq. 4.25 leads to linear softening branches in case of softening displacement path characterized by a constant ratio $s/v = s_1/v_1$, holding the condition of simultaneous failure in both directions. Eq. 4.25 can be justified considering that, while the strength of the interface is given as a physical parameter, the initial tangential stiffnesses K_τ and K_σ can be defined with the only purpose of best fitting the experimental data. This is possible because the displacements at the onset of damage (v_1, s_1), which define the initial stiffnesses, are very low in comparison with the ones at complete debonding (usually the ratio ranges between 1/6 and 1/12). Moreover, the global behavior, which is mainly governed by the fracture energy at disposal G_{TOT} and by the softening branch of the cohesive law, is barely influenced by the choice of (v_1, s_1) [71] once that suitable values of (v_2, s_2) have been defined. Such conditions lead to high values of the initial stiffness that may be seen as penalty parameters, aimed only to fit the experimental data, taking care of avoiding ill conditioning of the problem. Penalty parameters are also mandatory to ensure a good pre-cracking behavior and a good agreement between the cohesive models and the well established linear elastic fracture mechanics (LEFM) approach [71]. In this way, the displacements (v_1, s_1) result more related to the penalty coefficients than to the debonding behavior, therefore the hypothesis formulated in Eq. 4.25 does not affect the soundness of the method [71, 72]. Finally, if K_τ and K_σ can not be considered as penalty parameters, Eq. 4.25 assumes the role of an approximation, which is acceptable in the present case, as also stated in [72] but, in general, its eligibility should be checked [71].

The intersection between Eq. 4.24 and Eq. 4.26 (point E in Fig. 4.12b) defines the fracture energies $G_I(v,s)$ and $G_{II}(v,s)$ at disposal. Thus, the displacements at which the

softening branches end is

$$\boldsymbol{\rho}_2 = \begin{Bmatrix} v_2 \\ s_2 \end{Bmatrix} = \begin{Bmatrix} \dfrac{2G_I(v,s)}{\sigma_{\max}} \\ \dfrac{2G_{II}(v,s)}{\tau_{\max}} \end{Bmatrix} \tag{4.27}$$

It is now possible to completely define the total displacement law represented in Fig. 4.13a. In particular, the equivalent maximum stress $\overline{\sigma}_{eq}$ and the initial equivalent stiffness K_{eq} are written exploiting the bilinearity of the cohesive law:

$$\overline{\sigma}_{eq} = 2\frac{G_{TOT}(v,s)}{\delta_2} \tag{4.28}$$

$$K_{eq} = \frac{\overline{\sigma}_{eq}}{\delta_1} = 2\frac{G_{TOT}(v,s)}{\delta_1\delta_2} \tag{4.29}$$

For pure shear or traction the equivalent model degenerates into the pure mode laws, as shown in Fig. 4.12a points B (pure shear), and D (pure traction). It has to be noticed that in the case of tension (Fig. 4.11a and point C in Fig. 4.12a) the friction is ignored after complete debonding (i.e., $\tau_{frict} = 0$). On the contrary, for compression (Fig. 4.11 and point A in Fig. 4.12a) the fracture energy available during debonding remains equal to Γ_{II} and the increment of the maximum tangential stress is supposed due to friction only (i.e., the curve continues after the softening branch with a horizontal plateau $\tau_{frict} = \tau_{max} - \tau_0$).

Once the total displacement law is defined, it is possible to introduce a damage parameter D [64] that governs its softening behavior (Fig. 4.13b):

$$D(v,s) = \begin{cases} 0 & \delta(v,s) \leq \delta_1 \\ \frac{\delta_2(\delta(v,s)-\delta_1)}{\delta(v,s)(\delta_2-\delta_1)} & \delta_1 < \delta(v,s) < \delta_2 \\ 1 & \delta(v,s) \geq \delta_2 \end{cases} \tag{4.30}$$

where D ranges between 0 (undamaged state) and 1 (fully damaged state or debonded interface). Therefore, the fully coupled cohesive law in term of total displacement jump δ results:

$$\sigma_{eq} = (1 - D(v,s))K_{eq}\delta(v,s) \tag{4.31}$$

Splitting the equivalent stress into the peeling and shear components gives:

$$\boldsymbol{\sigma}(v,s) = \begin{Bmatrix} \sigma(v,s) \\ \tau(v,s) \end{Bmatrix} = (1 - D(v,s))\boldsymbol{K}\boldsymbol{\rho} \tag{4.32}$$

The coupled laws are bilinear in the particular case of constant ratio s/v during the whole softening process. Nevertheless, also in the general case, the softening branches are not far from linearity (as observable in par. 4.3.7.3), confirming the rationality of the formulated assumptions.

4.3.5 Numerical solution via finite difference method

To solve the numerical problem a strategy similar to what illustrated for the pure mode-II model in par. 4.2.3 is used. The only difference is the number of unknowns and equations that has growth from two to six. Indeed, the vector collecting the unknowns is now $\boldsymbol{y} = [N, V, M, u, v, \varphi]^T$, the vectors have dimension $[6 \times 1]$ and the matrices $[6 \times 6]$. Nevertheless the general formulation from Eqs. 4.6-4.11 is still valid, while the detailed description of the numerical strategy and the matrices employed are reported in App. B.

4.3.6 Validation and comparison with experimental results

To validate the model, some comparisons with experimental data published in the literature were carried out. In particular, results illustrated in par. 3.2 and published in [1] and data from Chajes et al. [2] and Mazzotti et al. [3] were chosen because the bonded lengths l_b span from short to long.

4.3.6.1 Calibration of the parameters

To determine the main features of the interface in pure tensile and tangential stress state a unified approach was followed, starting from the mechanical parameters summarized in Tab. 4.2. The mode-II fracture toughness, if not provided by the authors (as in [1, 3]), was calculated from the maximum debonding force of the longest specimens solving for Γ_{II} the formula proposed in [8]:

$$F_{\max} = b_f \sqrt{2 E_f t_f \Gamma_{II}} \tag{4.33}$$

The approach is admissible because in long specimens the pure mode-II sliding process prevails, as demonstrated in par. 3.2. Moreover, Eq. 4.33 is not related to any empirical or semi-empirical coefficients (see for instance [8, 9]) but it descends from a well established mechanical model (see par. 2.1.1). In this way, the introduction of new errors caused by coefficients not directly calibrated on the used tests has been avoided. If not directly specified (as in [1, 3]), the maximum shear stress attainable in pure mode-II was determined as:

$$\tau_0 = \frac{2\Gamma_{II}}{s_2} \tag{4.34}$$

where the slip s_2 was esteemed from the experimental $\tau - s$ laws obtained by integrating the strains measured over the reinforcement with the method detailed in par. 3.2.2.3. The mode-I fracture toughness was determined, following [131], as:

$$\Gamma_I = G_{f0}\left(\frac{f_{cm}}{f_{cm,0}}\right)^{0.7} \tag{4.35}$$

where G_{f0} is a coefficient related to the maximum aggregate diameter d_{max}, equal to 0.030 N/mm for $d_{max} = 16$ mm and 0.058 N/mm if $d_{max} = 32$ mm, and $f_{cm,0} = 10$ MPa. The only exception is done for the results presented in par. 3.2 where the value of the mode-I fracture toughness is esteemed from flexural tests as explained in par. 3.2.1.3. In addition, since the flexural tensile strength $f_{t,flex}$ is determined, the direct tensile strength is here calculated following what stated in [110] as $f_{ct} = 0.5f_{t,flex}$. In [3] the tensile splitting strength $f_{t,split}$ was determined, which is related to the mean direct tensile strength by the relationship suggested by [131] $f_{ct} = 0.9f_{t,split}$. Differently, in [2] the direct tensile strength was esteemed using the formula suggested by [110] as $f_{ct} = 0.3f_c^{(2/3)}$. The stiffnesses of the linear initial branches K_σ and K_τ were determined by means of a trial-and-error procedure to best fit the numerical pull-out curves to the experimental ones. The parameters adopted in the following simulations are reported in Tab. 4.3. For all the simulations the friction angle was $\phi=30°$. For the numerical model, the pulling force applied to the reinforcement was calculated as $F = N(L)$. Finally, since in the experimental tests displacements and strains were measured at the top of the reinforcement, for proper comparisons the numerical results were computed at the top surface, i.e. $\overline{s} = u + \varphi t_f/2$ and $\overline{\varepsilon} = N/E_f A_f - M t_f/2E_f I_f$.

Table 4.2: Mechanical properties of the materials employed in the tests used to validate the model.

Ref.	E_f [GPa]	E_c [MPa]	ν_c [-]	$\mathcal{G}_c$ [MPa]	f_c [MPa]	f_{ct} [MPa]	E_a [MPa]	ν_a [-]	$\mathcal{G}_a$ [MPa]
[1]	168 500	28 700	0.2	11 900	37.2	3.0	3 500	0.3	1 350
[2]	108 300	32 400	0.2	13 500	36.4	2.9	1 600	0.3	609
[3]	165 500	30 700	0.2	12 510	52.6	3.4	12 840	0.3	4 950

Table 4.3: Adopted parameters of the interface laws.

Ref.	τ_0 [MPa]	Γ_{II} [N/mm]	K_τ [N/mm^3]	f_{ct} [MPa]	Γ_I [N/mm]	K_σ [N/mm^3]
[1]	6.5	0.60	170	2.4	0.10	410
[2]	7.0	0.98	245	2.9	0.07	615
[3] [1]	9.1	0.53	525	3.4	0.14	1 300
[3] [2]	6.6	0.54	320	3.4	0.14	795

[1] b_f=50mm. [2] b_f=80mm.

Table 4.4: Stiffnesses and values of the different thicknesses composing the compliance volume.

Ref.	K_τ [N/mm^3]	K_σ [N/mm^3]	t_a [mm]	t_c [mm]
[1]	170	410	1.20	55
[2]	245	615	1.06	20
[3] [1]	525	1 300	1.50	20
[3] [2]	320	795	1.50	35

[1] b_f=50mm. [2] b_f=80mm.

4.3.6.2 Comparison with the results of par. 3.2 - Carrara et al. [1]

In the following the experimental results illulstrated in par. 3.2 are simulated. The values of the mechanical characteristics employed in the analyses are summarized in Tab. 4.2.

In Fig. 4.14 numerical and experimental results are compared for the specimens with bonded length l_b of 150 mm (*Ca_150/30*) and 30 mm (*Ca_30/30*). For short bonded lengths highly scattered experimental results have been observed (Fig. 4.14c), because of the local conditions (e.g. heterogeneities, defects, and aggregate size) that influence deeply the global and local behavior. Nevertheless, the trends of the pull-out curves and strain profiles are well predicted.

For long bonded lengths the global behavior is accurately reproduced (Fig. 4.14a) and the strain profiles are caught until the beginning of the unstable phase (Fig. 4.14b). The curves appear close to the ones obtained using the classic pure shear model described in

par. 4.2.4 and similar to the one adopted in [40] (dotted curves in Figs. 4.14a,c), which are computed using the parameters of the pure mode-II law reported in Tab. 4.1 and used also in Tab. 4.3.
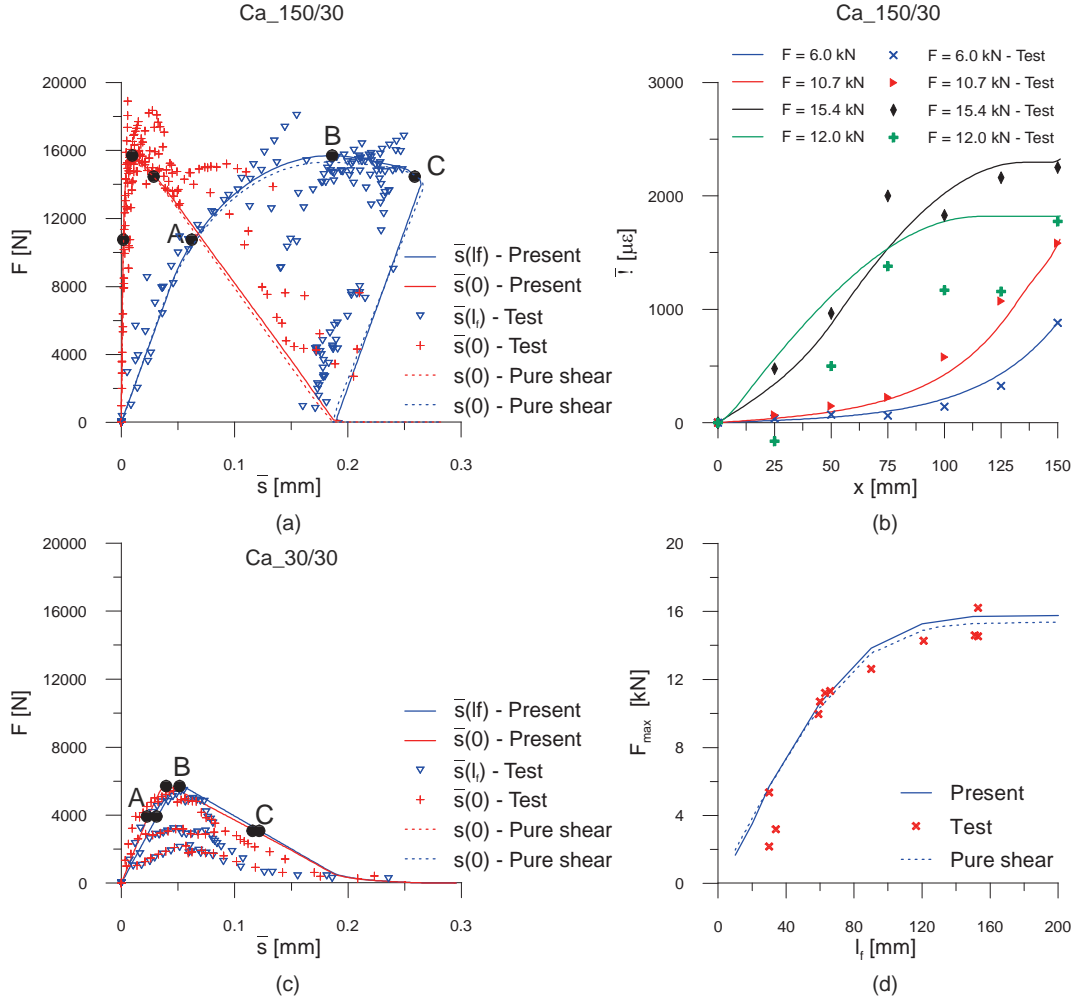
Figure 4.14: Comparison between numerical and experimental results [1] (a) global behavior of *Ca_150/30* test, (b) strain profiles at various load levels for *Ca_150/30* test, (c) global behavior of *Ca_30/30* test, (d) maximum pulling force vs. bonded length curve.

In Figs. 4.15, 4.16 the numerical solutions along the bonded length of specimens *Ca_150/30* and *Ca_30/30* respectively are reported at various instants of the debonding process (represented with dots in Fig. 4.14a,c). In Fig. 4.17 the damage maps are reproduced. It must be highlighted that, in order to reproduce the damage maps, the width represented in the picture is only indicative because the model proposed here is
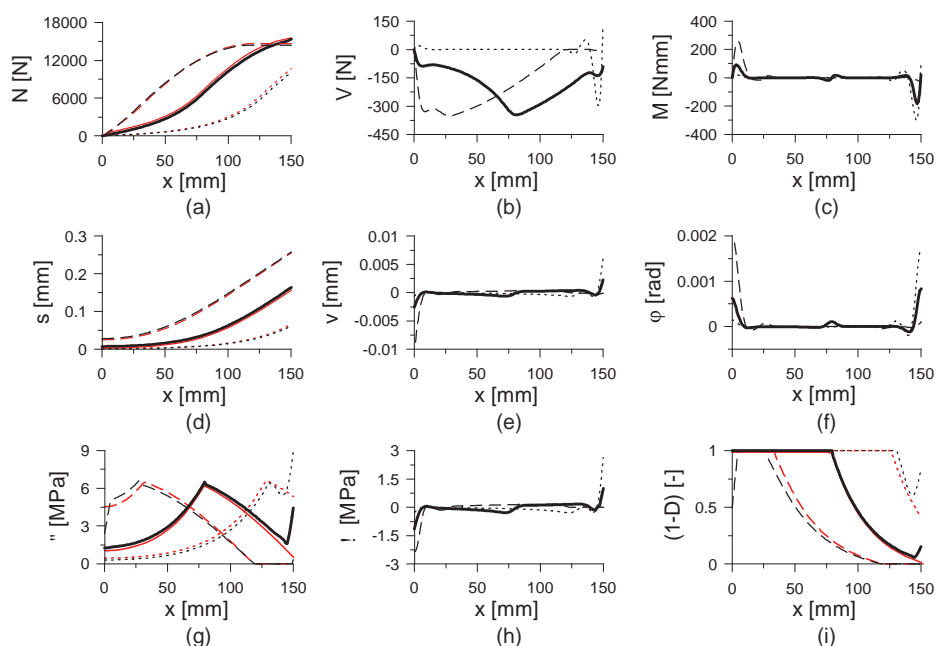
Figure 4.15: Numerical results for the specimen *Ca_150/30* at the load levels A=···, B=——
and C=−− of Fig. 4.14a. (a) Axial force; (b) shear force; (c) bending moment; (d) slip; (e)
opening displacements; (f) rotation; (g) bond stress; (h) peeling stress; (i) damage. (Classic
shear model results are reported in red).

plane and cannot reproduce the transversal behavior of the FRP.

The present model is able to reproduce the two-way debonding experimentally observed
in long bonded lengths, whereas the pure shear model does not (see par. 4.2.4). Indeed, the
damage in the ascending branch (point *A* in Fig. 4.14a) presents a high damage level (up
to 0.4) at the loaded end, whereas the free end appears still intact (dotted curve Fig. 4.15i
and Fig. 4.17a). During the sub-horizontal plateau (point *B* in Fig. 4.14a), the damage at
the loaded end increases and propagates toward the free end (solid line in Fig. 4.15i and
Fig. 4.17b). Approaching the unstable snap-back branch (points *C* in Fig. 4.14a), the crack
propagating from the loaded end has experienced only a limited widening and a second
crack is present at the free end (dashed line in Fig. 4.15i and Fig. 4.17c). Differently,
as outlined in par. 4.2.4, in the pure shear model the damage starts at the loaded end
and propagates toward the opposite side until the complete debonding (red curves in
Fig. 4.15i).

Concerning short bonded lengths, the free end debonding is correctly reproduced as
clearly outlined in Fig. 4.17c-e. Indeed, the debonding begins at the free end during the
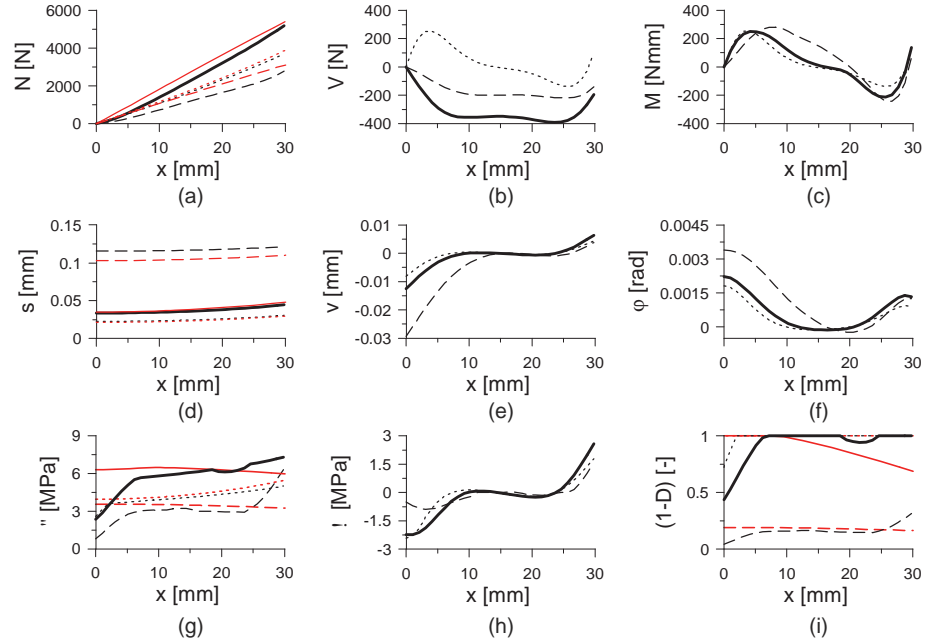
Figure 4.16: Numerical results for the specimen $Ca\_30/30$ at the load levels A=$\cdots$, B=——
and C=$--$ of Fig. 4.14c. (a) Axial force; (b) shear force; (c) bending moment; (d) slip; (e)
opening displacements; (f) rotation; (g) bond stress; (h) peeling stress; (i) damage. (Classic
shear model results are reported in red).
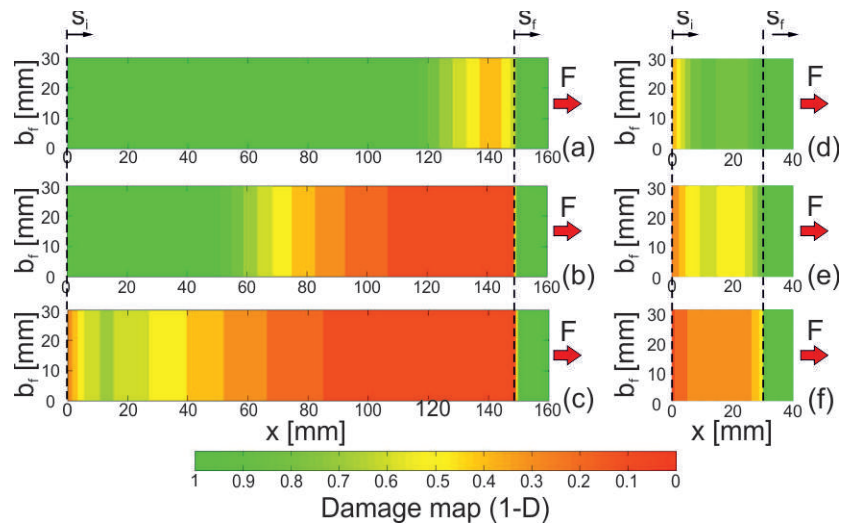
Figure 4.17: Damage maps for the load levels of Fig. 4.14a,c: (a) $Ca\_150/30$ point A; (b)
$Ca\_150/30$ point B; (c) $Ca\_150/30$ point C; (d) $Ca\_30/30$ point A; (e) $Ca\_30/30$ point B; (f)
$Ca\_30/30$ point C.

loading phase (dotted line in Fig. 4.16i and Fig. 4.17c related to point A in Fig. 4.14c), as in the experimental tests. Then, the damage propagates toward the loaded end until the peak load (solid line Fig. 4.16i and Fig. 4.17d related to point B in Fig. 4.14c) and the subsequent softening stage (dashed line in Fig. 4.16i and Fig. 4.17e related to point C in Fig. 4.14c). Differently, for the pure shear model the damage of the interface monotonically increases from the free end to the loaded one.

The maximum force F_{max} is well reproduced for all the specimen lengths l_b (Fig. 4.14d), and the prediction is similar to the one achieved with the classic pure shear model (dashed line in Fig. 4.14d).

Numerical results emphasize also how the out-of-plane (i.e. peeling) displacements can affect the failure mode. In Fig. 4.18 the vertical displacement from the analyses are shown. It is possible to observe how, the two-way debonding is associated with high values of the uplifting at the free end during the late stage of loading only (point C in Fig. 4.18a and dashed curve in Fig. 4.15e), while during the early phase the tangential displacement prevail (Fig. 4.15d), clarifying the formation of two cracks. On the contrary, for short bonded lengths, the free end debonding is associated with high values of the uplifting since the very beginning of the test (point a in Fig. 4.18b and dotted curve in Fig. 4.16e). As the debonding progresses the out-of-plane displacement continues to increase, explaining the crack propagation observed during the experimental tests.

4.3.6.3 Comparison with Chajes et al. [2]

Chajes et al. [2] executed four single-lap shear tests using a CFRP plate of width b_f of 25.40 mm (1 in), thickness t_f of 1.02 mm and varying the bonded length from 50.8 mm (2 in) to 203.2 mm (8 in). The mean thickness of the glue layer t_a was 1.60 mm. The various mechanical properties of the materials employed are summarized in Tab. 4.2.

In Fig. 4.19 the comparisons between experimental and numerical results are reported for the specimens with bonded length l_b of 203.2 mm ($Ch\_203/25$) and 50.8 mm ($Ch\_50/25$). The experimental pull-out curves were calculated by integrating the published strain profiles starting from the free end, where the displacement $\overline{s}(0)$ was neglected. This is generally correct for long bonded lengths and until the peak, but in the post-peak branch or for short bonded lengths the displacement at the free end is similar to the one at the loaded end. For this reason the comparisons with the experimental results have been performed using also the value of $\overline{s}(l_f) - \overline{s}(0)$. Apart a limited scattering for high
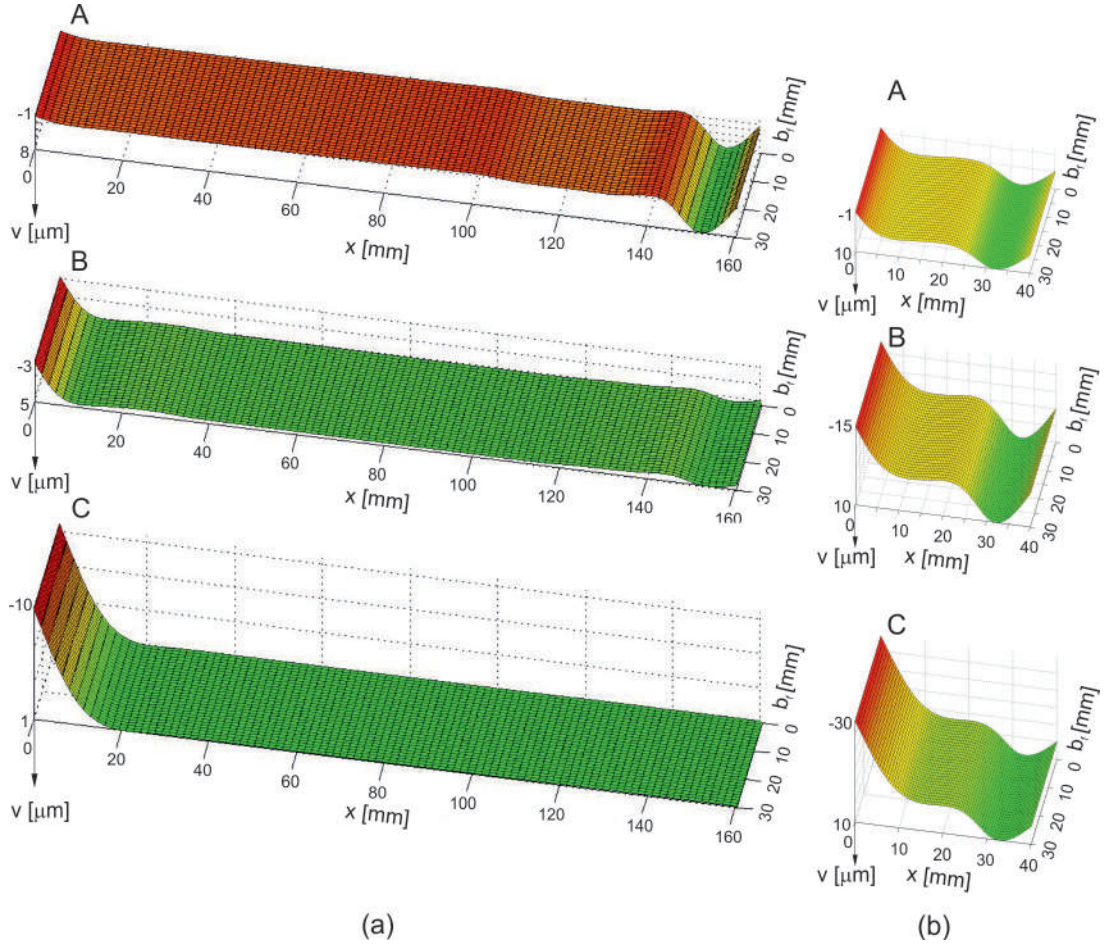
Figure 4.18: Out-of-plane displacements for the load levels of Fig. 4.14a,c: (a) specimen *Ca_150/30*; (b) specimen *Ca_30/30*.

load levels in short bonded lengths, due to the unavoidable influence of heterogeneities, a very good agreement is found. In particular, the global behavior until the peak load is well predicted (Fig. 4.19a,c), as well as the trend of the strain along the bonded length (Fig. 4.19b). The maximum transmissible force $\hat{F}$ as a function of the bonded length l_b is adequately reproduced (Fig. 4.19d); the only exception is the specimen with l_b=101.6mm for which the experimental maximum pulling force appears anomalous also in other studies (e.g. [3]).
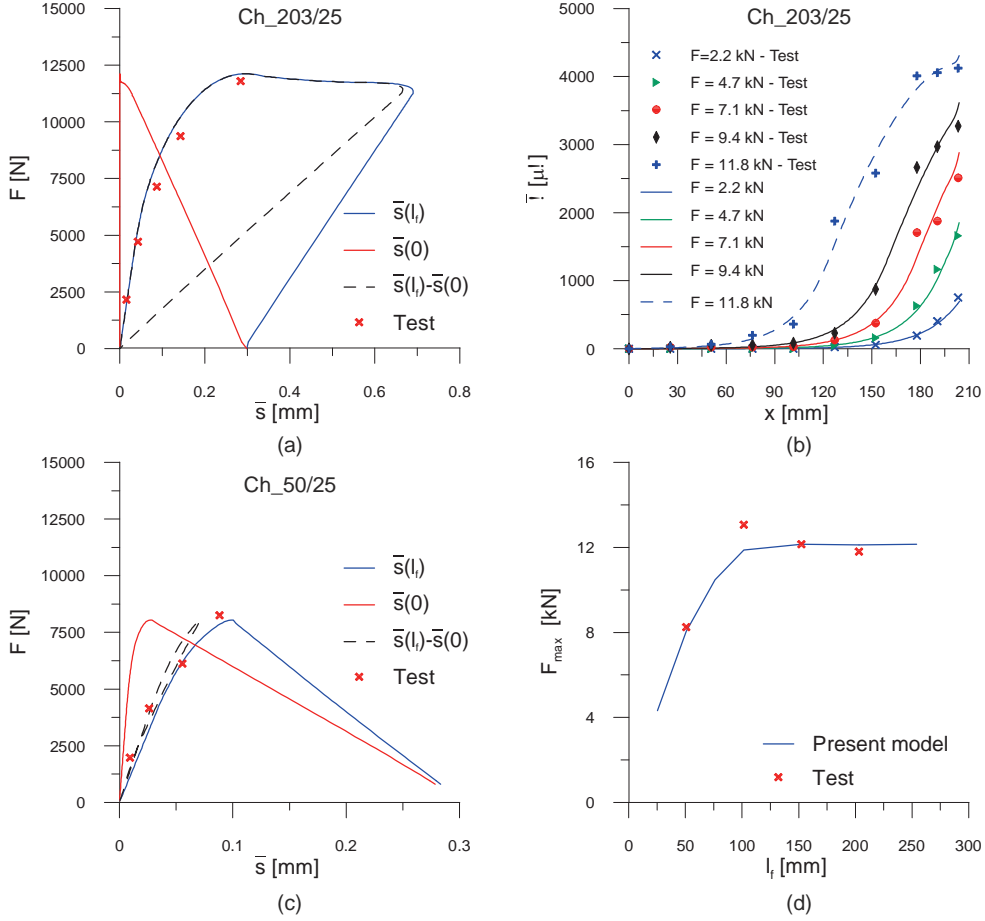
Figure 4.19: Comparison between numerical and experimental results [2] (a) global behavior of *Ch_203/25* test, (b) strain profiles at various load levels for *Ch_203/25* test, (c) global behavior of *Ch_50/25* test, (d) maximum pulling force vs. bonded length curve.

4.3.6.4 Comparison with Mazzotti et al. [3]

Mazzotti et al. [3] executed some experimental tests using plate widths of 50mm and 80mm and bonded lengths of 50-100-200-400 mm. The mean thicknesses of the plate t_f and of the adhesive t_a were 1.2 mm and 1.5 mm respectively. The bonded lengths of the specimens started 40 mm far (*Setup B*) or in correspondence (*Setup A*) of the block edge. For the comparisons, only the *Setup B* tests are taken into account, because the proposed model does not reproduce edge effects. The main mechanical properties of the materials are presented in Tab. 4.2.

In Fig. 4.20 the numerical analyses and the experimental results are compared for the
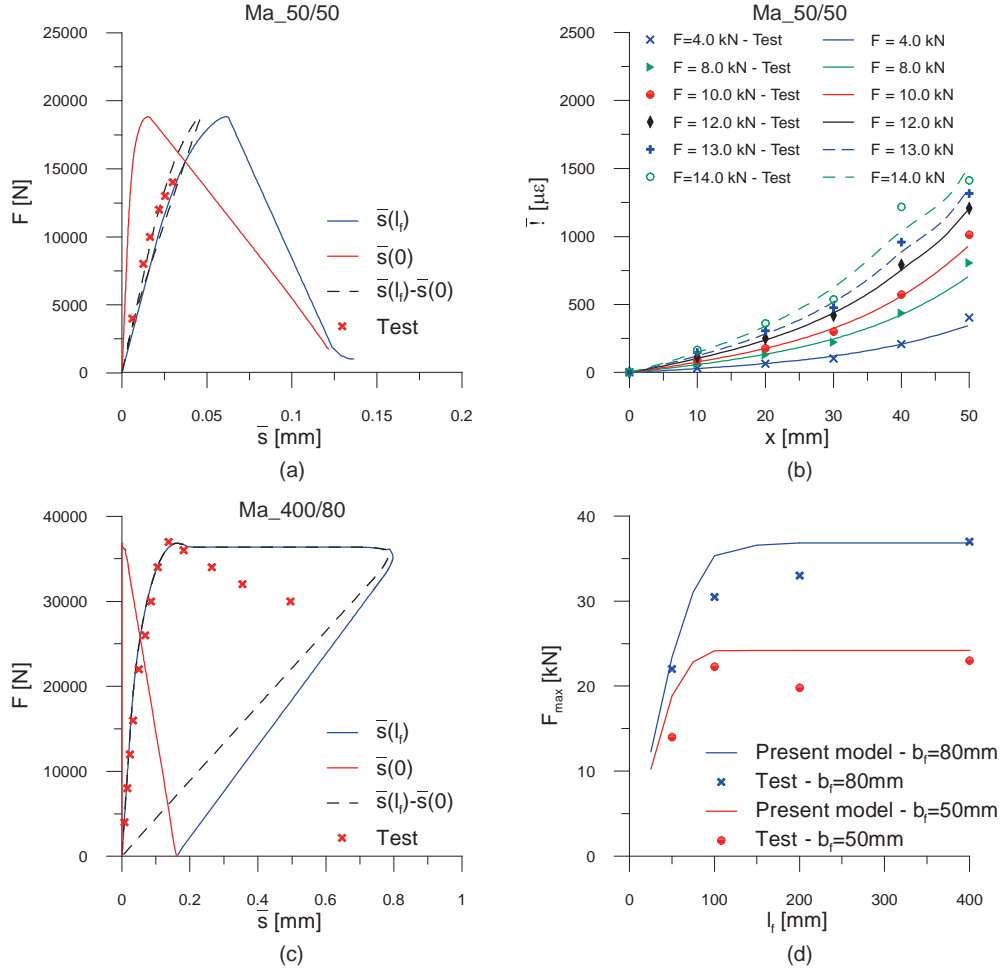
Figure 4.20: Comparison between experimental and numerical results [3] (a) global behavior of *Ma_50/50* test, (b) strain profiles at various load levels for *Ma_50/50* test, (c) global behavior of *Ma_400/80* test, (d) maximum pulling force vs. bonded length curve.

specimens with l_b=50 mm and b_f=50 mm (*Ma_50/50*) as well as l_b=400 mm and b_f=80 mm (*Ma_400/80*). Pull-out curves are obtained by numerical integration of strain profiles, as in the previous par. 4.3.6.3. The global behavior is well predicted until the load peak of the pull-out curves (Fig. 4.20a,c). For long bonded lengths, after the peak the numerical curve displays a plateau whereas the experimental curve shows an unusual softening path (Fig. 4.20c), leading thus to a certain mismatch in the corresponding strain profiles. For the short bonded lengths the strain profiles are well predicted (Fig. 4.20b). Considering the unavoidable scattering of the experimental results, the maximum pulling force is well reproduced for all the specimen lengths (Fig. 4.20d).

4.3.7 Discussion of the results

4.3.7.1 Global behavior

As previously observed, the numerical and experimental pull-out curves are generally in good agreement. Nevertheless, a dispersion is observed for short bonded lengths, which is probably related to the substrate heterogeneities. For instance, in Fig. 4.14d the experimental values of $\hat{F}$ for the specimens with l_b=30 mm range from about 2.0 kN to 6.0 kN and the global curves are very scattered (Fig. 4.14c). Anyway, apart these very short lengths, the maximum pulling forces are predicted with good accuracy.

It must be highlighted that the post snap-back branch of the pull-out curves appears in the numerical analyses as a line, whilst the tests ([1, 83] and Fig. 4.14a) display a curve; the same occurs for the late loading phase. These differences are due to the choice of bilinear equivalent cohesive law. Adopting fully non-linear laws (for example [6]) would probably mitigate these differences. Finally, the comparisons with the classic pure shear model displayed good compatibility in pull-out curves and maximum debonding force prediction.

4.3.7.2 Interfacial LE stiffnesses

As observable in Tab. 4.3 the tangential stiffnesses K_τ for the various analyses are 2-3 times smaller than the normal stiffnesses K_σ. Such condition seems confirmed by the very small out-of-plane displacements reported, for example, in [1, 83, 126].

In [8] the initial LE tangential stiffness of the interface is obtained as:

$$K_\tau = \frac{c_1}{\frac{t_a}{\mathcal{G}_a} + \frac{t_c}{\mathcal{G}_c}}$$ (4.36)

where c_1 is a corrective coefficient ranging from 0.5 to 0.7 as a function of the thickness t_c. If c_1=1, Eq. 4.36 provides the equivalent stiffness of two springs in series representing the tangential elastic behavior of the adhesive layer $'a'$ and the deformable substrate $'c'$. Following the same approach, the LE stiffness in normal direction will be:

$$K_\sigma = \frac{c_2}{\frac{t_a}{E_a} + \frac{t_c}{E_c}}$$ (4.37)

The coefficients c_1 and c_2 should take into account the simplifying assumption of continuous and homogeneous support material and that the real process is three-dimensional. Moreover, c_1 and c_2 have to encompass all the aleatory and deterministic peculiarities of the substrate material not directly taken into account by the cohesive law parameters.

Indeed, some studies [1, 83] pointed out the role of parameters as the material employed (concrete, clay bricks or masonry blocks), the presence of aggregates or heterogeneities and their size, the strength and porosity of the substrate and the diffusion of the stresses inside the support block. Therefore, the parameters K_τ and K_σ can vary among a very wide range of values, as pointed out in Tab. 4.3. The coefficients c_1 and c_2 proposed in the code-standard [8] assume the meaning of conservative corrective parameters, which have to take into account the worst combination of factors affecting the debonding process.

For these reasons, the values of stiffnesses in normal and tangential directions are presented here imposing $c_1=c_2=1$. Starting from the fitted values of K_τ (Tab. 4.4), and the measured adhesive thicknesses t_a, it is possible to compute t_c by means of Eq. 4.36. As observable in Tab. 4.4, the values of t_c range between 20 and 55 mm, similarly to what esteemed in [6, 40, 117].

4.3.7.3 Local behavior: strain profiles, peak stresses and interface laws

The model correctly reproduces the strain profiles of the various tests, at least until the detachment of a bulb of substrate material at the free end. In [1, 33, 83] as well as in the previous Sect. 3, a wedge at the loaded end is sometimes observed. During the final part of the tests the local effects induced by the free end bending of the plate and the formations of the aforementioned bulbs prevail, changing drastically the physics of the problem, sometimes leading to a sign inversion of the strain values (e.g. in the experimental strain profile for F=12.0 kN, Fig. 4.14b). Indeed, the material wedge detached at the free end causes an increase in the opening displacements v, and thus of bending at the free end of the plate. Such behavior is responsible also of the overestimation of the free end slip illustrated in par. 3.2.2. As mentioned in par. 4.3.1, the present model misses such peculiarity, strongly related to the behavior of the disturbed regions of the compliance volume.

Considering the local influence of the peeling stresses, the proposed model reproduces the variations of maximum shear stress τ_{max} along the bonded length indirectly deduced with the experimental results presented in Sect. 3 (Fig. 4.21). Indeed, the plate bending induces normal stresses leading to a decrease or an increase of the shear strength in the zones subjected respectively to traction or compression. This peculiarity, which is strongly related to the observed changes in the failure mechanism (as better explained in par. 4.3.7.4), is missed by the classic pure shear model that, consequently, is not able to

reproduce correctly the failure process (see par. 4.2.4). In particular, for short bonded lengths the results in terms of bond stresses and damage profiles are totally contrasting (Figs. 4.16g,i).
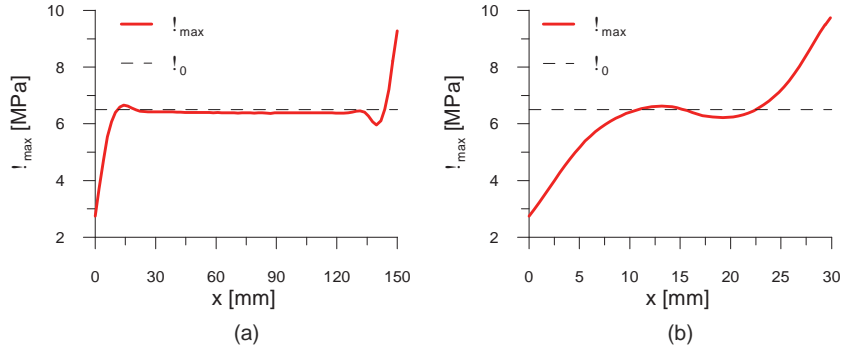
Figure 4.21: Maximum shear stresses along the bonded length. (a) Specimen $Ca\_150/30$, (b) specimen $Ca\_30/30$.

For the numerical simulations $Ca\_150/30$ and $Ca\_30/30$ Fig. 4.22 shows normal and tangential local cohesive laws at the free end (F), at the bonded length half-section (H), and at the loaded end (L). In particular, in Fig. 4.22c the curve L at the loaded end of the test $Ca\_150/30$ displays a horizontal friction branch after the softening phase of the cohesive law due to the presence of compressive stresses. This behavior was observed only in long bonded lengths; indeed no friction branches were reached for $Ca\_30/30$ test (Fig. 4.22f). Apart for the friction branch, no unloading paths have been observed in tangential direction (Figs. 4.22c,f).

For the normal behavior, Fig. 4.22b points out that significant peeling and compressive stresses are present in small portions at the free end and at the loaded end respectively. Differently, in the central part of the plate (curves H in Fig. 4.22) the values of the normal stress are very low, usually oscillating around zero and the local bond-slip relationship is similar to the one of the pure shear model (dashed curves in Figs. 4.22c,f). The last remark is also supported by the maximum tangential stress profiles (Fig. 4.21), which reveal a shear strength τ_{max} in the central part of the plate very close to τ_0. This confirms that, at least in the central part of the plate, the debonding can be approximated to a mode-II process, whilst at the loaded and free end a mixed process takes place. Finally, Fig. 4.22 demonstrates that the resulting cohesive laws are not far from bilinearity, as introduced in par. 4.3.4.2.
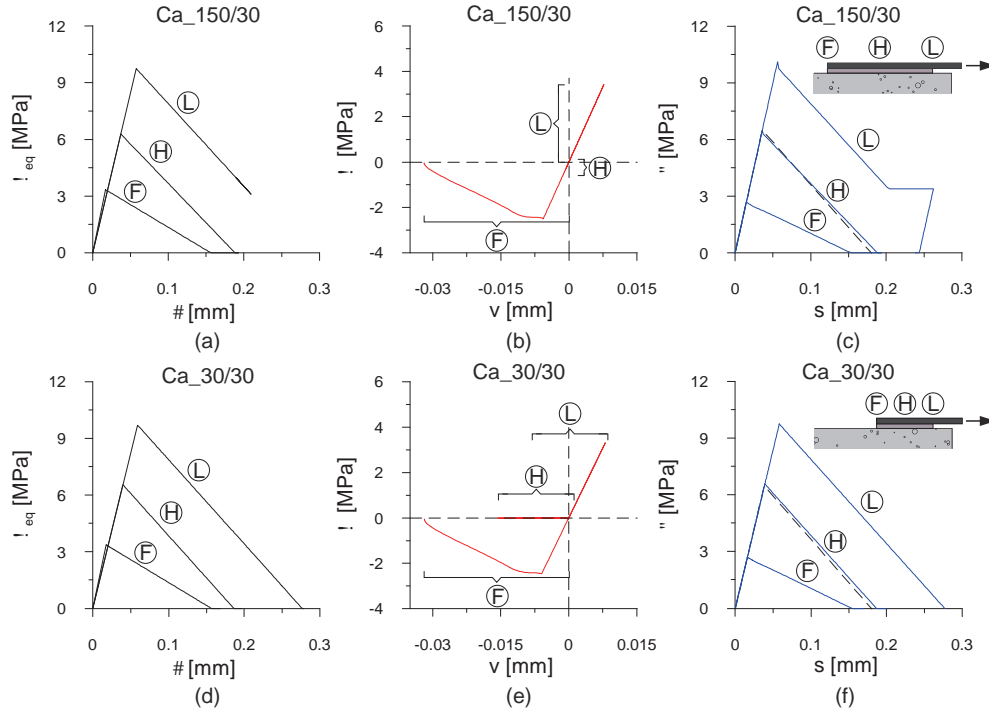
Figure 4.22: Cohesive laws from numerical analyses. (a) equivalent law of $Ca\_150/30$ test, (b) normal cohesive law of $Ca\_150/30$ test, (c) tangential cohesive law of $Ca\_150/30$ test, (d) equivalent law of $Ca\_30/30$ test, (e) normal cohesive law of $Ca\_30/30$ test, (f) tangential cohesive law of $Ca\_30/30$ test. *F=free end, H=bonded length half-section, L=loaded end*

The mixed mode influence is also clearly visible in Fig. 4.23 where are shown the $(\sigma_{max}, \tau_{max})$ and (G_{II}, G_I) points for the specimen $Ca\_150/30$ related respectively to the cracking and the failure criterion illustrated in par. 4.3.4. Fig. 4.23a clearly show that in the central part of the plate peeling stresses do not affect the pure-shear strength (i.e. $\sigma_{max} \simeq 0$), while there is an increase of shear strength at the loaded end due to compressive peeling stresses and a reduction of strength at the free end because of the tensile stresses present. Conversely, Fig. 4.23b highlights how the points of the interface at the free end are characterized by a reduction of the mode-II fracture energy at disposal accompanied by a more incisive role of the mode-I cracking process.

4.3.7.4 Debonding mechanism

Considering the debonding mechanism, the proposed model is able to predict, probably for the fist time for a simple cohesive zone model, the changes in the debonding mechanism
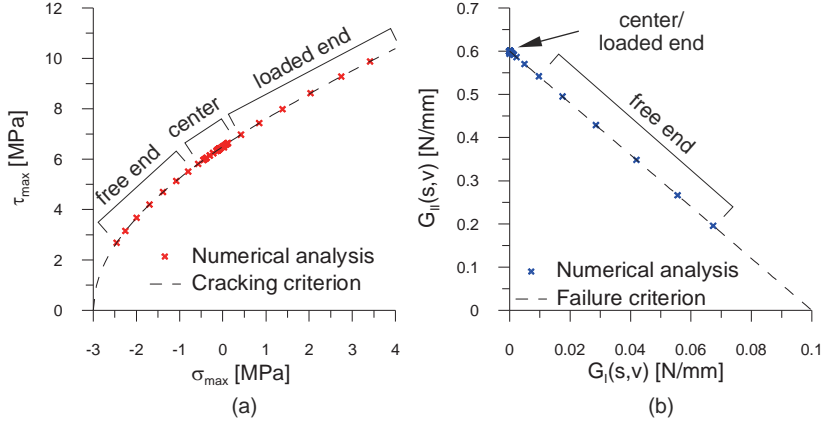
Figure 4.23: Specimen *Ca_150/30*: (a) cracking criterion; (b) failure criterion.

of the externally glued FRPs reinforcements. In fact, both the two-way debonding mechanism (for long bonded lengths) and the free end debonding (in short bonded lengths), observed experimentally in the experimental campaigns illustrated in Sect. 3, are correctly reproduced although missed by the classic pure shear model.

The changes in the failure mechanism are due to the presence of significant peeling stresses at the free end of the reinforcement, as explained in par. 4.3.7.3. Such stresses cause a radical change in the damage process. Indeed, the lower shear strength induced by plate bending at the free end allows damaging of this zone while the central part of the bonded reinforcement is still sound. Moreover, at the free end the fracture process deviates from the classic mode-II process and the mode-I influence becomes prominent. In this zone the formation of a material bulb leads to a debonding process strongly related to both the damage of the support material and of the interface. In other words, the failure process depends also on the stress state of the compliance volume that should be studied with sound models. Such observation leads to non-local models, as the one proposed by Marfia et al. [116], in which it is observable for long bonded lengths a damage of the free end of the plate while the central part is still sound.

4.3.8 Conclusive comments

A novel cohsive model which couples normal (peeling) and tangential (shear) stresses has been formulated and presented.

Some experimental tests from the literature ([1–3]) have been simulated and the results have been discussed. Moreover, analyses with already validated models have been performed and compared to previsions from the present model. A good agreement with tests is found and the improvements of the proposed model compared to pure shear model have been proved. In particular, it is possible to highlight that:

- The presence of significant normal stresses at the ends of the plate influences the maximum shear stress attainable leading to variable bond-slip laws along the bonded lengths;

- Taking into account the effects of out-of-plane displacements in reinforcements loaded in shear permits to predict the changes in the failure mechanism varying the initial glued length. These changes are completely missed by the classic pure shear model;

- The variation of the fracture process near the free end from a mainly mode-II to a mixed mode I+II deeply affects the physics of the problem.

For the cases studied here the stated effects occur in narrow zones and they result in a detrimental and enhancing bond behavior respectively at the free- and at the loaded end, which tend to balance each other. For these reasons the prediction of the maximum pulling force is close to the one obtained with a classic pure-shear model. However, peculiarities as the variation of the shear strength along the bonded length and, consequently, the relation between failure mechanism and initial bonded length, are completely missed by classic pure-shear model.

The present model can be thus regarded as an innovative tool to study the full range behavior of FRPs glued joints on quasi-brittle materials.

4.4   Introduction to cyclic models

The externally glued FRP strengthening technique is often adopted to increase the lifespan of structures subject to cyclic loading (most notably bridges [96]). However, a gradual deterioration of the bond between FRP and substrate may occur because of the accumulation of fatigue micro-cracking, plastic deformations and damage [5, 95, 101]. Several studies pointed out that debonding failure mechanisms often control the fatigue life of strengthened member subject to cyclic actions [4, 5, 95, 96, 98, 99]. Some of these mechanisms are triggered by the bond shear stresses generated at the interface as a result of the composite action [95]. In the case of concrete substrates, micro-cracks at the interface level form and gradually coalesce, resulting in a macro-crack that usually propagates a few millimeters inside the substrate until complete loss of bond of the composite system [65, 100, 101].

To date, fatigue life assessment is largely based on the Wöhler curve or the Paris law [65, 96, 100]. Anyway, as also reported in par. 2.5.2, in these terms the fatigue life prediction remains an empirical abstraction [101, 102], since the parameters of the evolution laws are typically not defined through mechanically sound rules but rather calibrated following a case-by-case approach [102]. Moreover, any deviation from the ideal condition underlying each theory, can lead to a significant mismatch in the previsions, hence many laws have been proposed for different specific situations [101, 102]. An alternative approach is the employment of numerical models (as for example [4, 65, 100, 101, 106] among others). Some of them (e.g. [4, 65, 132]) consider parameters needing a case-by-case experimental calibration similarly to the aforementioned empirical laws. Thus, the accuracy of these models outside the range of variables of the tests used to calibrate the parameters is open to question. A few authors adopted fracture, damage or plasticity theories (either coupled or not) to define the interface law (e.g. [101, 106]). Here, the local hysteretic response is ruled by internal parameters that should be physically explained. However, some of these models are not necessarily suitable for FRP reinforcements, having been proposed for very different material systems (as [101]); moreover, they are only amenable to finite element implementation [65, 100, 101]. On the other hand, the available simple models proposed for FRP strengthening (e.g. [106]) are not formulated in a thermodynamical framework, which opens the question of their energetic consistency.

Here, the first attempts in the formulation of a new numerical model able to simulate the interface behavior of a bonded joint between a FRP laminate and a quasi-brittle substrate under cyclic loadings are presented, trying to overcome the drawbacks highlighted in par. 2.5.2. Concerning equilibrium and kinematics the same assumption that holds for the classic pure shear model are adopted. Differently from monotonic models, the hysteretic interface law is defined by means of an admissible domain coupling linear softening and damage. Under monotonic loading, the mode-II bilinear cohesive relationship presented in par. 4.2 is reproduced and well-known results are recovered [48]. Post-failure friction and interlocking are neglected. The capability of the model to correctly predict the local and global behavior of an FRP bonded joint is demonstrated comparing the numerical predictions with available experimental results.

4.5 Coupled interface damage-elastoplasticity fatigue model

Except for the interface behavior, the considerations done for the solution of the differential system governing the debonding process in the pure shear model presented in par. 4.2 are here still valid, thus this section is only focused on the interface behavior description.

4.5.1 Cyclic interface behavior

4.5.1.1 Basic assumptions

A cyclic interface law which couples damage and plasticity by means of a properly defined yielding criterion is proposed [104, 133]. Under monotonic conditions, the bilinear mode-II cohesive law described in par. 4.2 and widely used in literature ([8, 9, 53, 61, 83, 87] among others) is reproduced (Fig. 4.24a).
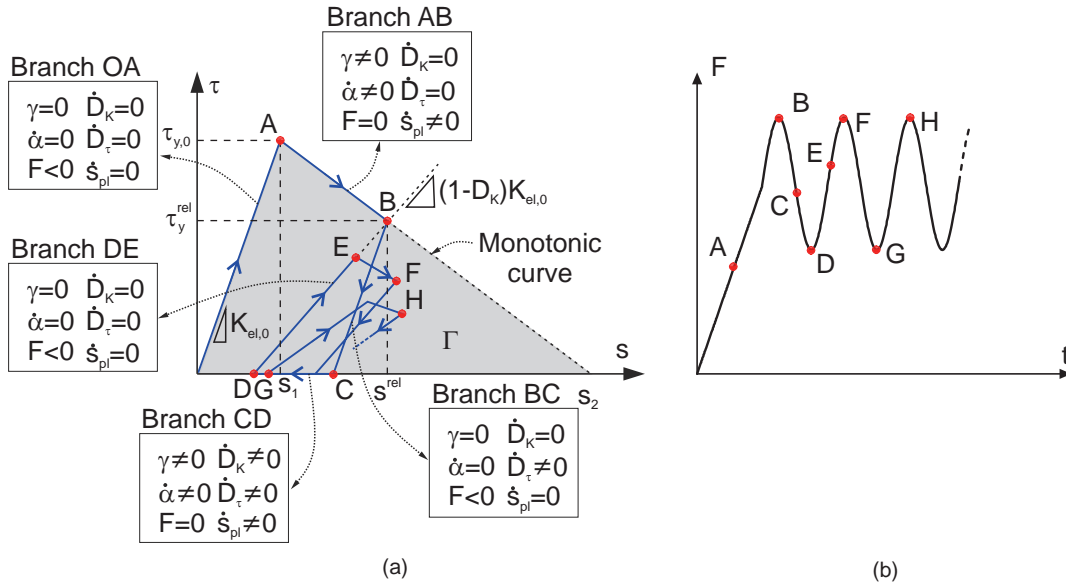
Figure 4.24: (a) Schematic representation of the interface law implemented with the evolution of the main variables and (b) example of a cyclic load history.

No sign inversion of the applied load is considered since this is the situation for which test results are available [4, 5, 95, 96]. Moreover, friction and interlocking between the faces of the debonding crack are neglected. The last two assumptions impose to restrict the bonding stresses to non-negative values and to maintain the lower bound of the yielding

criterion at $\tau = 0$. On the contrary, the upper bound of the admissible states domain should decrease according to the assumed linear softening (Fig. 4.24a).

In the present work the classic additive decomposition of the total slips s is assumed [103, 133, 134]

$$s = s_{el} + s_{pl} \tag{4.38}$$

where s_{el} and s_{pl} are respectively the elastic (or reversible) and the plastic (or irreversible) parts of the total slip. The bond stresses τ are written as [103, 133, 134]

$$\tau = (1 - D_K)K_{el,0}(s_{el}) = (1 - D_K)K_{el,0}(s - s_{pl}), \tag{4.39}$$

where $K_{el,0}$ is the initial linear elastic stiffness of the interface and D_K is a damage parameter governing the interface linear elastic stiffness degradation during load cycles (Fig. 4.24a). The rate of change of the tangential stress is

$$\begin{aligned} \dot{\tau} &= (1 - D_K)K_{el,0}\left(\dot{s} - \dot{s}_{pl}\right) - \dot{D}_K K_{el,0}\left(s - s_{pl}\right) \\ &= (1 - D_K)K_{el,0}\left(\dot{s} - \dot{s}_{pl}\right). \end{aligned} \tag{4.40}$$

where the term $\dot{D}_K K_{el,0}\left(s - s_{pl}\right)$ vanishes because $\dot{D}_K \neq 0$ if $\dot{s}_{pl} < 0$, which can happen only when $\dot{s}_{el} = \dot{s} - \dot{s}_{pl} = 0$ (Fig. 4.24 branch C-D).

The occurrence of a plastic flow is ruled by the following admissible states domain (i.e. a yielding function) [133], whose frontier gives the yielding condition

$$F(\tau, R \,|s_{pl}, \alpha, D_K, D_\tau) = |\eta| - \frac{(1 - D_\tau)}{2}\left[\tau_{y,0} + R\right] h(s - s_{pl}), \tag{4.41}$$

where $\tau_{y,0}$ is the initial yielding stress of the interface (namely, the monotonic bond strength), D_τ is a damage parameter controlling the loss of bond strength due to the cyclic actions, R is the thermodynamical force associated with the plastic behavior and conjugated with the internal hardening variable α. Furthermore, the quantity η is expressed by the following relationship

$$\eta = \tau - qh(s - s_{pl}), \tag{4.42}$$

where

$$q = \frac{(1 - D_\tau)}{2}\left[\tau_{y,0} + R\right]. \tag{4.43}$$

Finally, the function $h(\bullet)$ is the Heaviside step function defined as

$$h(\xi) = \begin{cases} 0 & \text{if } \xi \leq 0 \\ 1 & \text{if } \xi > 0. \end{cases} \tag{4.44}$$

The conjugated softening variable R is assumed to follow the linear relationship

$$R = K_{pl}\alpha, \tag{4.45}$$

where K_{pl} actually is a softening modulus (i.e. $K_{pl} < 0$) governing the contraction of the elastic domain [133]. It is worth to note that the parameter q of Eq. 4.43 acts in Eq. 4.41 as a back stress in presence of kinematic hardening [133] (i.e. $\tau - q = \eta$). Anyway, it is not an independent state variable but is defined as a function of α to take into account the evolution of the center of the elastic domain induced by the asymmetry of the interface law.

It is now possible to write Eq. 4.41 as

$$F = \left| (1 - D_K)K_{el,0}(s - s_{pl}) - \frac{(1 - D_\tau)}{2} \left[\tau_{y,0} + K_{pl}\alpha \right] h(s - s_{pl}) \right| - \cdots$$
$$\cdots - \frac{(1 - D_\tau)}{2} \left[\tau_{y,0} + K_{pl}\alpha \right] h(s - s_{pl}). \tag{4.46}$$

4.5.1.2 Thermodynamical formulation

The free energy of the system can be defined by the Helmholtz potential Θ as [104, 135]

$$\Theta = \Theta\left(s_{el}, \alpha, D_K, D_\tau\right) = \Theta_{el}\left(s_{el}, D_K, D_\tau\right) + \Theta_{pl}\left(\alpha, D_K, D_\tau\right), \tag{4.47}$$

where the subscripts "el" and "pl" state respectively for the elastic and plastic processes. Hence, the second law of thermodynamics can be expresses, for an isothermal process, by the Clausius-Planck inequality [104, 135]

$$\tau\dot{s} - \dot{\Theta} \geq 0, \tag{4.48}$$

where $\dot{\xi}$ points out the rate of variation of the quantity ξ. Substituting

$$\dot{\Theta} = \frac{\partial\Theta_{el}}{\partial s_{el}}\dot{s}_{el} + \frac{\partial\Theta_{el}}{\partial D_K}\dot{D}_K + \frac{\partial\Theta_{el}}{\partial D_\tau}\dot{D}_\tau + \frac{\partial\Theta_{pl}}{\partial\alpha}\dot{\alpha} + \frac{\partial\Theta_{pl}}{\partial D_K}\dot{D}_K + \frac{\partial\Theta_{pl}}{\partial D_\tau}\dot{D}_\tau \tag{4.49}$$

into Eq. 4.48 leads to

$$\left(\tau - \frac{\partial\Theta_{el}}{\partial s_{el}} \right)\dot{s} + \frac{\partial\Theta_{el}}{\partial s_{el}}\dot{s}_{pl} - \frac{\partial\Theta_{el}}{\partial D_K}\dot{D}_K - \frac{\partial\Theta_{el}}{\partial D_\tau}\dot{D}_\tau - \frac{\partial\Theta_{pl}}{\partial\alpha}\dot{\alpha}\cdots$$
$$\cdots - \frac{\partial\Theta_{pl}}{\partial D_K}\dot{D}_K - \frac{\partial\Theta_{pl}}{\partial D_\tau}\dot{D}_\tau \geqslant 0. \tag{4.50}$$

Table 4.5: Main thermodynamical variables.

Name	Variable Observed	Internal	Dual variable
Total slip	s		τ
Elastic slip		s_{el}	τ
Plastic slip		s_{pl}	$-\tau$
Softening		α	R
Kinematic hardening		$q(\alpha, R)$	$X(\alpha, R)$
Stiffness degradation		D_K	Y_K
Bond strength reduction		D_τ	Y_τ

Since the previous Eq. 4.50 should encompass any thermodynamically consistent process [135], the following equivalence holds

$$\tau = \frac{\partial \Theta_{el}}{\partial s_{el}}, \tag{4.51}$$

while the reduced Clausius-Planck equation becomes

$$\tau \dot{s}_{pl} - \frac{\partial \Theta}{\partial D_K} \dot{D}_K - \frac{\partial \Theta}{\partial D_\tau} \dot{D}_\tau - \frac{\partial \Theta_{pl}}{\partial \alpha} \dot{\alpha} \geqslant 0. \tag{4.52}$$

Then, the following equivalences can be written [104]

$$R = \frac{\partial \Theta_{pl}}{\partial \alpha}, \qquad Y_K = \frac{\partial \Theta}{\partial D_K}, \qquad Y_\tau = \frac{\partial \Theta}{\partial D_\tau}, \tag{4.53}$$

where Y_K and Y_τ are the damage sources related to the degradation at the interface level of the stiffness and of the bond strength respectively. Now it is possible to define $\tau \dot{s}_{pl}$ as the power dissipated by the plastic process, while $R\dot{\alpha}$, $Y_K \dot{D}_K$ and $Y_\tau \dot{D}_\tau$ are the the energy release rates respectively related to the interface softening, to the stiffness degradation process and to the fatigue bond strength reduction [103, 134]. Thus, Eq. 4.52 assumes the form

$$\tau \dot{s}_{pl} - R\dot{\alpha} - Y_K \dot{D}_K - Y_\tau \dot{D}_\tau \geq 0. \tag{4.54}$$

Eq. 4.54 governs the coupled damage-plasticity cyclic behavior of the interface. The main variables that describe the model are summarized in Tab. 4.5.

To define the evolution laws of the various variables it is more convenient to use a dissipation potential ψ_D assumed composed of a damage $\psi_{DMG}(Y_K, Y_\tau \,|\, s_{pl}, \alpha, D_K, D_\tau)$

and a plastic contribution $\psi_{pl}(\tau, R \,|\, s_{pl}, \alpha, D_K, D_\tau)$ [103, 134]. Making use of the associative rule, i.e. $\psi_{pl} = F(\tau, R \,|\, s_{pl}, \alpha, D_K, D_\tau)$, it is possible to write

$$\psi_D = \psi_{DMG}(Y_K, Y_\tau \,|\, s_{pl}, \alpha, D_K, D_\tau) + F(\tau, R \,|\, s_{pl}, \alpha, D_K, D_\tau). \tag{4.55}$$

Introducing the plastic multiplier γ and considering that plastic processes are ruled by the Kuhn-Tucker conditions

$$F \leq 0, \ \gamma \geq 0 \text{ and } \gamma F = 0 \tag{4.56}$$

the assumption of generalized normality leads to the following evolution laws (Fig. 4.24a)

$$\dot{s}_{pl} = \gamma \frac{\partial \psi_D}{\partial \tau} = \gamma \frac{\partial F}{\partial \tau} = \gamma sign(\eta), \tag{4.57}$$

$$\dot{\alpha} = -\gamma \frac{\partial \psi_D}{\partial R} = -\gamma \frac{\partial F}{\partial R} = \gamma(1 - D_\tau)h(s - s_{pl}), \tag{4.58}$$

$$\dot{q} = \frac{\partial q}{\partial \alpha}\dot{\alpha} + \frac{\partial q}{\partial D_\tau}\dot{D}_\tau = \gamma \frac{(1 - D_\tau)^2}{2}K_{pl}h(s - s_{pl}) - \frac{1}{2}\left[\tau_{y,0} + R\right]\dot{D}_\tau, \tag{4.59}$$

where the function $sign(\xi)$ is defined as

$$sign(\xi) = \begin{cases} -1 & \text{if } \xi \leq 0^- \\ +1 & \text{if } \xi \geq 0^+. \end{cases} \tag{4.60}$$

It should be highlighted that in Eqs.4.57-4.59 the following property is used

$$F = 0 \Rightarrow h(s - s_{pl})sign(\eta) = h(s - s_{pl}). \tag{4.61}$$

In fact, Eq. 4.46 results nil in two cases

1. if $s - s_{pl} = s_{el} = 0$, which means that $\tau = 0$ and the x-axis is reached. In such situation $h(s - s_{pl}) = 0$, thus

$$sign(\eta)h(s - s_{pl}) = 0 \quad \forall \eta \in \mathbb{R}; \tag{4.62}$$

2. if

$$\tau = 2\frac{(1 - D_\tau)}{2}\left[\tau_{y,0} + K_{pl}\alpha\right]h(s - s_{pl}), \tag{4.63}$$

which means that the upper yielding limit is reached (i.e. $\tau > 0$). Hence, without loss of generality it is possible to write that the upper bound of the yielding function is

$$\tau_y = (1 - D_\tau)\left[\tau_{y,0} + K_{pl}\alpha\right]. \tag{4.64}$$

Comparing Eqs. 4.63 and 4.64 and excluding the case stated at the former point 1, it follows that $s - s_{pl} \geq 0$ (where the equal sign stands for the complete failure of the interface), then $h(s - s_{pl}) = 1$ and η can be written as follows

$$
\begin{aligned}
\eta &= 2\frac{(1 - D_\tau)}{2}\left[\tau_{y,0} + K_{pl}\alpha\right] - \frac{(1 - D_\tau)}{2}\left[\tau_{y,0} + K_{pl}\alpha\right]h(s - s_{pl}) \\
&= \frac{(1 - D_\tau)}{2}\left[\tau_{y,0} + K_{pl}\alpha\right] = \frac{1}{2}\tau_y \,,
\end{aligned}
\tag{4.65}
$$

with $sign(\eta) = +1$ and then

$$
sign(\eta)h(s - s_{pl}) = 1 \,. \tag{4.66}
$$

Finally, it is possible to state that, in those cases where the condition $F = 0$ is satisfied, Eqs. 4.62 and 4.66 can be condensed into the property of Eq. 4.61.

Similarly to Eqs. 4.57-4.59, the evolution laws for the damage parameters are obtained through the normality rule applied to the damage dissipative potential ψ_{DMG}, which is defined so to allow the following relationship for the bond strength related damage (Fig. 4.24a)

$$
\dot{D}_\tau = -\frac{\partial \psi_D}{\partial Y_\tau} = -\frac{\partial \psi_{DMG}}{\partial Y_\tau} = -\frac{\langle \dot{s} \rangle_- h(\tau_{y,0} - \tau_y)}{s_{f,u}}g(s)f(\tau) \,,
$$
$$
\text{with } D_\tau < \min\left[1, \int\limits_0^t \dot{D}_\tau dt\right] \,,
\tag{4.67}
$$

where $\langle \cdot \rangle_-$ are the Macaulay brackets selecting the negative part of a quantity and $h(\tau_0 - \tau_y)$ accounts for the absence of damage along the initial linear elastic branch of the interface law. The two functions $g(s)$ and $f(\tau)$ (here assumed constant and equal to 1) provide respectively the displacement crack nucleation threshold and the fatigue limit stress. Further, $s_{f,u}$ is a parameter called "*fatigue endurance slip*" that can be defined as the sum of the unloading displacement allowed prior to fatigue failure. From a different but complementary standpoint, $s_{f,u}$ can be regarded as a scaling parameter that rules the effects of fatigue on the actual bond strength (i.e. the yielding stress τ_y). Eq. 4.67 directly imply that the bond strength related damage evolves only during the cyclic unloading branches. The damage part of the dissipative potential should also satisfy, given an instant $t = \tilde{t}$,

the following evolution law (Fig. 4.24a)

$$\dot{D}_K = -\frac{\partial \psi_D}{\partial Y_K} = -\frac{\partial \psi_{DMG}}{\partial Y_K} = -\frac{\tau_y^{rel} \langle \dot{s}_{pl} \rangle_-}{K_{el,0} \left(s^{rel} - s \right)^2},$$

$$\text{with } D_K < \min \left[1, \int_0^t \dot{D}_K dt \right], \tag{4.68}$$

with the further condition

$$\text{if } D_K > D_K^{lim}, \text{ then } D_K = 1, \tag{4.69}$$

where s is the current slip and $(\tau_y^{rel}(\hat{t}), s^{rel} = s(\hat{t}))$ is the last softening point attained (i.e. the last upper yielding limit reached) at the time $\hat{t} \leq \tilde{t}$. In other words, $\tau_y^{rel}(\hat{t})$ and $s^{rel} = s(\hat{t})$ are the yielding stress and the relative slip set at the time $\hat{t} \leq \tilde{t}$ at the end of the last softening process (i.e. at the end of the former loading/reloading phase where a plastic flow occurs, thus when $\dot{\alpha} \neq 0$ and the yielding stress changes because of R, Fig. 4.24a). Further, the limit value D_K^{lim} for the stiffness related damage parameter reads

$$D_K^{lim} = 1 + \lambda \left(1 - D_\tau \right)^2 \text{ with } \lambda = \frac{K_{pl}}{K_{el,0}}. \tag{4.70}$$

From Eqs. 4.67, 4.68 it is trivial to determine that for both the damage parameters the non-negativity of the increments is satisfied [104], i.e. $D_i \geq 0$ for $i = \tau, K$.

The plastic multiplier can be defined considering the persistency condition [133]

$$\text{if } F = 0 \text{ then } \gamma \dot{F} = 0. \tag{4.71}$$

Recalling the chain rule of derivation ($\dot{\xi}(\eta) = (\partial \xi / \partial \eta)(\partial \eta / \partial t)$) it is obtained

$$\dot{F} = \frac{\partial F}{\partial \tau} \dot{\tau} + \frac{\partial F}{\partial \alpha} \dot{\alpha} + \frac{\partial F}{\partial D_\tau} \dot{D}_\tau + \frac{\partial F}{\partial D_K} \dot{D}_K. \tag{4.72}$$

Further, noting that $\partial \left| \bullet \right| / \partial t = sign(\bullet)$ and $h(\xi)^2 = h(\xi)$ and using Eqs. 4.57, 4.58, 4.67

and 4.68, the following relationship holds

$$
\begin{aligned}
\dot{F} ={}& sign(\eta)(1 - D_K)K_{el,0}(\dot{s} - \dot{s}_{pl}) + \cdots \\
&\cdots - \left[sign(\eta)\frac{(1 - D_\tau)}{2}K_{pl}h(s - s_{pl}) + \frac{(1 - D_\tau)}{2}K_{pl}h(s - s_{pl}) \right] \cdots \\
&\cdots \gamma(1 - D_\tau)h(s - s_{pl}) - \underbrace{\left[\frac{1}{2}sign(\eta)\left[\tau_{y,0} + R \right]h(s - s_{pl}) + \cdots \right.}_{\text{A}} \\
&\cdots \underbrace{\left. + \frac{1}{2}\left[\tau_{y,0} + R \right]h(s - s_{pl}) \right] \frac{\langle \dot{s} \rangle_- h(\tau_0 - \tau_y)}{s_{f,u}}g(s)f(\tau) + \cdots}_{\text{A}} \\
&\cdots + \underbrace{sign(\eta)K_{el,0}(s - s_{pl})\frac{\tau_y^{rel}(\hat{t})\langle \dot{s}_{pl} \rangle_-}{K_{el,0}\left(s^{rel} - s \right)^2}}_{\text{B}} \,.
\end{aligned}
\tag{4.73}
$$

Before reaching the analytical expression for γ it is necessary to consider the following remarks. The persistency condition holds when $F = 0$, hence the property of Eq. 4.61 is still valid. Moreover, during an unloading phase $\dot{s} < 0$ (i.e. $\langle \dot{s} \rangle_- \neq 0$), the yielding criterion can be reached only if $(s - s_{pl}) = 0$ and $h(s - s_{pl}) = 0$. Conversely, if $(s - s_{pl}) > 0 \Rightarrow h(s - s_{pl}) \neq 0$ (i.e. $\tau \to \tau_y$) and the yielding condition can be reached only for loading processes, namely $\langle \dot{s} \rangle_- = 0$. Thus, $F = 0$ means that either $h(s - s_{pl})$ or $\langle \dot{s} \rangle_-$ should be nil and the term pointed out with **A** in Eq. 4.73 is nil as well. Similarly, the term **B** is zero because when $F = 0$, either $(s - s_{pl})$ or $\langle \dot{s}_{pl} \rangle_-$ (note that this is more restrictive than $\langle \dot{s} \rangle_-$) are nil. To sum up, the aforesaid property can be stated as follows

$$
F = 0 \Rightarrow (s - s_{pl})\langle \dot{s} \rangle_- = 0 \,.
\tag{4.74}
$$

Finally, Eq. 4.73 can be reduced to

$$
\dot{F} = sign(\eta)(1 - D_K)K_{el,0}(\dot{s} - \dot{s}_{pl}) - \gamma(1 - D_\tau)^2 K_{pl}h(s - s_{pl})
\tag{4.75}
$$

Eq. 4.71 leads, when a plastic flow occurs (i.e. $\gamma \neq 0$), to the condition $\dot{F} = 0$, then from Eq. 4.75 is obtained the following

$$
\begin{aligned}
\gamma &= \frac{(1 - D_K)K_{el,0}}{K_{el} + (1 - D_\tau)^2 K_{pl}h(s - s_{pl})}\dot{s}\,sign(\eta) \\
&= \frac{(1 - D_K)K_{el,0}}{(1 - D_K)K_{el,0} + (1 - D_\tau)^2 K_{pl}h(s - s_{pl})}|\dot{s}| \geq 0 \,.
\end{aligned}
\tag{4.76}
$$

Note that the non-negativity of the plastic multiplier required by the Kuhn-Tucker conditions (i.e. $\gamma \geq 0$) is automatically guaranteed by the condition $D_K \leq D_K^{lim}$ of Eq. 4.70, which now finds its justification. Hence, keeping in mind that K_{pl} is a negative plastic modulus, for $D_K \geq D_K^{lim}$ the denominator of Eq. 4.76 becomes non positive.

In Fig. 4.24a the resulting interface law and the evolution of the main parameters are represented for the load history of Fig. 4.24b. Note that for monotonic load conditions the classical bilinear interface law and the corresponding results are recovered. The proposed model requires calibration of the monotonic bilinear interface law, and of the additional parameter $s_{f,u}$ that controls the fatigue endurance. The physical meaning of this parameter enables its calibration with experimental observations.

4.5.2 Incremental solution via FDM approach

The proposed interface model can be implemented into a code similar to the one described in detail for the pure shear model (see par. 4.2). The only formal difference is that, instead of the absolute quantities $\boldsymbol{y}(x_i)$ and $\boldsymbol{\alpha}$ and K_{sec}, the time-incremental quantities $\Delta\boldsymbol{y}(x_i)$ and $\Delta\boldsymbol{\alpha}$ and K_{tg} should be used. Indeed, since the actual response of the interface does not depend only on tha actual stress state but also from the load history [133], a time incremental approach is used here associated with the classical finite difference method (FDM) for the space decomposition.

For the complete description of the FDM approach see par. 4.2 and App. A. For the time decomposition, it is assumed that that the solution at the ith time step (i.e. at the time t) is known. Once an increment of the driving variable is given, the solution at the time step $i + 1$ (i.e. at the time $t + \Delta t$ where Δt is a finite quantity) can be obtained confusing the correct solution of a general quantity $\xi(t + \Delta t)$ with its incremental approximation $\xi^{i+1} = \xi^i + \Delta t f(\xi^i) = \xi^i + \Delta\xi^{i+1}$. Nevertheless, in this case a so-called *return mapping algorithm* is needed. This latter is necessary in models using plasticity to determine at a given time step if a plastic flow occurs or not. Hence, in the numerical procedure finite increments of the variables are used in place of time derivatives as in the mathematical formulation (i.e. $(\partial \bullet /\partial t) = \dot{\bullet} \rightarrow \Delta\bullet = \bullet(t + \Delta t) - \bullet(t)$), thus violations of the Kuhn-Tucker condition $F \leq 0$ are possible (i.e. $F > 0$). For this reason a routine should be defined to compute the "finite" plastic multiplier $\Delta\gamma^{(i+1)}$ at the $(i + 1)^{th}$ time step so to obtain again $F = 0$. On the contrary, if $F < 0$ the system is considered as linear elastic and it is univocally determined. The complete description of the return

mapping algorithm is reported in App. C, restricting the analysis to quasi-static processes (i.e. when the inertial forces can be neglected). Moreover, in App. C it is also derived the expression for the tangential modulus K_{tg} to be employed in the numerical procedure.

4.5.3 Comparison with experimental results

Experimental data from Ko and Sato [4] and Carloni et al. [5] are used to validate the proposed model. In particular, the first tested variable amplitude cycles, while the in the latter constant amplitude load cycles were studied. For each test performed, a calibration procedure similar to what described in par. 4.3.6.1 was adopted. In particular, both studies performed also monotonic tests that were used as paradigmatic tests to highlight differences with the cyclic loading. Here, the maximum monotonic debonding force F_{max} is used to obtain the interface fracture energy Γ_f, while the monotonic bond strength $\tau_{y,0}$ and the slip at peak bond strength s_1 (Fig. 4.24a) are estimated from the published monotonic bond-slip curves. The ultimate slip s_2 follows from Γ_f and $\tau_{y,0}$, whereas the initial elastic stiffness $K_{el,0}$ is computed from $\tau_{y,0}$ and s_1. In absence of direct measurements, the parameter $s_{f,u}$ is calibrated from the cyclic experimental results.

4.5.3.1 Variable amplitude cycles - Ko & Sato [4]

Ko and Sato [4] investigated the bonding behavior of FRP strengthened concrete prisms under variable amplitude cyclic loadings changing three different parameters: the kind of fiber (aramid, carbon and polyacetal), the number of composite layers used (single or double layer) and the cyclic loading history. In particular, the authors adopted two different variable amplitude load history named Cyclic 1 and Cyclic 2, in both the cases each cycle involved complete unloadings (i.e. until $F = 0$). In the following, are analyzed the specimens subject to Cyclic 1 load history, where the first and second unloading corresponded respectively to 1/3 and 2/3 of the maximum monotonic load F_{max}. Then, each subsequent unloading took place every tenths of the ultimate monotonic displacement (i.e. every 1/10 of s_2). The specimens were composed of two FRP sheets glued on two opposite faces of a concrete block (double lap shear test), which was divided in two portions by a crack in the middle as initial notch (Fig. 4.25). Then, a pulling force was applied to both the concrete blocks by means of two embedded steel rebars (Fig. 4.25).

The bonded length for each specimen is l_b=300 mm while the FRP has a width of b_f=50 mm a Young's modulus E_f=261 GPa and an equivalent thickness t_f=0.167 mm.
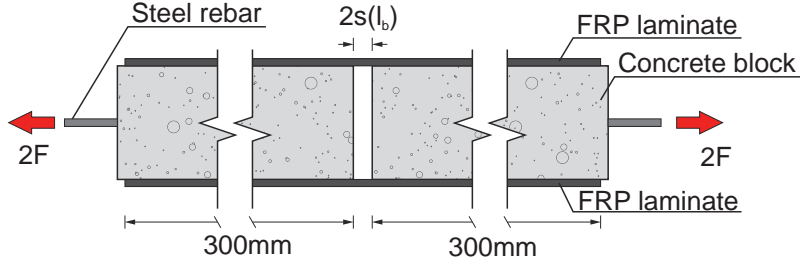
Figure 4.25: Scheme of the specimens used by Ko and Sato [4].

Table 4.6: Parameters adopted for cyclic analyses.

Test	$\tau_{y,0}$ [MPa]	$K_{el,0}$ [MPa/mm]	Γ_f [N/mm]	s_1 [mm]	s_2 [mm]	K_{pl} [MPa/mm]	$s_{f,u}$ [mm]
$\mathbf{C14}^{(1)}$	3.50	364.5	0.50	$9.6 \cdot 10^{-3}$	$2.9 \cdot 10^{-1}$	-12.25	3.0
$\mathbf{A25}^{(1)}$	2.25	364.5	0.80	$6.2 \cdot 10^{-3}$	$7.1 \cdot 10^{-1}$	-3.16	7.0
$\mathbf{A14}^{(1)}$	2.25	364.5	0.96	$6.2 \cdot 10^{-3}$	$8.5 \cdot 10^{-1}$	-2.64	8.5
$\mathbf{DS\text{-}F1}^{(2)}$	6.50	162.5	1.20	$4.0 \cdot 10^{-2}$	$3.7 \cdot 10^{-1}$	-17.60	30.0

[1] from Ko & Sato [4]; [2] from Carloni et al. [5]

The parameter used for the simulation of the specimens label with C14, A25 and A14 are summarized in Tab. 4.6.

In Fig. 4.26 are reported the comparisons between numerical and experimental results for the analyzed tests from [4]. A satisfactory agreement is observable, although the slip recovery at complete unloading is underestimated. This is because for a complete unloading (i.e. F=0) a residual slip at the loaded end would imply a constant value of slip along a portion of the plate (i.e. from the loaded end until the first undamaged section) because no strain variation would be present (otherwise a stress transfer would occurs). Anyway, this residual displacement applied to the undamaged part of the interface, in absence of friction or interlocking phenomena, would imply, in contrast with the assumption of zero force in the FRP, non-zero bond stresses in some portions of the glued length (because of its linear elastic behavior). Moreover, from Fig. 4.26d it is possible to observe how the global behavior changes with the model parameters (see Tab. 4.6).

In Fig. 4.27 the local numerical interface laws are reported for different points along the bonded length. The degradation of the interface stiffness is observable as well as a slight reduction of the ultimate slip attained in comparison with the monotonic law.
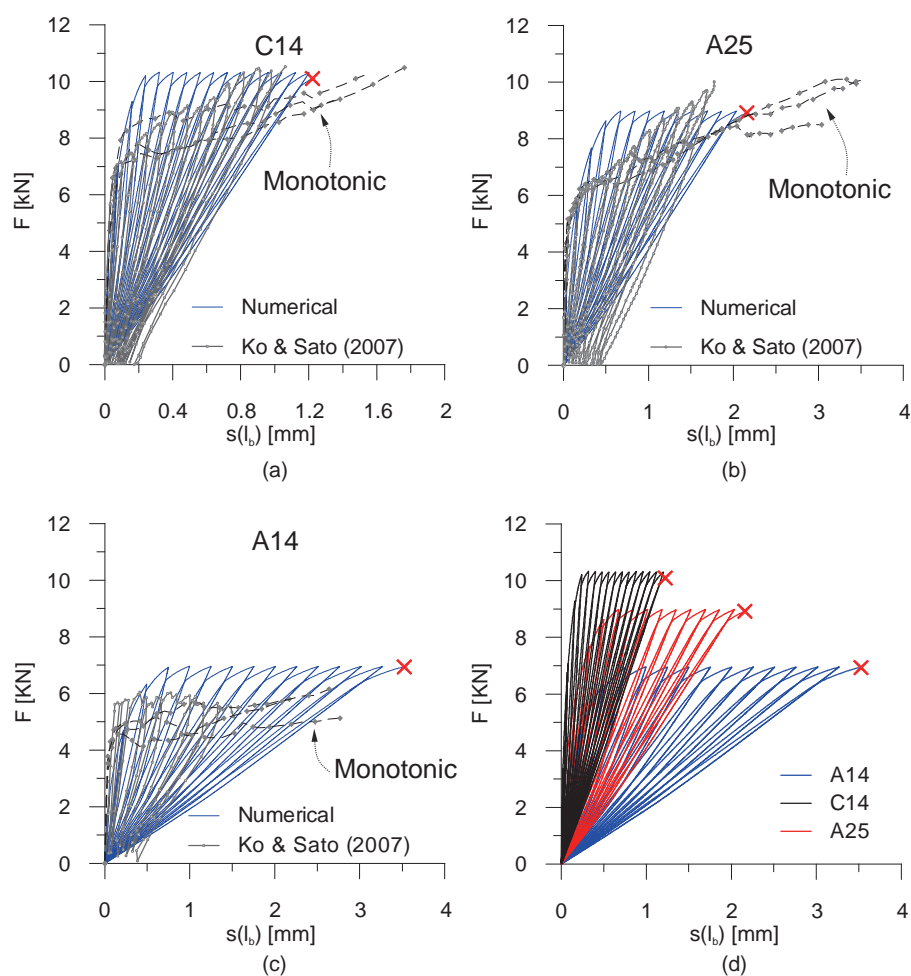
Figure 4.26: Tests from Ko and Sato [4]: (a) numerical vs. experimental pull-out curve for the test C14; (b) numerical vs. experimental pull-out curve for the test A25; (c) numerical vs. experimental pull-out curve for the test A14; (d) comparison between the numerical curves.

Moreover, it is possible to notice that the shape of the interface law in different locations is quite similar to the monotonic one. This fact is probably due by the high values of load attained during the tests. Hence, in this case the softening-plastic behavior, governing the monotonic response, prevail against the cyclic damage, i.e. the global behavior results more similar to the one observed during monotonic tests.
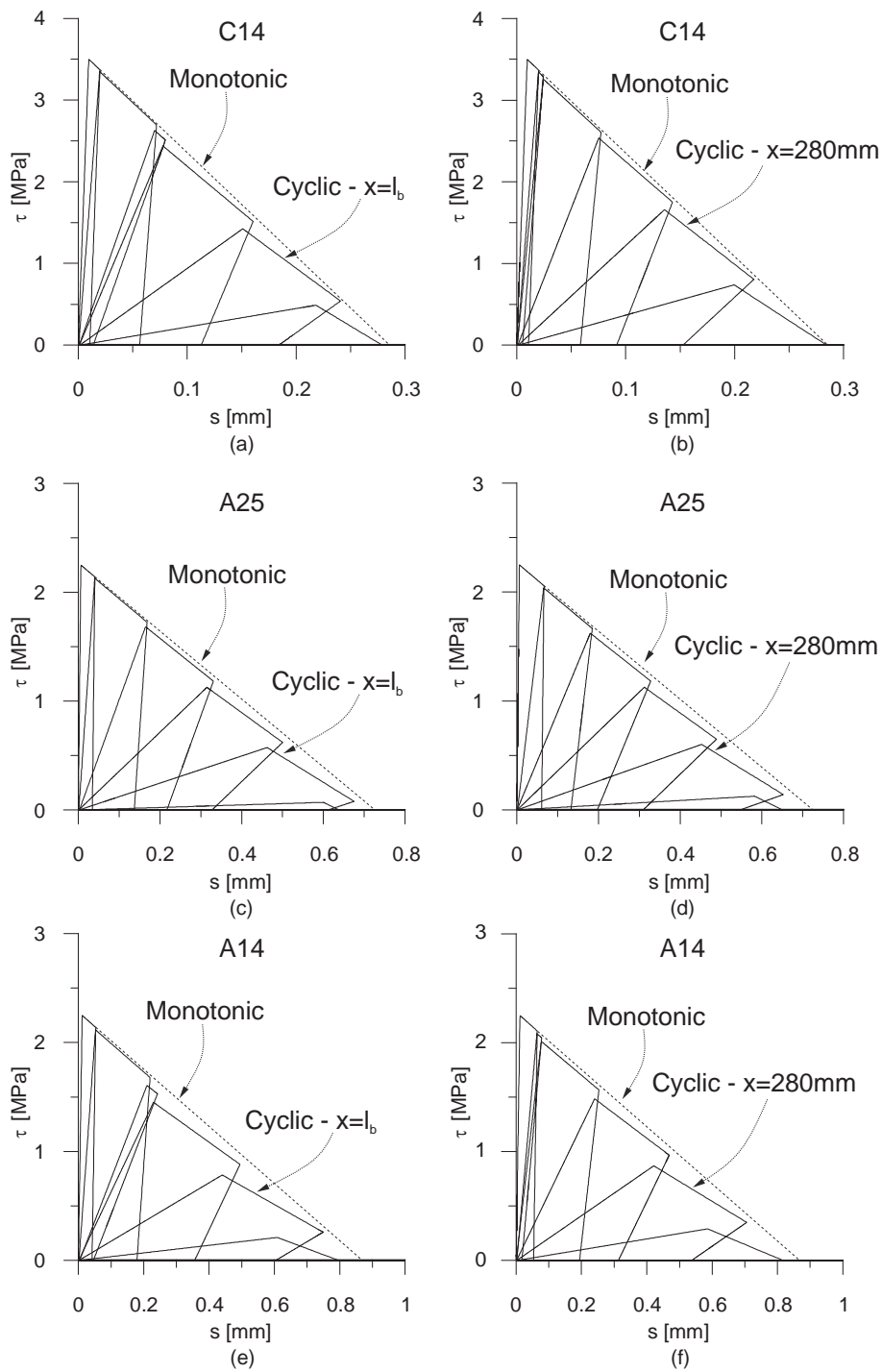
Figure 4.27: Numerical local interface laws for the specimens in Ko and Sato [4]: (a) loaded end point for test C14; (b) point at $x=280$ mm for test C14; (c) loaded end point for test A25; (d) point at $x=280$ mm for test A25; (e) loaded end point for test A14; (f) point at $x=280$ mm for test A14.

4.5.3.2 Constant amplitude cycles - Carloni et al. [5]

Carloni et al. [5] deeply investigate the deterioration of the bonding effectiveness under constant amplitude fatigue loadings using single lap shear test specimens, whose scheme is sketched in Fig. 4.28. The authors mainly focused on the role of the load amplitude on the fatigue life assessment, on the length of the stress transfer zone and on the post-fatigue monotonic behavior. In this case the bonded length and the reinforcement width are respectively l_b=152 mm and b_f=25 mm, while the composite Young's modulus is E_f=230 GPa with an equivalent thickness t_f=0.167 mm. The parameters use to simulate the test labeled with DS-F1 are reported in Tab. 4.6. For this specimen, the load history is characterized by a nominal amplitude of 4.75 kN with a mean load value of 3.63 kN (i.e., with a maximum and a minimum applied load respectively of 6.00 kN and 1.25 kN). The number of cycles prior to failure is N_f=1290.
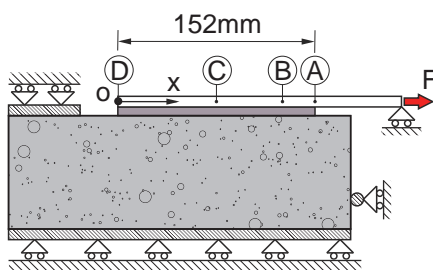
Figure 4.28: Scheme of the specimens used by Carloni et al. [5].

Fig. 4.29 shows the comparison between theoretical and numerical results for the test label with DS-F1 by Carloni et al. [5]. A very good agreement is observable for both the global equilibrium curve (Fig. 4.29a) and the trend of the loaded and free end displacements with the number of cycles (Fig. 4.29b). Moreover, the number of cycle to failure is well reproduced considering the high scattering of the results usually highlighted for the FRP tests [4, 5, 95]. Indeed, the numerically predicted value is $N_{f,num}$=1149 (Fig. 4.29b), which means a tolerance of the 10% with respect to the experimental evidence. Finally, a slight underestimation of the free end displacement is still visible (Fig. 4.29), but is less relevant than the one observed for the Ko and Sato [4] specimens in Fig. 4.26a-c.

In Fig. 4.30 the numerical local interface laws are depicted at different locations along the bonded length (indicated with A-B-C-D in Fig. 4.28). An embrittlement of the local cyclic behavior with respect of the monotonic behavior is observed (Fig. 4.30), however
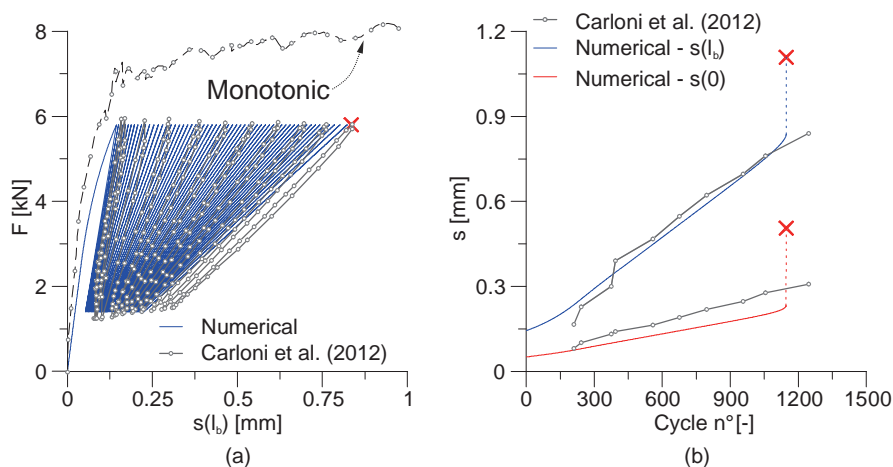
Figure 4.29: Numerical vs. experimental results for the specimen DS-F1 in Carloni et al. [5]: (a) global pull-out curve (1 cycle every 20 is plotted for clarity) and (b) loaded and free end displacement vs. number of cycles.

this does not affect significantly the maximum attained displacement which is close to the monotonic one (Fig. 4.29a). Moreover, comparing the four curves for the points A-D is it interesting to note that the local interface law has a significantly different shape from the (triangular) monotonic curve near the loaded end, whereas this difference is less pronounced in the central part of the glued length (Figs. 4.29b,c). Further, in the central part of the plate (i.e. Figs. 4.29b,c are very similar) the behavior is significantly different from the loaded (Fig. 4.29a) and free end (Figs. 4.29d). In particular, at the loaded end a large softening phase is noticeable during the first cycle (Fig. 4.29a) while at the free end the interface remains in the linear elastic regime until the complete failure of the joint (Fig. 4.29d), namely until the maximum force in a cycle cannot be sustained any more by the remaining glued length.

4.5.4 Conclusive comments

The performed tests proved that the proposed model is able to reproduce the cyclic behavior of FRP reinforcements externally bonded on quasi-brittle materials. In particular, the capability to correctly reproduce the fatigue behavior in case of variable as well as constant amplitude load cycles has been demonstrated. However, a slight underestimation of the slip recovery is noticed, especially in case of complete unloading as a result of the assumed absence of friction and interlocking effects. The number of cycles prior to failure
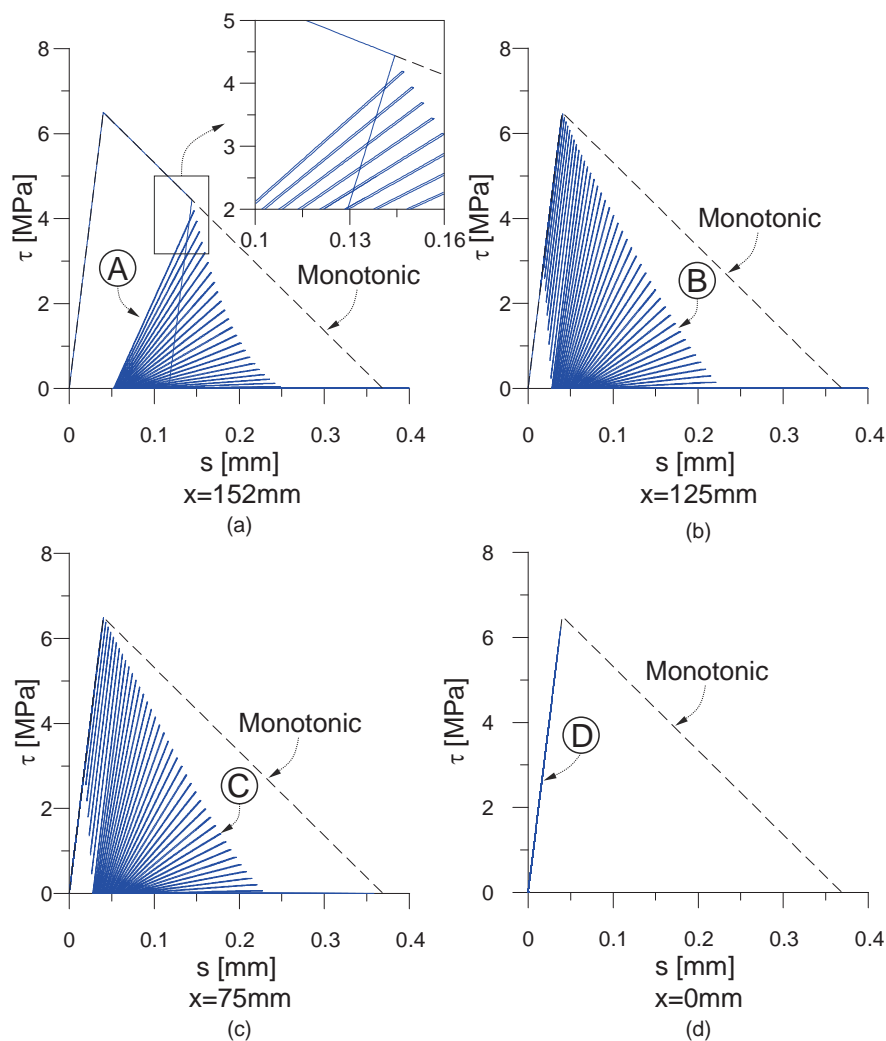
Figure 4.30: Numerical local interface laws for the points A-D highlighted in Fig. 4.28 for the specimen DS-F1 in Carloni et al. [5] (1 cycle every 10 is plotted for clarity): (a) point A - x=152 mm (loaded end); (b) point B - x=125 mm; (c) point C - x=75 mm; (d) point D - x=0 mm (free end).

is well predicted, and so is the global behavior observable from the global pull-out curves. The maximum and minimum displacements attained during the cycles are satisfactorily reproduced and the number of cycles prior to failure are in good agreement with the experimental results. An effect of embrittlement of the local interface laws with respect to the monotonic law is observed. This, however, seems to exert a limited influence on the maximum displacement attained, which is similar to the one reached under monotonic

conditions. Finally, comparing the numerical interface laws at different locations along the bonded length, it is possible to observe a change in the local behavior near the loaded-end with respect to the points along the central part of the glued length as well as in comparison with the monotonic law. Differently, at the free-end, the numerical curves reveal that no softening takes place before the complete failure of the glued joint.

The proposed thermodynamically consistent model requires the calibration of only one parameter $s_{f,u}$ (namely, the fatigue endurance parameter), in addition to the monotonic mode-II interface law (here Γ_f, $\tau_{y,0}$ and s_1). The physical meaning of $s_{f,u}$ as the sum of the unloading displacements allowed prior to complete dobonding, enables its calibration with experimental observations.

While more analyses are needed to confirm the obtained results, the approach presented appears to be a very promising tool to study the fatigue life of bonded joints. A simple calibration of the fatigue endurance parameter using a relative small number of experimental tests would allow the extension of the prediction of the fatigue behavior of a bonded joint to conditions different from the tested ones.

5

Design of FRP-masonry reinforcement

Abstract

In the present section a statistical assessment of a new design procedure to estimate the resistance against debonding of composite fabrics externally glued on masonry substrates is presented. Based on recent experimental campaigns, a database on bond test results between fiber reinforced polymer and masonry is collected and, after an overview of the design rules at disposal, an alternative formula is proposed starting from theoretical and experimental evidence. The main parameters influencing the ultimate load are defined through a correlation analysis and different assessment approaches are accounted for. Finally, the capabilities of the proposed approach are evaluated and the advantages with respect to existing formulas are discussed.

5.1 Introduction

In common practice, the employment of fiber reinforced polymers (FRP) as external reinforcement is based on several empirical and semi-empirical design formulas. Installation rules, design principles and loads, safety requirements and acceptable properties for the employed materials are coded in different guidelines (e.g. [8–11]).

Numerical and analytical investigations (such as [24, 40, 41, 53, 54, 66, 83, 86, 116, 127, 136–140] among others) provided parametric relationships able to define the resistance against debonding as a function of the main parameters involved. Most of the practical design rules available to date (e.g. [8, 9]) were based on such studies where empirical coefficients calibrated on experimental results (such as [1, 3, 33, 38, 58, 59, 62, 94, 141]

5. DESIGN OF FRP-MASONRY REINFORCEMENT

among others) are introduced [142–144].

Differently than concrete substrates, whose design rules were calibrated on a wide number of tests, for masonry only a limited number of studies are available in the literature. The lack of knowledge is even worsened by the intrinsic high heterogeneity of the material and by the possible variety of "masonry". Indeed, the term "masonry" can represent the brick units, the units joined with different kinds of mortar (namely masonry blocks) and a wide variety of units (i.e., artificial clay bricks or natural stone such as tuff, limestone and calcareous stone). Only the Italian guideline CNR-DT 200 [8] provides a section specifically devoted to the design of composite reinforcements applied to masonry including relationships calibrated on a database of FRP-masonry bond tests. Nevertheless, the adopted database was not as large as the one available for concrete and in the last period a number of new results on the subject have appeared in the literature.

Furthermore, as debated in par. 2.4, the test setup adopted to characterize the bond behavior may have a great influence on the final results (see par. 2.4 for a review of the setup-related problems). Stating the wide variety of setups proposed in literature [3, 30, 58], calibration of design rules has not to be independent from the test setup used to obtain experimental data. This limit once more the number of results available to calibrate design rules, which thus can lead to incorrect or anti-economical predictions of the strength of the reinforcements. In par. 3.3.3.5 it has been demonstrated the lack of accuracy of the guideline [7], highlighting the need of new design rules.

Taking advantage of new experimental studies (in particular the evidence illustrated in par. 3.3) and starting from theoretical considerations, in the present section the practical design of FRP reinforcements applied on masonry substrates is improved by means of statistical methods.

To the purpose, a database of bond tests is collected and, after an overview of the design formulas at disposal, a correlation analysis is performed in order to define the major parameters influencing the debonding phenomenon. Then, alternative design formula for the prediction of the mean value of the maximum debonding force F_{max} is statistically assessed and its characteristic value (i.e. within a confidence interval of the 95%) is derived by the "design assisted by testing" approach suggested in [20]. Finally, the proposed approach is statistically compared with other design formulas nowadays available (in particular [8] and those illustrated in the following par. 5.2) and its advantages are debated.
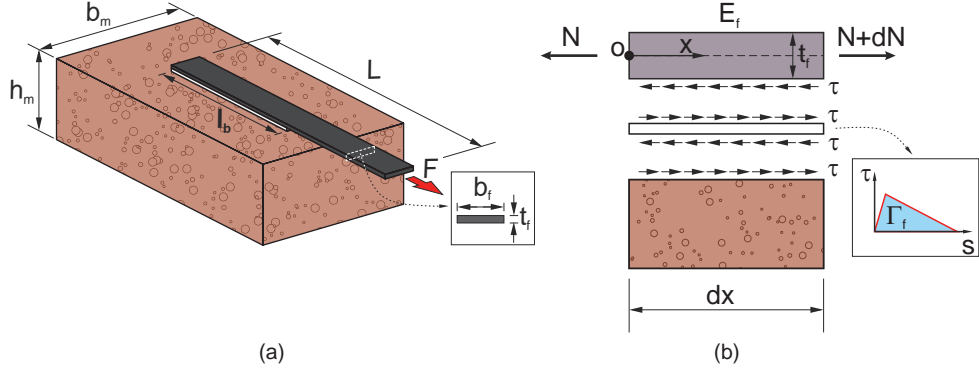
Figure 5.1: (a) Geometry of a generic test specimen. (b) Equilibrium of a portion of FRP reinforcement.

5.2   Overview of some existing capacity models

An overview of the existing design formulas at disposal, which will be used for comparison with experimental results, is presented. The adopted notation is given in Fig. 5.1. Assuming as rough approximation and for comparisons matters only that the main processes related to the debonding failure are common in concrete and in masonry substrates, in the present overview have been included also rules originally proposed for FRP-concrete glued joints, i.e. [9–13]. This choice is mandatory since the lack of relationships in the common design practice specifically proposed for masonry (the only exception is [8]). Moreover, as a matter of fact, in the past, some guidelines (e.g. the 2004 version of the CNR-DT200 guideline [7]) adjusted to masonry the design principles developed for concrete substrates [141].

CNR-DT 200/2012   In the Italian guideline [8], two distinct rules for masonry and concrete are proposed which differ only for the empirical coefficients statistically assessed. The maximum debonding force is calculated using the same formula deduced in par. 2.1.1, as

$$F_{\max,CNR} = b_f \sqrt{2 E_f t_f \Gamma_{f,CNR}} \, , \tag{5.1}$$

where $\Gamma_{f,CNR}$ is the mode-II interface fracture energy given by the semi-empirical formula

$$\Gamma_{f,CNR} = k_G k_{b,CNR} \sqrt{f_{cm} f_{ct}} \, , \tag{5.2}$$

where k_G is an experimentally calibrated coefficient, whose main value in absence of specific tests can be assumed equal to 0.093 for the clay bricks, 0.157 for the tuff stone elements and

0.022 for the calcareous (or calcarenite) stone and limestone units. The term $\sqrt{f_{cm}f_{ct,th}}$ is defined as twice the cohesion calculated adopting a Mohr-Coulomb criterion [143] to take into account the longitudinal confinement stresses arising from the bond stress diffusion into the substrate [79, 143]. The width coefficient $k_{b,CNR}$ takes into account the transversal diffusion effect related to the width ratio $\lambda_w = b_f/b_m$ [25, 94]

$$k_{b,CNR} = \sqrt{\frac{3 - \lambda_w}{1 + \lambda_w}}\,. \tag{5.3}$$

For lower values of λ_w the bond stress can propagate in a larger width than that of the plate, involving a certain volume aside of the glued area and resulting thus in an higher fracture energy [79, 141] and in a three dimensional failure mechanism as stated in par. 3.3. Approaching $\lambda_w = 1$ this effect vanishes. The tensile strength of the substrate f_{ct}, if not directly estimated, can be assumed equal to

$$f_{ct} = f_{ct,th} = 0.1 f_{cm}\,. \tag{5.4}$$

JSCE 2001 The Japanese Society of Civil Engineers (JSCE) guideline for FRP-concrete bonded joints [11] defines the maximum allowed tensile stress in the reinforcement prior to debonding as

$$\sigma_{f,\max,JSCE} = \sqrt{\frac{2\Gamma_{f,JSCE}E_f}{nt_f}}\,, \tag{5.5}$$

where n is the number of applied FRP layers. Eq. 5.5 leads straightforward to Eq. 5.1 for $n = 1$, since the theoretical basis for the two codes is the same. However, in the JSCE approach the fracture energy can be kept constant and equal to $\Gamma_{f,JSCE} = 0.5$ N/mm as suggested by [11] or can be deduced using the Wu and Niu equation [145] $\Gamma_{f,JSCE} = 0.644 f_{cm}^{0.19}$. Differently from [8], the two formulas are completely empirical and calibrated on a FRP-concrete test database.

ACI 440.2R-08 (2008) Based on a FRP-concrete database, the ACI guideline for the reinforcement of concrete members with externally glued FRPs [10], empirically defines the resistance against debonding as

$$F_{\max,ACI} = E_f t_f b_f \varepsilon_{f,\max,ACI} = 0.41 b_f \sqrt{\frac{E_f t_f f_{cm}}{n}} \leq 0.9 \varepsilon_{f,ult} E_f t_f b_f\,. \tag{5.6}$$

where $\varepsilon_{f,ult}$ and $\varepsilon_{f,\max,ACI}$ are respectively the maximum tensile and the debonding-limit strains in the reinforcement and n is the number of applied layers.

***fib* bulletin 14 (2001)** The *fib* code [9] modified a model originally proposed by Neubauer and Rostasy [146], which, in turn, is based on the studies of Holzenkämpfer [147]. In [9] two coefficients were added: α_{fib} encompassing the detrimental effects of shear cracks ($\alpha_{fib} = 0.9$ in members liable to wide shear cracks, 1 otherwise) and k_c, equal to 0.67 or 1 respectively for low or normal compacted gluing surfaces. The FRP-concrete maximum debonding force is computed as

$$F_{\max,fib} = \alpha_{fib} c_1 k_c k_{b,Nied.} b_f \sqrt{E_f t_f f_{ctm}}, \tag{5.7}$$

where $c_1 = 0.64$ is an empirical coefficient estimated using a database of CFRP-concrete tests by Neubauer and Rostasy [146]. The width coefficient $k_{b,Nied.}$, originally defined by Niedermeier [13], is

$$k_{b,Nied.} = 1.06 \sqrt{\frac{2 - \lambda_w}{1 + \frac{b_f}{400}}} \geq 1, \tag{5.8}$$

which holds for $\lambda_w \geq 0.33$. In the following analysis it is assumed that $\alpha_{fib} = k_c = 1$ and, since in the *fib* code [9] no theoretical relation for the tensile strength is provided, Eq. 5.4 is applied.

Chen & Teng model (2001) Chen and Teng [12] estimate the maximum force attainable in a FRP-concrete glued joint as

$$F_{\max,C-T} = \alpha_{C-T} k_{b,C-T} b_f \sqrt{t_f E_f \sqrt{f_{cm}}} \quad \text{with} \quad k_{b,C-T} = \sqrt{\frac{2 - \lambda_w}{1 + \lambda_w}}. \tag{5.9}$$

The coefficient α_{C-T} was calibrated on a database of FRP-concrete bonded joint leading to a mean value of 0.427.

Niedermeier model (1996) Niedermeier [13] introduced a modified version of the Holzenkämpfer model [147], which predicts the maximum force transmissible by a glued FRP joint as

$$F_{\max,Nied.} = 0.78 b_f \sqrt{2 E_f t_f \Gamma_{f,Nied}} \quad \text{with} \quad \Gamma_{f,Nied.} = c_{f,N-R} k_{b,Nied.}^2 f_{ct}, \tag{5.10}$$

in which the width coefficient is reported in Eq. 5.8. The coefficient $c_{f,N-R} = 0.204$ was proposed by Neubauer and Rostasy [146] using a series of 51 CFRP-concrete double lap shear tests. Since the value of the experimental strength of the substrate is not usually available in the design practice, here Eq. 5.4 was applied.

5.3 Database of FRP-masonry pull-out tests results and comparison with design formulas

In order to propose reliable rules for the design of the externally glued FRP reinforcements on masonry substrate, a database of pull-out test results from different experimental campaigns was collected and used to assess the design formulas at disposal as well as the new ones proposed here. Statistical comparisons between the maximum debonding force calculated with the design rules ($F_{max,th}$) and obtained in experimental tests ($F_{max,exp}$) were performed (see par. 5.3.2 for a description of the database). A total of 399 tests from literature have been collected and analyzed [32, 33, 38, 58, 68, 89, 92, 141, 148–156]. The database is reported in App. D, whilst selection criteria are stated in par. 5.3.1 and the classification rules are reported in par. 5.3.2.

5.3.1 Selection criteria of the experimental results

The first aspect taken into account in collecting the data was the type of masonry substrate: only the tests on clay brick units, tuff blocks and limestones or calcareous stones as supports were investigated, and the statistical analysis was performed separately for each type. Moreover, given the existing wide variety of masonry bond patterns only tests on units were considered. In fact, the bond between units can differ by many features: the composition of the mortar (e.g. lime or concrete based mortar), the dimension of the joints and units (in particular, the development of L_{eff} can be allowed or not within two subsequent mortar joints), the texture of the surface (e.g. in relation to the longitudinal or extrusion direction for clay bricks and to the stratification plane for natural stones), the angle in the bonding plane between the longitudinal axes of the reinforcement and the joints. Unfortunately, the number of experimental tests available is not sufficient to encompass all these variables. Some recent studies [37, 141] highlighted that the presence of mortar joints along the bonding plane seems to do not deeply affect the ultimate pulling force. Nevertheless, mortar joints seem to trigger a peculiar local behavior because of the heterogeneities they introduce along the bonding plane [32, 37] (see also par. 3.3.3.3). Indeed, oscillations in the strain profiles were observed similarly to what happens in FRP reinforced concrete in correspondence of big aggregates [36]. To date it is not clear if such localized effects can involve also changes in the global behavior (i.e. in the maximum

pulling force) under different circumstances than those accounted in the aforementioned studies, thus this issue needs further and deeper investigations.

In the database, only results coming from SLS and DLS tests were collected (see par. 2.4 for an overview of the test setups), since they are less influenced by the problems highlighted in par. 2.4 respect to beam setups. Furthermore, to limit the presence of tests where the maximum debonding force attainable is not reached (i.e. for $l_b < L_{eff}$) data from specimens with bonded length shorter than 100mm were discarded. Were excluded from the database also those tests where auxiliary anchorages of the FRP were employed (i.e., enclosures, bolts or steel and composite plates) or more than one layer of composite was applied. Finally, only results of tests where the joint interface was mainly subject to shear stresses and that displayed debonding failure with removal of a layer of substrate material were used, i.e. no mixed mode tests or specimens showing failure due to delamination or fiber tensile rupture were accounted.

5.3.2 The bond tests database

Width b_f, bonded length l_b, thickness t_f and Young's modulus E_f of the composite declared by the authors were taken into account. In the calculations the FRP nominal thicknesses provided by the producers and reported in the published papers $t_f = t_{f,eq}$ were adopted (i.e., the thickness of solely fibers providing mechanical properties equal to the matrix-fibers laminate), since the effective thickness is usually unknown during the design phase. Results obtained with different types of fibers were examined: carbon (C), glass (G), basalt (B) and steel (S).

Concerning the support prisms, the cross-section dimensions (width b_m and height h_m) were exploited for the analysis together with the mechanical parameters such as the Young's modulus E_m, the compressive strength f_{cm} and, if estimated, the experimental tensile strength $f_{ct,exp}$. The latter was employed only for comparison purposes since in the common practice the tensile strength is not usually tested directly but it is computed starting from the compressive strength using theoretical or empirical relationships. The frequency distributions f of the various parameters related to the FRP and to the masonry support are reported in Fig. 5.2 for the clay brick specimens. It is possible to observe that the bonded length l_b of the 92.8% of the tests falls between 150 and 170 mm (Fig. 5.2b), which is a quite well accepted upper limit for the effective bonded length on masonry

[8, 141]. The values of $E_f t_f$ of the majority of the results is between 10 and 100 kN/mm (Fig. 5.2c), which are common values for FRP fabrics applied with the wet lay-up method.
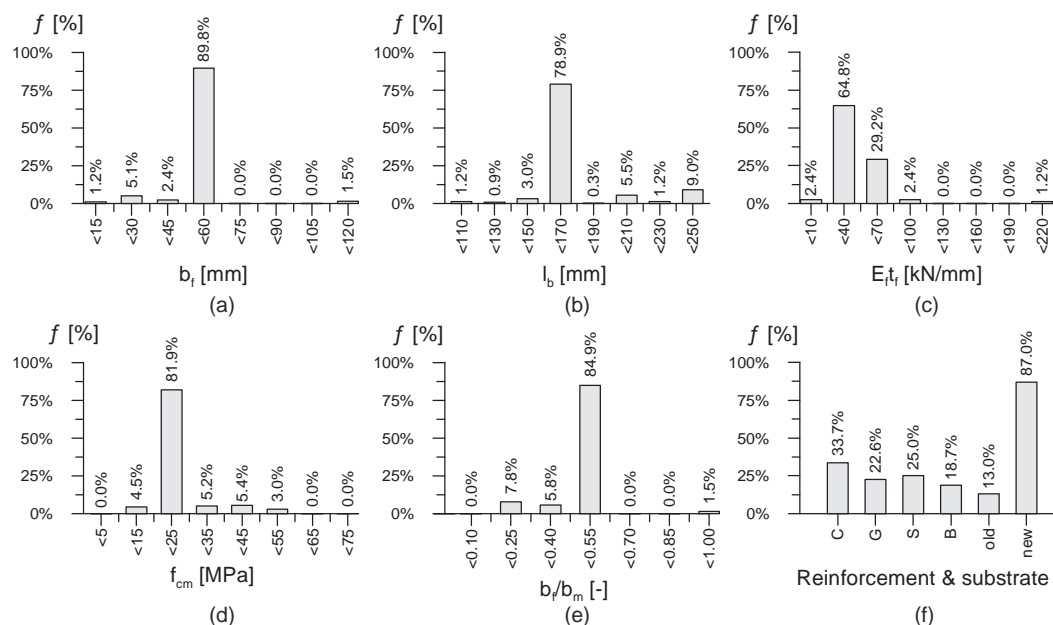
Figure 5.2: Distributions of the frequency f of the main parameters of the collected database for the clay brick specimens: (a) plate width; (b) bonded length; (c) reinforcement stiffness per unit width; (d) compressive strength of the substrate; (e) width ratio; (f) different kinds of substrate and reinforcements (*C - Carbon FRP; G - Glass FRP; B - Basalt FRP; S - Steel RP; old - ancient bricks; new - recent bricks*).

In Tab. 5.1 the number N of collected tests and the range of variation of the analyzed parameters are reported each type of substrate. These values have to be intended as limits for the application of the proposed formulas. The compressive strength of the bricks varies in a large range (from 7.3 to 50.9 MPa) due to the different varieties of clay masonry substrates. Ancient and industrial bricks were grouped into a single class, although recent studies [38, 141, 148] pointed out differences in behavior between them related to capability of the glue to penetrate into the substrate. This aspect needs some further investigations to be quantitatively taken into account and is out of the scopes of the present study.

Natural stones were subdivided in two main groups as also suggested in [8]: tuff and calcareous stone or limestone (e.g. leccese stone). In fact, some studies [68, 89, 140, 143, 154] revealed that these two kinds of stones are definitely not comparable from the bond

Table 5.1: Range of variation of the main parameters of the tests taken into account for the database.

Support material	N [-]	l_b [mm]	b_f [mm]	t_f [mm]	$E_f t_f$ [kN/mm]	λ_w [-]	f_{cm} [MPa]
Clay brick	332	100-250	12-117	0.097-1.200	8.8-192.0	0.12-0.98	7.3-50.9
Tuff	27	150-245	80-123	0.164-0.480	27.6-45.5	0.40-1.00	4.41-5
Limestone	40	150-246	80-129	0.130-0.370	27.6-45.5	0.40-1.00	2.3-70.0

Table 5.2: Range of variation of the reinforcement stiffness per unit width of the various kinds of fibers considered.

Fiber type	Carbon - C	Glass - G	Basalt - B	Steel - S
k_f range [kN/mm]	37.7-192.0	8.8-27.6	12.4	11.4-45.0

capacity standpoint since their very different mechanical and physical properties. Indeed, Tab. 5.1 highlights that tuff, being a very porous material developed by consolidation of volcanic eruption ashes, is usually weaker than calcareous stone and limestone that, on the contrary, are very compact materials composed of a calcium-carbonate matrix precipitated from leaking water and solidifying an initially incoherent mass composed by calcareous and quartz particles.

The reinforcement stiffness per unit width $k_f = E_f t_f$ (Tab. 5.1) spans a range of values of more than one order of magnitude, Tab. 5.2 reports the ranges of variation of k_f for each fiber type analyzed, while Fig. 5.2c reports its frequency distribution for clay bricks.

5.3.3 Comparison between experimental and theoretical results

The comparisons between theoretical and experimental results are reported in Figs. 5.3-5.5 for the various substrates analyzed. For each approach are reported the maximum debonding force ($F_{max,th} - F_{max,exp}$ graphs in Figs. 5.3-5.5) and the computed lognormal cumulative probability distributions (CPD) of the safety factor $\delta = F_{max,exp}/F_{max,th}$. The former permits to estimate if a theoretical relationship follows the global trend of the experimental results, whilst the CPD curves are useful to represent the dispersion of the data allowing to determine if a design formula is too conservative or it overestimates the
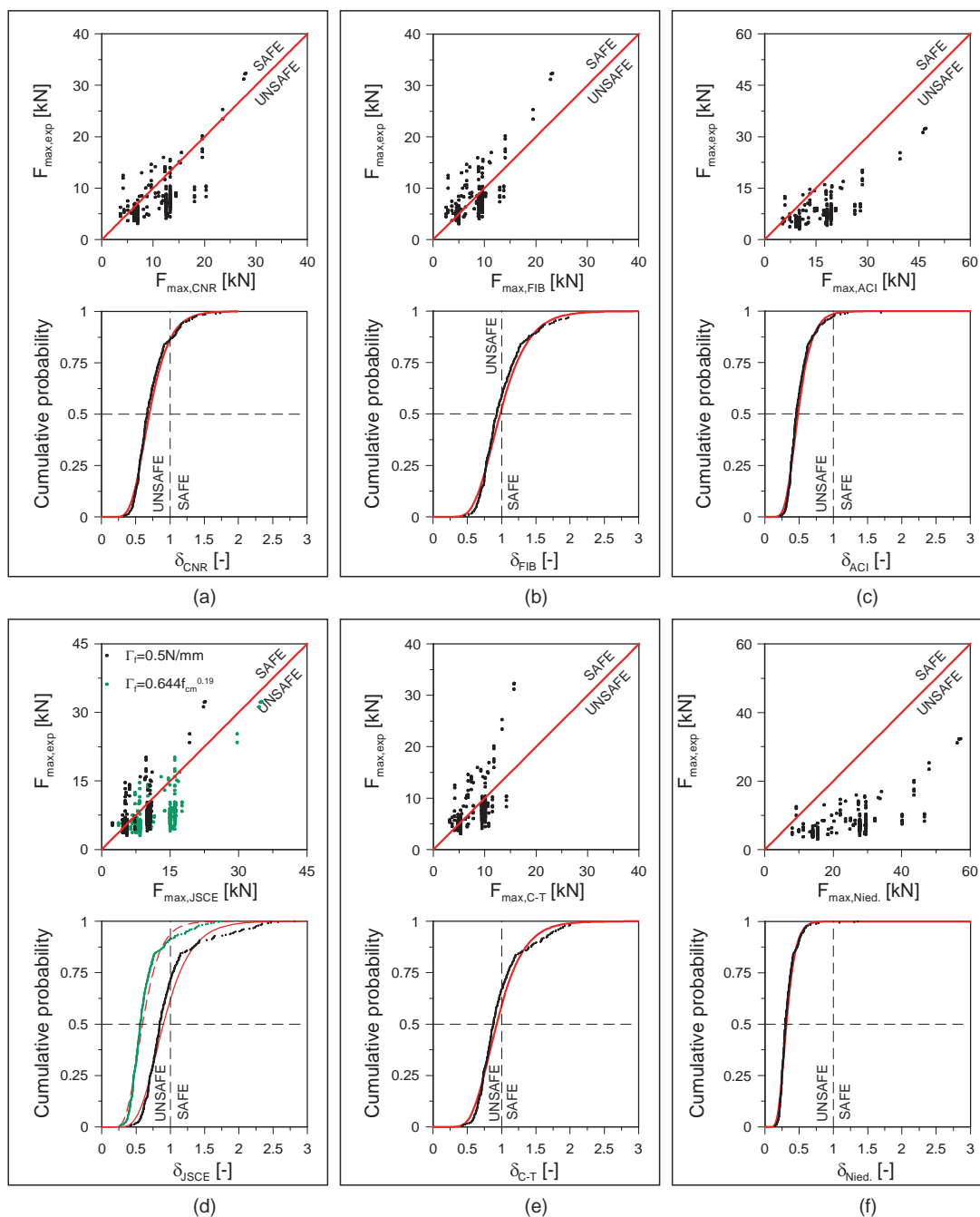
Figure 5.3: Overview of the design rules in literature: $F_{max,th} - F_{max,exp}$ plots and lognormal cumulative probability distributions (CPD) of the safety factor $\delta = F_{max,th}/F_{max,exp}$ for the clay brick results. (a) CNR [8]. (b) *fib* [9]. (c) ACI [10]. (d) JSCE [11]. (e) Chen and Teng model [12]. (f) Niedermeier model [13].
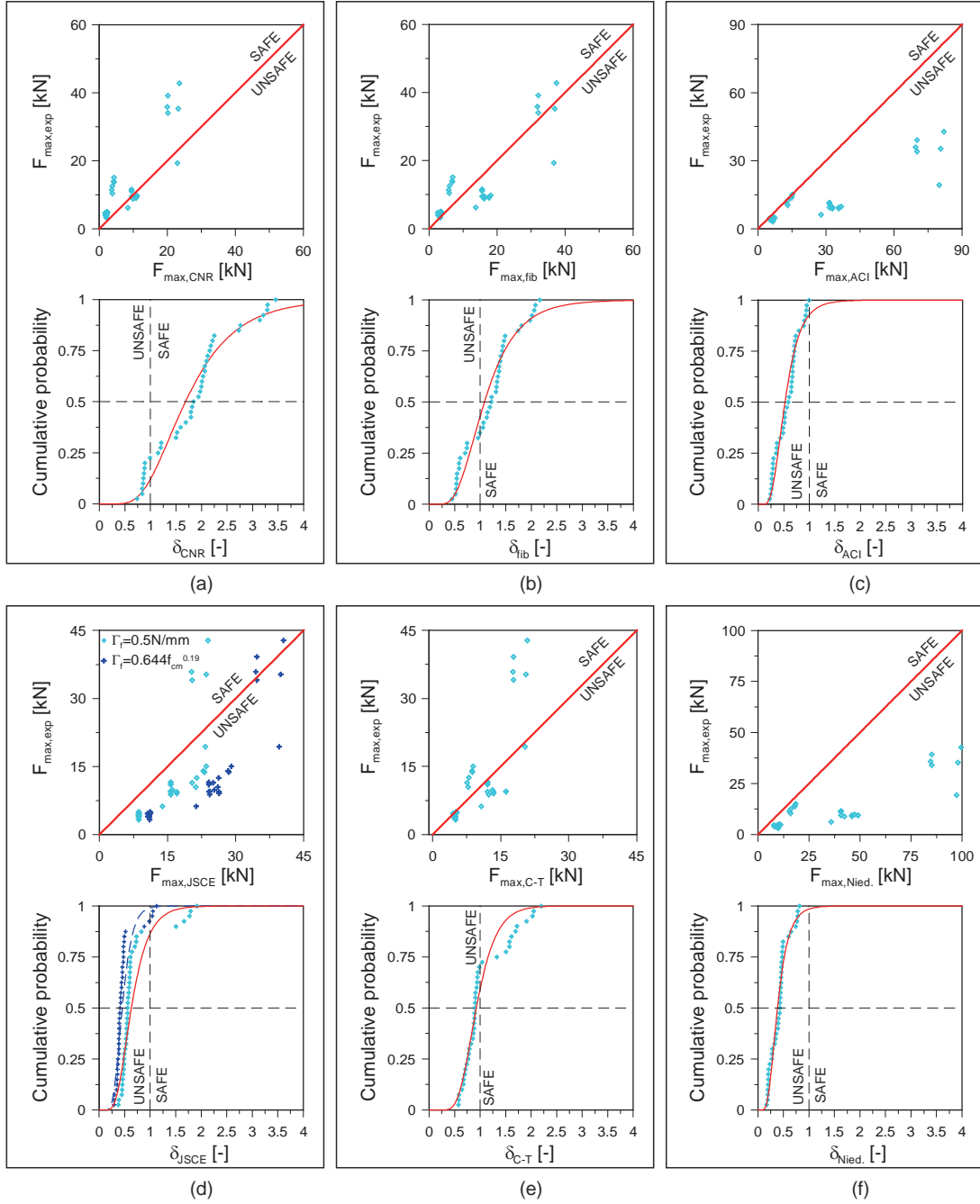
Figure 5.4: Overview of the design rules in literature: $F_{max,th} - F_{max,exp}$ plots and lognormal cumulative probability distributions (CPD) of the safety factor $\delta = F_{max,th}/F_{max,exp}$ for the limestone and calcareous stone results. (a) CNR [8]. (b) *fib* [9]. (c) ACI [10]. (d) JSCE [11]. (e) Chen and Teng model [12]. (f) Niedermeier model [13].
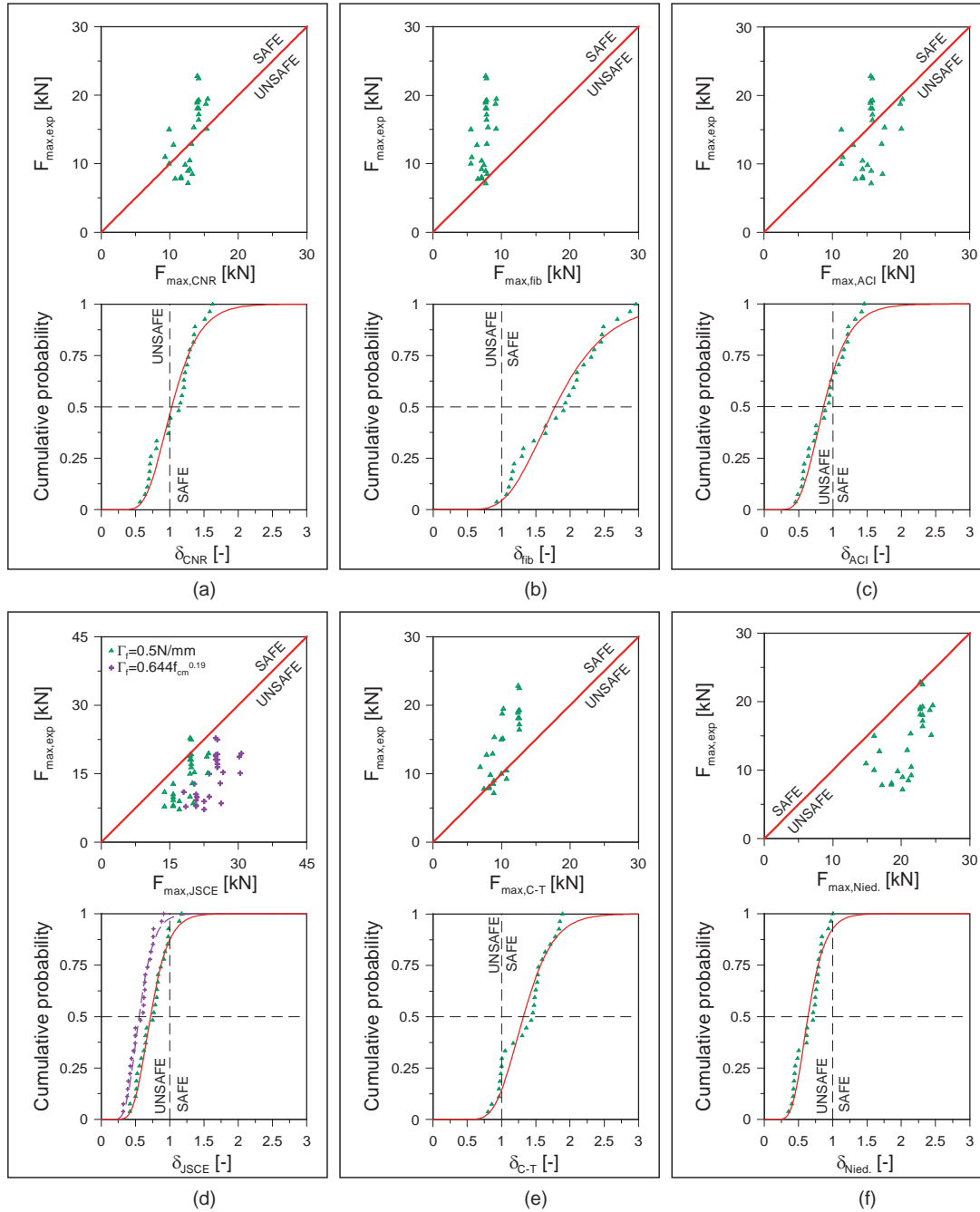
Figure 5.5: Overview of the design rules in literature: $F_{max,th} - F_{max,exp}$ plots and lognormal cumulative probability distributions (CPD) of the safety factor $\delta = F_{max,th}/F_{max,exp}$ for the tuff stone results. (a) CNR [8]. (b) *fib* [9]. (c) ACI [10]. (d) JSCE [11]. (e) Chen and Teng model [12]. (f) Niedermeier model [13].

ultimate resistance.

From Fig. 5.3 it is observable how the design rules examined often overestimate the maximum debonding force prior to failure of the clay bricks (i.e. $\delta = F_{max,exp}/F_{max,th} \leq 1$). Moreover, even if the substrate compressive strength f_{cm} spans, in the 87.1% of the data, between 25 and 35 MPa (Fig. 5.2d), that are usual values also for concrete, the formulas suitable for concrete do not fit for masonry (Fig. 5.3). Among the analyzed approaches, only the CNR code [8] provides a section specifically devoted to the design of FRP-masonry strengthening systems, which anyway frequently leads to unsafe predictions of the debonding load (Fig. 5.3a). Concerning the natural stone substrates, it is interesting to observe how a general inaccuracy is present (Figs. 5.4-5.5). For the limestones and calcareous stones, the maximum dobonding force is, except for the CNR approach [8] (Fig. 5.4a), overestimated, while for tuff stones ambiguous results are obtained (Fig. 5.5). In particular, the values of F_{max} are overestimated in the ACI 440, JSCE 2001, Chen & Teng and Niedermeier models [10–13] (Figs 5.5c-f) and they are underestimated in the CNR-DT200 and in the *fib* [8, 9] approaches (Figs. 5.5a,b). Moreover, the CNR model [8] (Fig. 5.5a) presents a large margin of error (i.e. the standard deviation is quite high, for more details see par. 5.6.2). As a matter of fact, for tuff stone this mismatch can be also due to different debonding mechanisms, as will be debated in detail in par. 5.6.2.

An overestimation of the debonding force attainable leads to a premature failure of the reinforcement, conversely its underestimation imply the use of more material than the minimum needed to reach the required safety factors. While the first condition must be avoided in order to preserve the life of the structure users, the latter leads to very expensive interventions, that can subtract resources useful to fix other vulnerabilities.

In general, Fig. 5.3-5.5 highlights that, often, the resistance for high strength reinforcements is the most overestimated. Thus, the obtained results point out the need of design formulas specifically calibrated for masonry. Moreover, Figs. 5.3d, 5.4d, 5.5d show the key role assumed by the fracture energy at disposal Γ_f, defined as the area encompassed by the interface constitutive law (Fig. 5.1b).

5.4 Capacity model for the design of FRP-masonry reinforcements: proposed strategy

In the following sections a statistical evaluation of the main parameters involved in the debonding mechanism is performed. Then, three semi-empirical approaches will be illustrated, firstly assessed for the clay brick substrate and then extended to natural stones. In particular, the three approaches presented are a mono- and a two- parameters rule calibrated under the hypothesis of homoskedasticity of the data and a two-parameter rule fitted accounting for the heteroskedasticity of the experimental results.

5.4.1 Main parameters involved

The statistical choice of the parameters directly related to the maximum debonding force F_{max} has been performed via Pearson's correlation analysis. Pearson's coefficients $\rho_{i,j} = \rho_{j,i}$ express the tendency of two aleatory variables X_i and X_j to be reciprocally related and read

$$\rho_{i,j} = \frac{\sigma_{i,j}}{\sigma_i \sigma_j}, \tag{5.11}$$

where $\sigma_{i,j}$, σ_i and σ_j are respectively the covariance and the standard deviation of the variables X_i and X_j. The coefficient ρ varies between -1 and +1, where the negative and positive sign indicates respectively an inverse or a direct correlation while the value 0 states no correlation. Since the direct dependence between F_{max} and b_f is well established, the analysis is performed using the normalized force F/b_f to minimize the possibility of spurious correlations. In Tab. 5.3 the results of the correlation analysis are reported.

The positive correlation between the geometry parameters of the support and of the FRP is due to the tendency of gluing bigger areas of reinforcements on bigger specimens. The limited correlation between the normalized force F/b_f and the bonded length points out that the maximum debonding force was reached (i.e. $l_b \geq L_{eff}$). Moreover, very low values of ρ are present also among the normalized force and the dimensions of the support cross-section $b_m \times h_m$, indicating that the "compliance volume" [83] was able to develop completely during the tests. Finally, the analysis highlights, as expected, the high influence of parameters such as the width ratio λ_w, the reinforcement stiffness per unit width $E_f t_f$ (with no predominant influence of E_f or t_f separately) and an important influence of the substrate compressive strength f_{cm}.

Table 5.3: Pearson's coefficients of the main parameters involved in the debonding phenomenon.

b_f	l_b	t_f	E_f	$E_f t_f$	b_m	h_m	λ_w	f_{cm}	F/b_f	
1.00	0.42	-0.22	-0.16	-0.30	0.06	0.53	0.99	-0.17	-0.36	b_f
	1.00	-0.11	-0.08	-0.16	0.40	0.39	0.36	0.06	0.07	l_b
		1.00	0.17	0.85	-0.02	0.09	-0.22	0.30	0.43	t_f
			1.00	0.66	0.24	-0.01	-0.19	0.02	0.37	E_f
				1.00	0.15	0.02	-0.31	0.20	0.50	$E_f t_f$
					1.00	-0.08	-0.09	-0.33	-0.06	b_m
		Sym.				1.00	0.54	0.06	0.24	h_m
							1.00	-0.12	-0.36	λ_w
								1.00	0.59	f_{cm}
									1.00	F/b_f

Even if a higher number of results probably would provide a more reliable correlation study, the present investigation can be considered plausible because it does not contradict the major assumptions or outcomes of the principal theories on the subject (as the ones presented in par. 5.2). Moreover, also other studies in the literature performed Pearson's analyses even with less data available (as for example in [142]).

5.4.2 Theoretical strength model

In the present work, the approach of the standard-code [8], briefly explained in par. 5.2, was adopted. This strategy was chosen since is the only one specifically proposed for the masonry substrates and because it matches with the results of the correlation analysis of par. 5.4.1.

In the CNR guidelines [8], the behavior of the interface is described by means of a bilinear curve relating the displacement discontinuity in tangential direction, namely *slip* or s, with the transferred bond stress τ. In [8], Eq. 5.1 is the closed form solution of the differential system of equations governing the debonding behavior [48, 50] and arising from the equilibrium of an infinitesimal portion of the strengthened system (Fig. 5.1b). The same formula arises also from the energetic balance of the LEFM approach illustrated in par. 2.1.1. Differently, the formula to calculate the fracture energy Γ_f (Eq. 5.2) is semi-empirical and related only to the mechanical parameters of the substrate because

the debonding crack develops inside the substrate only and the composite reinforcement behaves as linear-elastic.

The diffusion effects due to the width ratio λ_w are accounted in [8] by means of Eq. 5.3. Indeed, for decreasing values of λ_w the bond stresses can propagate in a larger width than that of the plate, thus a larger volume of substrate is involved and the fracture energy increase [79, 141]. Differently, approaching $\lambda_w = 1$ this effect vanishes.

In the present approach, it is assumed that Eq. 5.3 still holds, since the aim of the present work is not to investigate the width effect. Furthermore, it was supposed that a change in the reinforcement material (i.e., fiber, matrix or thickness) is related only to a modification of the value of $E_f t_f$.

5.4.3 First approach: two-parameter formula

Since the use of Eq. 5.4 does not lead to a high gain in term of safety (Fig. 5.6) as one could expect adopting an empirical approximated relationship instead of measured values, here the tensile strength of the substrate $f_{ct,th}$ was related to the compressive strength by the following relation

$$f_{ct,th} = c_0 f_{cm}^{\alpha} \,, \tag{5.12}$$

where c_0 and α are two parameters calibrated on the basis of experimental tests using the statistical approaches presented in the following sections. The adoption of a non-linear relationship between compressive and tensile strength is justified considering the quasi-brittle nature of the masonry material. Indeed, the formation of a crack is more related to the tensile strength of the material rather than to the compressive one and a linear trend would imply, for high values of the f_{cm}, a tensile strength in contrast with the experimental and theoretical evidence. The expression of Eq. 5.12 can thus be seen as the simplest non-linear relationship available.

Adopting Eq. 5.12 in Eqs. 5.1 and 5.2 and neglecting k_G, the following expression for the maximum force is obtained

$$F_{\max,th} = b_f \sqrt{2E_f t_f \Gamma_f} = c_1 f_{cm}^{\beta_1} b_f \sqrt{E_f t_f k_b} \,, \tag{5.13}$$

where $c_1 = \sqrt{2c_0^{0.5}}$ and $\beta_1 = 0.25\,(1+\alpha)$ are two parameters to be estimated on the basis of experimental tests.
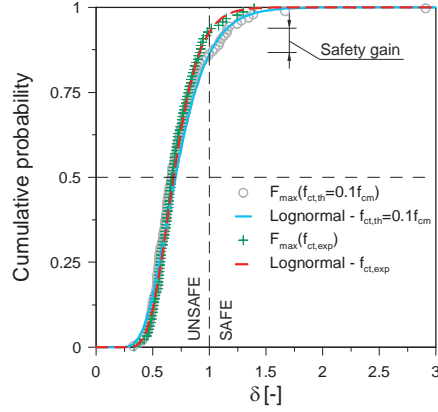
Figure 5.6: Comparison between the lognormal cumulative probability functions of the safety factors computed using the theoretical and the experimental tensile strengths of the specimens.

Eq. 5.13 is calibrated by an ordinary least square (OLS) linear regression starting from the experimental collected data. Eq. 5.13 can be linearized as follows

$$\log\left(F_{\max,th}\right) = \log\left(c_1 b_f \sqrt{E_f t_f k_b}\right) + \beta_1 \log(f_{cm}). \tag{5.14}$$

An OLS estimation of the two free parameters is possible by imposing $\{c_1, \beta_1\} = arg\,min\,\hat{\varepsilon}(c_1, \beta_1)$ with

$$\hat{\varepsilon}(c_1, \beta_1) = \sum_{i=1}^{N} \left[\varepsilon_i(c_1, \beta_1)\right]^2 = \sum_{i=1}^{N} \left[\log\left(F_{\max,th,i}\right) - \log\left(F_{\max,\exp,i}\right)\right]^2, \tag{5.15}$$

where the theoretical values come from Eq. 5.14 applied to the N tests.

Once calibrated, the resulting formula is tested for outliers with a significance level $\alpha_{outl}{=}5\%$ (namely a confidence interval $\beta_{outl}{=}95\%$) by means of the generalized extreme studentized deviate test (G-ESD test) proposed by Rosner in [157] applied to the safety factor $\delta = F_{max,exp}/F_{max,th}$. For a sample of data ξ composed by n values, this procedure is able to detect until r outliers by comparing the extreme studentized deviations

$$R_i = \frac{\max\left|\xi_i - \bar{\xi}\right|}{s_{\xi_i}} \quad \text{for} \quad i = 1, \ldots, r, \tag{5.16}$$

for r successive reduced samples ξ_i (each with mean value and the standard deviation $\bar{\xi}$ and s_{ξ_i}) with size spanning form n to $(n - r + 1)$. In particular, each step i considers a sample where the data labeled as outliers are removed. The ratios R_i are compared with
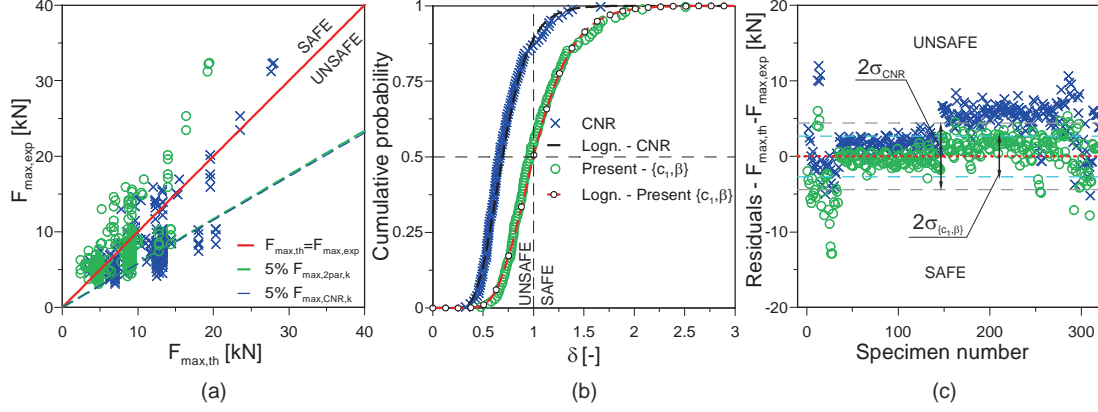
Figure 5.7: Comparison between the CNR approach [8] and the two-parameters formula proposed: (a) experimental vs. theoretical maximum debonding force; (b) lognormal cumulative probability functions of the safety factors; (c) residuals.

the threshold values

$$\lambda_i = \frac{(n-i)t_{p,n-i-1}}{\sqrt{\left((n-i-1)+t_{p,n-i-1}^2\right)(n-i+1)}} \quad \text{with } p = 1 - \frac{\alpha_{outl}}{2(n-i+1)}, \quad (5.17)$$

where $t_{p,n-i-1}$ represents the pth percentile of a t distribution with $(n-i+1)$ degrees of freedom. All the data for which $R_i \geq \lambda_i$ are labeled as outliers and removed from the fitting procedure. Then, the calibration and the G-ESD test are repeated until no outliers are found. For each testing phase the value of r was assumed large enough to obtain at least one value with $R_i < \lambda_i$. In [157] the author reported that this method is very effective for samples with $n \geq 25$, and reasonably accurate for $n \geq 15$. In this first approach three outliers have been detected and removed.

In Fig. 5.7 the results obtained with the present two-parameters formula are compared with the values from [8], whilst in Tab. 5.4 the numerical results of the fitting procedure are reported. Figs. 5.7b,c also show the relative cumulative probability functions of the safety factor $\delta = F_{max,exp}/F_{max,th}$ and the residuals (i.e., the difference between the theoretical and the experimental values of the maximum debonding force), that clearly evidence a gain in term of safety and accuracy. The same is observable in Fig. 5.8a where the probability density functions are reported. Moreover, the debonding strength as a function of f_{cm} is compared to the one suggested by [8] in Fig. 5.9, where the experimental points are reported as well.

Table 5.4: Mean values of the performed fittings and comparison with the CNR [8] prevision.

Fitting	Approach	Material	Mean values		σ
			β	c	[N]
Eq. 5.1	CNR [8]	Clay bricks	0.50	0.243	4385
Eq. 5.15	2 par.	Clay bricks	$0.54^{(\dagger)}$	$0.150^{(\dagger)}$	2685
Eq. 5.20	1 par.	Clay bricks	0.42	$0.220^{(\dagger)}$	2751
Eq. 5.21	Heter.	Clay bricks	$0.76^{(\dagger)}$	$0.074^{(\dagger)}$	2586
Eq. 5.1	CNR [8]	Limestone	0.50	0.118	7611
Eq. 5.20	1 par.	Limestone	0.42	$0.235^{(\dagger)}$	5250
Eq. 5.1	CNR [8]	Tuff stone	0.50	0.315	4205
Eq. 5.20	1 par.	Tuff stone	0.42	$0.391^{(\dagger)}$	3864

$^{(\dagger)}$ Experimentally calibrated parameters.

β and c are referred to the generic formula $F_{max} = c b_f f_{cm}^{\beta} \sqrt{k_b E_f t_f}$.
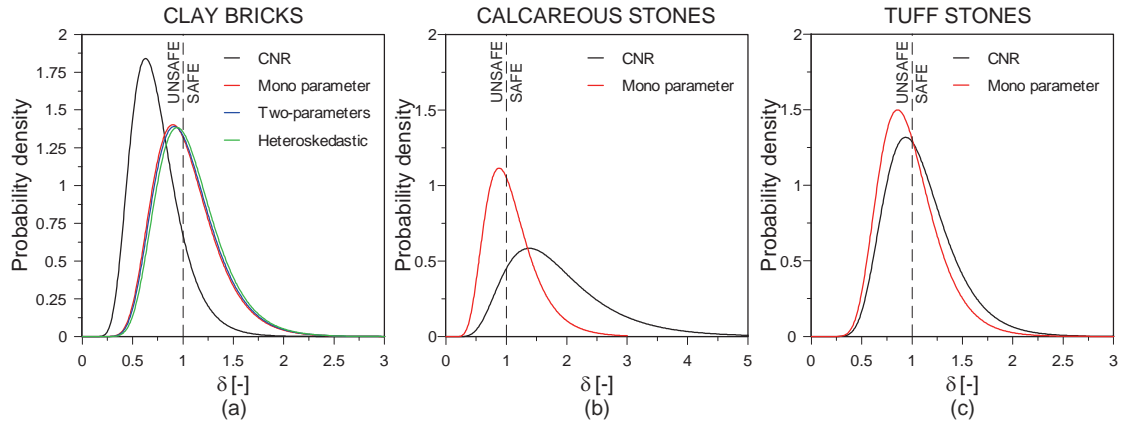
Figure 5.8: Comparisons between the probability density functions of the relationships suggested in [8] and the various approaches proposed herein: (a) clay brick substrate; (b) limestone and lccese-like stone substrate; (c) tuff stone substrate.

5.4.4 Second approach: mono-parameter formula

The mono-parameter model is based on the assumption that the tensile strength of the substrate can be written similarly to what suggested for concrete in the Eurocode 2 [110] and in the German guideline for the strengthening of concrete members with externally bonded FRP [19], namely

$$f_{ct,th} = c_2 f_{cm}^{(2/3)} , \tag{5.18}$$
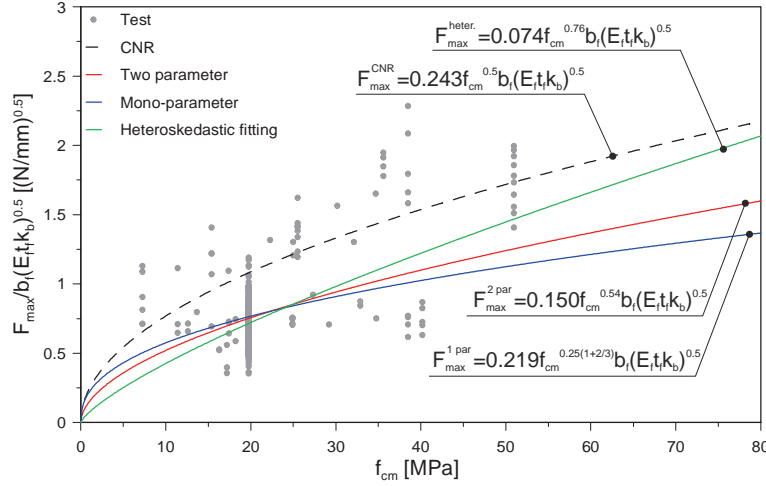
Figure 5.9: Comparisons between the resistance functions suggested in [8] and the various approaches proposed for the clay brick substrate.

thus the maximum debonding force can be calculated as

$$F_{\max,th} = c_3 f_{cm}^{0.42} b_f \sqrt{E_f t_f k_b} \,, \tag{5.19}$$

in which the only parameter needing calibration is $c_3 = \sqrt{2c_2^{0.5}}$.

Similarly to par. 5.4.3, an OLS fitting is performed, but in this case no linearization is needed and the objective function to be minimized reads as follow

$$\hat{\varepsilon}(c_3) = \sum_{i=1}^{N} [\varepsilon_i(c_3)]^2 = \sum_{i=1}^{N} [F_{\max,th,i} - F_{\max,\exp,i}]^2 \,. \tag{5.20}$$

The G-ESD procedure described in detected, also in this case, the same three outliers of par. 5.4.3.

The results of the fitting procedure are shown in Fig. 5.10 and compared with those obtained by use of the other resistance functions and with the collected tests in Figs. 5.8a and 5.9, whilst the numerical results are reported in Tab. 5.4.

5.4.5 Third approach: heteroskedastic fitting

Usually, in the literature, the maximum debonding force is measured and reported for each specimen, while the compressive strength is given as the average value of a number of samples for a set of results. Therefore, the experimental values are not continuously distributed with respect to f_{cm}, leading to the subdivision of the database in clusters
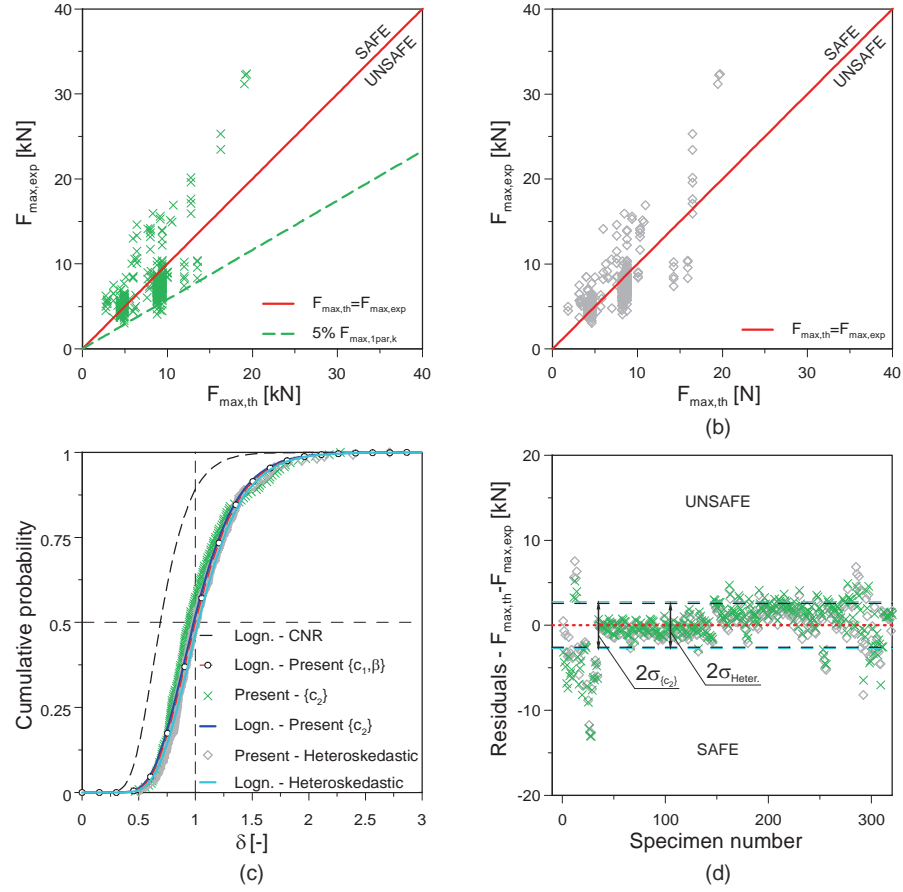
Figure 5.10: Mono-parameter and heteroskedastic fittings: (a) experimental vs. theoretical maximum debonding force for the mono-parameter formula; (b) experimental vs. theoretical maximum debonding force for the heteroskedastic fitting; (c) lognormal cumulative probability functions of the safety factors and comparison with the CNR and the two-parameters approaches; (d) residuals.

containing all the data characterized by the same value of compressive strength (Fig. 5.11). Thus, the average maximum debonding force of the ith cluster can be intended as a measurement with a level of accuracy (or reliability) equal to the reciprocal of its standard deviation $w_i = 1/\sigma_i$. In case of clusters composed only by one datum, the value of σ_i was assumed equal to the standard deviation of the entire representative sample. Hence, each datum has its own weight, namely an influence on the fitting procedure. This leads to an *heteroskedastic* fitting that is different from the *homoskedastic* regressions illustrated in par. 5.4.3 and 5.4.4 where for each measurement the same level of uncertainty (i.e. its weight) is assumed.
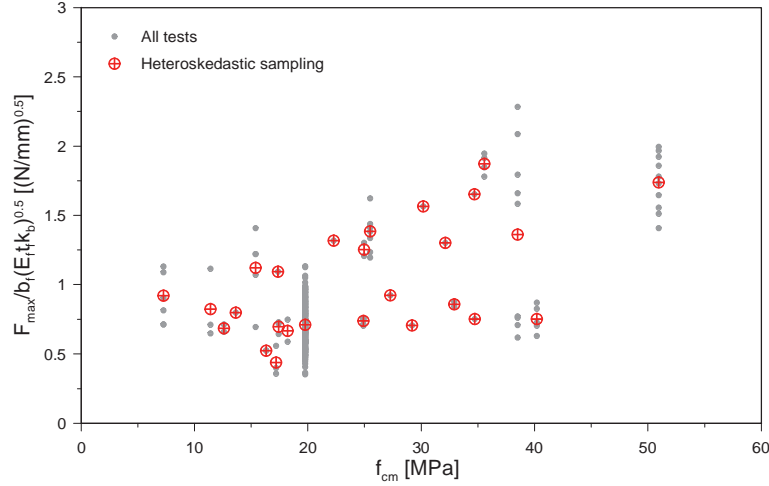
Figure 5.11: Heteroskedastic sampling of the results database.

This fitting problem was solved via Weighted Linear Least Square (WLLS) procedure using the linearized version of the two parameter model (Eq. 5.14). The procedure is the one illustrated in par. 5.4.3 in which the objective function is replaced with

$$\hat{\varepsilon}(c_4, \beta_2) = \sum_{i=1}^{m} w_i \left[\varepsilon_i(c_4, \beta_2)\right]^2 = \sum_{i=1}^{m} w_i \left[\log\left(F_{\max,th,i}\right) - \log\left(F_{\max,\exp,i}\right)\right]^2, \qquad (5.21)$$

where m is the number of clusters analyzed. In this case, the outliers research presented in par. 5.4.3 led to exclude from the fittings five tests.

The results are presented and compared with the other fitting strategies in Figs. 5.8a, 5.9 and 5.10, while the best-fitting parameters are summarized in Tab. 5.4.

5.4.6 First considerations on the approaches

Fig. 5.7 and Tab. 5.4 highlight for the two-parameter approach that the value of $c = c_1$ is not far from the CNR suggestion [8]. The same happens for the mono-parameter rule (Fig. 5.10a,c,d). Moreover, comparing the mono- and two-parameters formulas, it is observable how the two approaches leads to similar results (Figs. 5.8a and 5.10c), both in terms of calibrated parameters (i.e. β and c, Tab. 5.4) than concerning the gain in safety. In particular, the value of β_1, that is fitted on the collected database of experimental results, is not far from the value suggested by [19, 110] and used for the mono-parameter formula in par. 5.4.4.

Concerning the heteroskedastic approach, it can be observed in Fig. 5.9 that the failure load is underestimated for low values of compressive strength and overestimated for high values of f_{cm} (Fig. 5.9). Moreover, in contrast with the homoskedastic mono- and two-parameters approaches, the value of $\beta = \beta_2$ is much higher than the one suggested by [8] (Tab. 5.4).

5.4.7 The "Design assisted by testing" approach

The European standard-code [20] permits to analyze experimental tests to limit uncertainties in resistance models and thus to derive design rules for structural members (point D3 of [20]). In [20], it is suggested to statistically assess a design formula comparing the experimental and theoretical results as in Fig. 5.7a or Fig. 5.10a,b and then the theoretical resistance function should be corrected by means of a Least Square slope coefficient b defined as

$$b = \frac{\sum\limits_{i=1}^{N} F_{\max,\exp,i} F_{\max,th,i}}{\sum\limits_{i=1}^{N} F^2_{\max,th,i}} \, . \tag{5.22}$$

This procedure allows to calibrate only one (corrective) parameter, while the approach presented in par. 5.4.3 involves two parameters. However, using in Eq. 5.22 the fitted relationship of Eq. 5.13 it results that $b \simeq 1.0$ (i.e. almost no "correction"), stating the "statistical equivalence" of the two methods. Differently, Eq. 5.22 follows directly from the method illustrated in par. 5.4.4 for the mono-parameter fitting. In [20] it is specifically stated that the representative sample must be homoskedastic, thus what illustrated in the present section cannot be applied to the heteroskedastic fitting of par. 5.4.5

Once the design formula is assessed, the characteristic value of the resistance is defined using the variance of the safety factor δ and neglecting the variance of f_{cm} since its coefficient of variation is usually not reported in the papers. Assuming a lognormal distribution for the safety factors δ_i, now intended as an estimator of the error committed with the theoretical formula, it is possible to define the variance s^2_Δ and the mean value $\bar{\Delta}$ of the lognormal variable $\Delta_i = \log(\delta_i)$ as

$$s^2_\Delta = \frac{1}{n-1} \sum_{i=1}^{N} (\Delta_i - \bar{\Delta})^2 \quad \text{with} \quad \bar{\Delta} = \frac{1}{n} \sum_{i=1}^{n} \Delta_i \, . \tag{5.23}$$

Finally the characteristic value of the maximum debonding force can be expressed for a representative sample with $N \geq 100$ as:

$$F_{\max,k} = \left[c f_{cm}^{\beta} b_f \sqrt{E_f t_f k_b} \right] e^{\left(-k_\infty s_\Delta - 0.5 s_\Delta^2 \right)} = c_k f_{cm}^{\beta} b_f \sqrt{E_f t_f k_b} , \qquad (5.24)$$

where the parameters (c, β) are respectively the coefficient and the exponent of the design formula summarized in Tab. 5.4 and $c_k = c k_{5\%} = c e^{\left(-k_\infty s_\Delta - 0.5 s_\Delta^2 \right)}$. The coefficient $k_\infty = 1.64$ is the 5% characteristic fractile factor in case of a very large number of measurements (i.e., $N \geq 100$). The characteristic values for the mono- and two-parameters models are reported in Tab. 5.5 whilst in Figs. 5.7a and 5.10a the characteristic resistance functions are plotted together with the mean ones with a dashed line.

5.5   Extension of the strategy to natural stone substrates

Since the number of experimental points is limited and the distribution is too scattered to perform a two-parameters (par. 5.4.3) or a heteroskedastic (par. 5.4.5) fitting for the natural stone substrates (either for limestone or tuff), in these cases only mono-parametric fitting was performed. Moreover, as briefly outlined in par. 5.4.6 and better explained in par. 5.6.1, the heteroskedastic approach does not provide reliable prevision of the failure loads for the tests accounted, whilst the mono- and two-parameters predictive formulas give similar results (Figs. 5.8a and 5.10c).

Assuming that the tensile strength of the substrate can be written as in Eq. 5.18 and adopting the objective functions of Eq. 5.20, two different fittings for the calcareous stones and for the tuff stones were performed. The results are summarized in Tab. 5.4 and 5.5 and illustrated in Figs. 5.12 and 5.13. Comparisons between the present approach and the results predicted with the CNR-DT suggestions [8] are presented in Figs. 5.8b,c and 5.14. Here, the value of the 5% characteristic fractile factor adopted was $k_{40} = 1.72$ for the limestone (N=40) and $k_{27} = 1.74$ for the tuff stone (N=27).

5.6   Discussion of the results

5.6.1   Clay brick substrate

Figs. 5.6 and 5.7b show that the CNR relationship [8] of Eq. 5.1, overestimates (i.e. $\delta \leq 1$) the maximum debonding force of about the 85-90% of the tests considered in the
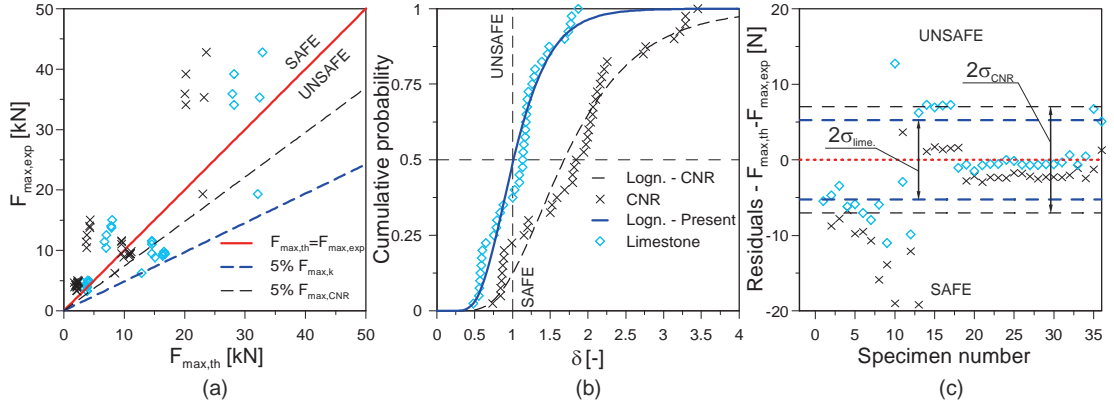
Figure 5.12: Comparison between the CNR formula and the performed fitting for the limestone and calcareous stone substrate: (a) experimental vs. theoretical maximum dedonding force; (b) lognormal cumulative probability functions of the safety factors; (d) residuals.
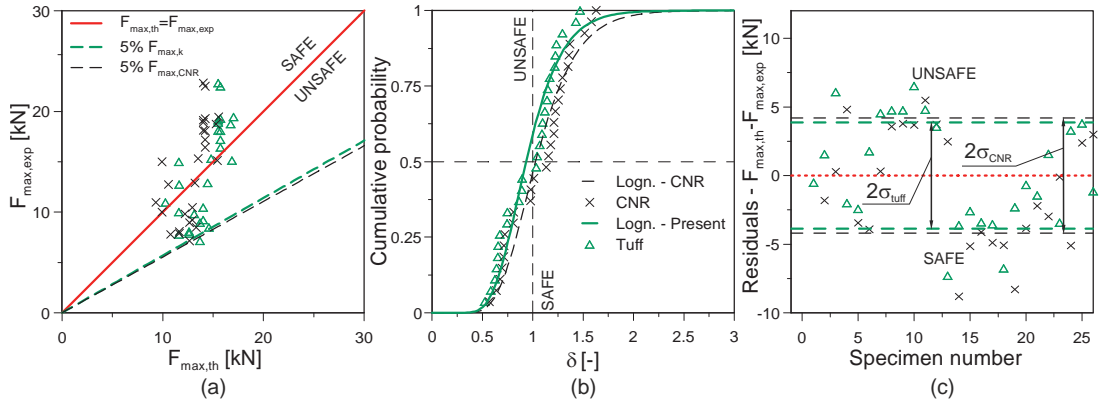
Figure 5.13: Comparison between the CNR formula and the performed fitting for the tuff substrate: (a) experimental vs. theoretical maximum debonding force; (b) lognormal cumulative probability functions of the safety factors; (d) residuals.

database. The two- and mono-parameter approaches proposed here seem to overcome this problem (Fig. 5.9) thus leading to a gain in safety (Figs. 5.7b and 5.10c). Comparing these approaches to the ones accounted in the literature overview of par. 5.2 (Fig. 5.15a,d), a decreased percentage of overestimated results is, once more, usually observable. This is also confirmed by the residual values (Figs. 5.7c and 5.10d) which appear more concentrated along the zero line. A decrease of the variance σ is also clearly reached as shown in Tab. 5.4. It can be also observed that the mono- and the two-parameters fittings give similar results in term of maximum debonding force F_{max} (Figs. 5.7a, 5.9 and 5.10a) and safety factor (Fig. 5.10c).
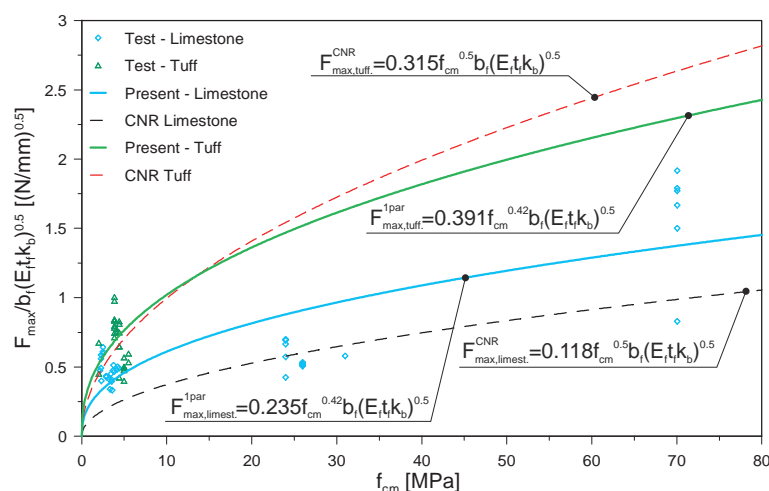
Figure 5.14: Comparisons between the resistance functions suggested by [8] and the proposed approach for the limestone and the tuff stone substrates.

Differently, as briefly outlined in par. 5.4.6, the heteroskedastic fitting appears not reliable since the values of the exponent for f_{cm} is rather high ($\beta = 0.76$), involving a tensile strength f_{ct} growing much more than linearly with the compressive strength of the substrate ($\alpha = 2.04$). This fact is in contrast with theoretical considerations and justifies the extremely low values of F_{max} for low compressive strengths of the substrates and vice versa for high strength substrates. Probably this is the result of the very limited number of clusters (about 26) recognized within the collected data, leading to a poor grid of experimental points. For these reasons the heteroskedastic rule is excluded from the comparison in Fig. 5.15a,d.

5.6.2   Natural stone substrates

Figs. 5.12a and b show how the CNR prevision for limestone and calcareous stones is too conservative, inducing an anti-economic design of the FRP interventions. The proposed approach limits this trend reducing the residuals between the theoretical and the experimental values of F_{max} (Fig. 5.12c), especially for low values of the substrate compressive strength (Fig. 5.14). The relationships illustrated in the overview of par. 5.2 applied to calcareous stones lead to puzzling and sometimes conflicting results, since an overestimation or underestimation of the debonding capacity can be obtained by simply changing the evaluation approach (Fig. 5.15b,e). The mono parameter formula presented

Table 5.5: Characteristic values of the performed fittings and comparison with the CNR [8] prevision.

Fitting	Approach	Material	$k_{5\%}$	c_k
Eq. 5.1	CNR [8]	Clay bricks	0.577	0.140
Eq. 5.15	2 par.	Clay bricks	$0.584^{(a)}$	0.088
Eq. 5.20	1 par.	Clay bricks	$0.582^{(a)}$	0.128
Eq. 5.1	CNR [8]	Limestone	0.738	0.087
Eq. 5.20	1 par.	Limestone	$0.510^{(b)}$	0.114
Eq. 5.1	CNR [8]	Tuff stone	0.553	0.174
Eq. 5.20	1 par.	Tuff stone	$0.570^{(c)}$	0.222

[a] $k_\infty = 1.64$. [b] $k_{40} = 1.72$. [c] $k_{27} = 1.74$.

$c_k = ck_{5\%} = ce^{\left(-k_n s_\Delta - 0.5 s_\Delta^2\right)}$ with $k_{5\%}$ from [20]

here generally permits a clear gain in term of accuracy (Fig. 5.15b,e).

Concerning the tuff substrate, the proposed mono-parameter rule leads to reliable prevision of the debonding strength of the FRP reinforcements, anyway there is only a limited improvement in comparison with the CNR approach (Figs. 5.13a and b). This is probably due to the very low number of tests at disposal in literature and to the fact that the values of the substrate strength taken into account span a narrow range (Fig. 5.14). When compared to other approaches from literature (Fig. 5.15c,f), the proposed formula leads to a general gain in reliability confirming the validity of the method.

It should be highlighted here that, for natural stone masonry substrates, the number of the tests available to date are limited (N=40 for limestones or calcareous stones and N=27 for tuff stones). Furthermore, some studies available in the literature (e.g. [68, 89, 143, 154] among others) revealed that tuff stone, differently from calcareous stone, can display failure mechanisms quite different from other masonry substrates because of its different material texture and microstructure. Thus a deeper investigation on the subject is needed to obtain more appropriate design rules for this kind of stone. Nevertheless, natural stone masonry constitutes one of the oldest construction material and it is used in a wide number of historical buildings needing structural interventions to be protected and preserved from aging. As outlined in par. 5.1, the reinforcement with externally glued FRPs is one of the most attractive and effective strengthening technique since it permits a good gain in terms of safety besides a limited impact on the historical and artistic heritage. For these
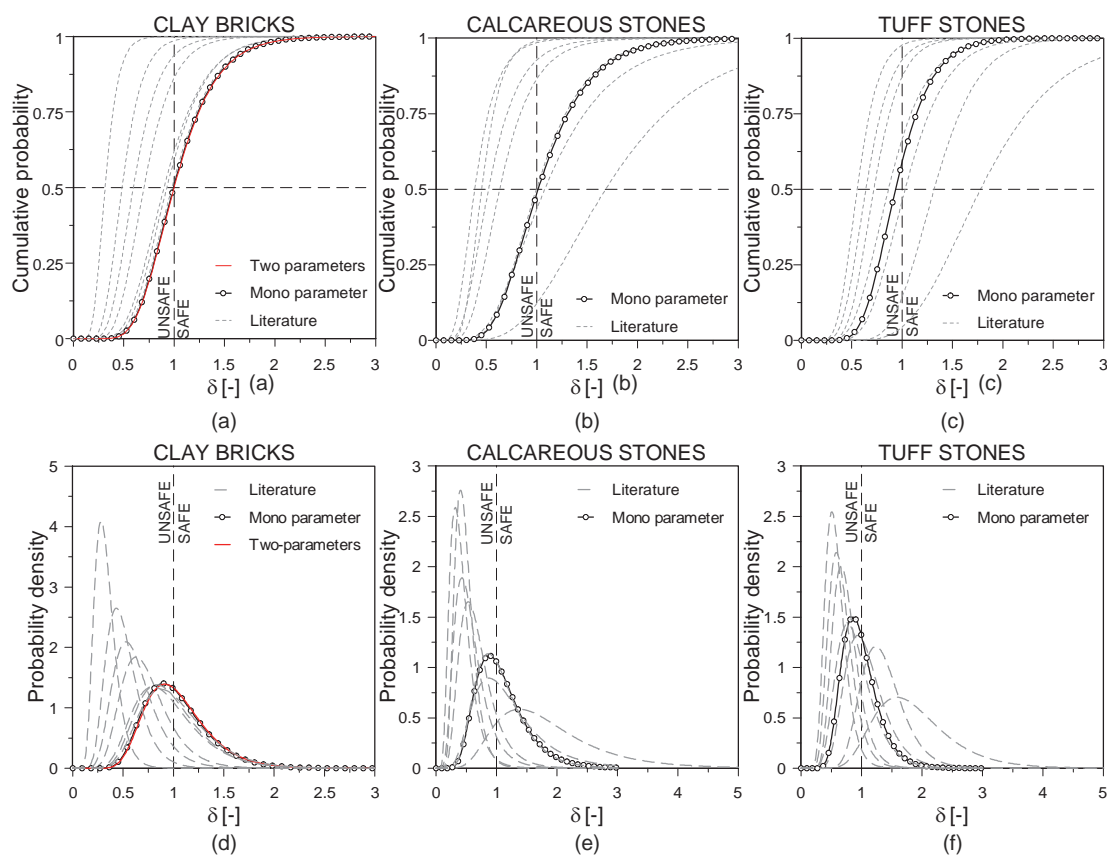
Figure 5.15: Comparisons between the different relationships available in literature illustrated in par. 5.2 and the proposed approaches. (a) Cumulative probability functions for clay brick substrate. (b) Cumulative probability functions for calcarenite and calcareous stones. (c) Cumulative probability functions for tuff stones. (d) Probability density functions for clay brick substrate. (e) Probability density functions for calcarenite and calcareous stones. (f) Probability density functions for tuff stones.

reasons, while other experimental evidence to better calibrate design rules are needed and desirable, the actual common practice has to be based on the the available literature, as was done by other authors (as for example [143]) and even proposed in some guidelines (as in [8]). Thus, for the actual state of knowledge the presented approach, even if not unique [8, 143], can be conceived as a good approximation.

5.7 Conclusive comments

In the present section an alternative design formula for the ultimate debonding strength between FRP reinforcements and masonry substrates is proposed. To date, the strengthening by means of FRP composites of masonry elements is specifically accounted only in the CNR guideline [8], which is thus considered as paradigmatic approach for the comparisons. Starting from the closed form solution of the debonding problem (Eq. 5.1) adopted in [8], a semi-empirical strategy is defined. The capacity against debonding of an FRP-masonry system is calculated as a function of the width b_f, thickness t_f and Young's modulus E_f of the FRP reinforcement and of the compressive strength of the substrate f_{cm}. The transversal effects due to the width ratio $\lambda_w = b_f/b_m$ is accounted using the relation suggested in [8] (Eq. 5.3). A novel empirical power relationship between f_{ct} and f_{cm} is introduced to avoid direct dependence with the substrate tensile strength. Differently from [8], here the experimentally calibrated parameters are directly stated into the expression defining F_{max}.

Finally, statistical methods were used to calibrate the proposed relationships. In particular, the comparison with [8] permits to draw the following conclusions:

- for the clay bricks, both the mono- and two-parameter homoskedastic fittings proposed give good results and limit the overestimation of the debonding resistance highlighted for [8], leading to a safer estimation of the ultimate pulling force for the FRP reinforcements;

- heteroskedastic fitting for clay bricks leads to results which are in contrast with the theoretical considerations and to inaccurate evaluation of the ultimate load. This result is probably due to the sparsity of the experimental points when data are grouped into clusters of measurements (Fig. 5.11);

- for the limestones and the calcareous stones, the predictions coming from [8] slightly underestimate the maximum debonding force applicable. The homoskedastic mono parametric model proposed limits this trend allowing a more economic employment of the FRP reinforcements. Compared with other approaches it permits a more accurate previsions of the debonding strength;

- for tuff substrates, the proposed relationship does not involve a significant improvement in accuracy with respect to [8], probably due to the limited number of data

available. Nevertheless, the predictions coming from the calibrated mono-parameter formula are in good agreement with the experimental data and often lead to a more precise evaluation of F_{max} in comparison with other approaches.

To conclude, even if more experimental data are needed in order to confirm the obtained results, the proposed approach seems to lead to reliable previsions of the debonding resistance of FRP reinforcements applied to masonry. In particular, a general gain in accuracy with respect to other formulas available in literature is highlighted

6

Final remarks

6.1 Summary of the results

In this section the major findings arisen during the present work are summarized, in order to give a global view of the thesis.

This work is subdivided in four main phases that can be seen as one the outcome of the other:

1. Literature overview and study of the state of the art and its advancements;

2. Experimental studies;

3. Numerical modeling of the phenomena and validation with experimental data;

4. Formulation and assessment of simple rules for the design practice.

The evidence arisen represent a step forward in the understanding of the mechanics of the debonding phenomenon, from the experimental, numerical and design practice standpoints. In particular, the following results were obtained:

- **Experimental setup** a new single-lap pure-shear test setup has been developed and validated for the characterization of the FRP reinforcements applied on quasi-brittle materials as masonry or concrete. Indeed, it has been demonstrated that it permits a deeper investigation of the debonding mechanism by making available, for the first time, the entire equilibrium path (pull-out curve) included its possible unstable snap-back branch;

6. FINAL REMARKS

- **Experimental debonding behavior** new evidence on the debonding failure mechanisms of FRP composites externally glued on concrete and clay brick masonry have been found. A dependence with the initial bonded length was observed, i.e. for short bonded length a unique crack nucleating at the free-end and propagating toward the loaded one was observed. Differently, for long bonded length was noticed a *"two-way debonding mechanism"*, involving two different cracks that nucleate separately. The first one occurred at the loaded-end and propagates toward the free one during the first part of the test, the second appeared at the free-end and penetrate into the substrate material in direction of the first crack. During the initial phases of propagation both the cracks sometime kink into the support block resulting in a bulb of material detached. Moreover, it has been observed that reducing the initial bonded length the fracture energy dissipated is more similar to the mode-I fracture toughness. Conversely, for long bonded lengths the energy dissipation reaches higher values, typical of a mode-II process. Such observation imply that, at least for short bonded lengths, the influence of the mode-I (or opening) mode might be non-negligible;

- **Numerical modeling of the monotonic behavior** a novel monodimensional cohesive zone model coupling the tangential and the vertical (opening) behavior based on a widely used first-order approximation of the debonding phenomenon has been proposed and validated against available experimental results. From the performed analyses and comparisons, it has been proven that the model is able to reproduce the failure mechanism of an FRP glued joint as emerged from the experimental campaigns. While more analyses are needed to confirm and extend the obtained results, the proposed model appears a very promising tool to study the monotonic behavior of the externally bonded FRP reinforcement.

- **Numerical modeling of the cyclic behavior** trying to overcome the drawbacks of the available numerical models and empirical relationships to predict the lifespan of structural members reinforced with FRP materials and subject to cyclic loading, a novel model is proposed. The interface behavior is defined coupling damage and plasticity using an ad-hoc admissible domain function. Although a deeper validation is needed, the very good agreement of the first comparisons between experimental

and numerical data evidence that the proposed approach is a very promising technique to interpret the experimental data as well as to predict the fatigue behavior of a FRP glued joint.

- **Design rules assessment** it has been demonstrated how the design formulas nowadays available for the design of FRP reinforcement glued on masonry substrates are often too inaccurate. In particular, most of the rules accounted overestimate the maximum debonding force, condition that might lead to an unsafe design of the strengthening interventions. Trying to overcome this problem, a database of FRP-masonry bond tests results has been collected and used to assess and propose a new practical design formula to evaluate the maximum debonding force attainable in an FRP-masonry glued joint. Starting from theoretical considerations, three different approaches were accounted and then statistically compared with other rules available in the literature as well as with experimental data confirming a general gain in accuracy.

6.2 Open questions and possible developments

A series of issues remain still open since they are not taken into account in the present work.

For a correct understanding of the fatigue behavior of FRP applied on quasi-brittle materials, the study of the effects of cyclic actions on the interface behavior is mandatory [5, 95]. For this problem a general description of the debonding process by means of coupled damage-elastoplastic models is recommended because of the time-dependent history of the structural response. First attempts in this direction have been performed and illustrated in par. 4.5 and very promising results have been achieved, but more investigations are needed. In this field, the study of the visco-plastic behavior is also of interest, especially to investigate the influence of the applied load frequency on fatigue performance.

Another subject of concern is the aging of bonded assemblies that rules the durability of the strengthening interventions. In fact, externally glued FRP composites frequently are directly exposed to environmental conditions that can alter the bonding effectiveness. Studies on the consequences of temperatures and humidity cycles on the bonding behavior (i.e. on the interface stiffness and strength), freeze-thaw influence on crack propagations and effects of the exposition to the sunlight (i.e. ultra-violet and infra-red radiation)

are still on their infancy and only few publications are available in the literature (e.g. [86, 108, 136, 155, 158, 159]).

Finally, some recent results [38, 141] suggest that the role of the glue permeability of the substrate play an incisive role in the failure mechanism. Primarily, it influences the dissipated fracture energy, thus the load carrying capacity of the reinforcement. Today, it is not possible to quantify the influence of the substrate texture on the debonding mechanism and on the value of maximum load, thus a deeper investigation in this direction is needed. In particular, the study of the diffusion mechanism of the glue into the substrate and how it influences the fracture energy and the debonding process is of primary interest, especially for ancient masonry stating the wide variety of existent materials.

Appendices

Appendix A

Detailed description of the numerical FDM strategy for the pure shear model

Following Eq. 4.9, the governing system arising from Eqs. 4.1 and 4.3 can be written as

$$
\begin{cases}
\dfrac{N^{(i+1)} - N^{(i)}}{h_n} & = \quad \dfrac{1}{2}\left(\tau^{(i)}(s) + \tau^{(i+1)}(s)\right) b_f \\[2ex]
\dfrac{s^{(i+1)} - s^{(i)}}{h_n} & = \quad \dfrac{1}{2E_f b_f t_f}\left(N^{(i)} + N^{(i+1)}\right) \quad .
\end{cases}
\tag{A.1}
$$

In order to better menage the system, the following adimensional quantities, designated with $\tilde{\bullet}$, are introduced

$$
\tilde{N}^{(i)} = \dfrac{N^{(i)}}{b_f t_f \hat{\tau}_0} \; ;
\tag{A.2a}
$$

$$
\tilde{s}^{(i)} = \dfrac{s^{(i)}}{s_1} \; ;
\tag{A.2b}
$$

$$
\tilde{h}_n = \dfrac{h_n}{l_b} = \dfrac{1}{N-1} \; .
\tag{A.2c}
$$

where $\hat{\tau}_0$ is a properly selected adimensionalization stress parameter. Further, introducing also the interface law of Eq. 4.4, it is possible to write

$$
\begin{cases}
\dfrac{1}{\tilde{h}_n}\left(\tilde{N}^{(i+1)} - \tilde{N}^{(i)}\right) & = \quad \dfrac{s_1 l_b}{t_f \tau_0}\left((1 - D^{(i+1)})K_{el}^{(i+1)}\tilde{s}^{(i+1)} + (1 - D^{(i)})K_{el}^{(i)}\tilde{s}^{(i)}\right) \\[2ex]
\dfrac{1}{\tilde{h}_n}\left(\tilde{s}^{(i+1)} - \tilde{s}^{(i)}\right) & = \quad \dfrac{\hat{\tau}_0 l_b}{2E_f s_1}\left(\tilde{N}^{(i+1)} + \tilde{N}^{(i)}\right) \; .
\end{cases}
\tag{A.3}
$$

where $D^{(i)} = D(s(x_i))$ constitutes a non-linear term.

Eq. A.3 can be written in matrix form as follows,

$$\left\{ \frac{1}{\tilde{h}_n} \begin{bmatrix} -1 & 0 & | & 1 & 0 \\ 0 & -1 & | & 0 & 1 \end{bmatrix} - \frac{1}{2} \begin{bmatrix} 0 & \frac{s_1 l_b}{t_f \hat{\tau}_0} K_{sec}^{(i)} & | & 0 & \frac{s_1 l_b}{t_f \hat{\tau}_0} K_{sec}^{(i+1)} \\ \frac{\hat{\tau}_0 l_b}{E_f s_1} & 0 & | & \frac{\hat{\tau}_0 l_b}{E_f s_1} & 0 \end{bmatrix} \right\} \begin{bmatrix} \tilde{N}^{(i)} \\ \tilde{s}^{(i)} \\ \hline \tilde{N}^{(i+1)} \\ \tilde{s}^{(i+1)} \end{bmatrix} = \mathbf{0}, \quad (A.4)$$

or, in compact form

$$\left\{ \frac{1}{\tilde{h}_n} \begin{bmatrix} -\boldsymbol{I} & | & \boldsymbol{I} \end{bmatrix} - \frac{1}{2} \begin{bmatrix} \boldsymbol{A_i} & | & \boldsymbol{A_{i+1}} \end{bmatrix} \right\} \begin{bmatrix} \tilde{\boldsymbol{y}}^{(i)} \\ \hline \tilde{\boldsymbol{y}}^{(i+1)} \end{bmatrix} = \mathbf{0}, \quad (A.5)$$

where $\boldsymbol{I}$ is the $[k \times k]$ identity matrix (with $k = dim(\boldsymbol{y}^{(i)})$). The matrix of the non-linear coefficients is

$$\boldsymbol{A_i} = \begin{bmatrix} 0 & \frac{s_1 l_b}{t_f \hat{\tau}_0} K_{sec}^{(i)} \\ \frac{\hat{\tau}_0 l_b}{E_f s_1} & 0 \end{bmatrix} = \mathbf{0}. \quad (A.6)$$

where $K_{sec}^{(i)} = (1 - D^{(i)})K_{el}$ constitutes the non linear term.

A.1 Boundary conditions matrices

Concerning the boundary conditions and the right-hand side, the following cases, summarized in Fig. 4.2, are considered:

Loaded-end force driven process

$$\boldsymbol{B_0} = \begin{bmatrix} 1 & 0 \\ 0 & 0 \end{bmatrix}, \qquad \boldsymbol{B_{l_b}} = \begin{bmatrix} 0 & 0 \\ 1 & 0 \end{bmatrix}, \qquad \overline{\boldsymbol{\alpha}} = \begin{bmatrix} 0 \\ \frac{F}{b_f t_f \hat{\tau}_0} \end{bmatrix}. \quad (A.7)$$

Loaded-end displacement driven process

$$\boldsymbol{B_0} = \begin{bmatrix} 1 & 0 \\ 0 & 0 \end{bmatrix}, \qquad \boldsymbol{B_{l_b}} = \begin{bmatrix} 0 & 0 \\ 0 & 1 \end{bmatrix}, \qquad \overline{\boldsymbol{\alpha}} = \begin{bmatrix} 0 \\ \frac{\overline{s}^{(N)}}{s_1} \end{bmatrix}. \quad (A.8)$$

Free-end displacement driven process

$$\boldsymbol{B_0} = \begin{bmatrix} 1 & 0 \\ 0 & 1 \end{bmatrix}, \qquad \boldsymbol{B_{l_b}} = \begin{bmatrix} 0 & 0 \\ 0 & 0 \end{bmatrix}, \qquad \overline{\boldsymbol{\alpha}} = \begin{bmatrix} 0 \\ \frac{\overline{s}^{(0)}}{s_1} \end{bmatrix}. \quad (A.9)$$

Appendix B

Detailed description of the numerical FDM strategy for the mixed-mode model

Following Eq. 4.9, the governing system arising from Eqs. 4.14 and 4.15 can be written as

$$
\begin{cases}
\dfrac{N^{(i+1)} - N^{(i)}}{h_n} = \dfrac{1}{2}\left(\tau^{(i)}(s,v) + \tau^{(i+1)}(s,v)\right) b_f \\[2mm]
\dfrac{V^{(i+1)} - V^{(i)}}{h_n} = \dfrac{1}{2}\left(\sigma^{(i)}(s,v) + \sigma^{(i+1)}(s,v)\right) b_f \\[2mm]
\dfrac{M^{(i+1)} - M^{(i)}}{h_n} = \dfrac{1}{2}\left[\left(V^{(i)} + V^{(i+1)}\right) + \left(\tau^{(i)}(s,v) + \tau^{(i+1)}(s,v)\right) b_f \left(\dfrac{t_f}{2} + t_a\right)\right] \\[2mm]
\dfrac{u^{(i+1)} - u^{(i)}}{h_n} = \dfrac{1}{2E_f b_f t_f}\left(N^{(i)} + N^{(i+1)}\right) \\[2mm]
\dfrac{v^{(i+1)} - v^{(i)}}{h_n} = \dfrac{1}{2}\left(\varphi^{(i)} + \varphi^{(i+1)}\right) \\[2mm]
\dfrac{\varphi^{(i+1)} - \varphi^{(i)}}{h_n} = -\dfrac{12}{2 b_f t_f^3 E_f}\left(M^{(i)} + M^{(i+1)}\right)
\end{cases}
\tag{B.1}
$$

The following adimensional quantities are then introduced

$$
\tilde{N}^{(i)} = \frac{N^{(i)}}{b_f t_f \hat{\sigma}_0} \ ; \qquad \tilde{V}^{(i)} = \frac{V^{(i)}}{b_f t_f \hat{\sigma}_0} \ ; \quad \tilde{M}^{(i)} = \frac{M^{(i)}}{b_f t_f^2 \hat{\sigma}_0} \ ;
$$

$$
\tilde{u}^{(i)} = \frac{u^{(i)}}{s_1} \ ; \qquad\qquad \tilde{v}^{(i)} = \frac{v^{(i)}}{v_1} \ ; \qquad \tilde{\varphi}^{(i)} = \varphi^{(i)} \ ; \qquad \tilde{h}_n = \frac{h_n}{l_b} = \frac{1}{N-1} \ .
\tag{B.2}
$$

where $\hat{\sigma}_0$ is a properly selected adimensionalization stress parameter. Assuming $K_{s,\tau}^{(i)} =$

$(1 - D^{(i)}(s,v))K_\tau$ and $K_{s,\sigma}^{(i)} = (1 - D^{(i)}(s,v))K_\sigma$ and introducing the interface law of Eq. 4.32 into Eq. B.3, is possible to obtain the adimensional system

$$
\begin{cases}
\dfrac{1}{\tilde{h}_n}\left(\tilde{N}^{(i+1)} - \tilde{N}^{(i)}\right) &= \dfrac{s_1 l_b}{2t_f\hat{\sigma}_0}\left(K_{s,\tau}^{(i+1)}\left(\tilde{u}^{(i+1)} - \dfrac{t_f}{2}\tilde{\varphi}^{(i+1)}\right) + K_{s,\tau}^{(i)}\left(\tilde{u}^{(i)} - \dfrac{t_f}{2}\tilde{\varphi}^{(i)}\right)\right) \\[2mm]
\dfrac{1}{\tilde{h}_n}\left(\tilde{V}^{(i+1)} - \tilde{V}^{(i)}\right) &= \dfrac{v_1 l_b}{2t_f\hat{\sigma}_0}\left(K_{s,\sigma}^{(i+1)}\tilde{v}^{(i+1)} + K_{s,\sigma}^{(i)}\tilde{v}^{(i)}\right) \\[2mm]
\dfrac{1}{\tilde{h}_n}\left(\tilde{M}^{(i+1)} - \tilde{M}^{(i)}\right) &= \dfrac{l_b}{2t_f}\left(\tilde{V}^{(i+1)} + \tilde{V}^{(i)}\right) + \dfrac{s_1 l_b}{2t_f^2\hat{\sigma}_0}\left(\dfrac{t_f}{2} + t_a\right)\cdots \\[2mm]
&\quad \cdots\left(K_{s,\tau}^{(i+1)}\left(\tilde{u}^{(i+1)} - \dfrac{t_f}{2}\tilde{\varphi}^{(i+1)}\right) + K_{s,\tau}^{(i)}\left(\tilde{u}^{(i)} - \dfrac{t_f}{2}\tilde{\varphi}^{(i)}\right)\right) \\[2mm]
\dfrac{1}{\tilde{h}_n}\left(\tilde{u}^{(i+1)} - \tilde{u}^{(i)}\right) &= \dfrac{\hat{\tau}_0 l_b}{2E_f s_1}\left(\tilde{N}^{(i+1)} + \tilde{N}^{(i)}\right) \\[2mm]
\dfrac{1}{\tilde{h}_n}\left(\tilde{v}^{(i+1)} - \tilde{v}^{(i)}\right) &= \dfrac{l_b}{2v_1}\left(\tilde{\varphi}^{(i+1)} + \tilde{\varphi}^{(i)}\right) \\[2mm]
\dfrac{1}{\tilde{h}_n}\left(\tilde{\varphi}^{(i+1)} - \tilde{\varphi}^{(i)}\right) &= -\dfrac{12\hat{\sigma}_0 l_b}{E_f t_f}\left(\tilde{M}^{(i+1)} + \tilde{M}^{(i)}\right)
\end{cases}
\tag{B.3}
$$

where the expression for the slips $s = u - \varphi t_f/2$ is used. Eq. B.3 can be written in compact form as

$$
\left\{\frac{1}{\tilde{h}_n}\begin{bmatrix}-\boldsymbol{I} & \vdots & \boldsymbol{I}\end{bmatrix} - \frac{1}{2}\begin{bmatrix}\boldsymbol{A_i} & \vdots & \boldsymbol{A_{i+1}}\end{bmatrix}\right\}\begin{bmatrix}\tilde{\boldsymbol{y}}^{(i)} \\ \cdots \\ \tilde{\boldsymbol{y}}^{(i+1)}\end{bmatrix} = \boldsymbol{0}\,,
\tag{B.4}
$$

where $\boldsymbol{I}$ is the $[6 \times 6]$ identity matrix and $\tilde{\boldsymbol{y}}^{(i)} = \left[\tilde{N}^{(i)}, \tilde{V}^{(i)}, \tilde{M}^{(i)}, \tilde{u}^{(i)}, \tilde{v}^{(i)}, \tilde{\varphi}^{(i)}\right]^T$ is the vector collecting the adimensionalized unknowns.

The non-linear matrix of the coefficients is

$$
\boldsymbol{A_i} = \begin{bmatrix}
0 & 0 & 0 & \dfrac{s_1 l_b}{t_f\hat{\sigma}_0}K_{s,\tau}^{(i)} & 0 & -\dfrac{l_b}{2\sigma_0}K_{s,\tau}^{(i)} \\[3mm]
0 & 0 & 0 & 0 & \dfrac{v_1 l_b}{t_f\hat{\sigma}_0}K_{s,\sigma}^{(i)} & 0 \\[3mm]
0 & \dfrac{l_b}{t_f} & 0 & \dfrac{s_1 l_b}{t_f^2\hat{\sigma}_0}\left(\dfrac{t_f}{2} + t_a\right)K_{s,\tau}^{(i)} & 0 & \dfrac{l_b}{2t_f\hat{\sigma}_0}\left(\dfrac{t_f}{2} + t_a\right)K_{s,\tau}^{(i)} \\[3mm]
\dfrac{\hat{\sigma}_0 l_b}{E_f s_1} & 0 & 0 & 0 & 0 & 0 \\[3mm]
0 & 0 & 0 & 0 & 0 & \dfrac{l_b}{v_1} \\[3mm]
-\dfrac{12\hat{\sigma}_0 l_b}{E_f t_f} & 0 & 0 & 0 & 0 & 0
\end{bmatrix} = \boldsymbol{0}\,.
\tag{B.5}
$$

B.1 Boundary conditions matrices

Concerning the boundary conditions and the right-hand side, the following cases, summarized in Fig. 4.10, are considered:

Loaded-end force driven process

$$
\boldsymbol{B_0} =
\begin{bmatrix}
1 & & & & & \\
& 1 & & & & \\
& & 1 & & & \\
& & & 0 & & \\
& & & & 0 & \\
& & & & & 0
\end{bmatrix}, \quad
\boldsymbol{B_{l_b}} =
\begin{bmatrix}
0 & & & & & \\
& 0 & & & & \\
& & 0 & & & \\
1 & & & 0 & & \\
& & & & 1 & \\
& 1 & & & & 0
\end{bmatrix}, \quad
\overline{\boldsymbol{\alpha}} =
\begin{bmatrix}
0 \\
0 \\
0 \\
\frac{\overline{F}}{b_f t_f \hat{\sigma}_0} \\
0 \\
0
\end{bmatrix}. \quad \text{(B.6)}
$$

Loaded-end displacement driven process

$$
\boldsymbol{B_0} =
\begin{bmatrix}
1 & & & & & \\
& 1 & & & & \\
& & 1 & & & \\
& & & 0 & & \\
& & & & 0 & \\
& & & & & 0
\end{bmatrix}, \quad
\boldsymbol{B_{l_b}} =
\begin{bmatrix}
0 & & & & & \\
& 0 & & & & \\
& & 0 & & & \\
& & & 1 & & \\
& & & & 1 & \\
& 1 & & & & 0
\end{bmatrix}, \quad
\overline{\boldsymbol{\alpha}} =
\begin{bmatrix}
0 \\
0 \\
0 \\
\frac{\overline{u}^{(N)}}{s_1} \\
0 \\
0
\end{bmatrix}. \quad \text{(B.7)}
$$

Free-end displacement driven process

$$
\boldsymbol{B_0} =
\begin{bmatrix}
1 & & & & & \\
& 1 & & & & \\
& & 1 & & & \\
& & & 1 & & \\
& & & & 0 & \\
& & & & & 0
\end{bmatrix}, \quad
\boldsymbol{B_{l_b}} =
\begin{bmatrix}
0 & & & & & \\
& 0 & & & & \\
& & 0 & & & \\
& & & 0 & & \\
& & & & 1 & \\
& 1 & & & & 0
\end{bmatrix}, \quad
\overline{\boldsymbol{\alpha}} =
\begin{bmatrix}
0 \\
0 \\
0 \\
\frac{\overline{u}^{(0)}}{s_1} \\
0 \\
0
\end{bmatrix}. \quad \text{(B.8)}
$$

B. FDM APPROACH FOR THE MIXED-MODE MODEL

Appendix C

Procedure to solve the cyclic problem

C.1   Return mapping algorithm

In order to obtain, in a time-discretized setting, the variation of the state variables within a finite time step while fulfilling the Kuhn-Tucker conditions, it is necessary to define a suitable time integration algorithm, which is here chosen as a classical backward Euler/return mapping algorithm [133]. In the present work the driving variable is the total slip s. For a given increment Δs^{i+1} at the time step $i+1$, the following time discretized equations should be solved at each point of the domain

$$
\begin{cases}
s^{i+1} &= s^i + \Delta s^{i+1} \\[4pt]
\Delta s_{pl}^{i+1} &= \Delta\gamma^{i+1} sign(\eta) \\[4pt]
s_{pl}^{i+1} &= s_{pl}^i + \Delta s_{pl}^{i+1} \\[4pt]
\Delta s^{i+1} &= \Delta s_{el}^{i+1} + \Delta s_{pl}^{i+1} \\[4pt]
\Delta D_K^{i+1} &= -\dfrac{\tau_y^{rel,i+1}\langle\Delta s_{pl}^{i+1}\rangle_-}{K_{el,0}\left[(s^{rel,i+1}-s^i)^2 - \langle\Delta s_{pl}^{i+1}\rangle_-(s^{rel,i+1}-s^i)\right]} \\[10pt]
D_K^{i+1} &= \begin{cases} D_K^i + \Delta D_K^{i+1} & \text{if } D_K^i + \Delta D_K^{i+1} < \min\left(1, D_K^{lim}\right) \\ 1 & \text{otherwise} \end{cases} \\[10pt]
\tau^{i+1} &= (1-D_K^{i+1})K_{el,0}(s^{i+1}-s_{pl}^i) - (1-D_K^{i+1})K_{el,0}\Delta s_{pl}^{i+1} \\
&= \tau^i + \Delta\tau^{i+1} \\[4pt]
\Delta D_\tau^{i+1} &= -\dfrac{\langle\Delta s^{i+1}\rangle_- h(\tau_{y,0}-\tau_y)}{s_{f,u}}g(s)f(\tau) \\[8pt]
D_\tau^{i+1} &= \begin{cases} D_\tau^i + \Delta D_\tau^{i+1} & \text{if } D_\tau^i + \Delta D_\tau^{i+1} < 1 \\ 1 & \text{otherwise} \end{cases} \\[8pt]
\Delta\alpha^{i+1} &= \Delta\gamma^{i+1}\left(1-D_\tau^{i+1}\right)h(s^{i+1}-s_{pl}^{i+1}) \\[4pt]
\alpha^{i+1} &= \alpha^i + \Delta\alpha^{i+1} \\[4pt]
\Delta q^{i+1} &= \Delta\gamma^{i+1}\dfrac{\left(1-D_\tau^{i+1}\right)^2}{2}K_{pl}h(s^{i+1}-s_{pl}^{i+1})+ \\
&\quad +\dfrac{1}{2}\left(\tau_{y,0}+K_{pl}\alpha^{i+1}\right)\Delta D_\tau^{i+1} \\[4pt]
q^{i+1} &= q^i + \Delta q^{i+1} \\[4pt]
\eta^{i+1} &= \tau^{i+1} - q^{i+1}h(s^{i+1}-s_{pl}^{i+1}) \\[4pt]
F^{i+1} &= \left|\eta^{i+1}\right| - \dfrac{\left(1-D_\tau^{i+1}\right)}{2}\left(\tau_{y,0}+K_{pl}\alpha^{i+1}\right)h(s^{i+1}-s_{pl}^{i+1}) \leqslant 0\,.
\end{cases}
\tag{C.1}
$$

These relationships have been obtained from the time integration of Eqs. 4.67, 4.68, 4.57-4.59, 4.40 using the backward Euler algorithm, along with Eqs. 4.38, 4.41, 4.42.

To define the *actual* stress state it is possible to start assuming as a *trial* state a process in which no plastic flow takes place (i.e., $\Delta\gamma = 0$), thus

$$
\begin{cases}
s_{pl,TRIAL}^{i+1} & = s_{pl}^i \\[4pt]
\Delta s_{el,TRIAL}^{i+1} & = \Delta s^{i+1} \\[4pt]
D_{K,TRIAL}^{i+1} & = D_K^i \\[4pt]
\tau_{TRIAL}^{i+1} & = (1 - D_{K,TRIAL}^{i+1})K_{el,0}(s^{i+1} - s_{pl}^i) = \tau^i + \Delta\tau^{i+1} \\[4pt]
\alpha_{TRIAL}^{i+1} & = \alpha^i \\[4pt]
\Delta q_{TRIAL}^{i+1} & = \frac{1}{2}\left(\tau_{y,0} + K_{pl}\alpha_{TRIAL}^{i+1}\right)\Delta D_\tau^{i+1} \\[4pt]
q_{TRIAL}^{i+1} & = q^i + \Delta q_{TRIAL}^{i+1} \\[4pt]
\eta_{TRIAL}^{i+1} & = \tau^{i+1} - q_{TRIAL}^{i+1}h(s^{i+1} - s_{pl}^i) \\[4pt]
F_{TRIAL}^{i+1} & = \left|\eta_{TRIAL}^{i+1}\right| - \frac{\left(1 - D_\tau^{i+1}\right)}{2}\left(\tau_{y,0} + K_{pl}\alpha^i\right)h(s^{i+1} - s_{pl}^i).
\end{cases}
\tag{C.2}
$$

If $F_{TRIAL}^{i+1} \leq 0$, the assumed trial state is the real one and no further calculations are needed [133]. Conversely, $F_{TRIAL}^{i+1} > 0$ implies that the yielding limit has been exceeded, thus plastic flow takes place and the trial state must be corrected so as to obtain $F = 0$. Comparing Eqs. C.1$_7$ and C.2$_4$ it is possible to obtain

$$
\tau^{i+1} = \tau_{TRIAL}^{i+1} - (1 - D_K^{i+1})K_{el,0}\Delta s_{pl}^{i+1}.
\tag{C.3}
$$

Note that this relationship is valid for all the meaningful cases since $\Delta D_K^{i+1} \neq 0$ only at the lower bound of the admissible states domain (see Fig. 4.24a), but here $\Delta s_{el,TRIAL}^{i+1} < 0$ and $\tau_{TRIAL}^{i+1} < 0$ and $h(s^{i+1} - s_{pl}^i) = h(\Delta s_{el,TRIAL}^{i+1}) = 0$ (because at the lower bound $s^i - s_{pl}^i = 0$, Fig. 4.24a) leading to $F_{TRIAL}^{i+1} = |\tau_{TRIAL}^{i+1}| > 0$ independently from the value of $D_{K,TRIAL}^{i+1}$. Moreover, from Eq. 4.76, it is clear how the plastic multiplier in the latter case is always equal to unity leading to a perfectly plastic process (i.e., $\Delta s_{pl}^{i+1} = \Delta s^{i+1}$). On the contrary, for all the other possible branches $D_K^{i+1} = D_{K,TRIAL}^{i+1} = D_K^i$ because $\Delta D_K^{i+1} = 0$.

Subtracting Eq. C.1$_{14}$ multiplied by $h(s^{i+1} - s_{pl}^{i+1})$ from Eq. C.3, recalling Eqs. 4.61, C.2$_{6-8}$ and C.1$_{12,14}$ and manipulating the result we obtain

$$|\eta^{i+1}_{TRIAL}|sign(\eta^{i+1}_{TRIAL}) = \underbrace{\left[|\eta^{i+1}| + \Delta\gamma^{i+1}\left((1-D^{i+1}_K)K_{el,0}+\right.\right.}_{C}$$
$$\underbrace{\left. \left. +\frac{(1-D^{i+1}_\tau)^2}{2}K_{pl}h(s^{i+1}-s^{i+1}_{pl})\right)\right]}_{C}sign(\eta^{i+1}) \qquad (C.4)$$

Since the coefficient C in Eq. C.4 is non-negative (i.e. $C \geq 0$) because of Eq. 4.70, after some simple passages, it follows

$$\begin{cases} sign(\eta^{i+1}_{TRIAL}) = sign(\eta^{i+1}) \\ |\eta^{i+1}| = |\eta^{i+1}_{TRIAL}| - \Delta\gamma^{i+1}\left((1-D^{i+1}_K)K_{el,0}+\right. \\ \qquad \left. +\frac{(1-D^{i+1}_\tau)^2}{2}K_{pl}h(s^{i+1}-s^{i+1}_{pl})\right) \end{cases} \qquad (C.5)$$

By substituting Eq. C.5$_2$ into Eq. C.1$_{15}$, recalling Eq. C.1$_{10}$ and setting the result equal to zero it is possible to write

$$F^{i+1}_{TRIAL} - \Delta\gamma^{i+1}\left((1-D^{i+1}_K)K_{el,0} + \frac{(1-D^{i+1}_\tau)^2}{2}K_{pl}h(s^{i+1}-s^{i+1}_{pl}) + \right.$$
$$\left. -\frac{(1-D^{i+1}_\tau)^2}{2}K_{pl}h(s^{i+1}-s^{i+1}_{pl})\right) = 0 \qquad (C.6)$$

and then

$$\Delta\gamma^{i+1} = \frac{F^{i+1}_{TRIAL}}{(1-D^{i+1}_K)K_{el,0} + (1-D^{i+1}_\tau)^2 K_{pl}h(s^{i+1}-s^{i+1}_{pl})}. \qquad (C.7)$$

where, once more, the condition of Eq. 4.69 ensures the non-negativity of the plastic multiplier $\Delta\gamma^{i+1}$.

The flow chart for the implementation of the return mapping algorithm is reported in Figs. C.1, C.2.

C.2 Tangential modulus

In view of the numerical incremental implementation, it is convenient to introduce here the tangential stiffness modulus K_{tan} as

$$K_{tan} := \frac{\partial\tau}{\partial s}. \qquad (C.8)$$
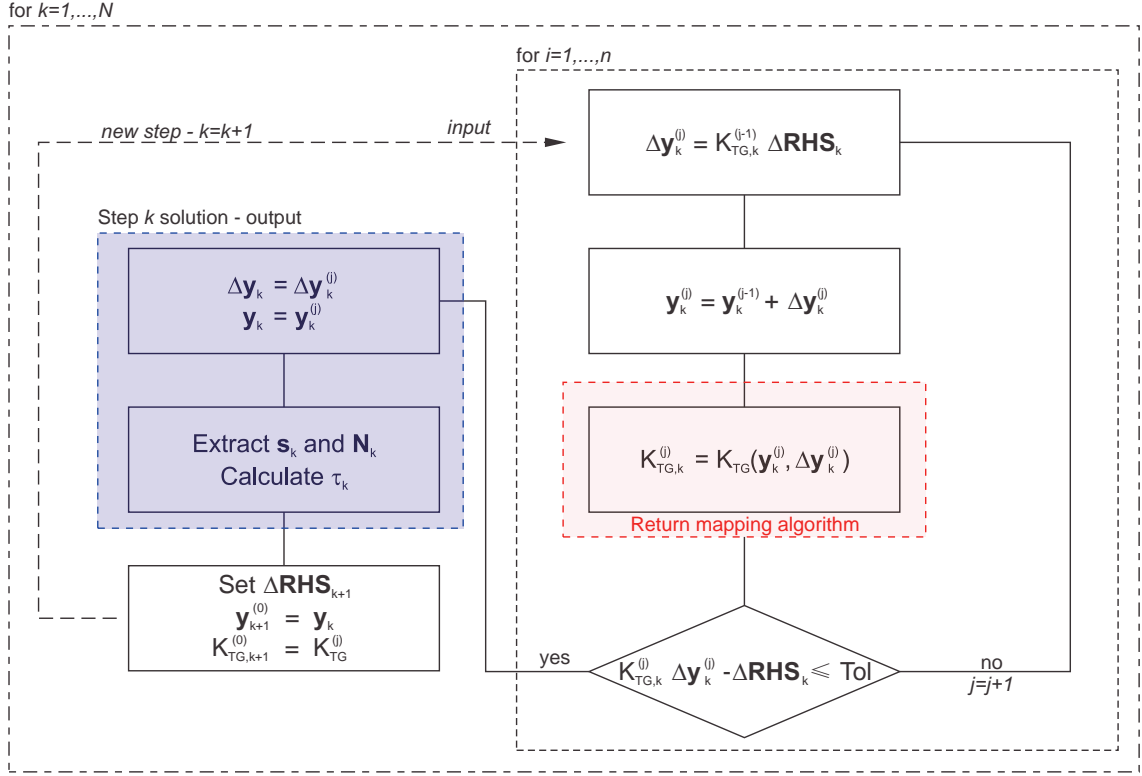
Figure C.1: Flow chart of the iterative loop for the solution of the incremental system within a single time step.

Then, the following relationship holds

$$\dot{\tau} = \frac{\partial \tau}{\partial t} = \frac{\partial \tau}{\partial s}\frac{\partial s}{\partial t} = K_{tan}\dot{s} \,.$$

(C.9)

Comparing Eq. C.9 with Eq. 4.40 and using Eq. 4.57 it follows

$$K_{tan}\dot{s} = (1 - D_K)\,K_{el,0}\,(\dot{s} - \gamma sign(\eta)) \,,$$

(C.10)

Recalling Eq. 4.76 and that $\gamma > 0$ when $F = 0$ and is zero otherwise (namely, when $F < 0$), from Eq. C.10 we obtain

$$K_{tan} = \begin{cases} \dfrac{(1 - D_K)K_{el,0}(1 - D_\tau)^2 K_{pl}h(s - s_{pl})}{(1 - D_K)K_{el,0} + (1 - D_\tau)^2 K_{pl}h(s - s_{pl})}, & F = 0, \gamma > 0 \\ (1 - D_K)K_{el,0}, & F < 0, \gamma = 0 \,. \end{cases}$$

(C.11)
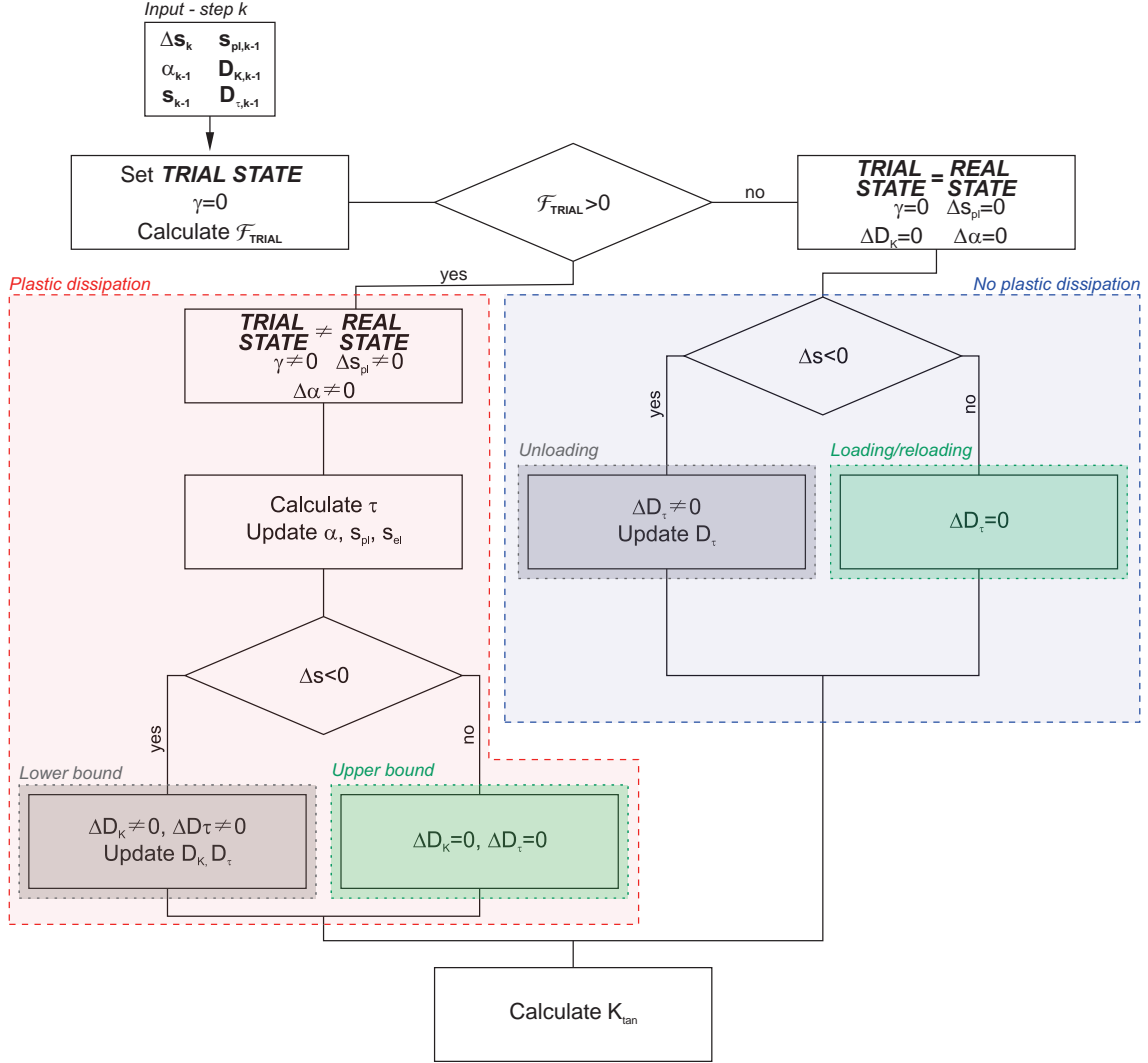
Figure C.2: Flow chart of the return mapping algorithm to calculate the real state of stress and the tangent stiffness.

where Eq. $C.11_1$ holds at the upper/lower bound of the admissible states domain (Fig. 4.24a branches A-B, C-D and E-F) and Eq. $C.11_2$ is valid for the (re)loading/unloading branch (Fig. 4.24a branches O-A, B-C and D-E).

Appendix D

FRP-masonry experimental results database

Table D.1: Database of experimental results used for the analyses

Ref.	$\mathbf{b_f}$ [mm]	$\mathbf{l_b}$ [mm]	$\mathbf{t_f}$ [mm]	$\mathbf{E_f}$ [GPa]	**Fiber**[a]	$\mathbf{b_m}$ [mm]	$\mathbf{h_m}$ [mm]	**Support material**[b]	$\mathbf{f_{cm}}$ [MPa]	$\mathbf{f_{tm,exp}}$ [c] [MPa]	$\mathbf{F_{max}}$ [kN]
[141]	35	150	0.230	390	C	147	61	B_old	12.6	1.6	9.1
	35	150	0.230	390	C	147	61	B_old	12.6	1.6	8.5
	35	150	0.230	390	C	131	59	B_old	11.4	1.9	14.1
	35	150	0.230	390	C	131	59	B_old	11.4	1.9	8.2
	35	150	0.230	390	C	131	59	B_old	11.4	1.9	9.0
	35	150	0.230	390	C	140	59	B_old	17.2	1.7	5.1
	35	150	0.230	390	C	140	59	B_old	17.2	1.7	7.1
	35	150	0.230	390	C	140	59	B_old	17.2	1.7	4.6
[149]	50	200	0.165	230	C	120	55	B_new	50.9	2.4	15.9
	50	200	0.165	230	C	120	55	B_new	50.9	2.4	17.1
	50	200	0.165	230	C	120	55	B_new	50.9	2.4	17.6
	50	200	0.165	230	C	120	55	B_new	50.9	2.4	19.6
	50	200	0.165	230	C	120	55	B_new	50.9	2.4	20.2
	50	200	0.230	65	G	120	55	B_new	50.9	2.4	11.7
	50	200	0.230	65	G	120	55	B_new	50.9	2.4	14.0
	50	200	0.230	65	G	120	55	B_new	50.9	2.4	13.7
	50	200	0.230	65	G	120	55	B_new	50.9	2.4	13.2
	50	200	0.230	65	G	120	55	B_new	50.9	2.4	14.2
[33]	25	120	1.200	160	C	120	55	B_new	38.5	-	10.3
	25	160	1.200	160	C	120	55	B_new	38.5	-	8.3
	25	120	1.200	160	C	120	55	B_new	38.5	-	10.4
	25	160	1.200	160	C	120	55	B_new	38.5	-	9.6
[38]	25	160	0.227	190	S	120	55	B_new	38.5	-	10.1
	25	160	0.227	190	S	120	55	B_new	38.5	-	13.4
	25	160	0.227	190	S	120	55	B_new	38.5	-	11.5
	25	160	0.227	190	S	120	55	B_new	38.5	-	10.6
	25	160	0.227	190	S	120	55	B_new	38.5	-	14.6
	25	160	0.227	190	S	120	55	B_old	34.7	-	10.6
	25	160	0.227	190	S	120	55	B_old	30.2	-	10.0
	25	160	0.227	190	S	120	55	B_old	32.1	-	8.3
	25	160	0.227	190	S	120	55	B_old	27.3	-	5.9
	25	160	0.227	190	S	120	55	B_old	22.3	-	8.4
	25	160	0.227	190	S	120	55	B_old	34.7	-	4.8

Table D.1 continues in the next page

[a] C = Carbon, G = Glass, B = Basalt, S = Steel

[b] B_old = Ancient brick, B_new = Recent brick, NS_limes. = Leccese like stone or limestone, NS_tuff = Tuff

[c] where splitting test was performed $f_{tm,exp} = 0.9 f_{tm,split}$; where flexural test was performed $f_{tm,exp} = 0.5 f_{tm,flex}$

D. FRP-MASONRY EXPERIMENTAL RESULTS DATABASE

Table D.1 continued from previous page

Ref.	b_f [mm]	l_b [mm]	t_f [mm]	E_f [GPa]	Fiber[a]	b_m [mm]	h_m [mm]	Support material[b]	f_{cm} [MPa]	$f_{tm,exp}$ [c] [MPa]	F_{max} [kN]
	25	160	0.227	190	S	120	55	B_old	17.4	-	7.0
	25	160	0.227	190	S	120	55	B_old	13.6	-	5.1
[92]	50	250	0.120	73	G	140	60	B_old	7.3	-	6.3
	50	250	0.120	73	G	140	60	B_old	7.3	-	4.5
	50	250	0.120	73	G	140	60	B_old	7.3	-	5.0
	50	250	0.170	240	C	140	60	B_old	7.3	-	13.0
	50	250	0.170	240	C	140	60	B_old	7.3	-	8.5
	50	250	0.170	240	C	140	60	B_old	7.3	-	8.5
	50	250	0.097	118	S	140	60	B_old	7.3	-	10.0
	50	250	0.097	118	S	140	60	B_old	7.3	-	12.5
	50	250	0.097	118	S	140	60	B_old	7.3	-	12.0
[32]	12	100	0.167	230	C	100	57	B_new	35.6	-	5.7
	12	100	0.167	230	C	100	57	B_new	35.6	-	5.8
	12	100	0.167	230	C	100	57	B_new	35.6	-	5.3
	12	100	0.167	230	C	100	57	B_new	35.6	-	5.5
[68]	129	243	0.342	81	G	129	120	NS_limes.	2.3	-	12.6
	123	243	0.342	81	G	123	120	NS_limes.	2.3	-	11.4
	128	243	0.342	81	G	128	120	NS_limes.	2.3	-	10.5
	118	242	0.164	230	C	118	120	NS_limes.	2.5	0.3	14.0
	119	241	0.164	230	C	119	120	NS_limes.	2.5	0.3	13.8
	121	242	0.164	230	C	121	120	NS_limes.	2.5	0.3	15.1
	123	245	0.342	81	G	123	120	NS_tuff	4.4	0.3	15.3
	120	243	0.342	81	G	120	120	NS_tuff	4.4	0.3	12.9
	121	241	0.342	81	G	121	120	NS_tuff	4.4	0.3	8.5
	119	244	0.164	230	C	119	120	NS_tuff	4.4	0.3	18.7
	121	236	0.164	230	C	121	120	NS_tuff	4.4	0.3	19.5
	120	241	0.164	230	C	120	120	NS_tuff	4.4	0.3	15.1
	116	235	0.342	81	G	120	120	B_new	25.0	5.0	23.5
	116	226	0.342	81	G	120	120	B_new	25.0	5.0	25.3
	115	243	0.164	230	C	120	120	B_new	25.5	5.0	31.2
	116	246	0.164	230	C	120	120	B_new	25.5	5.0	32.2
	117	245	0.164	230	C	120	120	B_new	25.5	5.0	32.4
	51	238	0.342	81	G	120	120	B_new	25.5	5.0	15.9
	57	238	0.342	81	G	120	120	B_new	25.5	5.0	15.3
	57	236	0.342	81	G	120	120	B_new	25.5	5.0	15.6
	56	237	0.164	230	C	120	120	B_new	25.5	5.0	14.9
	55	238	0.164	230	C	120	120	B_new	25.5	5.0	15.2
	57	238	0.164	230	C	120	120	B_new	25.5	5.0	16.9
	122	246	0.342	81	G	122	120	NS_limes.	70.0	5.7	35.9
	123	243	0.342	81	G	123	120	NS_limes.	70.0	5.7	34.1
	123	240	0.342	81	G	123	120	NS_limes.	70.0	5.7	39.2
	120	239	0.164	230	C	120	120	NS_limes.	70.0	5.7	19.3
	121	243	0.164	230	C	121	120	NS_limes.	70.0	5.7	35.3
	123	240	0.164	230	C	123	120	NS_limes.	70.0	5.7	42.8
[58]	50	160	0.120	84	G	120	55	B_new	19.8	1.8	3.8
	50	160	0.120	84	G	120	55	B_new	19.8	1.8	4.4
	50	160	0.120	84	G	120	55	B_new	19.8	1.8	4.5
	50	160	0.120	84	G	120	55	B_new	19.8	1.8	4.5
	50	160	0.120	84	G	120	55	B_new	19.8	1.8	4.6
	50	160	0.120	84	G	120	55	B_new	19.8	1.8	4.2
	50	160	0.120	84	G	120	55	B_new	19.8	1.8	4.6
	50	160	0.120	84	G	120	55	B_new	19.8	1.8	4.8
	50	160	0.120	84	G	120	55	B_new	19.8	1.8	5.1
	50	160	0.120	84	G	120	55	B_new	19.8	1.8	5.1
	50	160	0.120	84	G	120	55	B_new	19.8	1.8	3.7
	50	160	0.120	84	G	120	55	B_new	19.8	1.8	4.1
	50	160	0.120	84	G	120	55	B_new	19.8	1.8	4.2
	50	160	0.120	84	G	120	55	B_new	19.8	1.8	4.2
	50	160	0.120	84	G	120	55	B_new	19.8	1.8	5.5
	50	160	0.120	84	G	120	55	B_new	19.8	1.8	5.5
	50	160	0.120	84	G	120	55	B_new	19.8	1.8	5.6

Table D.1 continues in the next page

[a] C = Carbon, G = Glass, B = Basalt, S = Steel
[b] B_old = Ancient brick, B_new = Recent brick, NS_limes. = Leccese like stone or limestone, NS_tuff = Tuff
[c] where splitting test was performed $f_{tm,exp} = 0.9 f_{tm,split}$; where flexural test was performed $f_{tm,exp} = 0.5 f_{tm,flex}$

Ref.	b_f [mm]	l_b [mm]	t_f [mm]	E_f [GPa]	Fiber$^{(a)}$	b_m [mm]	h_m [mm]	Support material$^{(b)}$	f_{cm} [MPa]	$f_{tm,exp}$ $^{(c)}$ [MPa]	F_{max} [kN]
	50	160	0.120	84	G	120	55	B_new	19.8	1.8	4.2
	50	160	0.120	84	G	120	55	B_new	19.8	1.8	4.3
	50	160	0.120	84	G	120	55	B_new	19.8	1.8	4.3
	50	160	0.120	84	G	120	55	B_new	19.8	1.8	4.9
	50	160	0.120	84	G	120	55	B_new	19.8	1.8	5.2
	50	160	0.120	84	G	120	55	B_new	19.8	1.8	5.1
	50	160	0.120	84	G	120	55	B_new	19.8	1.8	3.7
	50	160	0.120	84	G	120	55	B_new	19.8	1.8	3.8
	50	160	0.120	84	G	120	55	B_new	19.8	1.8	4.0
	50	160	0.120	84	G	120	55	B_new	19.8	1.8	4.0
	50	160	0.120	84	G	120	55	B_new	19.8	1.8	4.7
	50	160	0.120	84	G	120	55	B_new	19.8	1.8	5.5
	50	160	0.120	84	G	120	55	B_new	19.8	1.8	5.6
	50	160	0.120	84	G	120	55	B_new	19.8	1.8	5.7
	50	160	0.120	84	G	120	55	B_new	19.8	1.8	6.9
	50	160	0.120	84	G	120	55	B_new	19.8	1.8	4.7
	50	160	0.120	84	G	120	55	B_new	19.8	1.8	4.8
	50	160	0.120	84	G	120	55	B_new	19.8	1.8	4.9
	50	160	0.120	84	G	120	55	B_new	19.8	1.8	6.2
	50	160	0.120	84	G	120	55	B_new	19.8	1.8	3.8
	50	160	0.120	84	G	120	55	B_new	19.8	1.8	3.9
	50	160	0.120	84	G	120	55	B_new	19.8	1.8	4.9
	50	160	0.120	84	G	120	55	B_new	19.8	1.8	5.0
	50	160	0.120	84	G	120	55	B_new	19.8	1.8	5.0
	50	160	0.120	84	G	120	55	B_new	19.8	1.8	4.2
	50	160	0.120	84	G	120	55	B_new	19.8	1.8	4.6
	50	160	0.120	84	G	120	55	B_new	19.8	1.8	4.7
	50	160	0.120	84	G	120	55	B_new	19.8	1.8	5.5
	50	160	0.120	84	G	120	55	B_new	19.8	1.8	4.5
	50	160	0.120	84	G	120	55	B_new	19.8	1.8	4.6
	50	160	0.120	84	G	120	55	B_new	19.8	1.8	5.0
	50	160	0.120	84	G	120	55	B_new	19.8	1.8	5.3
	50	160	0.120	84	G	120	55	B_new	19.8	1.8	5.3
	50	160	0.140	88	B	120	55	B_new	19.8	1.8	4.2
	50	160	0.140	88	B	120	55	B_new	19.8	1.8	4.3
	50	160	0.140	88	B	120	55	B_new	19.8	1.8	4.4
	50	160	0.140	88	B	120	55	B_new	19.8	1.8	4.5
	50	160	0.140	88	B	120	55	B_new	19.8	1.8	5.6
	50	160	0.140	88	B	120	55	B_new	19.8	1.8	5.1
	50	160	0.140	88	B	120	55	B_new	19.8	1.8	5.7
	50	160	0.140	88	B	120	55	B_new	19.8	1.8	5.7
	50	160	0.140	88	B	120	55	B_new	19.8	1.8	6.3
	50	160	0.140	88	B	120	55	B_new	19.8	1.8	5.9
	50	160	0.140	88	B	120	55	B_new	19.8	1.8	6.0
	50	160	0.140	88	B	120	55	B_new	19.8	1.8	6.1
	50	160	0.140	88	B	120	55	B_new	19.8	1.8	6.2
	50	160	0.140	88	B	120	55	B_new	19.8	1.8	6.3
	50	160	0.140	88	B	120	55	B_new	19.8	1.8	3.8
	50	160	0.140	88	B	120	55	B_new	19.8	1.8	4.7
	50	160	0.140	88	B	120	55	B_new	19.8	1.8	4.8
	50	160	0.140	88	B	120	55	B_new	19.8	1.8	5.4
	50	160	0.140	88	B	120	55	B_new	19.8	1.8	4.8
	50	160	0.140	88	B	120	55	B_new	19.8	1.8	5.3
	50	160	0.140	88	B	120	55	B_new	19.8	1.8	5.7
	50	160	0.140	88	B	120	55	B_new	19.8	1.8	5.9
	50	160	0.140	88	B	120	55	B_new	19.8	1.8	5.9
	50	160	0.140	88	B	120	55	B_new	19.8	1.8	4.4
	50	160	0.140	88	B	120	55	B_new	19.8	1.8	5.0
	50	160	0.140	88	B	120	55	B_new	19.8	1.8	5.1
	50	160	0.140	88	B	120	55	B_new	19.8	1.8	5.2
	50	160	0.140	88	B	120	55	B_new	19.8	1.8	6.4

Table D.1 continues in the next page
$^{(a)}$ C = Carbon, G = Glass, B = Basalt, S = Steel
$^{(b)}$ B_old = Ancient brick, B_new = Recent brick, NS_limes. = Leccese like stone or limestone, NS_tuff = Tuff
$^{(c)}$ where splitting test was performed $f_{tm,exp} = 0.9f_{tm,split}$; where flexural test was performed $f_{tm,exp} = 0.5f_{tm,flex}$

D. FRP-MASONRY EXPERIMENTAL RESULTS DATABASE

Ref.	b_f [mm]	l_b [mm]	t_f [mm]	E_f [GPa]	Fiber[a]	b_m [mm]	h_m [mm]	Support material[b]	f_{cm} [MPa]	$f_{tm,exp}$ [c] [MPa]	F_{max} [kN]
	50	160	0.140	88	B	120	55	B_new	19.8	1.8	4.7
	50	160	0.140	88	B	120	55	B_new	19.8	1.8	4.9
	50	160	0.140	88	B	120	55	B_new	19.8	1.8	5.0
	50	160	0.140	88	B	120	55	B_new	19.8	1.8	5.4
	50	160	0.140	88	B	120	55	B_new	19.8	1.8	6.0
	50	160	0.140	88	B	120	55	B_new	19.8	1.8	3.9
	50	160	0.140	88	B	120	55	B_new	19.8	1.8	4.7
	50	160	0.140	88	B	120	55	B_new	19.8	1.8	5.6
	50	160	0.140	88	B	120	55	B_new	19.8	1.8	5.9
	50	160	0.140	88	B	120	55	B_new	19.8	1.8	6.2
	50	160	0.140	88	B	120	55	B_new	19.8	1.8	3.1
	50	160	0.140	88	B	120	55	B_new	19.8	1.8	3.6
	50	160	0.140	88	B	120	55	B_new	19.8	1.8	4.7
	50	160	0.140	88	B	120	55	B_new	19.8	1.8	5.3
	50	160	0.140	88	B	120	55	B_new	19.8	1.8	5.6
	50	160	0.140	88	B	120	55	B_new	19.8	1.8	4.9
	50	160	0.140	88	B	120	55	B_new	19.8	1.8	5.2
	50	160	0.140	88	B	120	55	B_new	19.8	1.8	5.7
	50	160	0.140	88	B	120	55	B_new	19.8	1.8	5.7
	50	160	0.140	88	B	120	55	B_new	19.8	1.8	7.7
	50	160	0.140	88	B	120	55	B_new	19.8	1.8	3.3
	50	160	0.140	88	B	120	55	B_new	19.8	1.8	3.9
	50	160	0.140	88	B	120	55	B_new	19.8	1.8	4.3
	50	160	0.140	88	B	120	55	B_new	19.8	1.8	5.4
	50	160	0.140	88	B	120	55	B_new	19.8	1.8	5.9
	50	160	0.140	88	B	120	55	B_new	19.8	1.8	4.4
	50	160	0.140	88	B	120	55	B_new	19.8	1.8	4.7
	50	160	0.140	88	B	120	55	B_new	19.8	1.8	5.8
	50	160	0.140	88	B	120	55	B_new	19.8	1.8	6.4
	50	160	0.140	88	B	120	55	B_new	19.8	1.8	4.5
	50	160	0.140	88	B	120	55	B_new	19.8	1.8	6.1
	50	160	0.140	88	B	120	55	B_new	19.8	1.8	6.3
	50	160	0.140	88	B	120	55	B_new	19.8	1.8	6.3
	50	160	0.140	88	B	120	55	B_new	19.8	1.8	6.6
	50	160	0.170	234	C	120	55	B_new	19.8	1.8	5.8
	50	160	0.170	234	C	120	55	B_new	19.8	1.8	5.9
	50	160	0.170	234	C	120	55	B_new	19.8	1.8	6.3
	50	160	0.170	234	C	120	55	B_new	19.8	1.8	6.7
	50	160	0.170	234	C	120	55	B_new	19.8	1.8	6.8
	50	160	0.170	234	C	120	55	B_new	19.8	1.8	6.1
	50	160	0.170	234	C	120	55	B_new	19.8	1.8	6.1
	50	160	0.170	234	C	120	55	B_new	19.8	1.8	7.6
	50	160	0.170	234	C	120	55	B_new	19.8	1.8	7.9
	50	160	0.170	234	C	120	55	B_new	19.8	1.8	8.0
	50	160	0.170	234	C	120	55	B_new	19.8	1.8	6.9
	50	160	0.170	234	C	120	55	B_new	19.8	1.8	7.7
	50	160	0.170	234	C	120	55	B_new	19.8	1.8	7.9
	50	160	0.170	234	C	120	55	B_new	19.8	1.8	8.6
	50	160	0.170	234	C	120	55	B_new	19.8	1.8	8.8
	50	160	0.170	234	C	120	55	B_new	19.8	1.8	4.1
	50	160	0.170	234	C	120	55	B_new	19.8	1.8	5.2
	50	160	0.170	234	C	120	55	B_new	19.8	1.8	6.9
	50	160	0.170	234	C	120	55	B_new	19.8	1.8	7.4
	50	160	0.170	234	C	120	55	B_new	19.8	1.8	7.0
	50	160	0.170	234	C	120	55	B_new	19.8	1.8	7.2
	50	160	0.170	234	C	120	55	B_new	19.8	1.8	7.8
	50	160	0.170	234	C	120	55	B_new	19.8	1.8	7.8
	50	160	0.170	234	C	120	55	B_new	19.8	1.8	7.9
	50	160	0.170	234	C	120	55	B_new	19.8	1.8	5.3
	50	160	0.170	234	C	120	55	B_new	19.8	1.8	5.6
	50	160	0.170	234	C	120	55	B_new	19.8	1.8	6.8

[a] C = Carbon, G = Glass, B = Basalt, S = Steel
[b] B_old = Ancient brick, B_new = Recent brick, NS_limes. = Leccese like stone or limestone, NS_tuff = Tuff
[c] where splitting test was performed $f_{tm,exp} = 0.9 f_{tm,split}$; where flexural test was performed $f_{tm,exp} = 0.5 f_{tm,flex}$

Ref.	b_f [mm]	l_b [mm]	t_f [mm]	E_f [GPa]	Fiber[a]	b_m [mm]	h_m [mm]	Support material[b]	f_{cm} [MPa]	$f_{tm,exp}$ [c] [MPa]	F_{max} [kN]
	50	160	0.170	234	C	120	55	B_new	19.8	1.8	7.2
	50	160	0.170	234	C	120	55	B_new	19.8	1.8	8.1
	50	160	0.170	234	C	120	55	B_new	19.8	1.8	7.8
	50	160	0.170	234	C	120	55	B_new	19.8	1.8	8.6
	50	160	0.170	234	C	120	55	B_new	19.8	1.8	8.8
	50	160	0.170	234	C	120	55	B_new	19.8	1.8	9.9
	50	160	0.170	234	C	120	55	B_new	19.8	1.8	10.3
	50	160	0.170	234	C	120	55	B_new	19.8	1.8	5.7
	50	160	0.170	234	C	120	55	B_new	19.8	1.8	6.4
	50	160	0.170	234	C	120	55	B_new	19.8	1.8	7.1
	50	160	0.170	234	C	120	55	B_new	19.8	1.8	7.5
	50	160	0.170	234	C	120	55	B_new	19.8	1.8	8.3
	50	160	0.170	234	C	120	55	B_new	19.8	1.8	7.5
	50	160	0.170	234	C	120	55	B_new	19.8	1.8	7.6
	50	160	0.170	234	C	120	55	B_new	19.8	1.8	7.6
	50	160	0.170	234	C	120	55	B_new	19.8	1.8	8.4
	50	160	0.170	234	C	120	55	B_new	19.8	1.8	8.6
	50	160	0.170	234	C	120	55	B_new	19.8	1.8	4.7
	50	160	0.170	234	C	120	55	B_new	19.8	1.8	6.2
	50	160	0.170	234	C	120	55	B_new	19.8	1.8	6.7
	50	160	0.170	234	C	120	55	B_new	19.8	1.8	6.8
	50	160	0.170	234	C	120	55	B_new	19.8	1.8	7.1
	50	160	0.170	234	C	120	55	B_new	19.8	1.8	5.6
	50	160	0.170	234	C	120	55	B_new	19.8	1.8	6.3
	50	160	0.170	234	C	120	55	B_new	19.8	1.8	6.6
	50	160	0.170	234	C	120	55	B_new	19.8	1.8	7.6
	50	160	0.170	234	C	120	55	B_new	19.8	1.8	7.7
	50	160	0.170	234	C	120	55	B_new	19.8	1.8	6.2
	50	160	0.170	234	C	120	55	B_new	19.8	1.8	6.8
	50	160	0.170	234	C	120	55	B_new	19.8	1.8	6.8
	50	160	0.170	234	C	120	55	B_new	19.8	1.8	7.0
	50	160	0.170	234	C	120	55	B_new	19.8	1.8	7.0
	50	160	0.170	234	C	120	55	B_new	19.8	1.8	5.7
	50	160	0.170	234	C	120	55	B_new	19.8	1.8	6.5
	50	160	0.170	234	C	120	55	B_new	19.8	1.8	7.2
	50	160	0.170	234	C	120	55	B_new	19.8	1.8	8.2
	50	160	0.170	234	C	120	55	B_new	19.8	1.8	5.7
	50	160	0.170	234	C	120	55	B_new	19.8	1.8	6.0
	50	160	0.170	234	C	120	55	B_new	19.8	1.8	6.2
	50	160	0.170	234	C	120	55	B_new	19.8	1.8	6.6
	50	160	0.170	234	C	120	55	B_new	19.8	1.8	6.9
	50	160	0.231	195	S	120	55	B_new	19.8	1.8	5.7
	50	160	0.231	195	S	120	55	B_new	19.8	1.8	6.5
	50	160	0.231	195	S	120	55	B_new	19.8	1.8	6.7
	50	160	0.231	195	S	120	55	B_new	19.8	1.8	7.2
	50	160	0.231	195	S	120	55	B_new	19.8	1.8	7.5
	50	160	0.231	195	S	120	55	B_new	19.8	1.8	7.1
	50	160	0.231	195	S	120	55	B_new	19.8	1.8	7.3
	50	160	0.231	195	S	120	55	B_new	19.8	1.8	7.4
	50	160	0.231	195	S	120	55	B_new	19.8	1.8	7.9
	50	160	0.231	195	S	120	55	B_new	19.8	1.8	8.8
	50	160	0.231	195	S	120	55	B_new	19.8	1.8	6.6
	50	160	0.231	195	S	120	55	B_new	19.8	1.8	7.2
	50	160	0.231	195	S	120	55	B_new	19.8	1.8	7.8
	50	160	0.231	195	S	120	55	B_new	19.8	1.8	8.1
	50	160	0.231	195	S	120	55	B_new	19.8	1.8	9.5
	50	160	0.231	195	S	120	55	B_new	19.8	1.8	5.3
	50	160	0.231	195	S	120	55	B_new	19.8	1.8	6.9
	50	160	0.231	195	S	120	55	B_new	19.8	1.8	7.2
	50	160	0.231	195	S	120	55	B_new	19.8	1.8	10.4
	50	160	0.231	195	S	120	55	B_new	19.8	1.8	7.1

[a] C = Carbon, G = Glass, B = Basalt, S = Steel
[b] B_old = Ancient brick, B_new = Recent brick, NS_limes. = Leccese like stone or limestone, NS_tuff = Tuff
[c] where splitting test was performed $f_{tm,exp} = 0.9 f_{tm,split}$; where flexural test was performed $f_{tm,exp} = 0.5 f_{tm,flex}$

Table D.1 continued from previous page

Ref.	b_f [mm]	l_b [mm]	t_f [mm]	E_f [GPa]	Fiber[a]	b_m [mm]	h_m [mm]	Support material[b]	f_cm [MPa]	f_tm,exp [c] [MPa]	F_max [kN]
	50	160	0.231	195	S	120	55	B_new	19.8	1.8	7.9
	50	160	0.231	195	S	120	55	B_new	19.8	1.8	8.3
	50	160	0.231	195	S	120	55	B_new	19.8	1.8	8.4
	50	160	0.231	195	S	120	55	B_new	19.8	1.8	9.9
	50	160	0.231	195	S	120	55	B_new	19.8	1.8	7.7
	50	160	0.231	195	S	120	55	B_new	19.8	1.8	7.8
	50	160	0.231	195	S	120	55	B_new	19.8	1.8	8.9
	50	160	0.231	195	S	120	55	B_new	19.8	1.8	7.2
	50	160	0.231	195	S	120	55	B_new	19.8	1.8	8.5
	50	160	0.231	195	S	120	55	B_new	19.8	1.8	8.8
	50	160	0.231	195	S	120	55	B_new	19.8	1.8	9.6
	50	160	0.231	195	S	120	55	B_new	19.8	1.8	9.7
	50	160	0.231	195	S	120	55	B_new	19.8	1.8	5.8
	50	160	0.231	195	S	120	55	B_new	19.8	1.8	6.1
	50	160	0.231	195	S	120	55	B_new	19.8	1.8	7.4
	50	160	0.231	195	S	120	55	B_new	19.8	1.8	7.4
	50	160	0.231	195	S	120	55	B_new	19.8	1.8	7.9
	50	160	0.231	195	S	120	55	B_new	19.8	1.8	8.2
	50	160	0.231	195	S	120	55	B_new	19.8	1.8	12.2
	50	160	0.231	195	S	120	55	B_new	19.8	1.8	12.9
	50	160	0.231	195	S	120	55	B_new	19.8	1.8	13.9
	50	160	0.231	195	S	120	55	B_new	19.8	1.8	14.0
	50	160	0.231	195	S	120	55	B_new	19.8	1.8	6.4
	50	160	0.231	195	S	120	55	B_new	19.8	1.8	6.7
	50	160	0.231	195	S	120	55	B_new	19.8	1.8	6.8
	50	160	0.231	195	S	120	55	B_new	19.8	1.8	7.3
	50	160	0.231	195	S	120	55	B_new	19.8	1.8	8.1
	50	160	0.231	195	S	120	55	B_new	19.8	1.8	7.1
	50	160	0.231	195	S	120	55	B_new	19.8	1.8	7.3
	50	160	0.231	195	S	120	55	B_new	19.8	1.8	7.6
	50	160	0.231	195	S	120	55	B_new	19.8	1.8	8.8
	50	160	0.231	195	S	120	55	B_new	19.8	1.8	9.2
	50	160	0.231	195	S	120	55	B_new	19.8	1.8	7.1
	50	160	0.231	195	S	120	55	B_new	19.8	1.8	7.4
	50	160	0.231	195	S	120	55	B_new	19.8	1.8	8.0
	50	160	0.231	195	S	120	55	B_new	19.8	1.8	8.5
	50	160	0.231	195	S	120	55	B_new	19.8	1.8	9.2
	50	160	0.231	195	S	120	55	B_new	19.8	1.8	6.3
	50	160	0.231	195	S	120	55	B_new	19.8	1.8	6.4
	50	160	0.231	195	S	120	55	B_new	19.8	1.8	6.7
	50	160	0.231	195	S	120	55	B_new	19.8	1.8	8.7
	50	160	0.231	195	S	120	55	B_new	19.8	1.8	10.2
	50	160	0.231	195	S	120	55	B_new	19.8	1.8	4.5
	50	160	0.231	195	S	120	55	B_new	19.8	1.8	6.1
	50	160	0.231	195	S	120	55	B_new	19.8	1.8	6.3
	50	160	0.231	195	S	120	55	B_new	19.8	1.8	6.3
	50	160	0.231	195	S	120	55	B_new	19.8	1.8	6.6
[89]	80	150	0.165	234	C	100	100	NS_limes.	26.0	2.0	8.9
	80	150	0.185	246	C	100	100	NS_limes.	26.0	2.0	9.1
	80	150	0.185	246	C	100	100	NS_limes.	26.0	2.0	9.4
	80	150	0.165	234	C	100	100	NS_tuff	5.0	1.0	8.1
	80	150	0.165	234	C	100	100	NS_tuff	5.0	1.0	7.9
	80	150	0.185	246	C	100	100	NS_tuff	5.0	1.0	9.0
	80	150	0.185	246	C	100	100	NS_tuff	5.0	1.0	7.2
	80	150	0.165	234	C	200	100	NS_limes.	26.0	2.0	9.5
	80	150	0.165	234	C	200	100	NS_limes.	26.0	2.0	9.4
	80	150	0.165	234	C	200	100	NS_tuff	5.0	1.0	9.2
	80	150	0.165	234	C	200	100	NS_tuff	5.0	1.0	10.5
[156]	50	150	0.130	230	C	100	100	NS_limes.	3.7	0.2	5.0
	50	150	0.130	230	C	100	100	NS_limes.	2.3	0.2	3.9
	50	150	0.130	230	C	100	100	NS_limes.	2.2	0.2	4.7

Table D.1 continues in the next page

[a] C = Carbon, G = Glass, B = Basalt, S = Steel

[b] B_old = Ancient brick, B_new = Recent brick, NS_limes. = Leccese like stone or limestone, NS_tuff = Tuff

[c] where splitting test was performed $f_{tm,exp} = 0.9 f_{tm,split}$; where flexural test was performed $f_{tm,exp} = 0.5 f_{tm,flex}$

Table D.1 continued from previous page

Ref.	b_f [mm]	l_b [mm]	t_f [mm]	E_f [GPa]	Fiber[a]	b_m [mm]	h_m [mm]	Support material[b]	f_{cm} [MPa]	$f_{tm,exp}$ [c] [MPa]	F_{max} [kN]
	50	150	0.130	230	C	100	100	NS_limes.	2.9	0.2	4.3
	50	150	0.130	230	C	100	100	NS_limes.	4.1	0.2	4.7
	50	150	0.130	230	C	100	100	NS_limes.	4.4	0.2	4.8
	50	150	0.130	230	C	100	100	NS_limes.	3.5	0.2	3.9
	50	150	0.130	230	C	100	100	NS_limes.	3.5	0.2	4.0
	50	150	0.130	230	C	100	100	NS_limes.	2.9	0.2	4.2
	50	100	0.130	230	C	100	100	NS_limes.	4.2	0.2	4.9
	50	100	0.130	230	C	100	100	NS_limes.	2.9	0.2	4.3
	50	100	0.130	230	C	100	100	NS_limes.	3.4	0.2	4.4
	50	100	0.130	230	C	100	100	NS_limes.	3.8	0.2	4.6
	50	100	0.130	230	C	100	100	NS_limes.	3.2	0.2	4.1
	50	100	0.130	230	C	100	100	NS_limes.	3.6	0.2	3.3
	50	100	0.130	230	C	100	100	NS_limes.	3.7	0.2	4.7
	50	100	0.130	230	C	100	100	NS_limes.	3.3	0.2	3.4
[150]	50	120	0.170	240	C	140	35	B_old	24.9	1.9	8.4
	50	150	0.170	240	C	140	35	B_old	24.9	1.9	8.5
	50	180	0.170	240	C	140	35	B_old	24.9	1.9	9.0
	50	210	0.170	240	C	140	35	B_old	24.9	1.9	9.0
	50	290	0.170	240	C	140	35	B_old	24.9	1.9	9.0
	50	290	0.170	240	C	140	35	B_old	24.9	1.9	9.0
	50	150	0.170	240	C	120	55	B_new	17.4	1.9	7.6
	50	215	0.170	240	C	120	55	B_new	17.4	1.9	8.5
	50	240	0.170	240	C	120	55	B_new	17.4	1.9	8.6
	50	215	0.170	240	C	120	55	B_new	40.2	1.9	7.4
	50	230	0.170	240	C	120	55	B_new	40.2	1.9	8.3
	50	235	0.170	240	C	120	55	B_new	40.2	1.9	9.7
	50	240	0.170	240	C	120	55	B_new	40.2	1.9	8.5
	50	250	0.170	240	C	120	55	B_new	40.2	1.9	10.2
[151]	50	200	0.172	124	G	120	55	B_old	16.3	1.8	4.4
	50	200	0.172	124	G	120	55	B_old	16.3	1.8	4.5
	50	200	0.172	124	G	120	55	B_old	18.2	3.0	5.0
	50	200	0.172	124	G	120	55	B_old	18.2	3.0	6.3
	50	200	0.172	124	G	110	60	B_old	32.9	3.6	7.1
	50	200	0.172	124	G	110	60	B_old	32.9	3.6	7.3
	50	200	0.172	124	G	127	50	B_old	29.2	4.9	6.0
[148]	50	250	0.120	70	G	120	50	B_old	15.4	1.6	3.7
	50	250	0.120	70	G	120	50	B_old	15.4	1.6	6.5
	50	250	0.120	70	G	120	50	B_old	15.4	1.6	6.5
	50	250	0.120	70	G	120	50	B_old	15.4	1.6	5.7
	50	250	0.120	70	G	120	50	B_old	15.4	1.6	7.5
[152]	100	300	0.164	230	C	250	110	NS_tuff	3.8	0.4	22.8
	100	300	0.164	230	C	250	110	NS_tuff	3.8	0.4	19.1
	100	300	0.164	230	C	250	110	NS_tuff	3.8	0.4	18.1
	100	300	0.164	230	C	250	110	NS_tuff	3.8	0.4	18.9
	100	300	0.480	81	G	250	110	NS_tuff	3.8	0.4	19.3
	100	300	0.480	81	G	250	110	NS_tuff	3.8	0.4	22.5
	100	300	0.480	81	G	250	110	NS_tuff	3.8	0.4	18.1
	100	300	0.480	81	G	250	110	NS_tuff	3.8	0.4	16.4
	100	300	0.480	81	G	250	110	NS_tuff	3.8	0.4	17.2
[153]	100	200	0.165	230	C	206	260	NS_tuff	2.0	-	10.0
	100	200	0.165	230	C	206	260	NS_tuff	2.0	-	15.0
[155]	80	150	0.165	245	C	100	100	NS_limes.	31.0	3.9	9.8
[154]	80	150	0.165	234	C	100	100	NS_limes.	24.0	3.3	9.5
	80	150	0.165	234	C	100	100	NS_limes.	24.0	3.3	11.5
	80	150	0.165	234	C	100	100	NS_limes.	24.0	3.3	11.6
	80	150	0.165	234	C	100	100	NS_limes.	24.0	3.3	11.0
	80	150	0.370	81	G	100	100	NS_limes.	24.0	3.3	6.2
	80	150	0.165	234	C	100	100	NS_tuff	5.5	0.8	9.8
	80	150	0.370	81	G	100	100	NS_tuff	5.5	0.8	7.8
	80	150	0.165	234	C	100	100	NS_tuff	4.1	0.4	12.8
	80	150	0.370	81	G	100	100	NS_tuff	4.1	0.4	11.0

Table D.1 ends from the previous page

[a] C = Carbon, G = Glass, B = Basalt, S = Steel

[b] B_old = Ancient brick, B_new = Recent brick, NS_limes. = Leccese like stone or limestone, NS_tuff = Tuff

[c] where splitting test was performed $f_{tm,exp} = 0.9 f_{tm,split}$; where flexural test was performed $f_{tm,exp} = 0.5 f_{tm,flex}$

References

[1] P. Carrara, D. Ferretti, F. Freddi, G. Rosati, Shear tests of carbon fiber plates bonded to concrete with control of snap-back, Eng Fract Mech 78 (15) (2011) 2663–2678. vii, xvii, 63, 68, 112, 113, 114, 115, 122, 123, 127, 147

[2] M. J. Chajes, W. W. Finch, T. F. Januszka, T. A. J. Thomson, Bond and force transfer of composite-material plates bonded to concrete, ACI Struct J 93 (2) (1996) 208–217. vii, xvii, 8, 9, 10, 112, 113, 114, 118, 120

[3] C. Mazzotti, M. Savoia, B. Ferracuti, An experimental study on delamination of FRP plates bonded to concrete, Constr Build Mater 22 (7) (2008) 1409–1421. vii, xvii, 7, 9, 10, 12, 19, 20, 35, 37, 49, 50, 64, 79, 81, 112, 113, 114, 119, 120, 121, 127, 147, 148

[4] H. Ko, Y. Sato, Bond stress–slip relationship between FRP sheet and concrete under cyclic load, J Compos Constr 11 (4) (2007) 419–426. vii, xviii, 28, 29, 128, 130, 139, 140, 141, 142, 143

[5] C. Carloni, K. V. Subramaniam, M. Savoia, C. Mazzotti, Experimental determination of FRP–concrete cohesive interface properties under fatigue loading, Compos Struct 94 (4) (2012) 1288–1296. vii, xviii, 28, 35, 128, 130, 139, 140, 143, 144, 145, 179

[6] B. Ferracuti, M. Savoia, C. Mazzotti, Interface law for FRP–concrete delamination, Compos Struct 80 (4) (2007) 523–531. xiii, 10, 12, 15, 16, 19, 22, 48, 53, 54, 83, 92, 95, 103, 122, 123

[7] CNR, DT-200/2004 - Guide for the Design and Construction of Externally Bonded FRP Systems for Strengthening Existing Structures, National Research Council, Rome, Italy, 2004. xiii, xxvii, 19, 26, 48, 52, 53, 54, 55, 71, 82, 83, 84, 87, 148, 149

[8] CNR, DT-200/2012 - Istruzioni per la progettazione, l'esecuzione ed il controllo di interventi di consolidamento statico mediante l'utilizzo di compositi fibrorinforzati (in Italian), Consiglio Nazionale delle Ricerche, Rome, Italy, 2012. xix, xx, xxii, xxvii, 2, 5, 8, 9, 23, 26, 92, 95, 112, 122, 123, 130, 147, 148, 149, 150, 154, 156, 157, 158, 159, 161, 162, 164, 165, 166, 168, 169, 170, 172, 173, 174, 175

[9] FIB, Bulletin 14 - Externally bonded FRP reinforcement for RC structures, Fèdèration International du Bèton, Lausanne, Switzerland, 2001. xix, xxvii, 23, 26, 36, 52, 53, 55, 71, 87, 95, 112, 130, 147, 149, 151, 156, 157, 158, 159

[10] ACI, 440.2R-08. Guide for the design and construction of externally bonded FRP systems for strengthening concrete structures, American Concrete Institute, Farmington Hills, Michigan, 2008. xix, xxvii, 8, 9, 150, 156, 157, 158, 159

[11] JSCE, Recommendations for upgrading of concrete structures with use of continuous fiber sheets, Japan Society of Civil Engineers, Concrete Engineering Series, Tokyo, Japan, 2001. xix, xxvii, 2, 19, 147, 150, 156, 157, 158

[12] J. Chen, J. Teng, Anchorage strength models for FRP and steel plates bonded to concrete, J Struct Eng 127 (7) (2001) 784–791. xix, 8, 14, 23, 95, 151, 156, 157, 158

[13] R. Niedermeier, Stellungnahme zur richtlinie für das verkleben von betonbautelien durch ankleben von stahllaschen (in German), University of Munich, Munich, Germany, 1996. xix, 149, 151, 156, 157, 158, 159

[14] Italian ministry for cultural heritage and activities, Guidelines for evaluation and mitigation of seismic risk to cultural heritage. (ISBN: 978-88-492-1269-3), Gengemi ed., Rome, Italy, 2007. 1

[15] US department of the interior, Standards for rehabilitation & illustrated guidelines on sustainability for rehabilitating historic buildings, Washington DC, USA, 1997. 1

[16] M. Corradi, A. Borri, A. Vignoli, Strengthening techniques tested on masonry structures struck by the Umbria–Marche earthquake of 1997–1998, Constr Build Mater 16 (4) (2002) 229–239. 1, 7

[17] E. Cosenza, I. Iervolino, Case study: seismic retrofitting of a medieval bell tower with FRP, J Compos Constr (June) (2007) 319–327. 1, 7

[18] S. Smith, J. Teng, FRP-strengthened RC beams. I: review of debonding strength models, Eng Struct 24 (4) (2002) 385–395. 2, 7, 95, 107

[19] German Commitee for Reinforced Concrete, DafStb Guideline. On the reinforcement of concrete parts with adhesive bonding (Draft 2012), Deutscher Ausschuss für Stahlbeton e. V. – DAfStb, Berlin-Tiergarten, Germany, 2012. 2, 165, 168

[20] European Committee for Standardization, BS EN 1990:2002 - Eurocode 0: Basis of structural design, in: Eurocode 0, Vol. 1, UNI-EN, Bruxelles, Belgium, 2002. 5, 148, 169, 173

[21] O. Buyukozturk, B. Hearing, Failure behavior of pre-cracked concrete beams retrofitted with FRP, J Compos Constr 2 (3) (1998) 138–144. 7

[22] T. Krevaikas, T. Triantafillou, Masonry confinement with fiber-reinforced polymers, J Compos Constr (2) (2005) 128–135.

[23] R. Olivito, F. Zuccarello, Experimental analysis on durability of brick-masonry panels subjected to cyclic loads, Struct Dur & Health Mon 2 (1) (2006) 19–27. 7

[24] L. Ascione, L. Feo, Modeling of composite/concrete interface of RC beams strengthened with composite laminates, Compos Part B - Eng 31 (6-7) (2000) 535–540. 7, 92, 105, 147

REFERENCES

[25] K. V. Subramaniam, C. Carloni, L. Nobile, Width effect in the interface fracture during shear debonding of FRP sheets from concrete, Eng Fract Mech 74 (4) (2007) 578–594. 7, 8, 9, 11, 12, 13, 19, 25, 28, 35, 64, 86, 93, 150

[26] T. Triantafillou, N. Plevris, Strengthening of RC beams with epoxy-bonded fibre-composite materials, Mater Struct (1992) 201–211. 7, 15, 16

[27] D. J. Oehlers, Ductility of FRP plated flexural members, Cem Concr Compos 28 (10) (2006) 898–905. 7

[28] D. V. Oliveira, I. Basilio, P. B. Lourenço, Experimental bond behavior of FRP sheets glued on brick masonry, J Compos Constr 15 (1) (2011) 32–41. 8, 12, 19, 20, 27, 86

[29] J. Teng, S. Smith, J. Yao, J. Chen, Intermediate crack-induced debonding in RC beams and slabs, Constr Build Mater 17 (6-7) (2003) 447–462. 8, 9

[30] C. Mazzotti, M. Savoia, B. Ferracuti, A new single-shear set-up for stable debonding of FRP–concrete joints, Constr Build Mater 23 (4) (2009) 1529–1537. 7, 8, 9, 12, 19, 23, 24, 25, 35, 37, 148

[31] J. Chen, W. Pan, Three dimensional stress distribution in FRP-to-concrete bond test specimens, Constr Build Mater 20 (1-2) (2006) 46–58. 8, 9, 23

[32] C. Carloni, K. V. Subramaniam, FRP-Masonry debonding: numerical and experimental study of the role of mortar joints, J Compos Constr 16 (5) (2012) 581–589. 9, 10, 152, 196

[33] E. Grande, M. Imbimbo, E. Sacco, Bond behaviour of CFRP laminates glued on clay bricks: Experimental and numerical study, Compos Part B - Eng 42 (2) (2011) 330–340. 8, 9, 12, 27, 86, 123, 147, 152, 195

[34] J. Yao, J. Teng, J. Chen, Experimental study on FRP-to-concrete bonded joints, Compos Part B - Eng 36 (2) (2005) 99–113. 8, 19, 23, 24, 41

[35] J. Chen, Z. Yang, G. Holt, Frp or steel plate-to-concrete bonded joints: Effect of test methods on experimental bond strength, Steel Compos Struct 1 (2) (2001) 231–244. 8, 19, 23

[36] M. Ali-Ahmad, K. Subramaniam, M. Ghosn, Experimental investigation and fracture analysis of debonding between concrete and FRP Sheets, J Eng Mech 132 (9) (2006) 914–923. 9, 11, 12, 13, 20, 25, 35, 77, 81, 103, 152

[37] C. Carloni, K. Subramaniam, Investigation of the interface fracture during debonding between FRP and masonry, Adv Strct Eng 12 (5) (2009) 731–743. 12, 13, 16, 20, 26, 27, 28, 71, 86, 152

[38] E. Grande, M. Imbimbo, E. Sacco, Bond behavior of historical clay bricks strengthened with steel reinforced polymers (SRP), Materials 4 (3) (2011) 585–600. 9, 26, 27, 62, 65, 71, 74, 147, 152, 154, 180, 195

[39] M. Ali-Ahmad, K. V. Subramaniam, M. Ghosn, Analysis of scaling and instability in FRP-concrete shear debonding for beam-strengthening applications, J Eng Mech 133 (1) (2007) 58–65. 9, 10, 11, 12, 13, 14, 35

[40] B. Ferracuti, M. Savoia, C. Mazzotti, A numerical model for FRP-concrete delamination, Compos Part B - Eng 37 (4-5) (2006) 356–364. 22, 23, 24, 88, 92, 96, 102, 103, 115, 123, 147

[41] F. Freddi, M. Savoia, Analysis of FRP-concrete debonding via boundary integral equations, Eng Fract Mech 75 (6) (2008) 1666–1683. 9, 10, 12, 15, 16, 19, 23, 35, 37, 51, 53, 54, 55, 57, 103, 147

[42] O. Buyukozturk, O. Gunes, E. Karaca, Progress on understanding debonding problems in reinforced concrete and steel members strengthened using FRP composites, Constr Build Mater 18 (1) (2004) 9–19. 11

[43] C. K. Leung, Delamination failure in concrete beams retrofitted with a bonded plate, J Mater Civ Eng (April) (2001) 106–113. 11

[44] B. Täljsten, Strengthening of Beams by Plate Bonding, J Mater Civ Eng 9 (4) (1997) 206–212. 12, 14, 15, 18, 19

[45] Z. Wu, H. Yuan, H. Niu, Stress Transfer and Fracture Propagation in Different Kinds of Adhesive Joints, J Eng Mech 128 (5) (2002) 562–573. 14, 15, 16, 18, 22, 95

[46] X. Lu, J. Teng, L. Ye, J. Jiang, Bond–slip models for FRP sheets/plates bonded to concrete, Eng Struct 27 (6) (2005) 920–937. 12, 14, 19, 20, 22, 95

[47] L. Bizindavyi, K. Neale, Transfer lengths and bond strengths for composites bonded to concrete, J Compos Constr (November) (1999) 153–160. 14

[48] H. Yuan, J. Teng, R. Seracino, Z. Wu, J. Yao, Full-range behavior of FRP-to-concrete bonded joints, Eng Struct 26 (5) (2004) 553–565. 14, 18, 20, 22, 28, 129, 161

[49] B. Täljsten, Strengthening of concrete prisms using the plate-bonding technique, Int J Fract 82 (3) (1996) 253–266. 14, 15, 16, 18, 95

[50] H. Yuan, Z. Wu, H. Yoshizawa, Theoretical solutions on interfacial stress transfer of externally bonded steel/composite laminates, Struct Eng Earthq 18 (1) (2001) 27s–39s. 14, 22, 95, 161

[51] O. Rabinovitch, Fracture-mechanics failure criteria for RC beams strengthened with FRP strips—a simplified approach, Compos Struct 64 (3-4) (2004) 479–492. 15, 16, 20

[52] A. Hillerborg, The theoretical basis of a method to determine the fracture energy G_F of concrete, Mater & Struct 18 (106) (1985) 291–296. 15

[53] L. De Lorenzis, G. Zavarise, Modeling of mixed-mode debonding in the peel test applied to superficial reinforcements, Int J Sol Struct 45 (20) (2008) 5419–5436. 15, 19, 22, 88, 92, 95, 102, 105, 109, 130, 147

[54] A. Franco, G. Royer-Carfagni, Energetic balance in the debonding of a reinforcing stringer: Effect of the substrate elasticity, Int J Sol Struct 50 (11-12) (2013) 1954–1965. 16, 147

[55] E. Grande, M. Imbimbo, E. Sacco, Simple model for bond behavior of masonry elements strengthened with FRP, J Compos Constr 15 (June) (2011) 354. 18, 27, 83, 103

[56] K. Brosens, Anchorage of externally bonded steel plates and CFRP laminates for the strengthening of concrete elements, Ph.D. thesis, Katholieke University of Leuven (2001). 19, 23, 83

[57] J. Pan, C. K. Leung, Debonding along the FRP–concrete interface under combined pulling/peeling effects, Eng Fract Mech 74 (1-2) (2007) 132–150. 19, 24, 41

[58] M. R. Valluzzi, D. V. Oliveira, A. Caratelli, et al., Round Robin Test for composite-to-brick shear bond characterization, Mater & Struct 45 (12) (2012) 1761–1791. 24, 147, 148, 152, 196

[59] L. De Lorenzis, B. Miller, A. Nanni, Bond of FRP laminates to concrete, ACI Mater J 98 (3) (2001) 256–264. 23, 25, 37, 147

[60] H. Toutanji, G. Ortiz, The effect of surface preparation on the bond interface between FRP sheets and concrete members, Compos Struct 53 (4) (2001) 457–462. 19, 37

[61] O. Rabinovitch, Cohesive interface modeling of debonding failure in FRP strengthened beams, J Eng Mech 134 (7) (2008) 578–588. 19, 20, 22, 88, 92, 95, 102, 103, 105, 130

[62] C. Carloni, K. V. Subramaniam, Direct determination of cohesive stress transfer during debonding of FRP from concrete, Compos Struct 93 (1) (2010) 184–192. 93, 147

[63] L. De Lorenzis, D. Fernando, J.-G. Teng, Coupled mixed-mode cohesive zone modeling of interfacial debonding in simply supported plated beams, Int J Sol Struct 50 (14-15) (2013) 2477–2494. 19, 92, 103

[64] A. Turon, P. Camanho, J. Costa, C. Dávila, A damage model for the simulation of delamination in advanced composites under variable-mode loading, Mech Mater 38 (11) (2006) 1072–1089. 19, 22, 92, 108, 111

[65] A. Turon, P. Camanho, J. Costa, An interface damage model for the simulation of delamination under variable-mode ratio in composite materials, NASA Technical report (October). 19, 28, 29, 128

[66] L. De Lorenzis, Some recent results and open issues on interface modeling in civil engineering structures, Mater & Struct 45 (4) (2012) 477–503. 19, 20, 22, 23, 48, 92, 93, 103, 147

[67] A.-H. Zureick, R. M. Bennett, B. R. Ellingwood, Statistical characterization of fiber-reinforced polymer composite material properties for structural design, J Struct Eng 132 (8) (2006) 1320–1327. 19

[68] C. Faella, G. Camorani, E. Martinelli, S. O. Paciello, F. Perri, Bond behaviour of FRP strips glued on masonry: Experimental investigation and empirical formulation, Constr Build Mater 31 (2012) 353–363. 19, 152, 154, 173, 196

[69] A. Griffith, The phenomena of rupture and flow in solids, Phil Trans Royal Soc London A: Math Phys & Eng Sci 221 (1921) 163–198. 20

[70] O. Rabinovitch, Debonding analysis of fiber-reinforced-polymer strengthened beams: Cohesive zone modeling versus a linear elastic fracture mechanics approach, Eng Fract Mech 75 (10) (2008) 2842–2859. 20

[71] G. Alfano, M. Crisfield, Finite element interface models for the delamination analysis of laminated composites: mechanical and computational issues, Int J Numer Meth Engng 50 (7) (2001) 1701–1736. 20, 22, 53, 110

[72] G. Alfano, E. Sacco, Combining interface damage and friction in a cohesive-zone model, Int J Numer Meth Eng 68 (5) (2006) 542–582. 20, 22, 110

[73] G. I. Barenblatt, The formation of equilibrium cracks during brittle fracture. General ideas and hypotheses. Axially-simmetric cracks, Prikl Mat Mech 23 (3) (1959) 434–444. 20, 21, 105

[74] G. I. Barenblatt, The mathematical theory of equilibrium cracks formed in brittle fracture, Prikl Mat Mech 4 (1961) 3–56.

[75] D. Dugdale, Yielding of steel sheets containing slits, J Mech Phys Sol 8 (2) (1960) 100 – 104.

[76] A. Hillerborg, M. Modeer, P. Petersson, Analysis of crack formation and crack growth in concrete by means of fracture mechanics and finite elements, Cem Concr Res 6 (1976) 773–782. 20, 21, 22, 105

[77] L. De Lorenzis, G. Zavarise, Interfacial stress analysis and prediction of debonding for a thin plate bonded to a curved substrate, Int J Nonlin Mech 44 (4) (2009) 358–370. 22, 92

[78] E. Martinelli, C. Czaderski, M. Motavalli, Modeling in-plane and out-of-plane displacement fields in pull-off tests on FRP strips, Eng Struct 33 (12) (2011) 3715–3725. 22, 88, 92, 102, 105

[79] F. Ceroni, B. Ferracuti, M. Pecce, M. Savoia, FRP externally bonded systems for a sustainable strengthening of masonry structures, in: Proc. of the 4th Int. Conf. on durability & sustainability of Fibre Reinforced Polymer (FRP) composites for construction and rehabilitation, CDCC, Quebec City, Canada, 2011. 23, 150, 162

[80] D. Ferretti, E. Coïsson, G. Rosati, Test on bond between concrete and cfrp by means of espi interferometry, in: Proceedings of FRPRCS-8 conference, University of Patras, Patras, Greece, July, 2007, pp. 1–10. 23

[81] M. Savoia, C. Mazzotti, B. Ferracuti, et al., Effetto del sistema di prova sulla resistenza per aderenza calcestruzzo-FRP. (In italian), in: XX Convegno IGF Torino 2009, 24-26 June, 2009, pp. 225–236. 24

[82] M. Savoia, A. Bilotta, F. Ceroni, M. Di Ludovico, G. Fava, B. Ferracuti, C. Mazzotti, E. Nigro, R. Olivito, M. Pecce, C. Poggi, Experimental Round Robin test on FRP–concrete bonding, in: I. Australia (Ed.), Proceedings of FRPRCS-9, Sydney Australia, 13-15 July 2009, 2009, pp. 1–4. 24

[83] P. Carrara, D. Ferretti, A finite-difference model with mixed interface laws for shear tests of FRP plates bonded to concrete, Compos Part B - Eng 54 (2013) 329–342. 24, 28, 122, 123, 130, 147, 160

[84] A. Aprile, L. Feo, Concrete cover rip-off of R/C beams strengthened with FRP composites, Compos Part B - Eng 38 (5-6) (2007) 759–771. 25

REFERENCES

[85] E. Benvenuti, O. Vitarelli, A. Tralli, Delamination of FRP-reinforced concrete by means of an extended finite element formulation, Compos Part B - Eng 43 (8) (2012) 3258–3269. 25, 107

[86] K. Benzarti, F. Freddi, M. Frémond, A damage model to predict the durability of bonded assemblies. Part I: Debonding behavior of FRP strengthened concrete structures, Constr Build Mater 25 (2) (2011) 547–555. 53, 92, 147, 180

[87] L. De Lorenzis, G. Zavarise, Cohesive zone modeling of interfacial stresses in plated beams, Int J Sol Struct 46 (24) (2009) 4181–4191. 25, 88, 95, 102, 103, 105, 130

[88] M. Aiello, M. Sciolti, Masonry structures strengthened with frp sheets: experimental investigation of bond between frp laminates and ashlars, Int J Rest Build Monum 9 (6) (2003) 639–662. 26, 27

[89] M. A. Aiello, M. S. Sciolti, Bond analysis of masonry structures strengthened with CFRP sheets, Constr Build Mater 20 (1-2) (2006) 90–100. 152, 154, 173, 200

[90] M. Aiello, M. Sciolti, T. Triantafillou, Experimental debonding tests between ancient masonry and CFRP, in: Proceedings of FRPRCS-8 conference, University of Patras, Patras, Greece, July, 2007, pp. 1–9. 26

[91] L. Ascione, L. Feo, F. Fraternali, Load carrying capacity of 2D FRP/strengthened masonry structures, Compos Part B - Eng 36 (8) (2005) 619–626. 27

[92] R. Capozucca, Experimental FRP/SRP–historic masonry delamination, Compos Struct 92 (4) (2010) 891–903. 27, 152, 196

[93] C. Willis, Q. Yang, R. Seracino, M. Griffith, Bond behaviour of FRP-to-clay brick masonry joints, Eng Struct 31 (11) (2009) 2580–2587. 27

[94] K. V. Subramaniam, C. Carloni, L. Nobile, An understanding of the width effect in FRP-concrete debonding, Strain 47 (2) (2011) 127–137. 28, 35, 93, 147, 150

[95] C. Carloni, K. V. Subramaniam, Investigation of subcritical fatigue crack growth in FRP/concrete cohesive interface using digital image analysis, Compos Part B - Eng 51 (2013) 35–43. 28, 128, 130, 143, 179

[96] T. Leusmann, H. Budelmann, Fatigue design concept for externally bonded CFRP-plates, in: Proc. of the 6th International Conference on FRP Composites in Civil Engineering, International Institute for FRP in Costruction (IIFC), Rome, Italy, 2012, pp. 1–9. 28, 128, 130

[97] A. Nizic, R. Niedermeier, K. Zilch, Behavior of externally bonded reinforcement under low cycle fatigue loading, in: Proc. of FRPRCS-9 Conference, Vol. 1, Sydney, Australia, 2009, pp. 13–16.

[98] L. Bizindavyi, K. W. Neale, M. a. Erki, Experimental Investigation of Bonded Fiber Reinforced Polymer-Concrete Joints under Cyclic Loading, J Compos Constr 7 (2) (2003) 127–134. 128

[99] E. Ferrier, Fatigue of CFRPs externally bonded to concrete, Mater Struct 38 (275) (2004) 39–46. 28, 128

[100] P. Camanho, C. G. Dávila, M. de Moura, Numerical simulation of mixed-mode progressive delamination in composite materials, J Comp Mater 37 (16) (2003) 1415–1438. 28, 29, 128

[101] K. Roe, T. Siegmund, An irreversible cohesive zone model for interface fatigue crack growth simulation, Eng Fract Mech 70 (2) (2003) 209–232. 28, 29, 128

[102] O. Nguyen, E. Repetto, M. Ortiz, R. Radovitzky, A cohesive model of fatigue crack growth, International Journal of Fracture 110 (4) (2001) 351–369. 28, 29, 128

[103] J. Lemaitre, Coupled elast-plasticity and damage constitutive equation, Comp Meth App Mech Eng 51 (1985) 31–49. 28, 131, 133, 134

[104] J. Lemaitre, R. Desmorat, Engineering damage mechanics, Springer-Verlag, Berlin/Heidelberg, 2005. 28, 130, 132, 133, 136

[105] E. Martinelli, A. Caggiano, A novel numerical approach for modelling the monotonic and cyclic response of FRP strips glued to concrete, in: Proc. of the second conference on smart monitoring assessment and rehabilitation of civil structures, Istanbul, Turkey, 2013, pp. 1–8. 29

[106] E. Martinelli, A. Caggiano, A Unified Theoretical Model for the Monotonic and Cyclic Response of FRP Strips Glued to Concrete, Polymers 6 (2) (2014) 370–381. 29, 128

[107] B. Ghiassi, G. Marcari, D. V. Oliveira, P. B. Lourenço, Numerical analysis of bond behavior between masonry bricks and composite materials, Eng Struct 43 (2012) 210–220. 35

[108] B. Ghiassi, J. Xavier, D. V. Oliveira, P. B. Lourenço, Application of digital image correlation in investigating the bond between FRP and masonry, Compos Struct 106 (2013) 340–349. 35, 180

[109] A. Bilotta, C. Faella, E. Martinelli, E. Nigro, Indirect identification method of bilinear interface laws for FRP bonded on a concrete substrate, J Compos Constr (2) (2011) 171–184. 35, 82

[110] European Committee for Standardization, BS EN 1992-1-1:2004 - Eurocode 2: Design of concrete structures - Part 1-1: General rules and rules for buildings, in: Eurocode 2, Vol. 1, UNI-EN, Bruxelles, Belgium, 2004, Ch. 2:1-1. 38, 113, 165, 168

[111] ASTM International, D638-08, Standard test method for tensile properties of plastics, ASTM International, West Conshohocken, USA, 2008. 38

[112] ASTM International, D3039/D3039M-08 - Standard test method for tensile properties of polymer matrix composite materials, ASTM International, West Conshohocken, USA, 2008. 39

[113] W. Bangerth, R. Hartmann, G. Kanschat, dealii Differential equations analysis library. Technical reference, http://www.dealii.org, West Conshohocken, USA, 2010. 52

[114] I. M. May, Y. Duan, A local arc-length procedure for strain softening, Compos Struct 64 (1-4) (1997) 297–303. 53

[115] F. Freddi, M. Frémond, Damage in domains and interfaces: a coupled predictive theory, J Mech Mater Struct 1 (7) (2006) 1205–1233. 53, 92

[116] S. Marfia, E. Sacco, J. Toti, A coupled interface-body nonlocal damage model for FRP strengthening detachment, Comput Mech 50 (3) (2011) 335–351. 53, 126, 147

[117] D. Ferretti, M. Savoia, Non-linear model for R/C tensile members strengthened by FRP-plates, Eng Fract Mech 124 (9) (2003) 1041–1083. 55, 96, 103, 123

[118] C. Leung, V. Li, Applications of a two-way debonding theory to short fibre composites, Composites 21 (4) (1990) 305 – 317. 57, 86, 88

[119] Interbau SRL, Voce di capitolato Carbostru T-System. Scheda tecnica rinforzo. (In italian), Milan, Italy, 2009. 63, 65, 68

[120] UNI, UNI-EN 772-11 - Methods of test of masonry units - Part 11: determination of water absorption of aggregate concrete, manufactured stone and natural stonemasonry unitsdue to capillaryaction and the initial rate of water absorption of clay masonry units, UNI, Brussels, Belgium, 2006. 65

[121] CNR-ICR, Document 14/83. Sezioni sottili e lucide di materiali lapidei: tecnica di allestimento. (In italian), CNR-ICR, Rome, Italy, 1983. 65

[122] UNI, UNI-EN 1015-11 - Methods of test for mortar for masonry - Part 11: determination of flexural and compressive strength of hardened mortar, UNI, Brussels, Belgium, 2007. 67

[123] P. Carrara, D. Ferretti, F. Freddi, Experimental tests on progressive debonding in ancient masonry prisms reinforced with CFRP sheets, in: Proceedings of the XX AIMETA congress, Published on-line, Bologna, 2011, pp. 1–10. 74, 81

[124] U. Neubauer, F. Rostasy, Bond failure of concrete fiber reinforced polymer plates at inclined cracks-experiments and fracture mechanics model, ACI Spec Pub 188 (1999) 369–382. 92

[125] H. Yuan, J. Chen, J. Teng, X. Lu, Interfacial stress analysis of a thin plate bonded to a rigid substrate and subjected to inclined loading, Int J Sol Struct 44 (16) (2007) 5247–5271. 92

[126] C. Czaderski, K. Soudki, M. Motavalli, Front and side view image correlation measurements on FRP to concrete pull-off bond tests, J Compos Constr 14 (4) (2010) 451–463. 93, 122

[127] F. Ascione, Mechanical behaviour of FRP adhesive joints: A theoretical model, Compos Part B - Eng 40 (2) (2009) 116–124. 95, 105, 109, 147

[128] U. Ascher, Numerical solution of boundary value problems for ordinary differential equations, Prentice-Hall, Englewood Cliffs, New Jersey, 1995. 96

[129] S. Smith, J. Teng, Interfacial stresses in plated beams, Eng Struct 23 (7) (2001) 857–871. 105

[130] I. Carol, C. Pere, M. Carlos, Normal/shear cracking model: application to discrete crack analysis, J Eng Mech 123 (8) (1997) 765–773. 107

[131] Comité Euro-International du Béton, CEB-FIP Model Code 1990, CEB-FIP, Lausanne, Switzerland, 1993. 113

[132] H. Diab, Z. Wu, K. Iwashita, Theoretical solution for fatigue debonding growth and fatigue life prediction of FRP-concrete interfaces, in: S. Smith (Ed.), Proc. of the Asia-Pacific conference on FRP in structures, APFIS, International Institute for FRP in Costruction (IIFC), 2007, pp. 913–922. 128

[133] J. Simo, T. Hughes, Computational inelasticity, Vol. 7, Springer-Verlag, Berlin/Heidelberg, 1998. 130, 131, 132, 136, 138, 189, 191

[134] J. Lemaitre, How to use damage mechanics, Nucl Eng Des 80 (1984) 233–245. 131, 133, 134

[135] E. W. V. Chaves, Notes on Continuum Mechanics, Lecture notes on numerical methods in engineering and sciences, Springer Netherlands, Dordrecht, 2013. 132, 133

[136] P. Argoul, K. Benzarti, F. Freddi, M. Frémond, T.-H. T. Nguyen, A damage model to predict the durability of bonded assemblies. Part II: Parameter identification and preliminary results for accelerated ageing tests, Constr Build Mater 25 (2) (2011) 556 – 567. 147, 180

[137] J. Toti, S. Marfia, E. Sacco, Coupled body-interface nonlocal damage model for FRP detachment, Comp Meth App Mech Eng 260 (2013) 1–23.

[138] G. Ruocci, P. Argoul, K. Benzarti, F. Freddi, An improved damage modelling to deal with the variability of fracture mechanisms in FRP reinforced concrete structures, Int J Adhes Adhes 45 (2013) 7–20.

[139] F. Ascione, Ultimate behaviour of adhesively bonded FRP lap joints, Compos Part B - Eng 40 (2) (2009) 107–115.

[140] F. Ceroni, A. Garofano, M. Pecce, Modelling of the bond behaviour of tuff elements externally bonded with FRP sheets, Compos Part B - Eng 59 (2014) 248–259. 147, 154

[141] P. Carrara, D. Ferretti, F. Freddi, Debonding behavior of ancient masonry elements strengthened with CFRP sheets, Compos Part B - Eng 45 (1) (2013) 800–810. 147, 149, 150, 152, 154, 162, 180, 195

[142] Y. J. Kim, K. A. Harries, Statistical Characterization of Reinforced Concrete Beams Strengthened with FRP Sheets, J Compos Constr 17 (3) (2013) 357–370. 148, 161

[143] F. Ceroni, B. Ferracuti, M. Pecce, M. Savoia, Assessment of a bond strength model for FRP reinforcement externally bonded over masonry blocks, Compos Part B - Eng 61 (2014) 147–161. 150, 154, 173, 174

[144] T. D'Antino, C. Pellegrino, Bond between FRP composites and concrete: assessment of design procedures and analytical models, Compos Part B - Eng 60 (2014) 440–456. 148

REFERENCES

[145] Z. Wu, H. Niu, Prediction of crack-induced debonding failure in R/C structures flexurally strengthened with externally bonded FRP composites, Doboku Gakkai Ronbunshuu E 63 (4) (2007) 620–639. 150

[146] U. Neubauer, F. S. Rostasy, Design aspects of concrete structures strengthened with externally bonded CFRP plates, in: Proc. 7th Int. Conf. on Structural Faults and Repairs, ECS, Edinburgh, Scotland, 1997, pp. 109–118. 151

[147] O. Holzenkämpfer, Ingenieurmodelle des verbundes geklebter bewehrung für betonbauteile (in German), Ph.D. thesis, University of Braunschweig, Braunschweig, Germany (1994). 151

[148] R. Capozucca, Effects of mortar layers in the delamination of GFRP bonded to historic masonry, Compos Part B - Eng 44 (1) (2013) 639–649. 152, 154, 201

[149] M. Panizza, E. Garbin, M. R. Valluzzi, C. Modena, Bond behaviour of CFRP and GFRP laminates on brick masonry, in: D'Ayala & Fodde (Ed.), Proc. of the 6th Int. Conf. on structural analysis of historical constructions, SAHC, Taylor & Francis, Bath, United Kingdom, 2008. 195

[150] R. Capozucca, Behavior of CFRP sheets bonded to historical masonry, in: S. Smith (Ed.), Proc. of the Asia-Pacific conference on FRP in structures - APFIS, International Institute for FRP in Costruction (IIFC), Hong Kong, China, 2007, pp. 723–728. 201

[151] C. Mazzotti, B. Ferracuti, A. Bellini, Experimental bond tests on masonry panels strengthening by FRP, in: Proc. of 6th Int. Conf. on FRP composites in civil engineering, CICE, International Institute for FRP in Costruction (IIFC), Rome, Italy, 2012. 201

[152] F. Ceroni, M. Pecce, A. Garofano, Bond tests on masonry elements externally strengthened with FRP materials, in: Proc. of 6th Int. Conf. on FRP composites in civil engineering, CICE, International Institute for FRP in Costruction (IIFC), Rome, Italy, 2012. 201

[153] E. Cosenza, G. Manfredi, A. Occhiuzzi, M. R. Pecce, Toward the investigation of the interface behavior between tuff masonry and FRP fabrics, in: Proc. of the Conf. on mechanics of masonry structures strengthened with FRP materials: testing, design, control, Venice, Italy, 2000. 201

[154] M. A. Aiello, M. S. Sciolti, Analysis of bond performance between FRP sheets and calcarenite stones under service and ultimate conditions, Mason Int 21 (1) (2008) 15–28. 154, 173, 201

[155] M. S. Sciolti, M. A. Aiello, M. Frigione, Influence of water on bond behavior between CFRP sheet and natural calcareous stones, Compos Part B - Eng 43 (8) (2012) 3239–3250. 180, 201

[156] M. Accardi, L. La Mendola, Stress transfer at the interface of bonded joints between FRP and calcarenite natural stone, in: Proc., IV Int. Seminar of Structural Analysis of Historical Constructions, Taylor and Francis, London, 2004, pp. 867–874. 152, 200

[157] B. Rosner, Percentage points for a generalized ESD many-outlier procedure, Technometrics 25 (2) (1983) 165–172. 163, 164

[158] H. Toutanji, W. Gomez, Durability characteristics of concrete beams externally bonded with FRP composite sheets, Cem Concr Compos 19 (4) (1997) 351–358. 180

[159] K. Benzarti, T. Nguyen, M. Frémond, P. Argoul, L. Central, P. Cedex, Durability of adhesively bonded joints: a predictive model coupling bulk and interfacial damage mechanisms, in: Proc. of the XVI ICCM conference, 2007, pp. 1–6. 180

Declaration of independent work

I herewith declare that I have produced this work without the prohibited assistance of third parties and without making use of aids other than those specified; notions taken over directly or indirectly from other sources have been identified as such. Furthermore, I state that all the work has been performed using original and allowed tools.

Finally, I formally declare that this thesis has not been previously presented in identical or similar form to any other German or foreign examination board and that no dissertation attempt has taken place before in this or any other institution.

The thesis work was conducted from 2011 to 2013 (corresponding to the XXVI Italian doctoral cycle) under the supervision of Prof. A. Vignoli (University of Florence) and Prof. H. Budelmann (Technische Universität of Braunschweig).

Parma, 20/03/2014